

AD-A090 042

NAVAL UNDERWATER SYSTEMS CENTER NEWPORT RI
DOPPLER SPECTRA OF BISTATIC REVERBERATION FROM THE SEA SURFACE. (U)
MAY 79 W I RODERICK

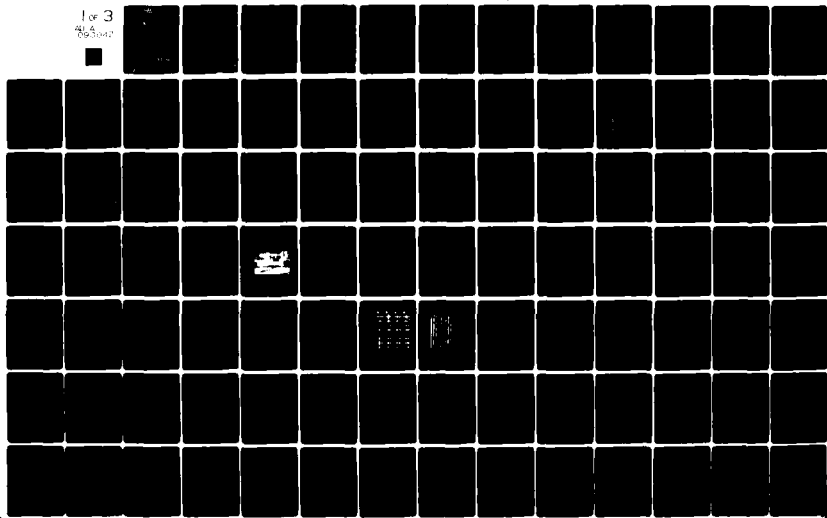
F/G 20/1

UNCLASSIFIED

NUSC-TR-6031

NL

1 of 3
44-853042



LEVEL ②
5
NUSC Technical Report 6031

AD A090042



NUSC Technical Report 6031



Doppler Spectra of Bistatic Reverberation From the Sea Surface

William I. Roderick
Special Projects Department

8 May 1979

DDC FILE COPY

NUSC
Naval Underwater Systems Center
Newport, Rhode Island • New London, Connecticut

Approved for public release; distribution unlimited.

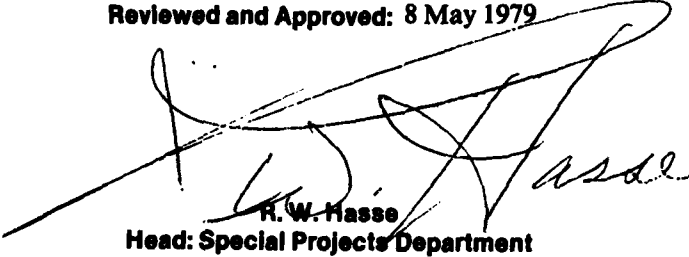
80 10 8 001

PREFACE

This report was accepted as a dissertation in partial fulfillment of the requirements for the degree of Doctor of Philosophy, Department of Electronic and Electrical Engineering, Faculty of Science and Engineering, University of Birmingham, England.

This work was accomplished under NUSC Project No. A-650-04, "Bistatic Surface Reverberation Measurements," Principal Investigator, William I. Roderick (Code 312). The sponsoring activity is the Naval Sea Systems Command, Program Manager, A. P. Franceschetti (Code SEA 06H1-4).

Reviewed and Approved: 8 May 1979



R. W. Hasse
Head: Special Projects Department

The author of this report is located at the
New London Laboratory, Naval Underwater Systems Center,
New London, Connecticut 06320.

NUSC - REPORT DOCUMENTATION PAGE			READ INSTRUCTIONS BEFORE COMPLETING FORM
1. REPORT NUMBER TR-6031	2. GOVT ACCESSION NO. AD-A090 042	3. RECIPIENT'S CATALOG NUMBER	
4. TITLE (and Subtitle) DOPPLER SPECTRA OF BISTATIC REVERBERATION FROM THE SEA SURFACE		5. TYPE OF REPORT & PERIOD COVERED 9 Doctoral thesis	
6. AUTHOR(s) William I. Roderick		7. CONTRACT OR GRANT NUMBER(s)	
8. PERFORMING ORGANIZATION NAME AND ADDRESS Naval Underwater Systems Center New London Laboratory New London, CT 06320		10. PROGRAM ELEMENT, PROJECT, TASK AREA & WORK UNIT NUMBERS A-650-04	
11. CONTROLLING OFFICE NAME AND ADDRESS Naval Sea Systems Command SEA 06H1-4 Washington, DC 20362		12. REPORT DATE 8 May 1979	
13. MONITORING AGENCY NAME & ADDRESS (if different from Controlling Office) Q263		14. NUMBER OF PAGES 254	
15. SECURITY CLASS. (of this report) UNCLASSIFIED		16. DECLASSIFICATION/DOWNGRADING SCHEDULE	
17. DISTRIBUTION STATEMENT (of this Report) Approved for public release; distribution unlimited.			
18. DISTRIBUTION STATEMENT (of the abstract entered in Block 20, if different from Report)			
19. SUPPLEMENTARY NOTES			
20. KEY WORDS (Continue on reverse side if necessary and identify by block number) Directional Spectrum Doppler Spectrum Sea Surface Reverberation			
21. ABSTRACT (Continue on reverse side if necessary and identify by block number) The Doppler spectra of sea surface reverberation have been investigated in a shallow water environment. A parametric array projected a narrow beam of acoustic energy at the surface and insonified on the surface a well-defined scattering area of limited extent. The surface generated reverberation was received on eight closely spaced hydrophones of a vertical array. The power spectral densities of the instantaneous reverberation -- the Doppler spectra -- were of primary interest in the analyses of the reverbera-			

20. (Continued)

tion data. Doppler spectra were measured as a function of the transmitted parametric difference frequency, the angle of incidence of the array to the sea surface, and the angle of scatter of the reverberation to the receiving hydrophones.

In concert with the reverberation experiment, the directional spectrum of the sea surface waves was measured with an acoustic wave height sensing system. A line array of acoustic wave height sensors simultaneously measured the time varying wave height at five discrete points on the sea surface.

Both the acoustic and oceanographic data processing involved the fast Fourier transform (FFT) processing of time series data segments. Segment weighting and (overlap) averaging were used to reduce frequency leakage and estimate variability. Doppler shifts, bandwidths, and the coefficients of variation of the spectral estimates were computed for the Doppler spectra. The sea surface directionality was computed via a spatial Fourier transform of the cross-spectral densities obtained from various combinations of wave height sensor pairs. Conventional 'delay and sum' methods and a high resolution maximum likelihood method were used in the computation of wavenumber spectral estimates.

Analyses of the Doppler spectra show a direction of Doppler shift in accordance with the direction of propagation of the surface waves. Also, the Doppler bandwidths are seen to increase with increasing transmit frequency and decrease with increasing incident angle. There is negligible variation in Doppler shift and bandwidth with scattering angle. The coefficients of variation of the spectral estimates are frequency dependent showing a minimum variability near the Doppler shift frequency and much higher variability on either side of the shift frequency.

It is concluded that the surface reverberation Doppler spectra and the sea surface directional spectrum represent a unique data collection that can be used for theoretical reverberation model development and subsequent model verification. Furthermore, the Doppler spectra are applicable to the system design and performance prediction of surface reverberation-limited sonar systems operating in low sea states and at similar sonar frequencies.

ACKNOWLEDGMENTS

As an external candidate for the degree of Ph.D., the author was fortunate to have Dr. H. O. Berkay as a university thesis supervisor and Dr. H. W. Marsh as an external supervisor. Their encouragement, guidance, and interest were especially appreciated.

The author is indebted to the Naval Underwater Systems Center for both the educational opportunity and the technical support. Thank you to S. C. Jackson for helping with equipment setup at the Block Island Facility; to R. W. Carone for fabrication of the surface wave measuring system; and to D. M. Potter and W. G. Kanabis for their computer programming services. The mechanical engineering support of P. S. Seaman for installing the underwater equipment was invaluable.

The author acknowledges the administrative support of his division supervisor, W. R. Schumacher, and the encouragement from his branch supervisor, Dr. F. R. DiNapoli, and former branch supervisor, S. R. Santaniello.

Many thanks to P. Herstein for his informal review of this thesis, and to S. Goos for her expert typing services.

Accession No.	_____
NTIS GRA&I	_____
DTIC TAB	_____
Unannounced	_____
Justification	_____
By _____	_____
Distribution	_____
Availability Code	_____
Dist	_____
Special	_____

TABLE OF CONTENTS

	<u>Page</u>
CHAPTER 1 <u>AN OVERVIEW</u>	
1.1 Introduction	1
1.2 Thesis Proposition Statement	1
1.3 Experimental Procedure	2
1.4 Experimental Precedents	2
1.5 Experimental Limitations	2
1.6 Previous Doppler Spectra Measurements	3
1.7 Thesis In Brief	6
CHAPTER 2 <u>ENVIRONMENTAL AND ACOUSTICAL PARAMETERS</u>	
2.1 Environment	9
2.11 Background	9
2.12 Experimental Site	9
2.2 Acoustic Parameters	11
2.3 Environmental and Acoustical Data Collection	14
CHAPTER 3 <u>PARAMETRIC ARRAY TRANSMISSION</u>	
3.1 Introduction	17
3.2 Primary Beam Characteristics	18
3.3 Parametric Array Characteristics	24
3.4 Transmitting System	27
3.5 Angle of Elevation: Control and Indication	34
CHAPTER 4 <u>ANALOGUE CONDITIONING AND DIGITAL CONVERSION OF REVERBERATION SIGNALS</u>	
4.1 Introduction	35
4.2 Hydrophones	35
4.3 Receiving System	37
4.4 Tape Recording and Playback System	37
4.5 Analogue-to-Digital Conversion	42
CHAPTER 5 <u>DIGITAL PROCESSING OF REVERBERATION SIGNALS</u>	
5.1 Introduction	43
5.2 Doppler Spectra Estimates	44
5.21 Formulating the Discrete Fourier Transforms	44
5.22 Choice of Data Window	45
5.23 Statistical Confidence of Doppler Spectra Estimates	47
5.24 Removal of Sinusoidal Interference	48
5.25 Linear Frequency Modulated Waveforms	52
5.3 Doppler Shifts and Bandwidths	53
5.4 Reference Signal Power Spectrum, Example of	54
5.5 Reverberation Doppler Spectra, Examples of	54
5.6 Coefficient of Variation of Spectral Estimates	58

TABLE OF CONTENTS (Cont'd)

	<u>Page</u>
CHAPTER 6 DOPPLER SPECTRA RESULTS	
6.1 Background	63
6.2 Doppler Spectra at Near Normal Incidence	64
6.3 Dependence of Doppler Spectra on Incidence Angle	64
6.4 Dependence of Doppler Spectra on Scattering Angle	68
6.5 Coefficient of Variation	68
CHAPTER 7 ESTIMATION METHODS FOR DETERMINING THE DIRECTIONAL CHARACTERISTICS OF THE SEA SURFACE FROM A LINE ARRAY OF WAVE HEIGHT SENSORS	
7.1 Introduction	73
7.2 Line Array Sensor Spacing and Orientation	74
7.3 Acoustic Surface Wave Sensing System	76
7.4 Sea Surface Properties	76
7.41 Some Spectral Properties of Sea Surface Waves	76
7.42 Spectrum of a Propagating Plane Wave	80
7.43 Effects of Temporal and Spatial Windows on Wavenumber- Frequency Spectrum	81
7.44 Determination of Surface Wave Directionality from a Line Array of Sensors	84
7.5 Estimation of Wavenumber Component-Frequency Spectrum from a Line Array Using Conventional Methods	85
7.6 Estimation of Wavenumber Component-Frequency Spectrum from a Line Array Using a High Resolution Maximum Likelihood Method	89
7.7 Digital Processing of Wave Height Data and Estimation of Normalized Cross Spectral Densities	95
7.8 Estimation of Directional Spectra from Cross-Spectral Density Estimates	98
CHAPTER 8 SEA SURFACE DIRECTIONALITY AND OTHER SPECTRAL ESTIMATES	
8.1 Introduction	101
8.2 One-Dimensional Wave Spectrum	101
8.3 Normalized Cross-Spectral Density Estimates	102
8.4 Comparison of Directional Estimation Methods	103
CHAPTER 9 CONCLUSIONS AND RECOMMENDATIONS FOR FUTURE RESEARCH	
9.1 Experiment in Review	119
9.2 Spectral Results in Review	120
9.3 Recommendations for Future Research	121
APPENDIX A REMOVAL OF SINUSOIDAL COMPONENT FROM REVERBERATION DATA.	123
APPENDIX B DIGITAL PROCESSING OF LFM REVERBERATION DATA	125

TABLE OF CONTENTS (Cont'd)

	<u>Page</u>
APPENDIX C <u>EXAMPLES OF DOPPLER SPECTRA ESTIMATED FROM REVERBERATION MEASURED ON TWO HYDROPHONES</u>	129
APPENDIX D <u>AN ACOUSTIC SYSTEM FOR MEASURING THE WAVE HEIGHT OF SEA SURFACE WAVES</u>	195
APPENDIX E <u>A FIVE SENSOR ACOUSTIC SYSTEM FOR MEASURING SURFACE WAVE DIRECTIONALITY</u>	205
APPENDIX F <u>DIRECTIONAL SPECTRUM OF THE SEA SURFACE</u>	209
REFERENCES	245

LIST OF SYMBOLS

a	piston radius, or shift in weighting function
$a(t)$	time varying envelope
A	an amplitude
A_{11}, A_{12}, A_{22}	constants
$A(X, f), A_{jl}(f)$	cross-spectral density
$A_k(n)$	Fourier coefficient
α	probability interval, or a constant, or a trigonometric substitution
α_T	absorbtion coefficient
B	a constant, or bandwidth
$B(f_n), B_{jm}(f_n)$	Fourier coefficient
$B(t-t_2)$	bottom reverberation signal
β	trigonometric substitution
$B(k_x)$	directional response
C	velocity of sound
$C(f)$	phase speed
C_1, C_2	summation values
C_n	amplitudes of sinusoidal components
CV	coefficient of variation
$C_{jl}(f)$	cospectrum of cross-spectral density
d	closest sensor separation
$D(\theta), D_R(\theta)$	directivity patterns
$D(f)$	Doppler spectrum
$D(\phi, f)$	directional wave spectrum
$D(t-t_0)$	direct path signal
DI	directivity index

δ	Dirac delta function
Δt	time interval
E	transducer efficiency
$E(t)$	electrical interference signal
$E(\alpha, \beta)$	mean square error
f, f_o, f'	acoustic, or surface frequency
f_d	difference frequency
f_i, f_j	instantaneous frequency and translated frequency
f_p, f_{p+q}	lower and upper frequency in reverberation spectrum
f_{ds}	Doppler shift frequency
f_{sp}	symmetrical power frequency
g	acceleration of gravity
$g(t)$	a time function
$G(f)$	Fourier transform of $g(t)$
G	roughness parameter
$G(\phi_m, f_m)$	a directional spectrum
$h(x, y, t)$	surface wave height
H	an amplitude
θ	angle of incidence, or angle for beampattern response
θ_d	half-power beamwidth
$\theta(f)$	argument of complex coherence
i	$\sqrt{-1}$, or an index
j	an index
$J_1(\cdot)$	first order Bessel function of the first kind
k	an index, or a wavenumber
k_o	acoustic, or surface wavenumber

k_x, k_{xo}	x axis wavenumber component
k_y, k_{yo}	y axis wavenumber component
$k_$	wavenumber of difference frequency
K	number of sensors, or LFM slope
l	an index
L	surface roughness wavelength, or number of spacings, or number of disjoint segments
L_o	source level
λ, λ_o	acoustic wavelength
Λ	surface wavelength
m	an index
M	number of reverberation records, or number of segments
O_F	overlap fraction
$p(t)$	time dependent pressure
P	final value in the limits of a summation, or maximum number of unique separation distances
P_o, P_1	pressure amplitudes
$P(f)$	power spectral density
$P(k_x, f)$	high resolution computation of wavenumber component-frequency spectrum
$q_{j1}(f)$	element of inverse cross-spectral density matrix
Q	final value in the limit of a summation
$Q_{j1}(f)$	quadrature spectrum
r	distance
r_{10}	depth of transducer
$r(t)$	time dependent reverberation

$r_k(j)$	samples of reverberation record
R	resistance, or distance from transducer to sea surface
$R(k_x, k_y, f)$	wavenumber-frequency spectrum
$\rho(\tau)$	temporal correlation
$\rho(x, y, \tau)$	spatial-temporal correlation function
S	area of transducer, a value in the limits of a summation
$s(t-t_1)$	surface reverberated signal
$s(k_x, f)$	spatial lag weighting computation of wavenumber component-frequency spectrum
$s'(k_x, f)$	spatial weighting computation of wavenumber component-frequency spectrum
$s(\phi, f)$	directional spectrum of surface waves
σ	RMS wave height
t, t_o, t_1, t_2	time
t_j	multipath arrival time
T	pulse length, or a repetition period, or a segment length
T_T	total record length
$T(t)$	a received signal
τ	time delay
U	wind speed
v_p	peak voltage
ϕ	angle of scatter, or a phase angle, or an azimuthal angle
ϕ_n	phase angles
w_j	spatial weights
$w(t)$	time dependent window
$w(j)$	data window
$w(X)$	spatial lag window

$w(X, Y, \tau)$	spatial-temporal window
W	a value in limits of a summation
$W(f)$	Fourier transform of time dependent window
$W(k_x, k_y, f)$	Fourier transform of spatial-temporal window
$W(k_x)$	Fourier transform of spatial lag window
x	a spatial coordinate
x_k, x_1	location of wave height sensors, samples of a reverberation return
X	spatial lag in x coordinate
χ	variable for Chi-square distribution
y	a spatial coordinate
$y(t)$	low frequency band of LFM product signals
$y'(t)$	product of transmitted and received LFM signals
Y	spatial lag in y coordinate
z	axial distance
$z(t)$	sum of multipath LFM signals
ω_0	angular frequency
$\langle \cdot \rangle$	ensemble average
$\hat{\cdot}$	estimate
\star	complex conjugate
\otimes	convolution
E	expected value
H8	designation, e.g., hydrophone eight
LFM	linear frequency modulation
MRA	maximum response axis

Prob	probability
RMS	root mean square
Var	variance

CHAPTER 1

AN OVERVIEW

1.1 INTRODUCTION

An active sonar system is often required to detect a target echo in the presence of a background noise interference that is signal generated. The signal generated noise is caused by scattering of the transmitted signal from either of the ocean's rough boundaries or by volume inhomogeneities. This type of background noise is known as reverberation.

For active sonar systems that propagate energy in shallow water, surface duct, bottom bounce, or convergence zone modes, the limiting background noise is often reverberation from the sea surface. Since the sea surface is spatially rough and time varying, the reverberated signals are modulated in amplitude and phase. Hence, the frequency (Doppler) spectrum of the reverberation is not the same as the transmitted frequency spectrum. Likewise, the frequency spectrum of the target echo differs from the transmit spectrum by an induced Doppler shift.

Intuitively, if the Doppler shift of the target echo is much greater than the effective bandwidth of the reverberation, then the sonar system's performance is not degraded by reverberation. Of course, this assumes that the sonar system has the appropriate spectral analysis capability. The system would be limited by other background interferences such as own ship's noise, ambient noise, or electrical noise. Hence, some of the pertinent questions for system design and performance prediction are simply: How is the reverberation power distributed in frequency and what relationship does the characteristics of the reverberation frequency spectrum have with the oceanographic, acoustic, and geometric factors that affect the reverberation process?

1.2 THESIS PROPOSITION STATEMENT

The Doppler spectrum of sea surface acoustic reverberation was measured in a shallow water experiment. The experimental objectives were to obtain the power spectral densities of the instantaneous reverberated signals as a function of acoustic frequency, angle of incidence and angle of scatter.

Supporting meteorologic and oceanographic data were obtained in concert with the acoustic measurements. Wind speed, wind direction, and the directional wave spectrum of the sea surface waves were the measured quantities. The environmental data were obtained to provide the required inputs to theoretical reverberation prediction models.

1.3 EXPERIMENTAL PROCEDURE

The experiment was conducted in the shallow waters of Block Island Sound (see Fig. 2-1). A parametric array was used to project a narrow beam of acoustic energy at the sea surface and insonify on the sea surface a well-defined scattering area of limited extent. The surface generated reverberation was received on eight closely spaced hydrophones of a vertical array. To generate reverberation signals that were statistically stationary, many waveforms of sufficiently long pulse length were transmitted. The reverberation was measured at various values of the transmitted difference frequency produced by the parametric array. Also, the angle of elevation of the array was electromechanically varied, and reverberation was measured at various values of the angle of incidence. Together with the reverberation measurements, the directional spectrum of the sea surface was measured with an array of wave height sensors. The sensors simultaneously measured the time varying wave height at discrete points on the sea surface.

A time period of eight hours was required to obtain a complete oceanographic-acoustic data set. This necessitated that the sea surface remain statistically stationary during the measurements. After many days of false starts - due to either equipment failures or nonstationary sea conditions - a complete data set was obtained. During the measurements, acoustic propagation was under isovelocity conditions and there was no evidence of a near-surface bubble layer.

1.4 EXPERIMENTAL PRECEDENTS

A parametric array was used as an acoustic projector. The array attributes of narrow beamwidth, absence of sidelobes, and broadband frequency coverage, made the array highly desirable in the shallow water environment.

The measurements were bistatic (projector and receiver in different locations) with a total of eight hydrophones to receive the surface reverberation. For each angle of incidence of the transmitted beam to the surface, the reverberation was received in a vertical plane at eight angles of scatter.

Since the directional properties of the sea surface are a required input to reverberation prediction models, the directionality of the surface waves was estimated from an array of wave height sensors. Thus, the acoustic and oceanographic data presented in this thesis may be used for reverberation model validation.

1.5 EXPERIMENTAL LIMITATIONS

Although the experiment was unique with respect to acoustic projector, multiple receivers, and oceanographic capability; the experiment also had its limitations: the broadband capability of the parametric source was utilized to obtain reverberation measurements at four pulsed CW frequencies covering the frequency band 3.5 to 9.0 kHz. The lowest transmitted frequency for obtaining data was limited by the low reverberation-to-noise ratio. (As

transmitted difference frequency is decreased, parametric array source level also decreases at approximately 12 dB/octave; and ambient noise increases at approximately 6 dB/octave.) The highest transmitted frequency was limited by the rapid drop off in receiving sensitivity (20 dB/octave) and also by the undesirable beampattern characteristics of the hydrophones at high frequencies. It should be noted that the vertical array of transducers used as hydrophones were not designed for this experiment, but were previously implanted in the Sound for other acoustic measurements. The beampattern characteristics of the hydrophones prohibited the absolute measurement of reverberation level.

The maximum incidence angle to the surface was restricted to about 60° (30° grazing) because of the low reverberation-to-noise ratio (sea surface scattering strength decreases with increasing incidence angle).

Even though a parametric array was used as a projector, multipath arrivals could not be entirely eliminated, particularly direct path and bottom scattered arrivals. Also, electrical pickup was another source of interference.

Lastly, the directional spectrum was measured from a line array of wave height sensors. The highest measurable surface wave frequency was approximately 1.2 Hz.

1.6 PREVIOUS DOPPLER SPECTRA MEASUREMENTS

Since World War II, the main emphasis in surface reverberation has been focused on determining the scattering strength of the sea surface. In particular, the research has been concerned with measuring and theoretically predicting the scattering strength with respect to acoustic frequency, grazing angle and sea state. The empirical equations of Chapman and Harris have been the most comprehensive and are presently the basis for most reverberation level model predictions [1-1]. However, the scattering strength parameter in a reverberation model has only limited usefulness. It does not answer how the reverberation power is distributed in frequency. With the advent of advanced signal processing systems, the Doppler spectrum of the reverberation power is important to sonar system design and performance prediction.

Previous acoustic Doppler spectra measurements have been conducted in tanks, a river, and shallow waters. Since there have been only a few measurements, the experimental techniques and results will be sited below.

The earliest experiment that measured the Doppler spectrum of surface scattered acoustic waves was performed by Liebermann [1-2]. Acoustic waves in air were scattered from capillary waves generated in a water tray by agitating the water surface with an electrodynamic transducer driven by white noise. Capillary water waves covered the frequency band 100 - 250 Hz. The acoustic source was projected at an incidence angle of 70° to the surface and the scattered energy was received at a 56° scattered angle.

Liebermann concluded that out of a broad spectrum of surface wave frequencies the wavelength most effective in scattering the acoustic energy is given by the familiar diffraction grating equation $L = \lambda (\sin\theta + \sin\phi)^{-1}$, where

L is the wavelength of the roughness, λ is the acoustic wavelength, and θ and ϕ are the respective angles of incidence and scatter. With the use of the dispersion equation for capillary waves, the Doppler shift of the scattered energy could be predicted.

In the experiment, the carrier frequency of the incident radiation was 78 kHz and the frequency content of the scattered energy was analyzed with a commercial spectrum analyzer. The spectral peak of the scattered energy was observed to be Doppler shifted from the carrier by 160 Hz -- no reference was made as to whether it was an up or down Doppler. The bandwidth of the reverberation (between halfpower points) was approximately 30 Hz. The theoretically predicted Doppler shift of 167 Hz was in close agreement to the measured value.

Mellen conducted the first underwater acoustic experiment that measured the Doppler spectra of surface generated reverberation [1-3]. The experiment took place in the Thames River estuary (CT, U.S.A.) using directional transducers resonant at 85 kHz and 1400 kHz. The angle of incidence with the river surface was fixed at 45° and the reverberation was received at the same angle with transducers identical to the transmit. Using a suitably calibrated single sideband receiver, a magnetic tape loop, and a narrow band spectrum analyzer, the frequency spectrum of the reverberation was measured.

Estimated wind speed during the experiment was 10 m/sec and the acoustic energy was launched down wind. At a transmit frequency of 85 kHz the bandwidth of the reverberation was approximately 50 Hz and the reverberation peak occurred at a Doppler shift of 25 Hz below the carrier. Mellen computed a theoretical Doppler shift of 19 Hz using the diffraction grating equation and the dispersion equation for gravity waves. Also, the measured down Doppler is in qualitative agreement with the direction of transmit, i.e., down wind.

Under the same wind conditions and geometry, but at a transmit frequency of 1400 kHz, the bandwidth of the reverberation increased to 400 Hz and the reverberation peak shifted to 420 Hz below the carrier. Using the same equations as Liebermann, the theoretical prediction of a 1030 Hz Doppler shift was not in good agreement with the measured. It was suggested that nonlinear surface effects were dominant, and thus the poor agreement with a theory based on linear assumptions.

In a tank experiment, Roderick measured the Doppler spectra of off-specular scattering from a traveling sinusoidal surface [1-4]. A gravity wave of known frequency, wave length, and wave height was generated on the water surface. Three identical acoustic transducers, resonant at 500 kHz, were projected at the water surface - for transmitting, receiving in the specular (reflection) direction, and receiving in the off-specular direction (towards backscatter).

The surface reflected and scattered received signals were amplified, filtered, bandshifted, and recorded on magnetic tape for later spectral analysis. A time compression spectrum analyzer was used for spectral analysis.

The effects of surface wave directionality were investigated at high gravity-wave frequencies. An offspecular receiver was directed at the surface, 10° from the specular direction, and 20° from the normal. A 6 Hz water wave frequency was generated on the surface with wavefronts propagating equivalent to an up wind condition. An up Doppler was measured at frequencies of 6 Hz and 12 Hz above the carrier frequency; which indicated the presence of second order scattering. The direction of surface wave propagation was reversed and a down Doppler was measured at frequencies of 6 Hz and 12 Hz below the carrier.

Igarshi and Stern, using transducers resonant at 15 kHz and 60 kHz, measured the Doppler shifts of reverberation at sea from a ship [1-5]. The transducers were rotatable in azimuth such that measurements could be obtained in up, down, and crosswave conditions. Sea wave conditions were monitored by visual observations; during the experiment wind speeds varied in the range 11 - 14 kts.

Most of the data were obtained at a grazing angle of 30° and with a transmitted pulse length of 110 msec. The data were processed on a commercial spectrum analyzer. It was observed that the Doppler shift was greater for the higher transmit frequency and was of the order of 10 - 20 Hz. Also, the Doppler shift systematically decreased to zero as the transducer was rotated from an upwave (or downwave) condition to a crosswave condition. At the 15 kHz transmit frequency the Doppler shift and bandwidth of the reverberation were much less and the spectrum of the reverberation retained the characteristics of the transmitted spectrum.

In a theoretical study of the spectral characteristics of reverberation, Faure established a relationship between the transmit signal spectrum and the spectrum of the reverberation [1-6]. The power spectrum of the reverberation was shown to be proportional to the convolution of the signal spectrum and the probability density of the Doppler shift. In turn, the Doppler shift probability density was functionally related to the probability density of the scatterer velocities. Thus, as in the Igarshi and Stern experiment, the transmit spectrum at 15 kHz dominated the convolution and the reverberation spectrum retained the transmit spectral shape.

Although the experimental results of Igarshi and Stern tend to confirm that the Doppler shift can be simply predicted from first order diffraction theory, the results of Swarts do not [1-7]. In the Swarts experiment, a bottom mounted transducer was rotated in azimuth to measure the effects of surface wave propagation. At a frequency of 28.2 kHz and a grazing angle of approximately 30° , Doppler shifts of 10 - 15 Hz were observed when transmitting either down or upwave. From diffraction theory, the predicted shift was 8.2 Hz. Also, the Doppler shift did not differ in data obtained at two quite different sea states.

As a final note, Crowther has described in a report (which, to my knowledge, does not appear in the open literature) a reverberation experiment that scattered 10 kHz sound from the sea surface [1-8]. It was found that the spectral shape of the reverberation appeared to be approximately Gaussian and there was no evidence of a narrow Doppler shifted spectral component predicted by resonant scattering theory.

1.7 THESIS IN BRIEF

Beginning in the next chapter, the physical layout of the experimental site and its surrounding environment is described. Emphasis is placed on the acoustic and geometric parameters involved in the experiment and the data collection procedure.

The parametric array and transmitting system is presented in CHAPTER 3. Because of the uniqueness of the parametric array in surface scattering experiments, considerable attention is given to the measured source level and beam-pattern characteristics. Presented are measurement results of parametric array primary and secondary fields which were obtained prior to implanting the array in Block Island Sound. The angle of elevation control and sensing system are briefly described. As would be expected following the discussion of the transmission system, the receiving system is presented in CHAPTER 4. Described is the analogue conditioning system from the hydrophone output to the tape recording input. Also presented are the tape recording procedures and the subsequent analogue-to-digital conversion.

Digital processing techniques for computing the Doppler spectra of the sea surface reverberation is presented in CHAPTER 5. The Doppler spectra were computed using fast Fourier transform (FFT) techniques. A discussion is given of the procedures for (1) removing a direct path interference from the data, (2) the windowing of the data samples to reduce frequency leakage, and (3) the ensemble averaging of power spectral densities to obtain estimates of the true Doppler spectra. The Doppler shift, Doppler bandwidth, and the coefficient of variation computations are also described.

Most importantly, in CHAPTER 6, the Doppler spectra results are presented and discussed in terms of their functional dependence on transmitted frequency, angle of incidence and angle of scatter.

Putting the reverberation aside, the measurement techniques and digital processing procedures for obtaining the directional wave spectrum of the sea surface waves is described in CHAPTER 7. Described is an acoustic wave measuring system that simultaneously measured the time varying wave height at five discrete points. This description is followed by the digital processing procedures that were used to compute the crossspectral densities from the five sensors using overlapped segments of weighted wave height data. A description is given of two conventional methods and a high resolution technique for estimating a surface wavenumber component-frequency spectrum.

In CHAPTER 8, a discussion is given of the directional spectra as a function of azimuthal angle. Other sea surface statistics are also presented.

Lastly, CHAPTER 9 gives the conclusions drawn from the acoustic and oceanographic measurements and recommendations are made for theoretical comparisons.

The appendices have been left for presentation of material believed to have been too detailed for inclusion in the main chapters. For example, the methods used in removing a sinusoidal component from the reverberation data are given in APPENDIX A. In an attempt to remove multipath interference,

linear frequency modulated (LFM) pulses were transmitted. The LFM waveform was also used to compute the Doppler spectrum and the technique is described in APPENDIX B. Some representative Doppler spectra are presented in CHAPTER 6. However, APPENDIX C contains the spectra and coefficient of variations obtained on two hydrophones, at four angles of incidence, and at four transmitted frequencies. A paper presented at the Eighty-Fourth Meeting of the Acoustical Society of America described the acoustic technique used to measure sea surface waves and is given in APPENDIX D. The electronic features of the transmit and receive system for the five sensor array are presented in APPENDIX E. Lastly, in APPENDIX F, the directional spectra of the surface waves are presented for the high resolution estimation method.

CHAPTER 2

ENVIRONMENTAL AND ACOUSTICAL PARAMETERS

2.1 ENVIRONMENT

2.11 BACKGROUND

The experiment was conducted in Block Island Sound, about 1.6 km northwest of Block Island, Rhode Island. The Sound is partially closed by land masses with Rhode Island 18 km to the north of the experimental site (Fig. 2-1). South to southwest of the site is the Atlantic Ocean; and southwest to northwest is a group of islands with Long Island, New York, the closest - 25 km away.

There has not been a detailed study of wind speeds and directions in the Sound. But some unpublished data reveal that the wind speeds are uniform across the Sound, highly variable on a day-to-day basis, and the predominant wind directions are from a southwest to northwest sector.

Water depth is fairly constant throughout the Sound at a mean depth of 33.5 m. The bottom topography at the site and in the eastern sector of the Sound is relatively flat and smooth [2-1]. However, divers have observed small amplitude sand waves in the vicinity of the site.

Archival data obtained from bathythermograph measurements show that the sound velocity structure in the Sound varies from a negative gradient in the summer to a slightly positive gradient in the winter [2-2]. The reverberation measurements were conducted in early October and for this time of year the velocity profile is isovelocity. A typical velocity for early October is 1509 m/sec.

The experimental site was situated close to the entrance of New Harbor, Block Island. Fishing trawlers and pleasure craft transiting the entrance were occasional sources of high ambient noise levels. Also, Coast Guard buoys which delineated the site, were sources of ambient noise transients due to the rattling of chains which tethered the buoys to anchors. Except for these variations, the shallow water ambient noise spectrum levels were wind dependent [2-3].

2.12 EXPERIMENTAL SITE

For the reverberation measurements, a parametric array was used as an acoustic projector and a vertical array of eight transducers was used to receive the reverberated signals. The transducers were mounted to a tower and the tower was supported at its base by a barge submerged in a water depth of

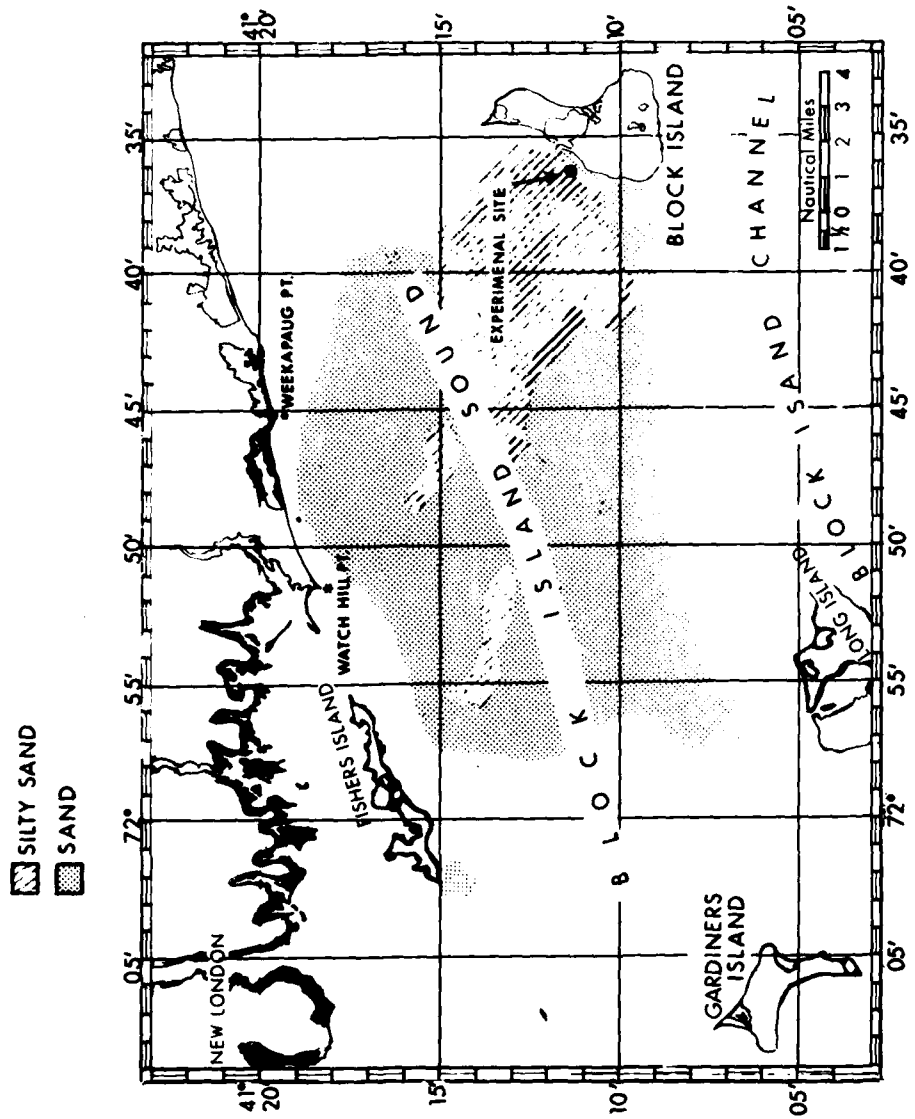


Figure 2-1. Block Island Sound and Location of Experimental Site

30.5 m (Fig. 2-2). The transducer array was not implanted for this experiment, but had been used in previous propagation measurements. Both the source and the hydrophones were cabled separately to a shore facility on Block Island via two multiconductor armored cables.

The parametric array was positioned on the barge deck, at an approximate depth of 27 m below the sea surface, and facing the direction of the prevailing winds at a bearing of 278°. The acoustic axis of the parametric array was aligned in a plane with the hydrophone array and separated from the array by 4.2 m. The center of the source was 0.61 m above the barge deck and could be rotated to point directly at a particular hydrophone as well as projected at the sea surface.

Eight of the linearly spaced hydrophones, with 1.04 m spacing, received the surface generated reverberation. The first hydrophone, hydrophone H1, was positioned 0.2 m above the barge deck.

To measure the directional characteristics of the sea surface, five upward looking transducers (inverted fathometers) were used to measure the time varying wave heights at five discrete points, simultaneously. The transducers were positioned in a horizontal line array with nonlinear spacings. There was a separation of 30.5 cm between two of the closest transducers and a maximum separation of 274.3 cm between the two most distant transducers. Using dual combinations of the five transducers it was possible to obtain contiguous discrete spacings at multiples of 30.5 cm from the array configuration. The array of wave height sensors were supported by the tower at a depth of approximately 3 m below the surface. To obtain the best resolution, the array was oriented such that broadside to the array faced the direction of the prevailing winds. A broadside bearing of 278° was chosen; thus endfire was on a bearing of 008°. As expected, a priori information was required with the line array to determine from which side of the array the surface waves were propagating. Visual observations of the sea surface and wind direction monitoring were used to resolve the front-to-back ambiguity of the array. The same multiconductor cable that powered the parametric array was used for transmitting/receiving with the acoustic wave height sensors.

2.2 ACOUSTIC PARAMETERS

During the measurements the velocity of sound was isovelocity. Hence, the angle of elevation at the parametric array was also the angle of incidence at the surface and refractive corrections were unnecessary.

Acoustic data were obtained at four angles of incidence: -4.7, 20, 40, and 60°. The -4.7° angle provided a specular reflection from the sea surface to hydrophone H4. Table 2-1 gives the scattering angles to each hydrophone associated with each angle of incidence.

At each angle of incidence the broadband capabilities of the parametric array were used to transmit sequentially four frequencies: 3.5, 5.0, 7.0 and 9.0 kHz. The narrow beamwidth of the array (3° between half-power points) was virtually independent of transmit frequency (see CHAPTER 3). The insonified area was also independent of transmitted pulse length; i.e., the

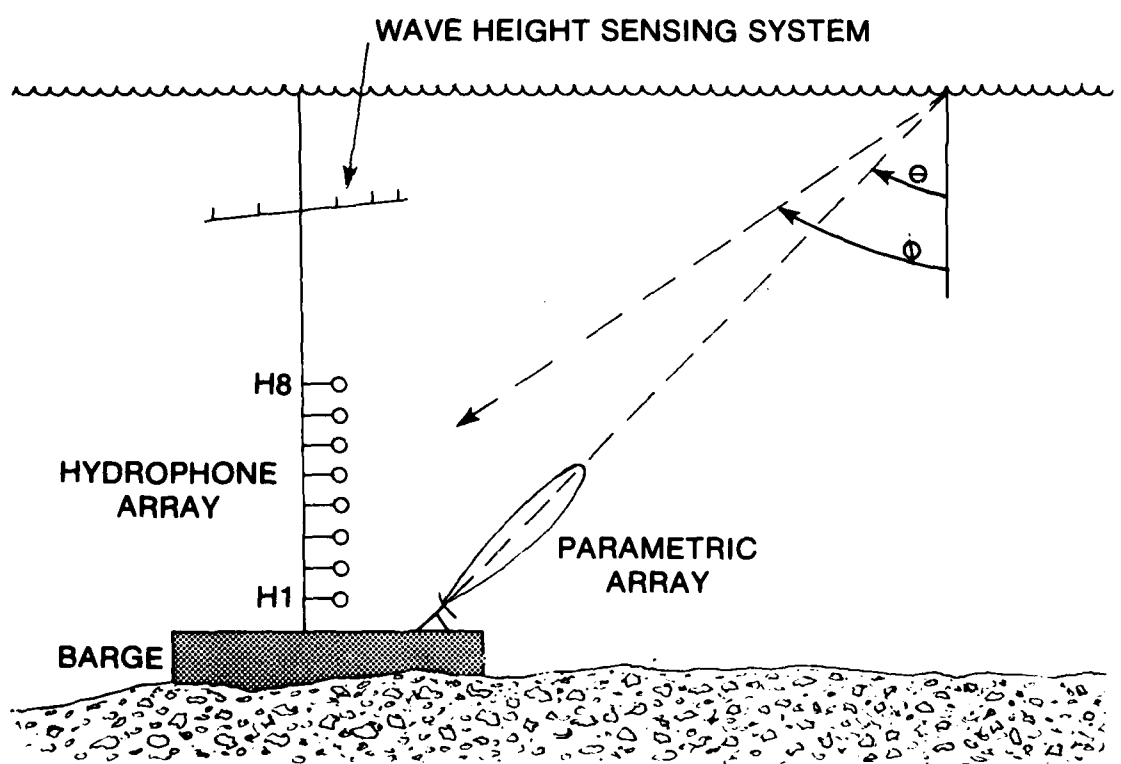


Figure 2-2. Relative Locations of Parametric Array, Hydrophone Array, and Wave Height Sensing System at Experimental Site. θ is the Angle of Incidence and ϕ is the Angle of Scatter.

Table 2-1. Scattering Angles to
the Eight Hydrophones Associated
with Each Angle of Incidence. H
Designates Hydrophone Number and
 θ Designates Angle of Incidence.

H \ θ	-4.7	20	40	60
1	4.1	27.1	44.4	61.7
2	4.3	28.0	45.5	62.6
3	4.5	29.0	46.7	63.6
4	4.7	30.0	47.9	64.5
5	4.9	31.0	49.1	65.5
6	5.1	32.3	50.4	66.5
7	5.3	33.5	51.8	67.4
8	5.6	34.9	53.2	68.5

transmitted pulse length was long enough to fill the entire beam of the parametric array and the surface reverberating area was dependent on the beamwidth alone [2-4]. The insonified area varies with incident angle; as an example, the area was a maximum of 11 m^2 at a 60° incident angle.

Although the parametric array could restrict the scattering area on the sea surface; it could not completely eliminate multipath interference. The major contributors to multipath interference were direct path and bottom scattered arrivals. The intensity of the direct path varied with parametric array elevation and hydrophone location, and was on the order of 55 dB down from the intensity on the maximum response axis of the parametric array. The direct path propagation time depended on hydrophone location and was approximately 2.8 to 5.7 msec. The difference in propagation time between direct and surface scattered paths was greater than 25 msec at all acoustic geometries. The bottom scattered interference paths resulted from acoustic energy in the parametric beam being initially reflected from the sea surface, propagated to the sea bottom, and then scattered by the bottom sand waves (Fig. 2-3). Bottom scattered energy could arrive at the hydrophones either by a direct return from bottom-to-hydrophone or by a return that involved another surface reflection. Observations of measured propagation time revealed that the preferred return was via the surface reflected path, i.e., direct backscatter along the incident path. Also, the difference in propagation time between the surface scattered and bottom scattered paths was greater than 25 msec.

To measure the reverberation Doppler spectra and to investigate the effects of multipath interference, the following waveforms were transmitted: 1000 msec pulsed CW, 25 msec pulsed CW and 500 msec linear frequency modulated (LFM) pulses with a 100 Hz bandwidth. The repetition period of all three waveforms was much longer than the time dispersion due to multipath.

The waveforms were transmitted to (1) determine the Doppler spectra of the surface reverberation, (2) determine the effects of multipath interference on the desired surface reverberated signals and (3) to resolve the multipath interference signals and obtain the Doppler spectra of the isolated surface reverberated signal with sufficiently high resolution. The 1000 msec pulsed CW waveform was the primary signal used to obtain the Doppler spectra of the surface reverberation. The spectral resolution of this pulse was on the order of 1 to 2 Hz, depending on the time window chosen for the digital processing (see CHAPTER 5). The 25 msec pulsed CW waveform was sent to resolve the multipath arrivals. Also, the LFM signal waveform was sent to both resolve the multipath arrivals and to obtain the Doppler spectra of the surface reverberation. The technique of obtaining the Doppler spectra of the reverberation utilizing LFM transmissions is discussed in CHAPTER 5 and APPENDIX B.

2.3 ENVIRONMENTAL AND ACOUSTICAL DATA COLLECTION

The following procedure was used in obtaining an environmental and acoustical data set. First, the wave heights were measured simultaneously and continuously for one hour and recorded on magnetic tape. For the next seven hours, the reverberation data were obtained. The parametric array was projected at near normal incidence (-4.7°) to the surface and the four difference frequencies were transmitted (i.e., generated by the nonlinear interaction of

two primary frequencies in the water). At each of the transmitted frequencies, three waveforms were sent: 25 msec pulsed CW, 1000 msec pulsed CW, and 500 msec pulsed LFM with a 100 Hz bandwidth. A large number of pulses were transmitted at each frequency to achieve statistical confidence in the estimates of the Doppler spectra. The instantaneous reverberation signals received on each of the eight hydrophones were band shifted to a lower frequency and were recorded on magnetic tape. The angle of incidence of the parametric source was then changed from near normal incidence to an incident angle of 20° and the same waveforms were transmitted at each of the four difference frequencies. The same procedures were followed for incident angles of 40 and 60°. Wind speed as a secondary indicator of sea surface stationarity was recorded continuously throughout the eight hour measurement period and the wind direction was monitored.

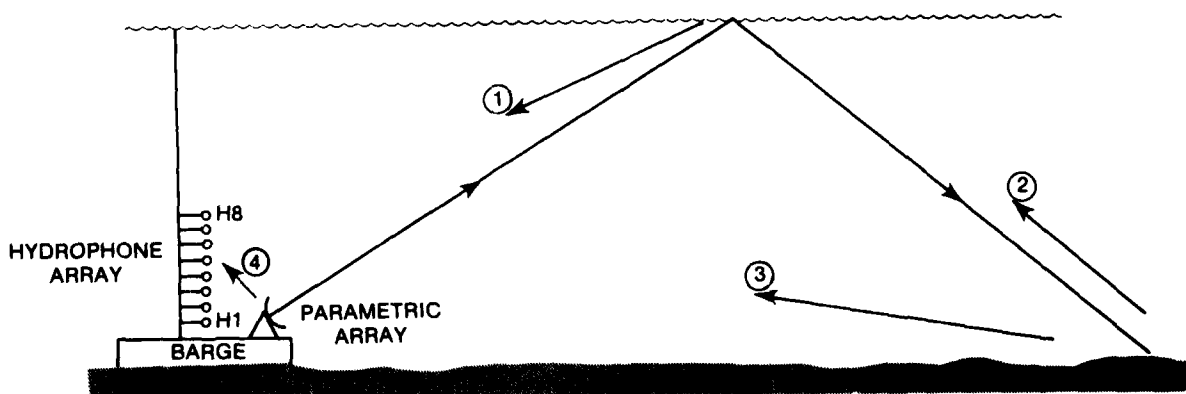


Figure 2-3. Ray Diagram of Major Arrivals at Hydrophone Array. Only Path (1) is desirable. Other paths shown are (2) Surface Reflected-Bottom Scattered-Surface Reflected (3) Surface Reflected-Bottom Scattered (4) Direct path

CHAPTER 3

PARAMETRIC ARRAY TRANSMISSION

3.1 INTRODUCTION

In experimental investigations of reverberation, it is often desirable to have an acoustic projector that insonifies an analytically known and well-defined area on the scattering boundary. Likewise, it is desirable to have a projector of low Q to adequately probe the frequency dependence of the scattering process. The inherent characteristics of the parametric array-narrow beamwidths at modestly low frequencies, a near absence of sidelobes, and a broad frequency band capability - prompted its use as a projector in this experiment.

Typically, a parametric array is generated by driving a directional transducer at two frequencies - the primary frequencies. Since the propagation of acoustic waves in a fluid medium is not quite a linear process [3-1], there is interaction between the frequencies. Not only are harmonics of each primary frequency generated; but intermodulation frequencies, such as sum and difference frequencies, are also generated. The secondary frequencies are generated along the length of the primary beam; and once generated, continue to propagate independent of the primary frequencies. The effective length of the primary beam, where the nonlinear interaction occurs, is determined by a combination of small-amplitude absorption and nonlinear absorption.

The lowest frequency generated is the difference between the two primary frequencies. Since small amplitude absorption (viscous) increases in proportion to frequency squared, the difference frequency is the least attenuated of any secondary frequency. Conceptually, the parametric array consists of the portion of the fluid in the interaction length of the primary beam where virtual sources reradiate acoustic energy at the difference frequency and other secondary frequencies.

Transmitting characteristics of parametric arrays have been extensively investigated - both experimentally and theoretically - since Westervelt's [3-2] original publication in 1963. Following Westervelt's theory on difference frequency generation in the near field by two plane, highly collimated, and attenuated primary frequencies, consideration was given to experimental investigation [3-3] - [3-7]. Theoretical analyses of the array continued with more realistic considerations that accounted for the directivity of the launching transducer [3-4], [3-6], [3-8]; the far field interaction effects resulting from reduced absorption at lower primary frequencies [3-9]; and nonlinear absorption in the near field [3-10], [3-11].

It is not the intent of this chapter to review the various models that have been developed to explain the behavior of parametric arrays. This information is readily available in the cited references. The intent is

firstly, to describe the electrical and acoustical properties of the transducer which launched the primary frequencies, and secondly, to describe the characteristics of the difference frequency which insonified the ocean surface. To verify proper generation of the parametric array, difference frequency source levels are compared to the Moffett and Mellen model 3-11. Thirdly, a description is given of the signal generating system and cabling used to power the transducer at the primary frequencies. Lastly, the transducer was remotely controlled in angle of elevation to obtain data with respect to the angle of incidence with the sea surface - a description of this system along with the position indicators is presented.

3.2 PRIMARY BEAM CHARACTERISTICS

Firstly, a decision was made to eliminate unforeseen difficulties that might arise in parametric transmission by using a similar transducer to one that had been previously evaluated [3-12]. A preliminary investigation revealed that the characteristics of the Edo Weston Model 6083 circular piston transducer were suited for the shallow water depths of Block Island Sound. This transducer consists of lead zirconate active elements positioned in a mosaic to give an effective radiating diameter of 25.4 cm and a resonance frequency near 250 kHz.

Prior to implantment in the Sound, a number of performance tests were conducted with the transducer at the NUSC Millstone Quarry Test Facility.

With a calibrated hydrophone situated in the far field and positioned on the maximum response axis (MRA) of the transducer, the transmitting voltage response was measured over a frequency band of 30 kHz. The pressure level at the hydrophone (30.5 m away) was referred to a unit distance of 1 m from the transducer by adding spherical spreading and absorption losses. With approximately 2 dB variation over the band, the transmitting voltage response averaged 191 dB re 1 μ Pa at 1 m for a voltage of 1 volt RMS across the transducer (Fig. 3-1).

Referring far field pressure levels to a reference distance of 1 m can result in erroneous values of near field quantities such as pressure, particle velocity, etc. It is well known that the near field pressure amplitude oscillates as a function of distance from the transducer with a dependence on transducer shape, size and radiating wavelength as depicted in Fig. 3-2 (a). Customarily, the near field is simplified by assuming that plane waves are confined in cross section to a radiating area S of the piston and extending from the piston face to a distance of $R_o = S/\lambda_o$, where R_o is the Rayleigh distance and λ_o is the wavelength C/f_o (Fig. 3-2 (b)). The pressure amplitude P_o of the near field plane waves is equal to the referred pressure P_1 at 1 m divided by R_o or P_1/R_o , as shown in Fig. 3-2(c). Thus, for the 25.4 cm diameter piston the near field was limited in cross section to an area of 507 cm² and extended to a Rayleigh distance of 8.8 m. The RMS source level is given by

$$L_o = 20 \log \frac{P_o R_o}{\sqrt{2}} , \text{ dB re } 1 \mu\text{Pa.m} . \quad (3-1)$$

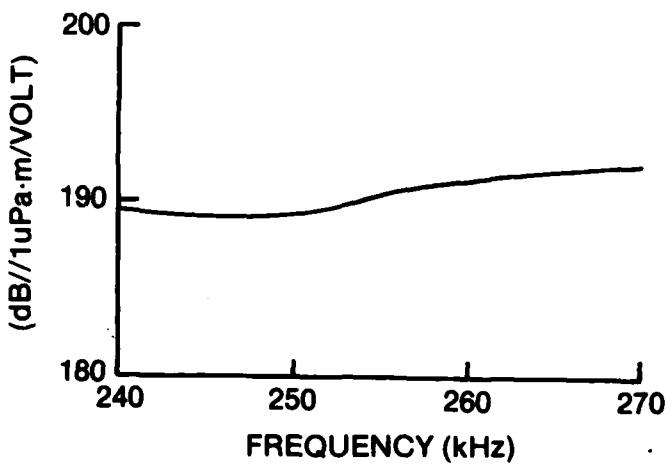


Figure 3-1. Transmitting Voltage Response
of Edo Weston Model 6083 Transducer Used
to Launch Primary Frequencies

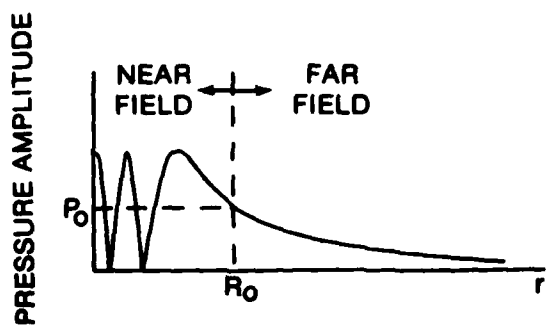


Figure 3-2(a). Near-to-Far Field Behavior
of Axial Pressure Amplitude of a
Typical Transducer

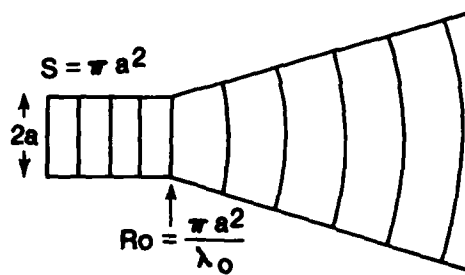


Figure 3-2(b). Cross Section of Circular
Piston Having Near Field Plane
Waves and Far Field
Spherical Waves

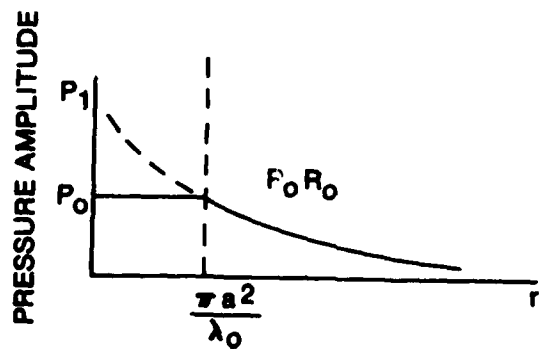


Figure 3-2(c). Pressure Amplitude a Constant
 P_0 in Near Field and $1/r$
Dependence in Far Field

The transducer's electrical impedance was calculated from measurements of input voltage, current, and voltage - current phase differences. At a frequency of 263.3 kHz which was close to the antiresonance frequency (frequency of maximum impedance), the impedance was purely resistive at a value of 88 ohms (Fig. 3-3). This frequency was chosen as the center of the primary frequencies since the magnitude of the impedances were practically equal for symmetrical deviations in primary frequencies and there was less than 1 dB variation in transmitting response out to the desired maximum frequency deviation (263.3 ± 4.5 kHz).

Far field primary beam patterns were measured by rotating the transducer about an axis perpendicular to the MRA of the transducer and measuring the pressure level in the far field. At a primary frequency of 263.3 kHz and a source level of 223.6 dB re 1 μ Pa.m, the beam pattern exhibited the typical characteristics of a circular piston as shown in the linear angle plot of Fig. 3-4. The measured total beamwidth between halfpower points was approximately 1.4° and the first order sidelobes were 17.5 dB down from the maximum response.

The beampattern characteristics were in good agreement with the classical equation [3-13] for the far field directivity $D(\theta)$ of a circular piston in an infinite baffle, which is given by

$$D(\theta) = 20 \log \left[\frac{2 J_1(k_o a \sin \theta)}{k_o a \sin \theta} \right], \quad (3-2)$$

where k_o is the acoustic wavenumber ω_o/c , a is the transducer radius, θ is the angle measured from the MRA, and $J_1(\cdot)$ is a first order Bessel function of the first kind. For the acoustic wavenumber and transducer radius, $k_o a = 138.67$ and (3-2) predicts a total beamwidth of 1.3° and first order sidelobes down 17.6 dB at an angle of 2.1° from the MRA. The directivity function $D(\theta)$ does not take into account finite amplitude effects, such that the comparison with the measured beampattern was made at a source level where nonlinear absorption was negligible. The effect of finite amplitudes can readily be seen as an effective increase in sidelobe levels relative to the maximum response as measured by Lockwood, Muir, and Blackstock at higher source levels with a circular piston [3-14].

From the above acoustical, electrical and directivity measurements, the electroacoustic efficiency was estimated to be 49%. This estimate was based on driving the transducer at a frequency of 263.3 kHz with a peak voltage V_p of 10 volts into a resistive load R of 88 ohms which resulted in a source level L_o of 208 dB re 1 μ Pa.m. The directivity index DI was computed from

$$\begin{aligned} DI &= 20 \log k_o a \\ &= 42.8 \text{ dB}, \end{aligned}$$

and the logarithm of the efficiency E is given by

$$10 \log E = L_o - 170.7 - 10 \log \frac{V^2}{2} + 10 \log R - DI.$$

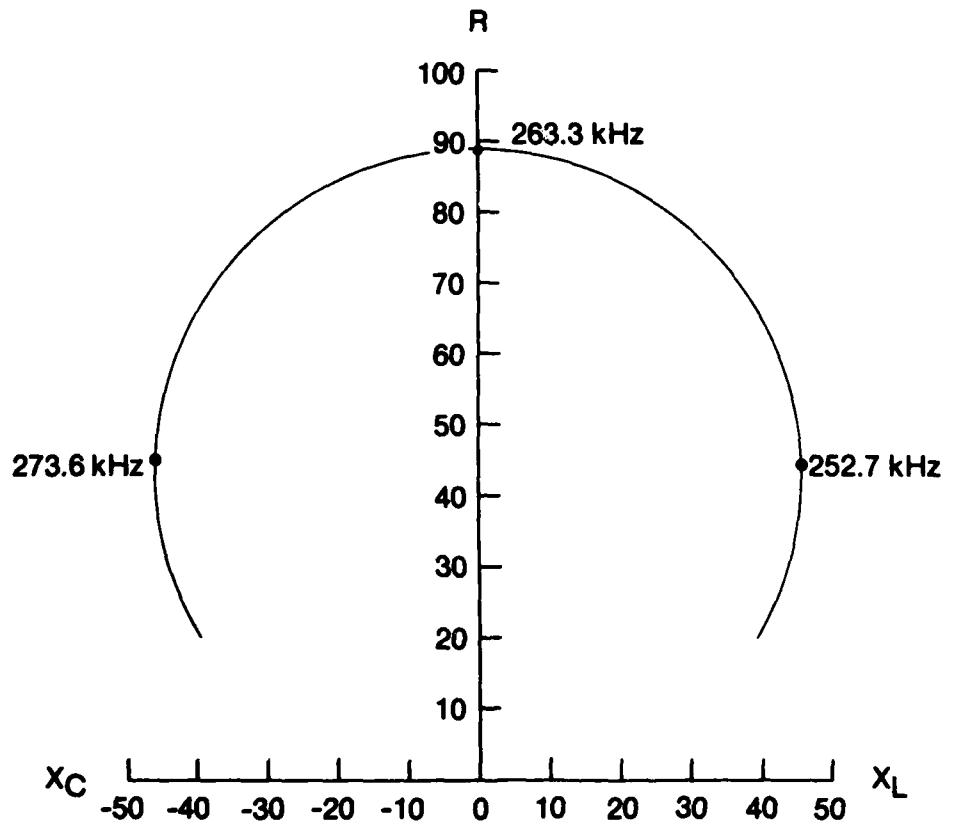


Figure 3-3. Water Impedance Loop of Launching Transducer

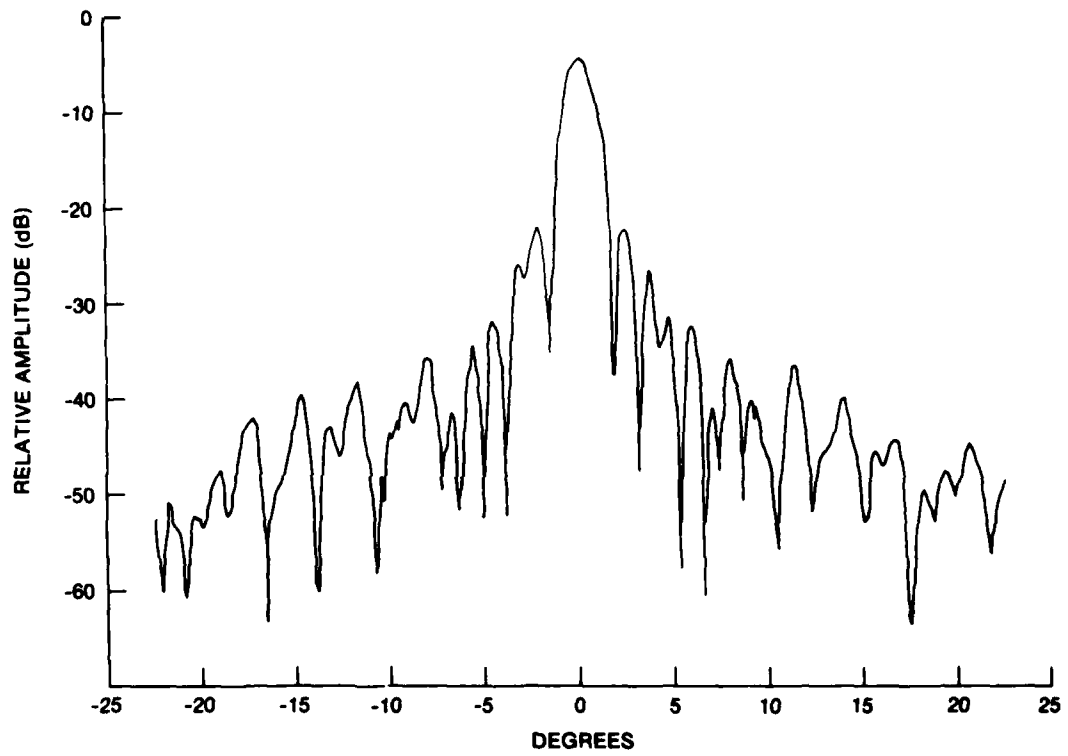


Figure 3-4. Primary Beampattern of 25.4 cm Diameter Piston
at a Frequency of 263.3 kHz

Because of the high directivity index it is possible to obtain relatively high source levels with low electrical powers. For example, the primary beam generated for the parametric array consisted of two equal amplitude sinusoidal frequencies positioned symmetrically in frequency about the center frequency ω_0 . A typical peak drive voltage across the transducer was 150 volts at each frequency which gives an approximate electrical power of 128 watts per frequency. Excluding nonlinear absorption, this results in a source level of 231.5 dB re 1 μ Pa.m per frequency. (From Merklinger [3-7], the nonlinear absorption would result in a 0.6 dB loss in source level based on the extra attenuation of the fundamental occurring in the near field plane wave model depicted in Fig. 3-2(c).) For each frequency, the peak pressure at the transducer face would be approximately .6 atm. with a radiated acoustic power of 61 watts.

3.3 PARAMETRIC ARRAY CHARACTERISTICS

Difference frequency characteristics were also measured at the Millstone Quarry Test Facility prior to implantment of the Edo Weston Transducer in Block Island Sound. With the transducer and a calibrated hydrophone at depths of 15 m and at a horizontal range separation of 30.5 m, difference frequency source levels and beampatterns were measured at discrete frequencies over the band from 3.5 to 10 kHz.

A simplified block diagram of the transmitting system is shown in Fig. 3-5. The output of the balance modulator consists of two equal amplitude sinusoidal signals at frequencies of $f_o \pm f_d/2$, where f_d is the difference frequency to be generated in the water and f_o is the center frequency at 263.3 kHz. The double sideband suppressed carrier signal is gated by the tone burst generator, amplified, and high pass filtered, where the filtering is used to remove direct radiation at the difference frequency which may have been generated by any nonlinearities in the power amplification process.

At the face of the transducer, the pressure $P(t)$ can be expressed as

$$\begin{aligned} P(t) &= P_o [\cos 2\pi(f_o + f_d/2)t + \cos 2\pi(f_o - f_d/2)t] \\ &= 2 P_o \cos 2\pi(f_d/2)t \cos 2\pi f_o t. \end{aligned} \quad (3-3)$$

The time varying pressure has a peak pressure of $2P_o$ every $2/f_d$ seconds. At the maximum primary source level generated per frequency, 236 dB re 1 μ Pa.m, the peak pressure at the transducer face was 2 atmospheres.

Using primary source level as a variable, difference frequency beampatterns and corresponding source levels are shown in Fig. 3-6 for a constant difference frequency of 8 kHz. Firstly, the beampatterns depict the familiar characteristics of narrow beamwidths and absence of sidelobes that are associated with the parametric array. If the two primary frequencies behaved as collimated plane waves and interacted in a column confined by the dimensions of the transducer, then the directivity of the difference frequency in the far field of the array is given by Westervelt as

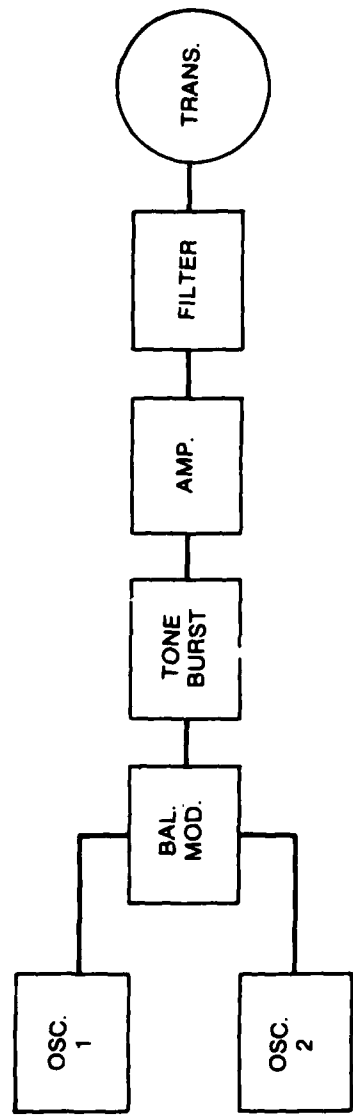


Figure 3-5. Simplified Block Diagram of Transmitting System for Parametric Array Calibration Measurements

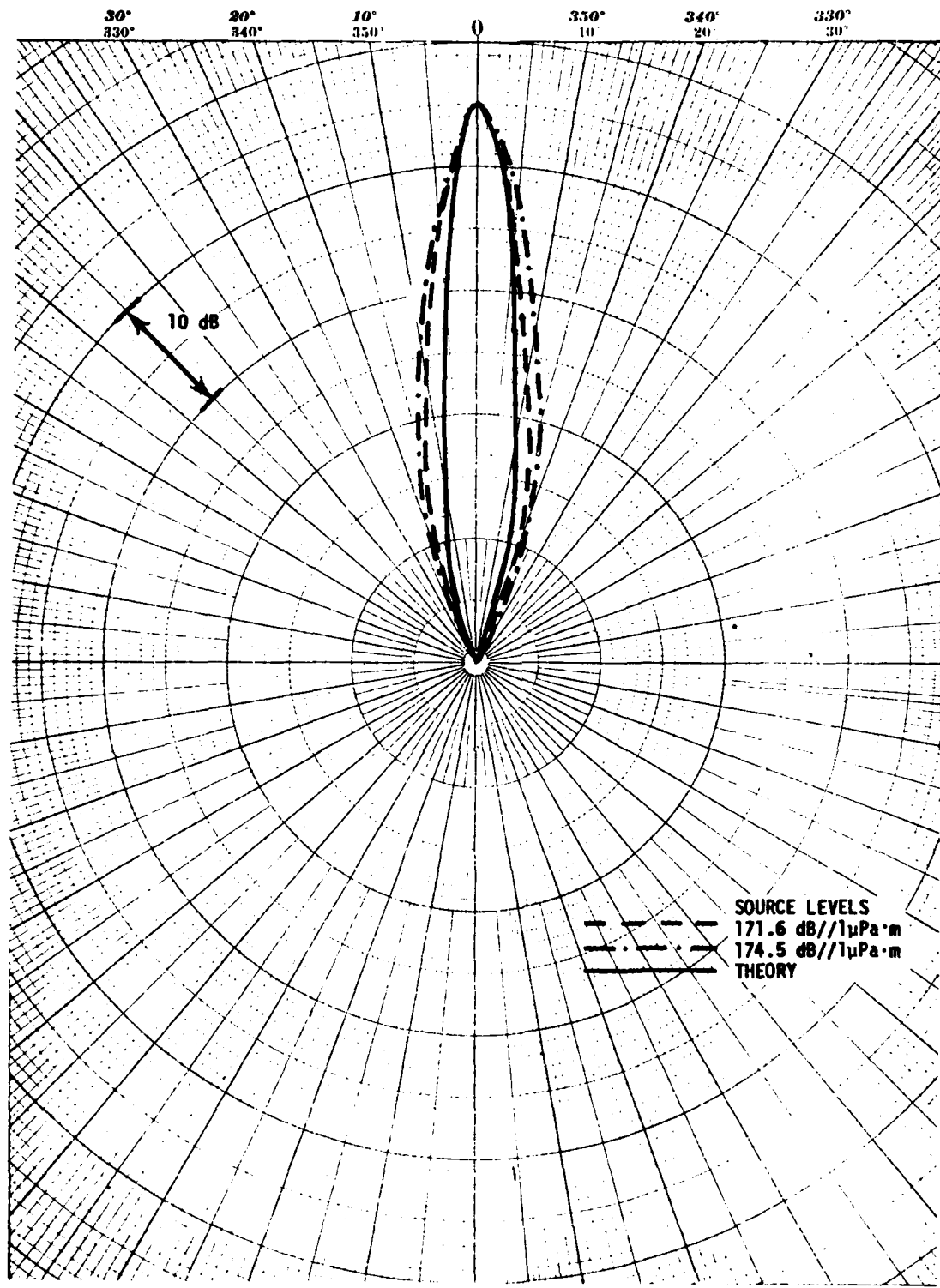


Figure 3-6. Comparison of Measured Difference Frequency Beampatterns with Theoretical Beampattern for Parametric Array Tapered by Linear Absorption. Difference Frequency was 8 kHz.

$$D_R(\theta) = \left[1 + i \left(\frac{2k}{\alpha_T} \right) \sin^2 (\theta/2) \right]^{-1}, \quad (3-4)$$

where in (3-4), k is the wavenumber of the difference frequency, α_T is the sum of the absorption coefficients of the primary frequencies minus the absorption coefficient of the difference frequency, and θ is the angle measured from the MRA of the transducer. From (3-4), the half-power beamwidth of the difference frequency is

$$2\theta_d = 4 \sin^{-1} (\alpha_T/2k)^{1/2}. \quad (3-5)$$

Also plotted in Fig. 3-6 is the theoretical beampattern (3-4) for a parametric array tapered by small-signal absorption. Note that the measured beampatterns are wider than the predicted and the beamwidths increase slightly with increasing primary source level.

Increasing the difference frequency beamwidth by solely increasing primary source level clearly exhibits the influence of finite amplitude effects. Thus, the effective parametric array length has been tapered by nonlinear absorption of the primary frequencies. This is analogous to increasing the beamwidth of a line array by reducing the array length or shading the elements of the array.

For more accurate predictions of the difference frequency directivity and source levels, the model must include both linear and nonlinear absorption. Moffett and Mellen [3-11] have derived a primary beam tapering function that includes both these effects. The model is based on the primary beam model of Fig. 2-2(b) and evaluation of the scattering integral described in [3-2]. Most importantly, the array tapering function accounts for linear and nonlinear absorption. The nonlinear absorption results from the loss of energy in the primary frequencies due to the progressive distortion of the amplitude modulated waveform described by (3-3).

Difference frequency source level predictions, obtained from parametric gain curves described in [3-11], were compared to the source levels measured at Millstone. The comparisons are shown in the three curves of Figs. 3-7 - 3-9 as a function of the downshift ratio f_0/f_d . The curves were generated for the three designated source levels and for $\alpha_{R_o} = 0.8$. Although there is good agreement, better agreement would be expected if the measurements were conducted in the far field of the array. This assessment is based on the observation that there is better agreement at the successively higher source levels (Figs. 3-8 and 3-9), where the array length becomes increasingly truncated by nonlinear absorption.

3.4 TRANSMITTING SYSTEM

For the reverberation measurements in Block Island Sound the block diagram in Fig. 3-10 shows the pertinent equipment installed as the transmitting system.

The EDI Weston transducer, powered by a CML amplifier, was coupled to shore via a 1675 m coaxial cable. The coaxial cable consisted of a copper

stranded wire center conductor which was insulated from a copper braided outer conductor by polyethelene. Characteristic impedance of the coax was 50 ohms and the measured power loss at the center frequency was 3 dB. A Marsh and Marine 36 pin connector joined the coax and the other conductors in the 3.8 cm diameter armoured cable to the transducer housing. The proximity of the connector pins limited the voltage and current to the transducer.

At a center frequency of 263.3 kHz, the measured input impedance of the coax with the transducer load was 45 ohms. A 3 dB power loss in the cable resulted in approximately equal voltage amplitudes at the coax input and across the 88 ohm transducer load. Since the drive voltage at the coax input was 600 volts peak-to-peak, the difference frequency source level values of Fig. 3-7 are applicable to the reverberation measurements.

A five pole Butterworth high pass L-C filter, which was matched to the cable input impedance and the CML transformer output impedance, rejected intermodulation difference frequencies generated in the power amplification process. With less than 1 dB insertion loss in the filter, the amplifier delivered an output peak envelope power of 1 kW.

As in the calibration measurements of the parametric acoustic array, a balanced modulator provided a double sideband suppressed carrier signal with frequency components $f_o \pm f_d/2$ positioned symmetrically about the transducers antiresonance frequency f_o . This signal was high pass filtered prior to driving the preamplifier stage of the CML amplifier. Using a balanced modulator required only one synthesizer (Monsanto) to maintain a stable (one part in 10^6) frequency difference. Also, only one frequency had to be adjusted to change the difference frequency and at the same time the center frequency remained constant. The H.P. oscillator provided the input to the carrier input to the modulator at a frequency of 263.3 kHz. The signal input to the modulator was a gated version of the synthesizer output from a tone burst generator.

The tone burst generator output also fed a multiplier (frequency doubler) to generate a reference signal. The reference signal initially consisted of a dc voltage which was removed by filtering in the receiving system, and a frequency at the difference frequency f_d . Thus the reference signal had the same pulse length as the water borne signal and was at the same frequency as the difference frequency generated by the water nonlinearities. Furthermore, the reference signal underwent the same signal conditioning as each of the hydrophone outputs and was analogue recorded and digitally processed in the same manner as the reverberation signals. Hence, the reference signal served as a monitor for the tape recording and playback frequency stabilities, and for checking processing errors incurred by the reverberation signals.

The transmitting system was manually controlled and was required to transmit four difference frequencies - 9.0, 7.0, 5.0, and 3.5 kHz. At each transmitted frequency, one of three waveforms could be sent: 25 msec and 1000 msec pulsed CW, and 500 msec pulsed LFM. The repetition periods were 1.0 sec, 10.0 sec and 5.0 sec for the respective waveforms.

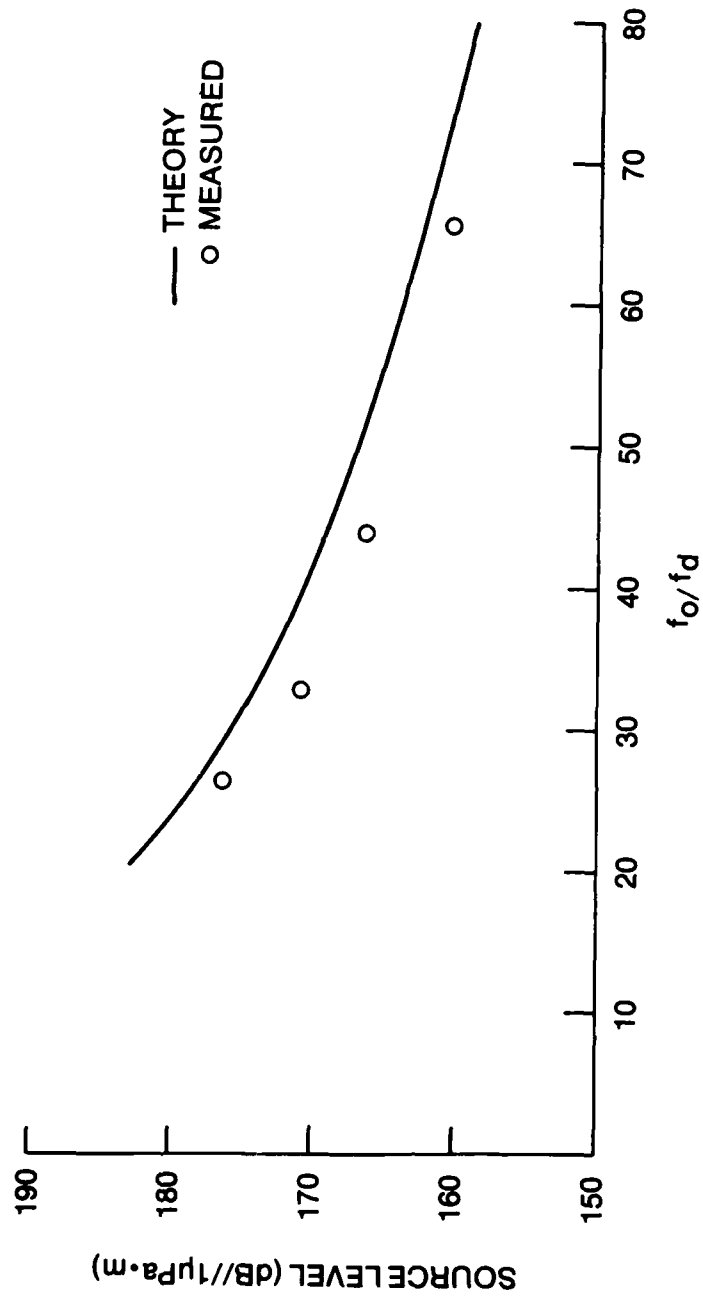


Figure 3-7. Comparison of Measured Difference Frequency Source Levels with Moffett and Melien Prediction. Scaled Source Level was 279.8 dB re 1 $\mu\text{Pa}\cdot\text{m}$ and Primary Center Frequency was 263.3 kHz

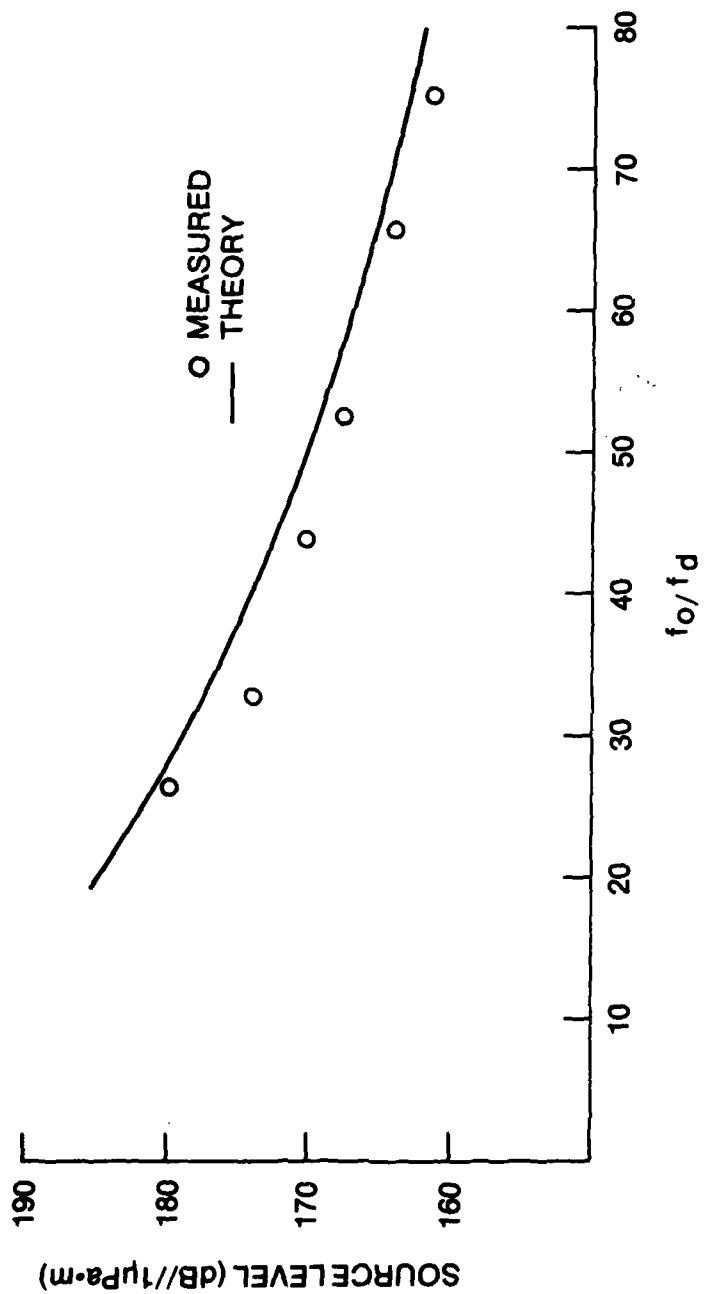


Figure 3-8. Comparison of Measured Difference Frequency Source Levels with Moffett and Melien Prediction. Scaled Primary Source Level was 282.3 dB re/ $\mu\text{Pa}\cdot\text{m}$ and Primary Center Frequency was 263.3 kHz.

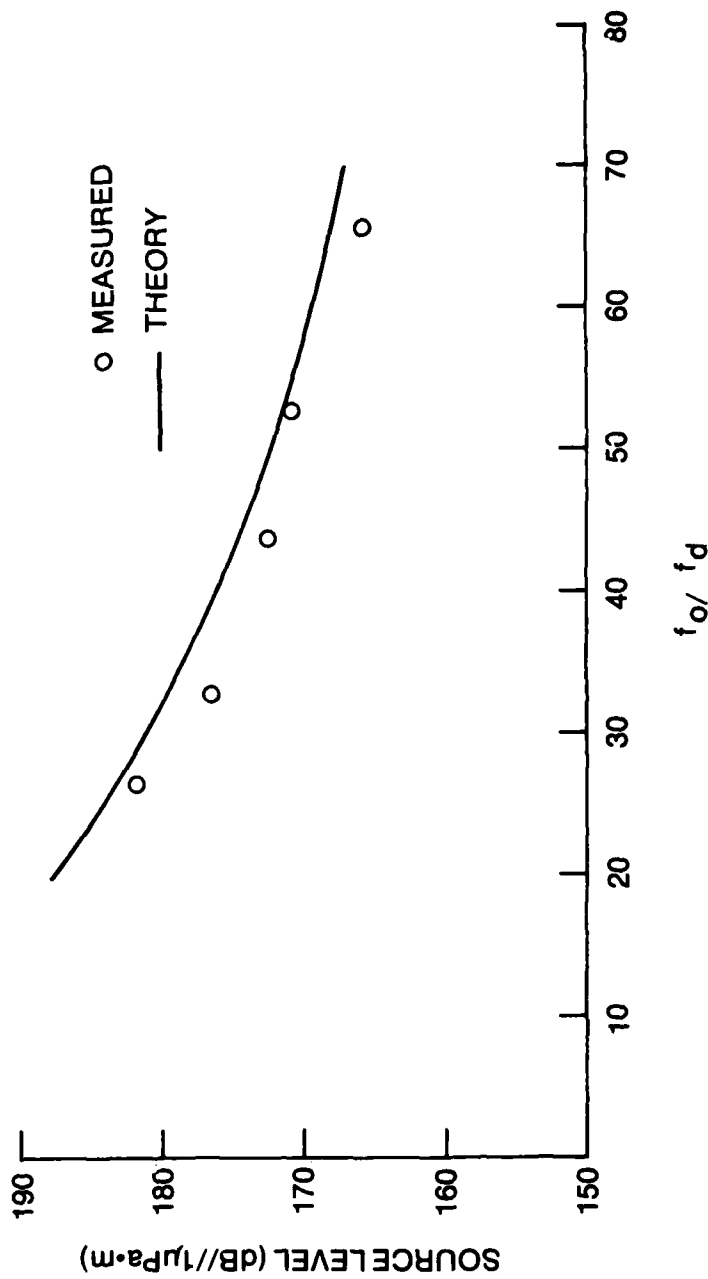


Figure 3-9. Comparison of Measured Difference Frequency Source Levels with Moffett and Melien Prediction. Scaled Primary Source Level was 284.3 dB re/ μ Pa·m and Primary Center Frequency was 263.3 kHz.

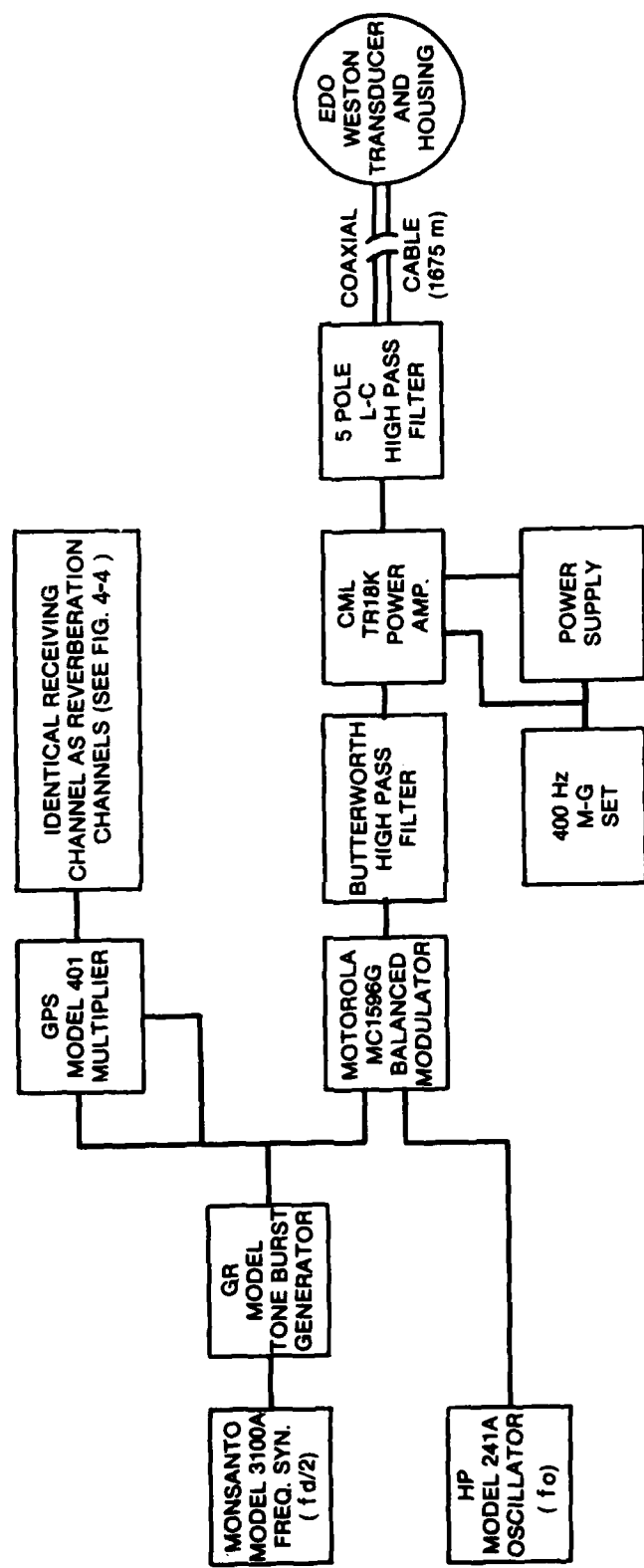


Figure 3-10. Block Diagram of Parametric Array Transmitting System

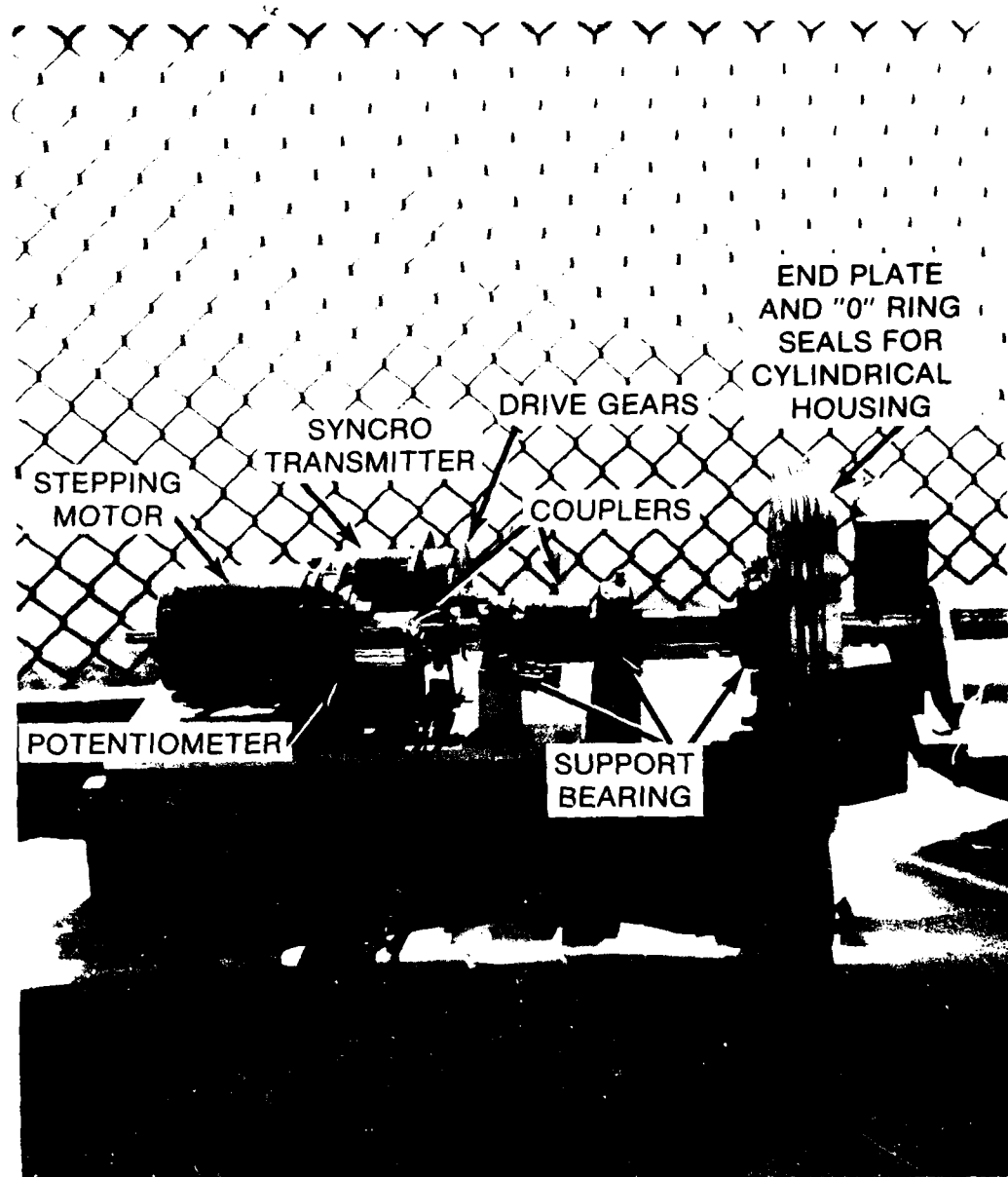


Figure 3-11. Photograph of Stepping Motor and Drive Train Used to Rotate Parametric Array; and Synchro Transmitter and Potentiometer Used to Sense Angle of Elevation.

3.5 ANGLE OF ELEVATION: CONTROL AND INDICATION

The parametric array was capable of rotation in angle of elevation over an angular sector of 180° (horizon to horizon). A DC stepping motor (SLO SYN 150 E) provided the necessary torque to rotate the transducer. The transducer was coupled to the motor via a shaft and gear reduction box. A baseplate supported the motor and angle indicating devices as shown in Fig. 3-11. Mounted to the baseplate are a stepping motor, synchro transmitter and feedback potentiometer. The synchro transmitter and potentiometer were geared to the shaft and were used to sense the angle of elevation of the transducer. Synchro, potentiometer, and DC stepping motor were cabled to the shore facility via the 36 conductor cable used to power the parametric array.

By pulsing the stepping motor with ± 15 volt pulses, the transducer could be incremented in angular steps of 0.1° . As the transducer rotated, the synchro transmitter, coupled with a one-to-one gear ratio to the shaft, rotated a synchro receiver located at the shore facility. Also, the potentiometer (5Ω) was geared to the shaft with a 10-to-1 gear ratio and served as one arm of a bridge circuit. The unbalancing of the bridge caused current to flow in a D'Arsonval μ amp meter. The meter was calibrated for 1μ amp of current flow per degree of rotation. Prior to installation, the transducer was leveled and both sensors, synchro receiver and D'Arsonval μ amp meter, were zeroed.

CHAPTER 4

ANALOGUE CONDITIONING AND DIGITAL CONVERSION OF REVERBERATION SIGNALS

4.1 INTRODUCTION

The primary functions of the receiving system were to identically condition the analogue reverberation signals for the in situ magnetic tape recording and subsequent digital processing at the NUSC laboratory. Overall receiving system design took into account background noise, tape recorder frequency instabilities, A/D conversion sampling rates, and dynamic ranges of the tape recorder and A/D converter,

Nine identical channels of signal conditioning were required for the receiving system: eight channels for the hydrophone outputs and one channel to condition the reference signal generated in the transmitting system (CHAPTER 3). To ease the receiving system requirements, the same system configuration was used to condition the three transmitted waveforms. Thus, the system bandwidth was greater than 100 Hz to accommodate the LFM waveform.

In this chapter a description is given of the receiving system - from the initial reception of the "raw" reverberation signals to the recording of the bandshifted signals on magnetic tape - and the subsequent digital conversion.

4.2. HYDROPHONES

International Transducer Corporation model 1022 free flooding ceramic ring transducers were used to receive the reverberation. As mentioned previously, these transducers were not selected nor implanted for this experiment, but had been selected for use in low frequency propagation studies. Because of the interest in low frequencies, the available calibration data on the ITC-1022 had been restricted to frequencies below 6 kHz. The receiving sensitivity of a typical transducer is shown in Fig. 4-1. An extrapolation is required to obtain an estimate of the receiving response at frequencies above 6 kHz. Since Doppler spectra can be a relative measurement, the absolute value of receiving sensitivity is unnecessary. However, it is required that the transducer have enough sensitivity and capacitance (in comparison to cable capacitance) to provide an output voltage that is high in comparison to receiving system noise.

The ring transducers have omnidirectional beampatterns in the horizontal and "doughnut - shape" in the vertical. A typical azimuthal beampattern, depicting the omnidirectional character of the transducer is shown in Fig. 4-2 at a frequency of 5 kHz. A beampattern, taken in the vertical, is shown in Fig. 4-3 at the same frequency. The vertical beampattern becomes more doughnut-shaped as frequency is increased.

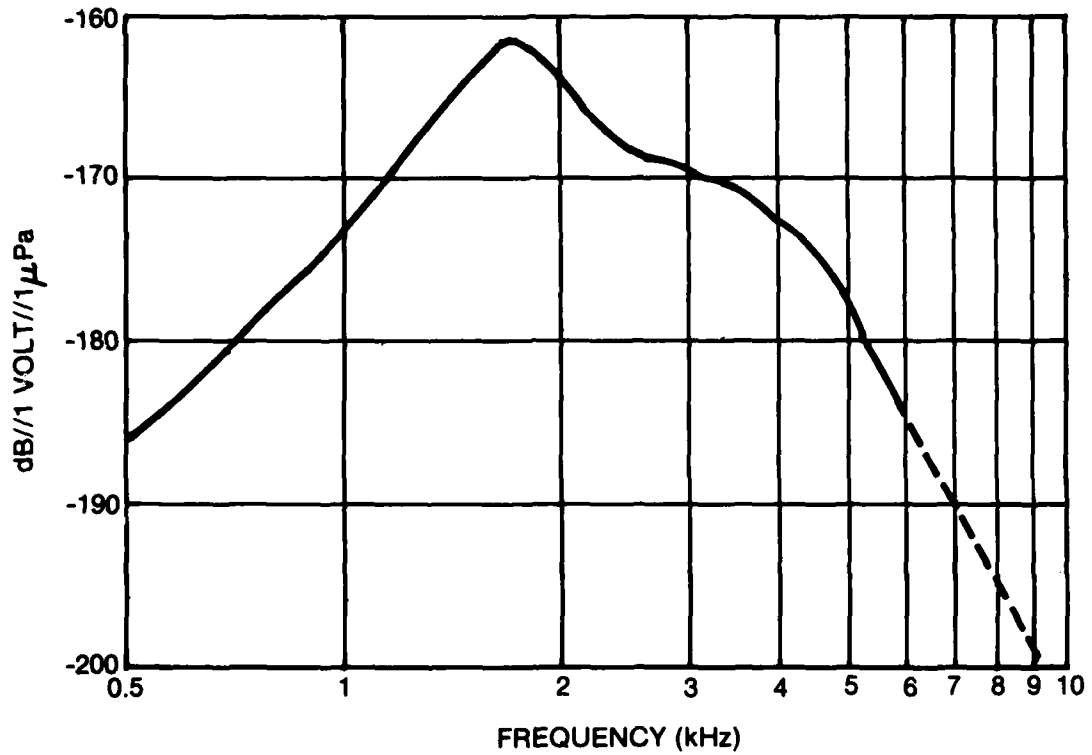


Figure 4-1. Receiving Sensitivity of a Typical ITC-1022 Transducer.
Dashed line is an Extrapolation to Higher Frequencies.

The eight transducers were individually cabled to the shore facility via a multiconductor single armored cable. Stranded wire conductors with polyethylene jackets coupled the hydrophones over 1680 m of cabling.

4.3 RECEIVING SYSTEM

At the shore facility, the hydrophone outputs were first isolated from ground by isolation transformers and then amplified by Ithaco Model 491 Amplifiers (Fig. 4-4). Prior to bandshifting the reverberation signals to a common lower frequency, the signals were bandpass filtered at the transmitted difference frequency.

IC operational amplifier active filters were used to bandpass filter the reverberated signals. By switching selected capacitors into a multiple feedback bandpass circuit [4-1] the center frequency of the bandpass filter could be set at the transmitted difference frequency. The Q of the bandpass filters was approximately 35 and independent of center frequency. The filter bandwidth was a minimum of 100 Hz at 3.5 kHz and a maximum of 257 Hz at 9 kHz. To obtain nearly identical bandpass filter responses, potentiometer adjustments could be made to adjust center frequency and bandwidth.

Following bandpass filtering and amplifying, the reverberation signals were bandshifted by DATA Model 401 all purpose multipliers to a lower common frequency of 220 Hz. That is, by multiplying the incoming signals by a frequency synthesizer signal at a frequency of 220 Hz below the transmitted difference frequency, upper and lower sidebands were produced at the multiplier output. The upper sideband was positioned at $2 f_d - 220$ Hz and the lower sideband was positioned at 220 Hz. Having the synthesizer frequency below the transmitted frequency ensured that the structure of the Doppler spectra was not reversed. The lower sideband was selected by a bandpass filter having a center frequency of 220 Hz and a bandwidth of 200 Hz. Reverberation signals at all difference frequencies were bandshifted to the same frequency band centered at 220 Hz.

Prior to tape recording the bandshifted reverberation, the signals were again amplified to ensure that the full dynamic range of the tape recorder was being utilized.

As discussed in CHAPTER 3, a reference signal was generated to simulate the water borne transmitted signal. The reference signal was conditioned by a receiving channel that was identical to the reverberated signal channels. The reference signal undergoes the same receiving system conditioning, tape recording and reproducing, A/D converting, and digital signal processing. Thus, the reference signal serves as a valuable check for conditioning or processing errors.

4.4 TAPE RECORDING AND PLAYBACK SYSTEM

The instantaneous bandshifted reverberation signals and reference signal were recorded on a Honeywell 5600 magnetic tape recorder at a tape speed of

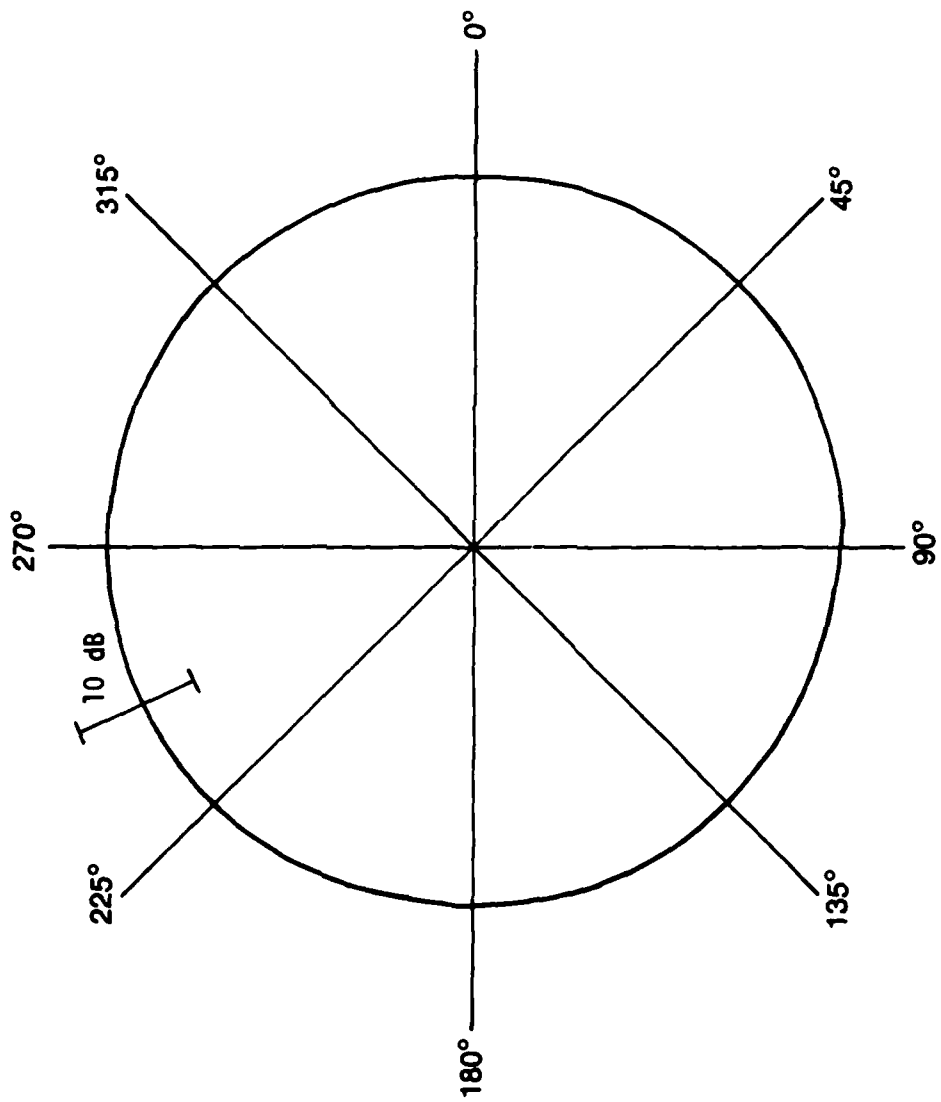


Figure 4-2. Azimuthal Beampattern of a Typical ITC-1022 Transducer

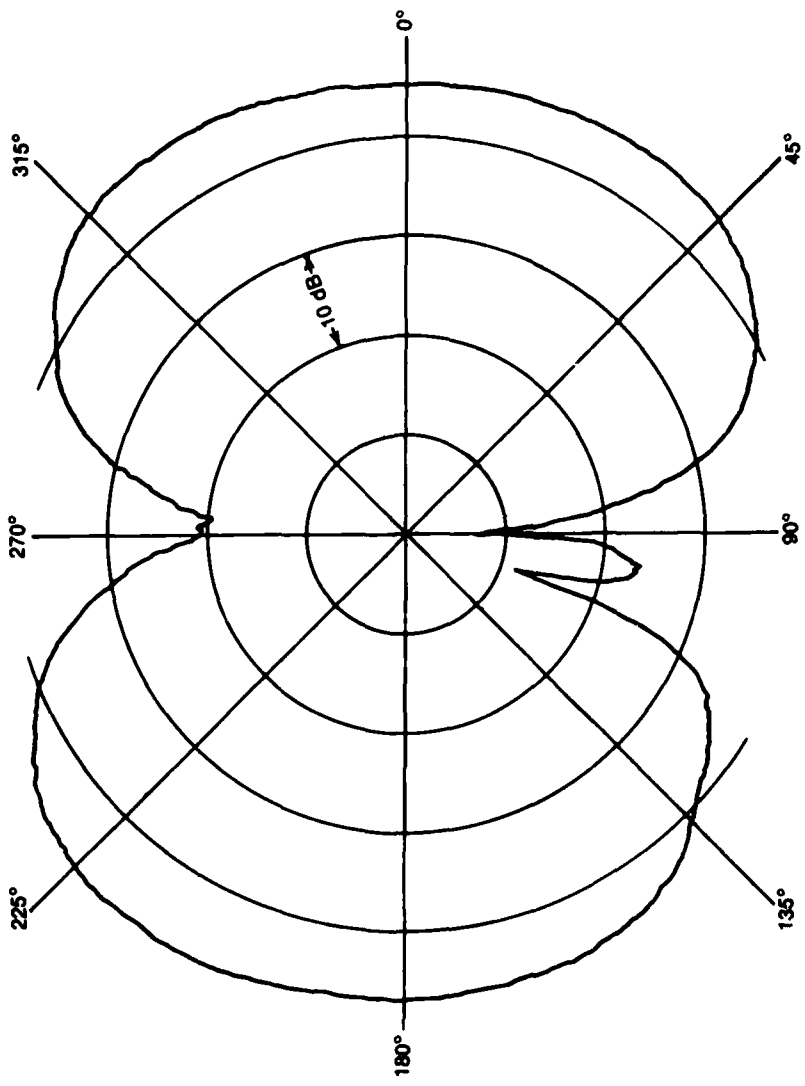


Figure 4-3. Vertical Beampattern of ITC-1022 Transducer at a Frequency of 5 kHz.

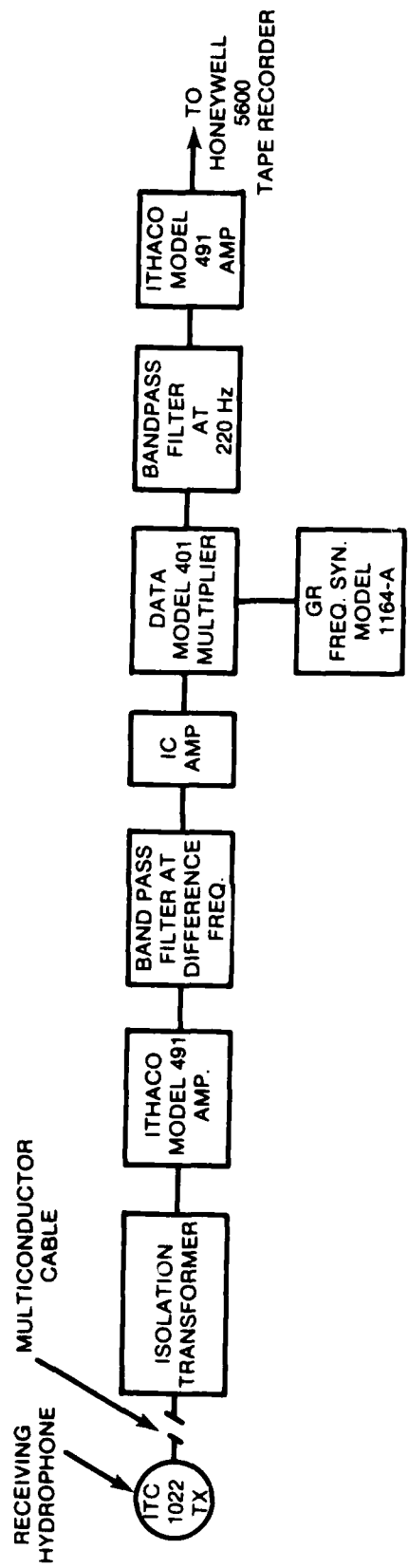


Figure 4-4. Single Channel of an Identical Nine Channel Receiving System for Analogue Conditioning of Reverberation and Reference Signals.

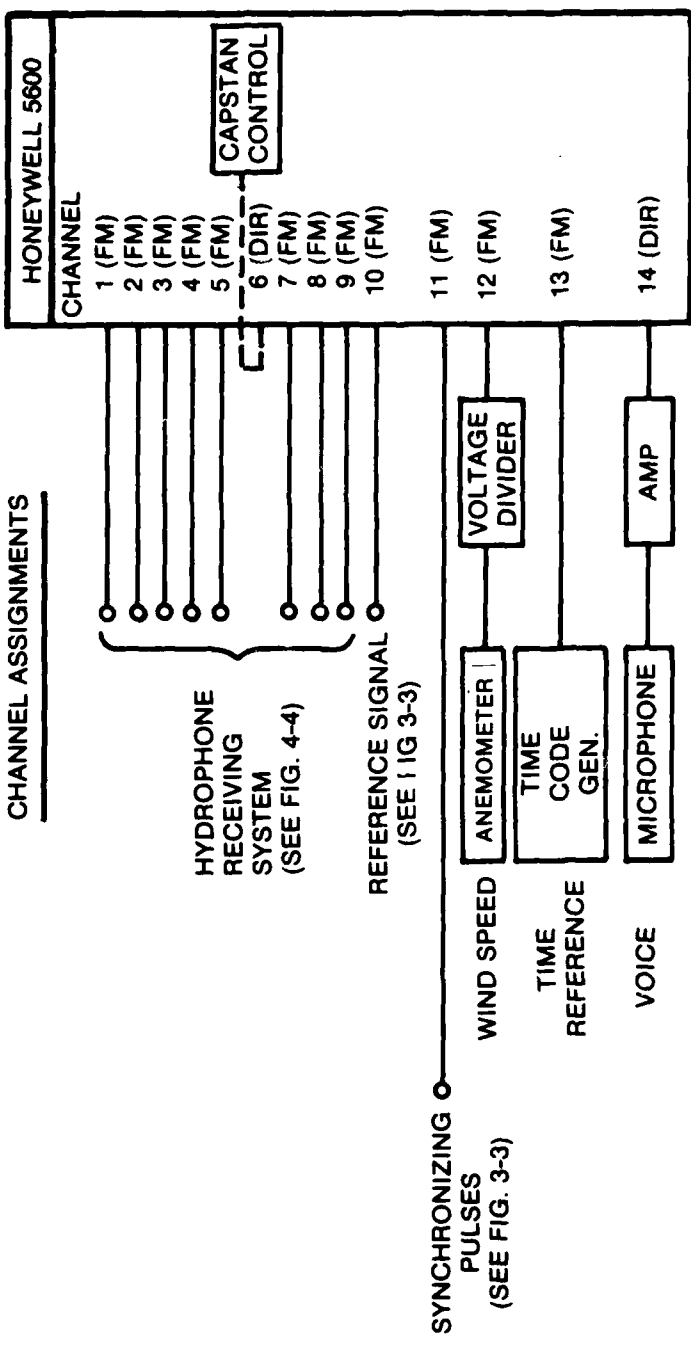


Figure 4-5. Signals Recorded on the Honeywell 5600 Analogue Tape Recorder.

7.5 inches/sec. FM record/reproduce electronics were used for the data and reference channels to obtain a high amplitude accuracy, uniform frequency response, and a broadband signal-to-noise ratio that was greater than 40 dB. A servo control signal was also recorded on tape to maintain tape speed (and hence, frequency) accuracy.

The channel configuration of the tape recorder system is shown in Fig. 4-5. All channels are FP record/reproduce except for the servo control and voice channels. Synchronizing pulses were generated on the initiation of every outgoing pulse. The pulses were obtained from the tone burst generator (Fig. 3-10) used in the transmitting system. The synchronizing pulses were used to initiate the A/D conversion process, to count pulses, and to serve as a reference to locate specific data samples. Also, a time code generator was used to identify pulses.

To reproduce the reverberation signals, the same tape recorder was used on playback. The reverberation and reference signal channels were first filtered by the 220 Hz bandpass filter used in the receiving system and the signals were amplified to utilize the full dynamic range of the A/D converter.

4.5 ANALOGUE-TO-DIGITAL CONVERSION

After the reverberation signals were reproduced, filtered and amplified, each data channel was converted to a digital signal at a rate of 1024 samples/sec. This sample rate was 4.7 times the center frequency of the 220 Hz bandpass filter output and approximately 3.7 times the highest frequency present in the LFM reverberation data. The sampled data were quantized into 4096 levels and were represented in digital format by a 12 bit word. The signal-to-quantization noise ratio was about 69 dB.

Data were recorded on digital tape synchronized to the threshold detection of the synchronizing pulse that was initiated on each transmitted pulse. All data channels were sampled at the same rate with a time delay of 20 μ sec between samples on adjacent channels. That is, after the synchronizing pulse was detected, 20 μ sec later the first data channel was sampled. Due to the 1024 sample rate, there was the possibility of having a $\pm 1/1024$ sec time displacement error in detecting the synchronizing pulse.

CHAPTER 5

DIGITAL PROCESSING OF REVERBERATION SIGNALS

5.1 INTRODUCTION

Prior to computing the Doppler spectra of the reverberation, the digitized data were divided into data sets. The reverberation returns from the 1000 msec pulsed CW waveforms formed the primary data sets for the spectral analysis.

Firstly, the sets were formed by segregating the data according to acoustic frequency angle of incidence and angle of scatter. Since there were eight hydrophones to receive the reverberation and four frequencies were transmitted at each of the four angles of incidences, there were a total of 128 reverberation data sets.

A reverberation data set consisted of M reverberation returns from the sea surface. That is following the transmission of a 1000 msec pulsed CW signal, a reverberation return was received. After a time delay of 10 sec between transmission, another 1000 msec waveform was transmitted and a second reverberation return was received. Because the spatially random sea surface was also time varying, the second reverberation return differed from the first. Then for M transmissions of the same waveform there were M nonidentical random reverberation returns. Each return constituted a sample record from the random reverberation process. In statistical nomenclature, the random reverberation process was represented by an ensemble of sample records for which there could be assigned a probability measure [5-1]. Since the experiment was performed under stable wind conditions, the data sets were homogeneous, i.e., the data came from the same parent population.

Each Doppler spectrum was computed from sampled values obtained as a function of time "along a reverberation record." Thus, for M reverberation records that were M computations of Doppler spectra in a data set. This method contrasts with the possibility of computing spectra from sampled values obtained "across the ensemble" at some specified time. The latter method is most appropriate for random processes that have statistical properties that depend on absolute time, i.e., processes that are nonstationary.

Generally, reverberation is a nonstationary process which can be readily observed by the gradual decrease in reverberation intensity with range (time). The nonstationarity is introduced through beampattern effects, variation in surface scattering strength with incident angle, and increasing propagation loss with range to points on the scattering surface. However, in this experiment the reverberation processes were tactfully assumed (without validation) to be stationary. The justification for this assumption was based on both acoustical and geometrical considerations. Firstly, the length of the transmitted pulse allowed complete and continuous insonification of the scattering

surface that was defined by the beamwidth confined the scattering area to such an extent that there would be negligible variation in sea surface. Thus, at each angle of incidence the reverberation was considered "locally stationary" [5-2]. For this experiment, local stationarity meant that the statistics (at least through the second order) remained invariant with positive and negative time translations ($\pm\tau$) about an absolute time t_1 , where t_1 was approximately equal to the two way travel time to and from the insonified sea surface plus one-half the transmitted pulse length. Thus, the Doppler spectra were computed from sampled values obtained over a "time window" in which the data were considered a stationary random process. The data samples used in the power spectral density computations were obtained over 870 msec time window following the onset of reverberation from the sea surface.

From the sampled data, the Doppler spectra were computed using the discrete version of the Fourier transform (DFT). A fast Fourier transform technique (Singleton's) was used to efficiently compute the DFT. Since the reverberation returns were nonidentical, the Doppler spectra computed from each of the transmissions also differed. What was obtained from each transmission was a spectral density $\hat{B}(f)$ whose ensemble estimated the true spectral density $D(f)$ of the random reverberation process.

The remainder of this chapter describes the digital signal processing procedures that led to an estimate of the true Doppler spectra. Included in the procedure is a technique that removed from the data samples a strong periodic component. The periodic component, at the difference frequency, was introduced into the data by interference from electrical pickup and a direct path arrival. Following the removal of the periodic component, the data samples were Hanning weighted to reduce frequency leakage (sidelobes) in the frequency domain. Also described is the variance reduction procedure obtained by ensemble averaging the power spectral densities generated from each transmission. Finally, the Doppler shift, the Doppler bandwidth, and coefficient of variation computations are described.

5.2 DOPPLER SPECTRA ESTIMATES

5.21 FORMULATING THE DISCRETE FOURIER TRANSFORMS

The Doppler spectra estimates were obtained via the discrete version of the Fourier transform. To avoid unnecessary confusion of having superfluous indices that identify transmit frequency angle of incidence and angle of scatter, the reverberation records will be indexed for sample record and for the sample within the record. This will result in no loss in generality and the other indices can be appended. Let $r_k(j)$, $j=0, 1, \dots, N-1$ be samples from the k^{th} sample record of the locally stationary random reverberation sequence. k indexes the total of M sample records (reverberation returns) within a data set. Before computing the discrete Fourier transform of each sample recorder, the data samples were weighted by a data window $w(j)$, $j=0, 1, \dots, N-1$ to form the product $r_k(j)w(j)$. The discrete Fourier transform for the weighted samples was evaluated from

$$A_k(n) = \frac{1}{N} \sum_{j=0}^{N-1} r_k(j)w(j)e^{-i2\pi j n/N}, \quad n=0,1,\dots,N-1 \quad . \quad (5-1)$$

As j indexes time in $r_k(j)$, n indexes the frequency of the Fourier coefficients $A_k(n)$. That is, the time associated with the j^{th} sample is $t=j(\Delta t)$; and likewise, the frequency associated with the n^{th} frequency point is $n/N\Delta t$. Where Δt has been designated the sampling period (1/1024 sec).

From the properties of the discrete Fourier transform (see, for the time domain with period $N\Delta t$; and similarly, the Fourier coefficients are periodic in the frequency domain with period $1/\Delta t$). For each reverberation return, the sample record consisted of 900 samples which resulted in a record length of $N\Delta t = 878.9$ msec. Ordinarily, this would give a frequency spacing for the Fourier coefficients every $1/N\Delta t = 1.14$ Hz. However, more finely spaced estimates for the Fourier coefficients were desired. The closer spaced estimates were obtained by "padding" the sampled data with a number of zeros equal to the number of data points. Thus, the record length was artificially increased in time to a length of $2N\Delta t$ and the frequency spacings decreased to $1/2N\Delta t$. The discrete Fourier transform was then given by

$$A'_k(n) = \frac{1}{2N} \sum_{j=0}^{2N-1} r_k(j)w(j)e^{-2\pi i j n/2N} \quad . \quad (5-2)$$

The Fourier coefficients were estimated every 0.57 Hz. To obtain the power spectral density of each sample record, the magnitude of the Fourier coefficients were squared, or

$$\hat{B}(f_n) = P(\Delta t) |A'_k(n)|^2 \quad , \quad (5-3)$$

where P is a factor (2.67) which accounts for the loss of power in the data due to the (Hanning) window. Also, the frequency spacing is

$$f_n = \frac{n}{2N\Delta t} \quad , \quad n = 0,1,\dots,N-1 \quad .$$

The Doppler spectra estimates $D(f)$ were obtained from ensemble averaging the periodograms, i.e.,

$$\hat{D}(f_n) = \frac{1}{M} \sum_{k=1}^M \hat{B}_k(f_n), \quad k=1,\dots,M \quad . \quad (5-4)$$

5.22 CHOICE OF DATA WINDOW

The Doppler spectra were computed from reverberation sample records of finite length. That is, each reverberation record consisted of 900 samples from the random reverberation sequence. Since it is well known in Fourier analysis that the transform on data of finite length will generate sidelobe

leakage effects. The leakage results from the assumption that the data being transformed is zero outside the interval of the truncated sample record. By truncating a sample record, it is in effect multiplying the data by a window that is unity over the record length and zero elsewhere.

The effects of the data window can be seen from the convolution integral 5-3. Consider the transform of a continuous sample record $r(t)$ which is multiplied by a data window $w(t)$ such that

$$g(t) = r(t)w(t) , \quad (5-5)$$

and

$$G(f) = \int_{-\infty}^{+\infty} r(t)w(t)e^{-i2\pi ft} dt . . . \quad (5-6)$$

The determination of $G(f)$ can be simplified by noting that multiplication in the time domain is equivalent to convolution in the frequency domain, or

$$G(f) = \int_{-\infty}^{+\infty} R(f') W(f-f') df' , \quad (5-7)$$

where $R(f)$ and $W(f)$ are the respective transforms of $r(t)$ and $w(t)$. If a sample record were simple truncated then the data window is given by

$$w(t) = \begin{cases} 1 & -\tau \leq t \leq +\tau \\ 0 & \text{elsewhere} \end{cases} , \quad (5-8)$$

and then

$$\begin{aligned} W(f) &= \int_{-\infty}^{\infty} w(t)e^{-i2\pi ft} dt \\ &= \frac{2\tau \sin 2\pi f\tau}{2\pi f\tau} . \end{aligned} \quad (5-9)$$

Thus, the effect of a rectangular window is to cause the familiar $\text{sinc } x \equiv \sin x/x$ pattern in the frequency domain. From (5-7), $G(f)$ can be written as

$$G(f) = \int_{-\infty}^{+\infty} R(f') \frac{2\tau \sin 2\pi(f-f')\tau}{2\pi(f-f')\tau} df' . \quad (5-10)$$

If the sample record $r(t)$ were a sinusoidal wave at frequency f_o , then the spectrum of $g(t)$ would consist of the sinc patterns centered at frequencies $\pm f_o$. For short time records (small τ) the spectral energy would be distributed over a broad spectrum of frequencies and conversely, for long time records (large τ) the energy would be distributed over a narrow spectrum of frequencies. Quantitatively, the bandwidth of the spectrum, defined between the

half power points, is $.88/2\tau$ for the rectangular window. Also, the level of the first order sidelobes are 13.3 dB down from the mainlobe level. Various data windows have been purposed to reduce the sidelobes in the frequency domain that are associated with the rectangular window. The Hann window offers a good compromise between decrease in energy leakage and increase in spectral bandwidth and was used to weight the reverberation sample records.

The Hann window is given by

$$w(t) = \begin{cases} \frac{1}{2} (1 + \cos \frac{\pi t}{\tau}), & -\tau \leq t \leq \tau \\ 0 & \text{elsewhere.} \end{cases} \quad (5-11)$$

The center of the sample record has a weight of unity and the weighting function decreases with a cosine shape to zero at each end of the record. From the Fourier integral and (5-11), the transform of the Hann window is

$$W(f) = \tau \left\{ \frac{\sin 2\pi f\tau}{2\pi f\tau} + \frac{\sin 2\pi\tau(f - \frac{1}{2\tau})}{4\pi\tau(f - \frac{1}{2\tau})} + \frac{\sin 2\pi\tau(f + \frac{1}{2\tau})}{4\pi\tau(f + \frac{1}{2\tau})} \right\}. \quad (5-12)$$

The Hanning spectral window consists of the summation of three sinc functions with the mainlobes displaced from each other by the reciprocal of the window length $1/2\tau$. The amplitude of the center mainlobe is twice the amplitude of the adjacent mainlobes. The effect of the summation is to reduce the overall sidelobe levels at the unwanted expense of increasing the bandwidth of the mainlobe. The first order sidelobe levels are 31.5 dB down the level of the rectangular spectral window. However, the width of the mainlobe has increased to $1.44/2\tau$. Since the Hanning weights were applied to reverberation records of length $2\tau = 878.9$ msec, the spectral resolution (defined between half-power points) was 1.64 Hz. The Hanning spectral window can be observed in the spectrum of the reference signal (see Fig. 5-3).

The terms of the digitized data $r_k(j)$, the Hann data window $w(j)$ can be expressed as

$$w(j) = \frac{1}{2} \left\{ 1 + \cos \left[2\pi \left(j - \frac{N-1}{2} \right) / (N-1) \right] \right\} \quad j=0,1,\dots,N-1. \quad (5-13)$$

The Hann window can be easily implemented in the frequency domain by convolution with the sequence $-1/4, 1/2, -1/4$.

5.23 STATISTICAL CONFIDENCE OF DOPPLER SPECTRA ESTIMATES

Due to the finite number of power spectral densities computed in each data set, there was an uncertainty as to how well the Doppler spectra estimate $D(f)$ estimated the "true" Doppler spectra $D(f)$ of the reverberation process. If it is assumed that the reverberation samples have a Gaussian probability density function and are uncorrelated, then from 5-4, the power spectral density $D(f)$ has a chi-square distribution with n degrees of freedom. The equivalent

degrees of freedom can be written in terms of the average spectral estimate $E\{\hat{D}(f)\}$ and the variance of the spectral estimate $\text{Var}\{\hat{D}(f)\}$, or

$$n = \frac{2E^2 \{\hat{D}(f)\}}{\text{Var}\{\hat{D}(f)\}} . \quad (5-14)$$

The average spectral estimate is equal to the convolution of the tube spectrum $D(f)$ with the spectral window $|W(f)|^2$ [5-5]. The variance of the spectral estimate depends on the autocorrelation of the data window, the number M of spectra in the ensemble average and the percent of overlap in the data windows [5-6]. For the processing of the reverberation records, there was no overlap, and under that condition, the equivalent degrees of freedom was equal to twice the number of spectra in the ensemble $n=2M$. The confidence interval for the Doppler spectra $D(f)$, which was based on the spectra estimate $\hat{D}(f)$, was calculated from the chi-square distribution by

$$\text{Prob} \left[\frac{n\hat{D}(f)}{\chi_n^2; \alpha/2} \leq D(f) \leq \frac{n\hat{D}(f)}{\chi_n^2; 1-\alpha/2} \right] = 1-\alpha, \quad (5-15)$$

where $1-\alpha$ is the confidence interval, and $\chi_n^2; \alpha/2$ is the $100 \alpha/2$ percentage point of the chi-square distribution.

To know with a 90% confidence that the true Doppler spectra $D(f)$ fell within a 3 dB spread of the estimated spectra $\hat{D}(f)$ required 50 degrees of freedom for the estimate. Thus, an ensemble average of 25 spectra was required.

5.24 REMOVAL OF SINUSOIDAL INTERFERENCE

Observation of the reverberation data revealed that there were three different sources of interference. Two of the sources involved water-borne arrivals--a direct path and a bottom scattered arrival. The third source of interference was caused by electrical pickup of the difference frequency during transmission.

To resolve the various multipath interferences, 25 msec CW pulses were transmitted at each angle of incidence and acoustic frequency. As an example, the received signals from the 25 msec transmitted pulses at a 7 kHz transmit frequency (bandshifted to 220 Hz) and an incident angle of 20° is shown in Fig. 5-1. The reference pulses (see CHAPTER 3), which were processed by an identical receiving channel as the hydrophone outputs, are the top trace (a). The lower eight traces are from the hydrophone channels. Four transmit pulses are shown and 156 msec of time is shown following each of the transmissions. (The receiving system gain is not the same which accounts for the differences in levels from channel-to-channel.)

The following observations can be made by referring to the output of hydrophone 8 (trace (b)): there is a direct path arrival prior to the onset

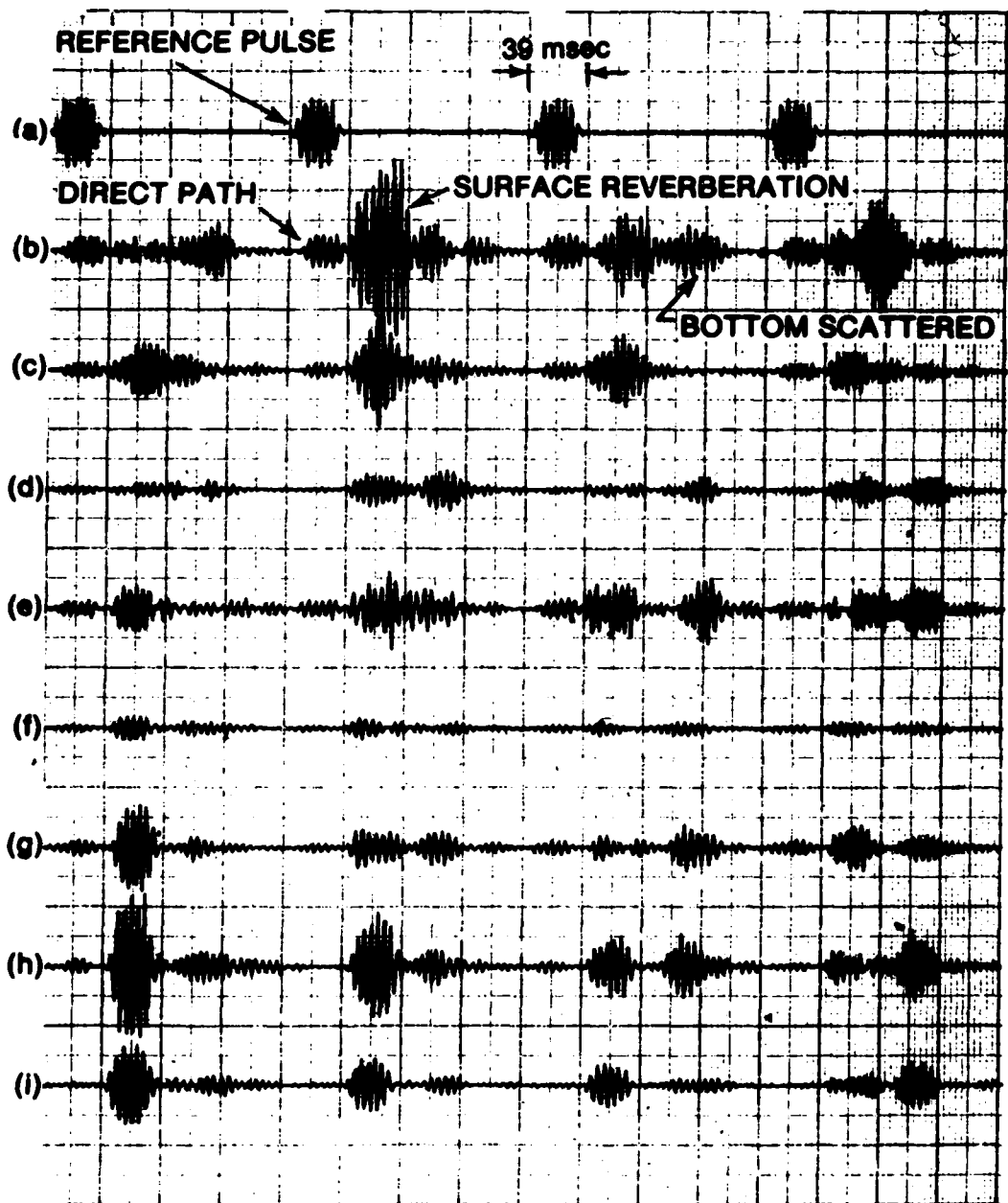


Figure 5-1. Traces from Four Transmitted 25 msec Pulses with 156 msec of Time Following the Initiation of Each Pulse. Trace (a) is the Output of the Reference Channel and Traces (b) through (i) are the Respective Hydrophone Outputs, H₃ through H₁ (see Fig. 2-2).

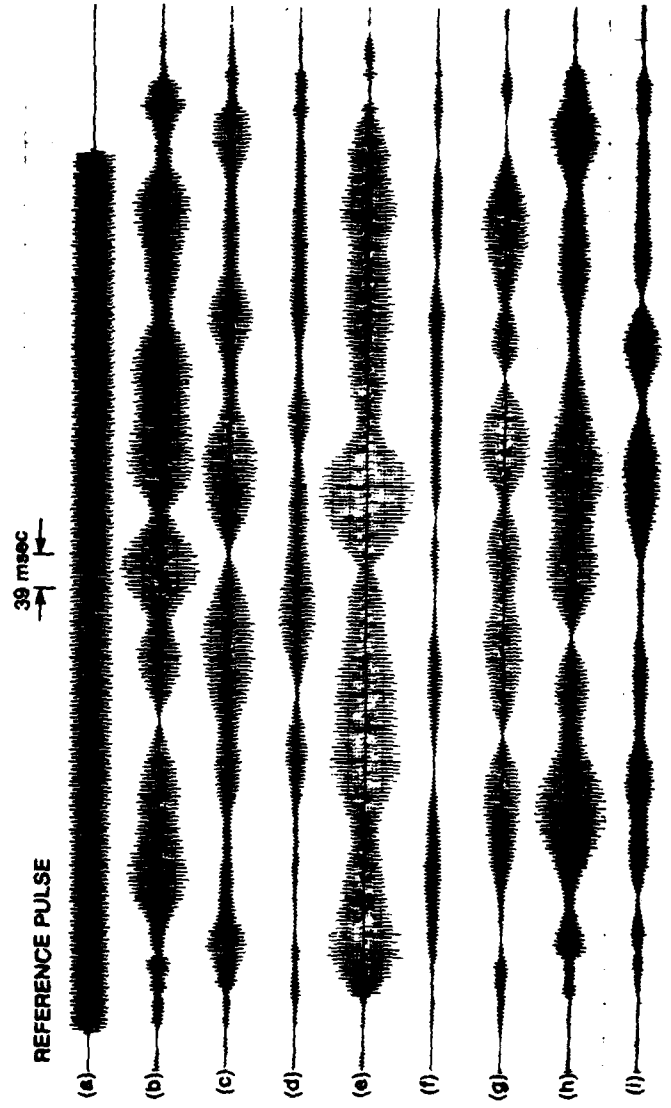


Figure 5-2. Traces From the Transmission of a 1000 msec Pulsed CW Waveform at a Frequency of 7 kHz (Bandshifted to 220 Hz). Trace (a) is the Reference Channel and Traces (b) through (i) are the Respective Hydrophone Outputs, H8 through H1 (see Figure 2-2).

of surface reverberation and the surface reverberation is followed by bottom scattered arrivals. The direct path is seen to have a constant level at each transmission. Referring to the other hydrophone outputs, the level of the direct path varies with hydrophone as seen by its absence on hydrophones 1 and 2 (traces (h) and (i), respectively). The amplitude fluctuations of the surface reverberation is more observable on the longer transmitted waveforms.

For the 1000 msec transmitted CW pulses, the pulses used in the computation of the Doppler spectra, the interference signals will overlap the desired surface reverberation. Thus, the surface reverberation returns will be contaminated. The received signals from 1.0 sec transmissions at a frequency of 7 kHz (bandshifted to 220 Hz) and a 20° incident angle is shown in Fig. 5-2. As in the previous figure, the top trace is the 1.0 sec reference signal and the lower eight traces are the received signals at the hydrophone outputs. Referring to hydrophone 8 (trace (b)), initially the direct path is observed and then after approximately 40 msec the reverberation predominates. The received signals on all hydrophone outputs last for approximately 80 msec beyond the end of transmission. Due to the close proximity of the hydrophone array to the parametric array, the last 80 msec of received signal is surface and bottom reverberation.

At the 40° and 60° incident angles, the surface reverberation level was much lower than at 20°. This was due primarily to two factors: a decrease in surface scattering strength with increasing incident angle and the increase in propagation loss with increasing distance to the surface. Thus, the direct path interference becomes more significant at the higher angles of incidence. Likewise, the electrical pickup interference becomes more significant.

A least mean square technique was used to remove the effects of the electrical interference, the direct path arrival and also the coherent part of the bottom scattered arrival. The technique consisted of removing from the total received signal on each hydrophone a sinusoidal component at the difference frequency with a least mean square criterion. Let $T(t)$ be the received signal and $A \cos(\omega_d t + \phi)$ be a sinusoidal component adjusted in amplitude A and phase ϕ such that

$$(T(t) - A \cos(\omega_d t + \phi))^2 \quad (5-16)$$

was minimized, where $T(t)$ consists of the summation of an electrical interference $E(t)$, a direct path $D(t)$, a surface reverberation $S(t)$, and a bottom reverberated arrival $B(t)$, or

$$T(t) = E(t) + D(t-t_0) + S(t-t_1) + B(t-t_2). \quad (5-17)$$

The times t_0 , t_1 , t_2 are the respective propagation time delays for the direct, surface, and bottom ($t_0 < t_1 < t_2$). Thus, for the time interval between t_2 and T , where T is the transmitted pulse length, all interference signals are represented in $T(t)$. During this time interval, the direct path and electrical interference signal have added to give a resultant sinusoidal component with amplitude and phase that is dependent on the amplitude and phase of the two interfering signals. The bottom scattered arrival cannot be considered simply as a sinusoidal component since this signal was initially

reflected (and scattered) from the sea surface. Thus, the bottom arrival is modulated in amplitude and phase by the sea surface (see, for example, [5-7]) and therefore consists of both coherent and incoherent energy. The coherent energy will add with the interference signals to produce a sinusoidal component that can be removed via (5-16).

The removal of the sinusoidal component from the total received signal will also affect the power spectra of the surface reverberation. This can be seen by expressing the surface reverberated signal $S(t)$ in a manner similar to S.O. Rice's treatment of shot effect current [5-8], or

$$S(t) = \sum_{n=1}^N C_n \cos(\omega_n t - \phi_n) , \quad (5-18)$$

where ϕ_1, \dots, ϕ_n are phase angles having a random distribution over 0 to 2π radians and the amplitudes C_n are related to the power spectrum $P(f_n)$ of the reverberation by

$$C_n = \sqrt{2\Delta f P(f_n)} , \quad (5-19)$$

and where

$$\omega_n = 2\pi f_n = 2\pi n \Delta f .$$

It can be seen that when the frequency in the reverberation band is the same as the transmitted difference frequency that this component will also be removed by (5-16).

The sinusoidal component that contaminated the surface reverberation data was removed by finding the best fitting sinusoid that minimized the energy in the total received signal. The actual procedures are described in APPENDIX A and the effects of the removal are discussed in SECTION 5.5.

5.25 LINEAR FREQUENCY MODULATED WAVEFORMS

A further attempt was made to isolate the surface reverberation from the direct path, electrical interference, and bottom reverberation. The procedure involved the transmission of linear frequency in the waveform; such that multipath arrivals arrive at the receiver with not only time delay differences, but also with frequency differences.

By transmitting LFM waveforms with 100 Hz bandwidths and 500 msec pulse lengths; and using appropriate signal processing techniques, it was possible to isolate the multipath arrivals in frequency and obtain the Doppler spectra of the reverberation. The center frequencies of the transmitted waveforms were the same as the pulsed CW waveforms - 3.5, 5.0, 7.0 and 9.0 kHz. The received reverberation, which included possible multipaths were digitally multiplied by a reference LFM waveform. The resulting time series was Hanning weighted and Fourier transformed to obtain power spectral density estimates.

Appendix B describes the technical procedures and results in estimating the Doppler spectra of the reverberation using LFM waveforms. Although the technique was only partially successful in estimating Doppler spectra, the technique may be advantageous in isolating multipath arrivals in other propagation experiments.

5.3 DOPPLER SHIFTS AND BANDWIDTHS

As described in SECTION 5.21, the Doppler spectra $\hat{D}(f)$ were computed by ensemble averaging 25 spectral estimates. The spectral estimates, which were based on (5-2) and (5-3), were computed from the reverberation returns of 25 consecutive transmissions of the 1000 msec CW pulses.

The Doppler spectra were then normalized by computing the fractional power in each frequency cell f_n , or

$$\hat{D}_N(f_n) = \frac{\hat{D}(f_n)}{\sum_{n=P}^{P+Q} \hat{D}(f_n)} , \quad (5-20)$$

where in the denominator, the summation gives the total power in the reverberation Doppler spectra, and $\hat{D}_N(f_n)$ is the normalized Doppler spectra. As indicated in the summation, the frequency band extends from f_p to f_{p+Q} . The normalized Doppler spectra was expressed in decibels as

$$10 \log \hat{D}_N(f_n) . \quad (5-21)$$

For each Doppler spectra, two parameters were computed: the Doppler shift frequency and the Doppler bandwidth.

The Doppler shift frequency was defined as the difference between the symmetrical power frequency f_{sp} and the transmitted difference frequency f_d , or

$$f_{ds} = f_{sp} - f_d . \quad (5-22)$$

The symmetrical power frequency is the frequency at which 50% of the power is above and below and was computed from

$$\sum_{n=P}^{P+S} \hat{D}_N(f_n) = \frac{1}{2} \sum_{n=P}^{P+Q} \hat{D}_N(f_n) . \quad (5-23)$$

The upper limit of the left hand summation defines the symmetrical frequency f_{sp} and the right hand summation gives the total reverberation power.

The Doppler bandwidth was obtained by summing spectral estimates at frequencies symmetrical about the Doppler shift frequency f_{ds} until half the reverberation power was computed. Thus the bandwidth $2 f_w$ can be defined as

$$\sum_{n=S-W}^{S+W} D_N(f_n) = \frac{1}{2} \sum_{n=P}^{P+Q} D_N(f_n) . \quad (5-24)$$

5.4 REFERENCE SIGNAL POWER SPECTRUM; EXAMPLE OF

The generation and subsequent conditioning of the reference signal has been discussed in CHAPTERS 3 and 4. As noted, the reference signal has the same pulse length and frequency as the difference frequency generated by the water nonlinearities. Also, the reference signal was conditioned by the same receiving system as the hydrophones and analogue recorded and digitally processed in the same manner as the reverberation signals. Therefore, the reference signal served as a monitor for the tape recording and playback frequency instabilities, and for checking processing errors incurred by the reverberation signals.

The power spectral density (in decibels) of a reference signal is shown in Fig. 5-3. The spectrum was obtained from the reference signals recorded at a 20° incident angle and a 7 kHz transmit frequency. The location of the spectral peak has been referred to a frequency of 0.0 Hz and the spectral estimates are spaced every 0.57 Hz. The spectrum was obtained from records 878.9 msec long and the data samples were Hanning weighted. The spectral shape is in good agreement with the Hanning spectral window which should have a half-power bandwidth of 1.64 Hz and first order sidelobes 31.5 dB down from the peak value.

5.5 REVERBERATION DOPPLER SPECTRA, EXAMPLES OF

The effects of removing a sinusoidal component from the received signal can be observed in the reverberation Doppler spectrum of Fig. 5-4. Also shown in the Figure legend are the computed Doppler shift and bandwidth as obtained from (5-21), (5-22), and (5-23). The spectrum was computed by ensemble averaging the power spectral density of 25 reverberation returns of the 1.0 sec transmitted CW pulses at an incident angle of 20° and a transmitted frequency of 7 kHz.

A "notch" of approximately 4 dB can be observed in the Doppler spectrum at the transmitted frequency. As in the previous example (Fig. 5-3), the transmitted frequency has been referred to a frequency of 0.0 Hz. The notch is a result of not only removing energy due to the interference signals, but also from the removal of energy from the surface reverberation. At frequencies displaced from the transmitted frequency, the spectral estimates are due to the surface reverberation. The spectral estimates at the transmitted frequency and at the adjacent frequencies have been curve fitted to represent the spectral estimates due to surface reverberation. The curve fitted spectral estimates are shown by the open circles. Examples will now be cited which do and do not have multipath interferences, and it will be shown that simple curve fitting of the spectral estimates about the transmitted frequency is a realistic representation of the surface reverberation Doppler spectra.

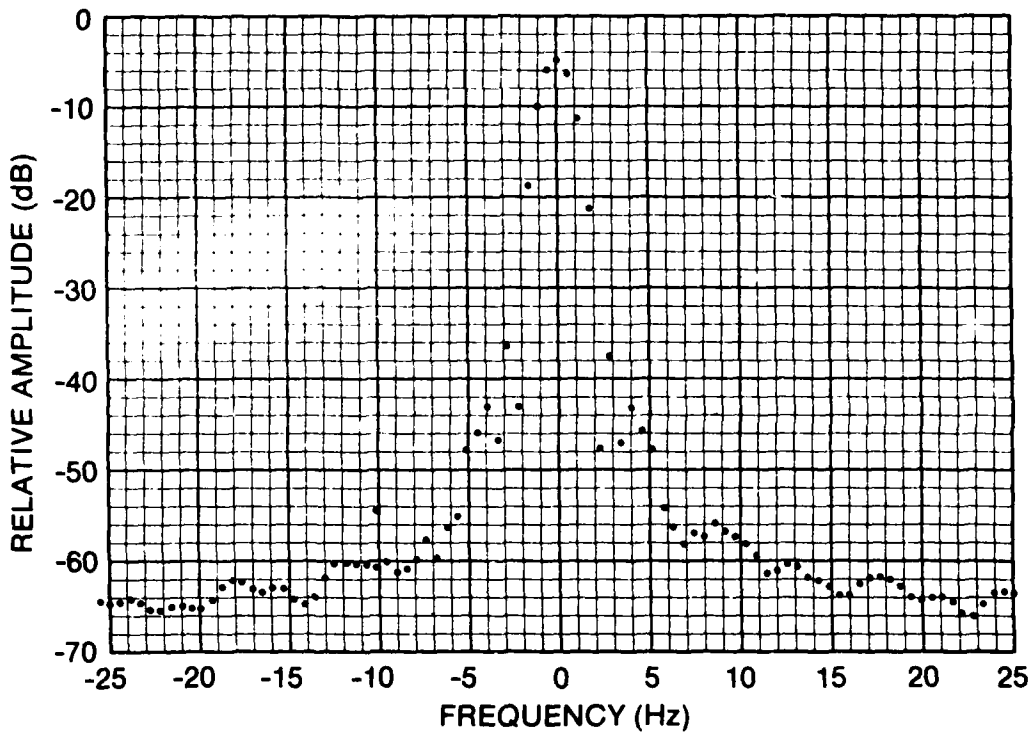


Figure 5-3. Power Spectral Density of Reference Signal Recorded During Transmission of 7 kHz CW 1000 msec Pulses at 20° Incident Angle.

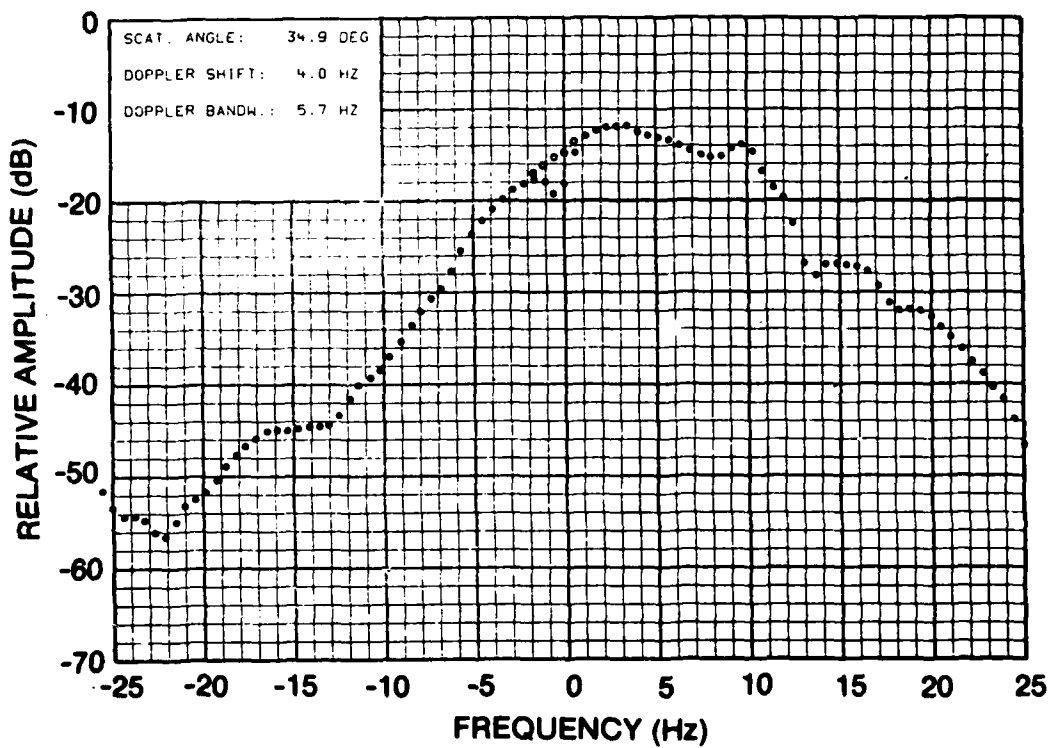


Figure 5-4. Doppler Spectrum of Reverberation Received on Hydrophone H8 (Scattering Angle 34.9°) for a Transmitted Frequency of 7 kHz and an Incident Angle of 20°. Open Circles in Vicinity of 0 Hertz were Curve Fitted where Sinusoidal Component was Removed.

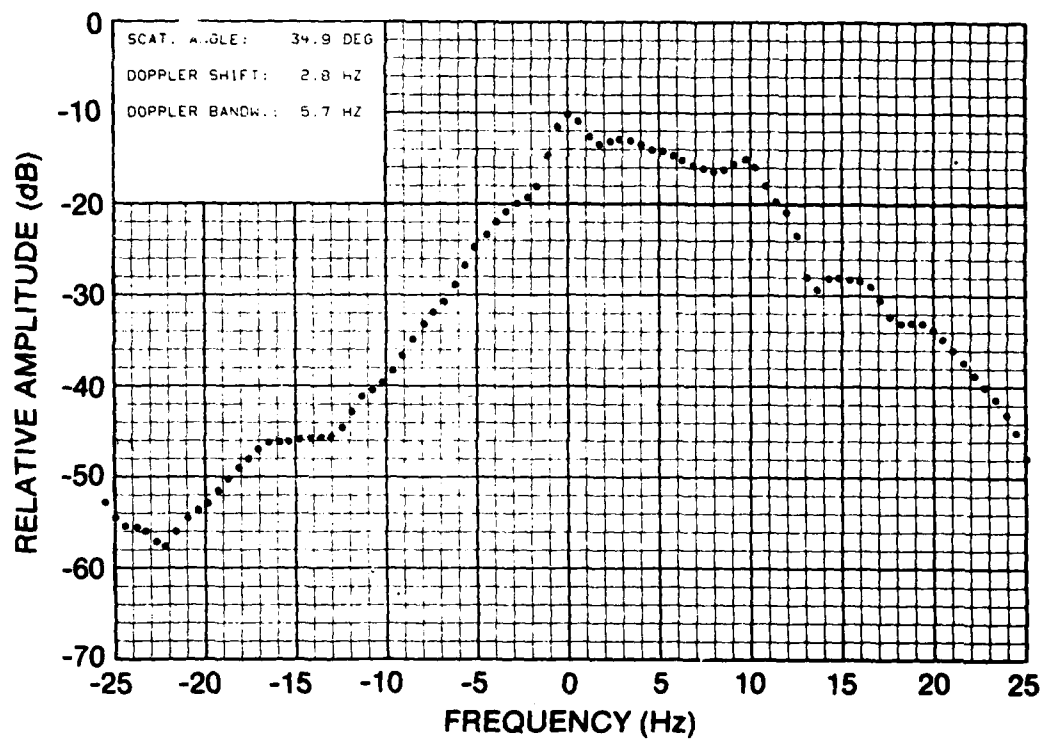


Figure 5-5. Doppler Spectrum of Reverberation Received on Hydrophone H8 (Scattering Angle of 34.9°) for a Transmitted Frequency of 7 kHz and an Incident Angle of 20°. No Sinusoidal Component was Removed from Data.

As mentioned previously, in respect to the direct path interference shown in Fig. 5-1, the direct path interference on hydrophone H1 was negligible in comparison to the direct path interference on hydrophone H8. The Doppler spectra for these two hydrophone outputs are shown in Figs. 5-5 and 5-6. No sinusoidal component has been removed in either of these spectra. The direct path interference can be seen at the transmitted frequency on hydrophone H8 and its absence is evident on hydrophone H1. The spectral estimates in both figures are nearly the same, except for the obvious spectral estimates effected by the direct path interference.

The Doppler spectra in Figs. 5-4 and 5-5 are for the same hydrophone output (H8) except that the direct path has been removed in Fig. 5-4 by the least mean square criterion discussed in Appendix A. The Doppler spectra shown in Fig. 5-7 is the same as Fig. 5-6 except that a sinusoidal component was subtracted from the data. Since there was no direct path interference on the hydrophone, the "notch" in Fig. 5-7 was due primarily to the removal of surface reverberation energy. It can be observed that the curve fitted spectral estimates in the vicinity of the transmitted frequency is in good agreement with the spectral estimates of Fig. 5-6.

5.6 COEFFICIENT OF VARIATION OF SPECTRAL ESTIMATES

The Doppler spectra estimates $\hat{B}(f_n)$ were computed by ensemble averaging the power spectral density estimates $\hat{B}_k(f_n)$ as given by (5-4). A measure of the variability of the estimates $\hat{B}_k(f_n)$ can be obtained by computing the coefficient of variation CV as defined by

$$CV = \frac{\sqrt{\text{Var}[\hat{B}(f_n)]}}{E[\hat{B}(f_n)]} . \quad (5-25)$$

where in (5-25) CV is the ratio of the standard deviation of the estimates at frequency location f_n to the average spectral estimate found at the same frequency. The coefficient of variation is a relative measurement which expresses the variability of the spectral estimate in relationship to the average estimate.

A typical example of the variability of the power spectral density estimates is shown in Fig. 5-8 where $10 \log(CV)$ has been plotted. This example describes the spectral variability for the Doppler spectra estimates given in Fig. 5-4. The standard deviation of the spectral estimates can be obtained from Figs. 5-4 and 5-8 via

$$10 \log \sqrt{\text{Var}[\hat{B}(f_n)]} = 10 \log CV + 10 \log (E[\hat{B}(f_n)]) . \quad (5-26)$$

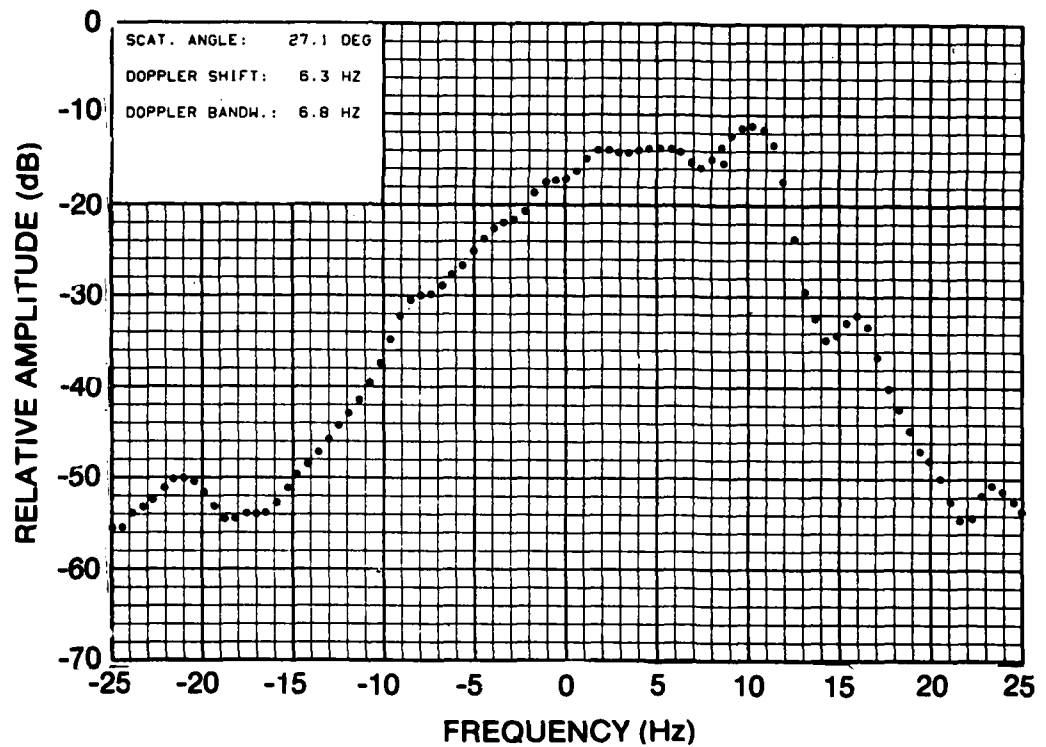


Figure 5-6. Doppler Spectrum of Reverberation Received on Hydrophone H1 (Scattering Angle of 27.1°) for a Transmitted Frequency of 7 kHz and an Incident Angle of 20° . No Sinusoidal Component was Removed from Data.

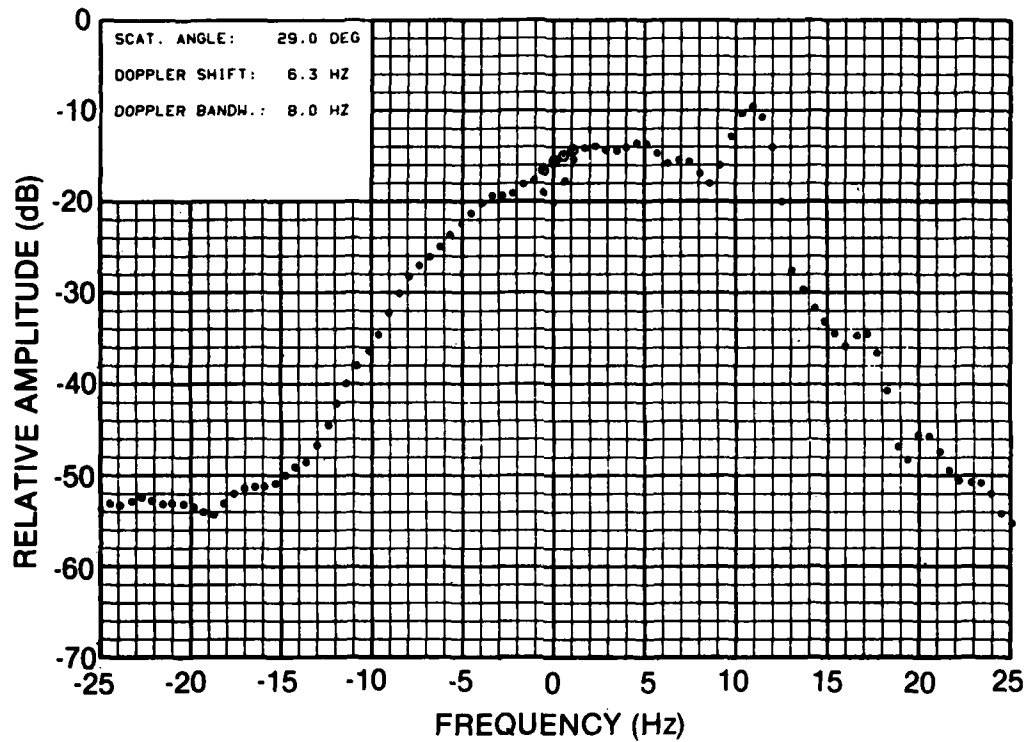


Figure 5-7. Doppler Spectrum of Reverberation Received on Hydrophone H1 (Scattering angle of 27.1°) for a Transmitted Frequency of 7 kHz and an Incident Angle of 20° . Sinusoidal Component has been subtracted from Data.

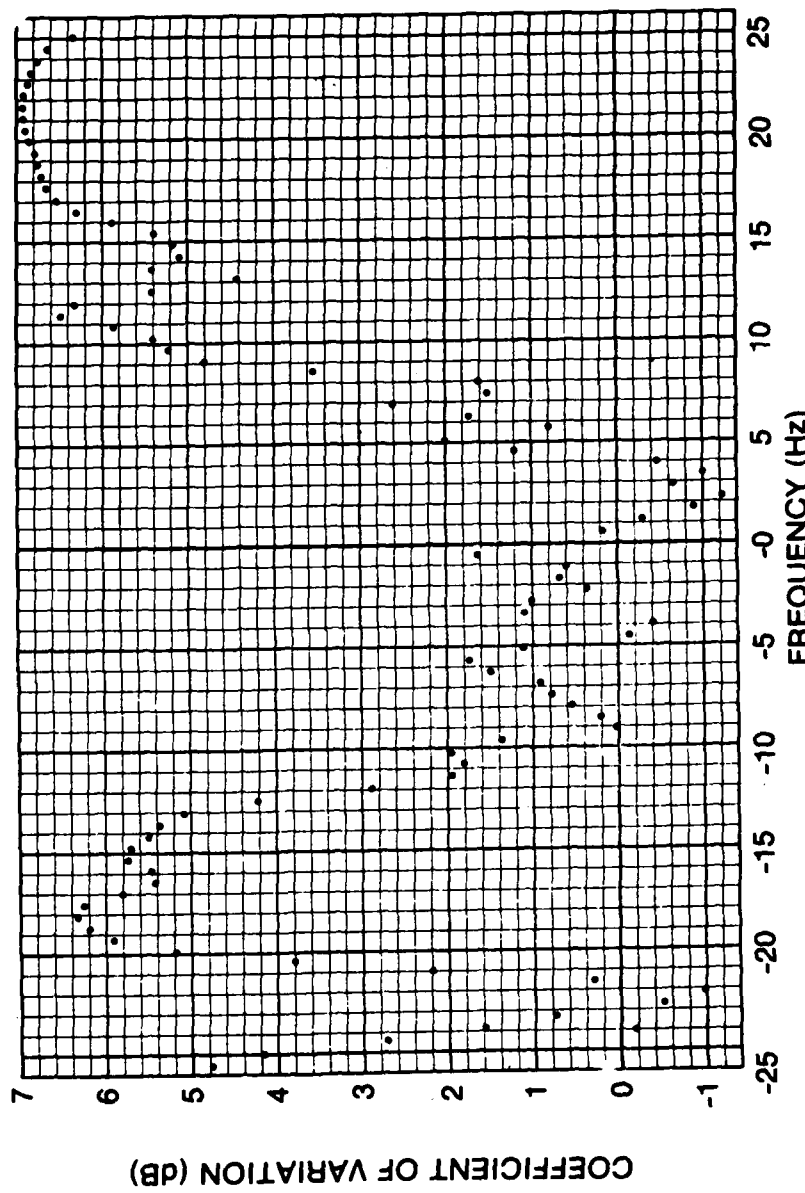


Figure 5-8. Coefficient of Variation (in dB) for a Transmitted Frequency of 7 kHz, an Incident Angle of 20°, and a Scattering Angle of 34.9°.

CHAPTER 6

DOPPLER SPECTRA RESULTS

6.1 BACKGROUND

A time period of approximately eight hours was required to obtain a complete acoustic and oceanographic data set. Prior to the acoustic measurement period, the oceanographic information was gathered with the hopes that the sea surface statistics would remain stationary throughout the measurement period for the Doppler spectra. Although the sea surface statistics could not be measured with the simultaneous acoustic measurements, wind speed and direction could be monitored throughout the eight hour period. The Doppler spectra results were obtained under stationary meteorological conditions.

During the measurement period the average wind speed was about 5 m/sec and the prevailing wind direction was from a westerly sector. Since the parametric array was aimed on a bearing of 278° (relative to magnetic north), the acoustic energy was transmitted into the wind. The sea surface consisted of sea waves generated by local winds with some low amplitude swell from a remote storm. The spectral energy on the sea surface was concentrated in a sea wave spectrum (see CHAPTER 8) which had maximum energy at frequencies in the vicinity of 0.27 Hz. The propagating direction of the frequency component of maximum power was at an angle of about 35° from the maximum response axis of the parametric array. The directional spectrum of the other surface wave frequencies was also concentrated close to the sector of acoustic transmission. The sea surface RMS wave height was 8.7 cm.

In terms of the acoustic wavelengths and transmit receive geometries, the apparent roughness [6-1] of the sea surface G can be expressed as

$$\sqrt{G} = \frac{2\pi\sigma}{\lambda} (\cos \theta + \cos \phi) , \quad (6-1)$$

where λ is the acoustic wavelength, σ is the RMS wave height, θ and ϕ are the respective angles of incidence and scatter - both measured from the normal to the sea surface. G is sometimes referred to as the Rayleigh roughness parameter. A surface is considered smooth if $G < 1$; and likewise, is considered rough if the converse is true. In the experiment G ranged from about 1.5 to 40 depending on the transmitted frequency and acoustic geometry. The surface appeared smoothest at a 3.5 kHz transmit frequency and at a 60° incident angle; and appeared roughest at a 9 kHz transmit frequency and at the near normal incident angle of -4.7°.

Visual observation of the sea surface showed that there were no white caps present. Also, using acoustic techniques to measure the time varying surface wave heights (CHAPTER 7) showed that there was no near surface bubble layer to affect the surface reverberation.

The data gathering sequence began at an incident angle of -4.7° with the transmission of three waveform types at difference frequencies of 9.0, 7.0, 5.0, and 3.5 kHz. The parametric array was then rotated to incident angles of 20, 40, and 60° and the same waveforms and frequencies were transmitted. Doppler spectra were computed from the reverberation returns from the 1000 msec pulsed CW waveform. Using signal processing techniques described in the previous chapter, the spectra were computed at a frequency resolution of 1.6 Hz and the 90% confidence limits of the spectral estimates were approximately ± 1.5 dB.

Not all of the Doppler spectra and their associated coefficients of variation are presented in this chapter. However, APPENDIX C does contain the spectra and coefficient of variations obtained on hydrophones H1 and H8 at each transmitted frequency and angle of incidence.

6.2 DOPPLER SPECTRA AT NEAR NORMAL INCIDENCE

With the parametric array trained at the sea surface at an incident angle of -4.7° , the energy reflected and scattered in the specular direction was received on the hydrophone array. The specular angle was computed to hydrophone H4 and was based on the horizontal separation between parametric and hydrophone arrays and their vertical distances to the sea surface. An indication of a specular reflection is when the Doppler spectrum of the received signal is symmetrical about the transmitted frequency [5-7]. The best example of a specular reflection was obtained on hydrophone H1 (scattering angle 4.1°) at a transmitted frequency of 9 kHz which is shown in Fig. 6-1. The computed Doppler shift was 0.0 Hz which indicates the symmetry in the spectrum. Note that the transmitted frequency has been referred to a frequency of zero Hertz. The Doppler bandwidth was 3.4 Hz between halfpower points and the spectrum was Gaussian in shape. The Doppler spectra obtained at other transmitted frequencies shows that the spectral bandwidths increase with increasing frequency (Fig. 6-2). The spectra were measured at a scattering angle of 4.1° . There was a slight Doppler shift (slight, in comparison to shifts at 20° incident angle) of approximately 1.1 Hz. The bandwidth of the 3.5 kHz spectrum was approximately one-third the bandwidth of the 9 kHz spectrum. Also, there was negligible difference in the spectra measured at the other scattering angles.

6.3 DEPENDENCE OF DOPPLER SPECTRA ON INCIDENCE ANGLE

Asymmetry was introduced into the character of the Doppler spectra as the incident angle was rotated to 20° . The reverberation Doppler spectra not only became asymmetrical, but the bandwidth of the reverberation also increased significantly. The Doppler shift at a 20° incident angle and at a transmitted frequency of 7 kHz was 6.3 Hz for a scattering angle of 27.1° (Fig. 6-3). The Doppler shift was approximately equal to the 6.8 Hz bandwidth of the reverberation. There was further asymmetry in the spectrum as shown by the peak in the power spectral density in the frequency band around 11 Hz.

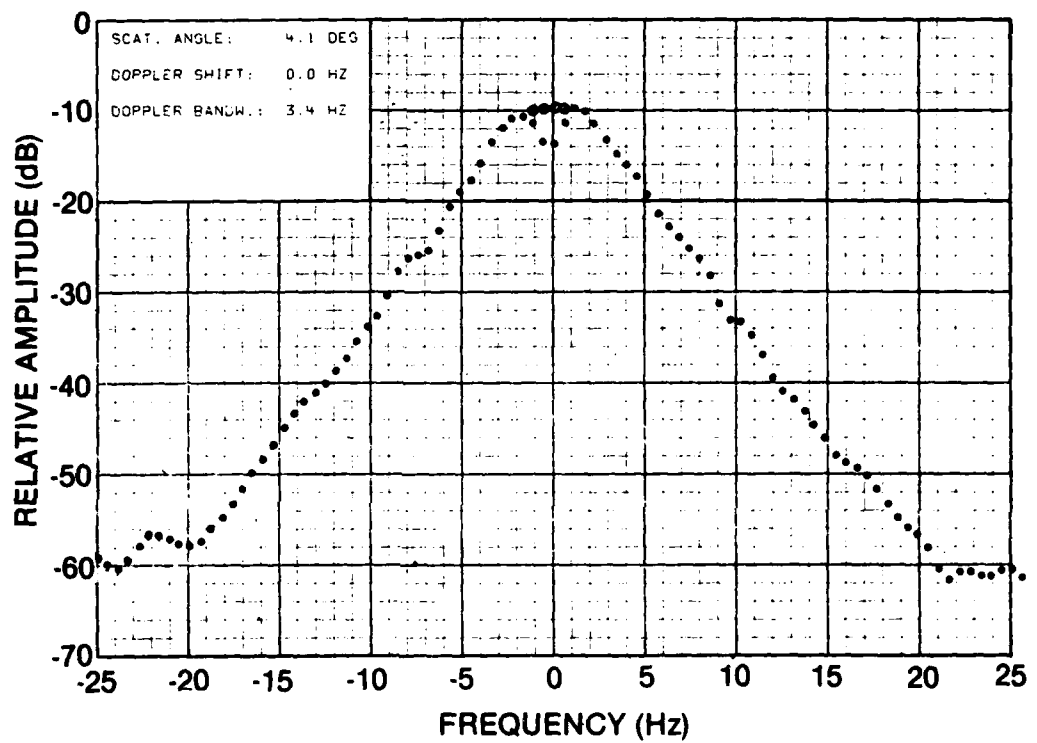


Figure 6-1: Doppler Spectrum Obtained at a 9 kHz Transmitted Frequency, at Near Normal Incidence (-4.7°), and at a Scattering Angle of 4.1° .

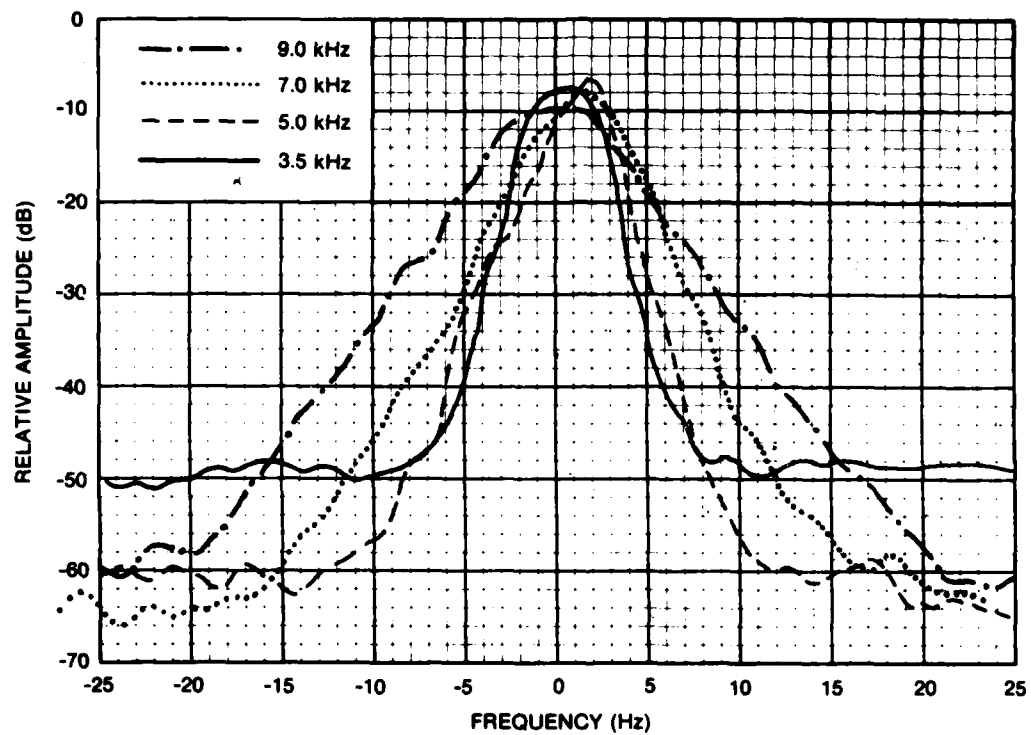


Figure 6-2: Doppler Spectra Obtained at the Four Indicated Transmit Frequencies, at an Incident Angle Near Normal (-4.7°), and a Scattering Angle of 4.1° .

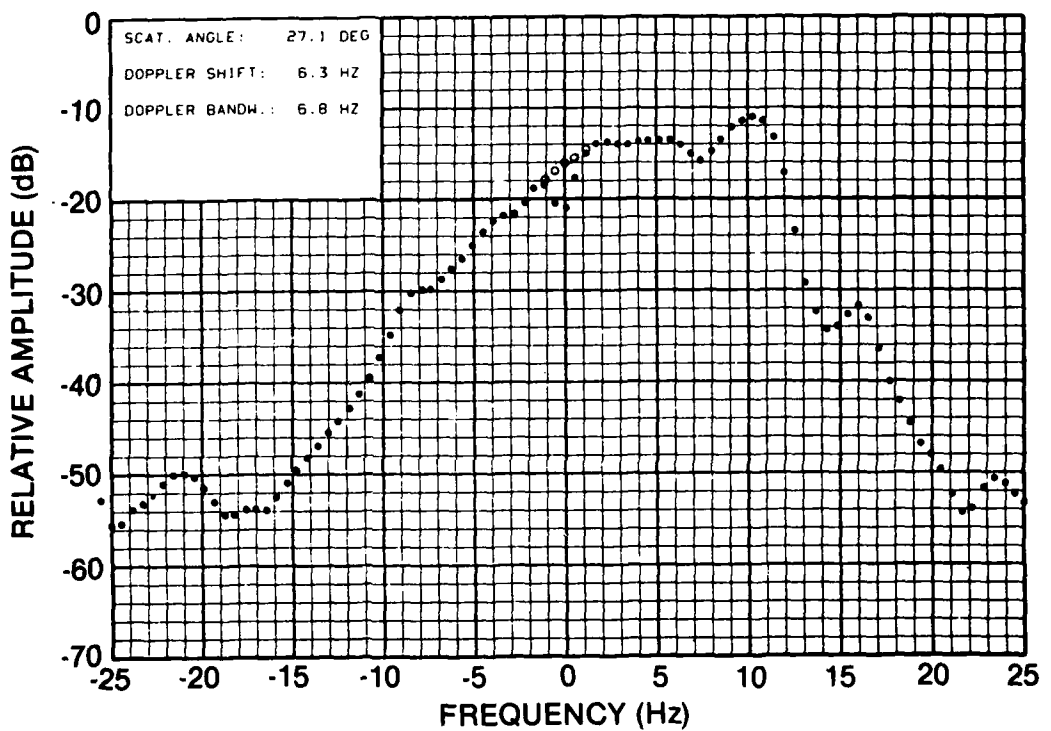


Figure 6-3: Doppler Spectrum of Reverberation Obtained at an Incident Angle of 20° , a Scattering Angle of 27.1° , and at a Transmitted Frequency of 7 kHz.

The measurement of a positive Doppler shift was in agreement with the direction of propagation of the sea waves. Although simple resonance theory was not directly applicable at these large Rayleigh roughness parameters (which was greater than 20 for 7 kHz at 20°), the theory predicted a positive Doppler shift at a frequency of 3.7 Hz.

The dependence of the spectra on incidence angle can be observed by keeping the frequency constant. Typically, the spectra measured as a function of incidence angle showed that the reverberation bandwidth decreased with increasing incident angle. Using the 9 kHz transmitted frequency as an example, the spectral variation with incidence angle can be observed from Fig. 6-4. The spectral bandwidth was a minimum at near normal incidence and a maximum at an incident angle of 20°. As the incident angle increased the spectral bandwidth drops off accordingly.

6.4 DEPENDENCE OF DOPPLER SPECTRA ON SCATTERING ANGLE

Regardless of transmitted frequency or angle of incidence, the spectra measured as a function of scattering angle showed little variation in spectral shape or computed Doppler shifts and bandwidths. As an example, the spectra shown in Fig. 6-5 were measured at a frequency of 5.0 kHz, at an incident angle of 20°, and at three scattering angles separated by approximately 4°. The spectral shapes are nearly identical with Doppler shifts of 2.3 Hz and bandwidths of 3.4 Hz.

6.5 COEFFICIENT OF VARIATION

The coefficient of variation expresses the variability of the spectral estimates in relationship to the average spectral estimate. The coefficient of variation should be a constant and equal to unity (0 dB) if the spectral estimates were computed from reverberation samples that have Gaussian probability distribution with zero means [6-2]. From (5-14) and (5-25) shows that

$$CV = \sqrt{\frac{n}{2}} , \quad (6-2)$$

where n is the number of degrees of freedom. Each spectral estimate has two degrees of freedom such that $CV = 1$.

In Fig. 6-6, $10 \log CV$ is plotted for each spectral estimate obtained from data at a 7 kHz transmit frequency and an incident angle of 20°. Note that in the vicinity of zero Doppler that the coefficient of variation is averaging about 0 dB. However, at higher and lower Doppler frequencies, $10 \log CV$ is approximately 6 dB.

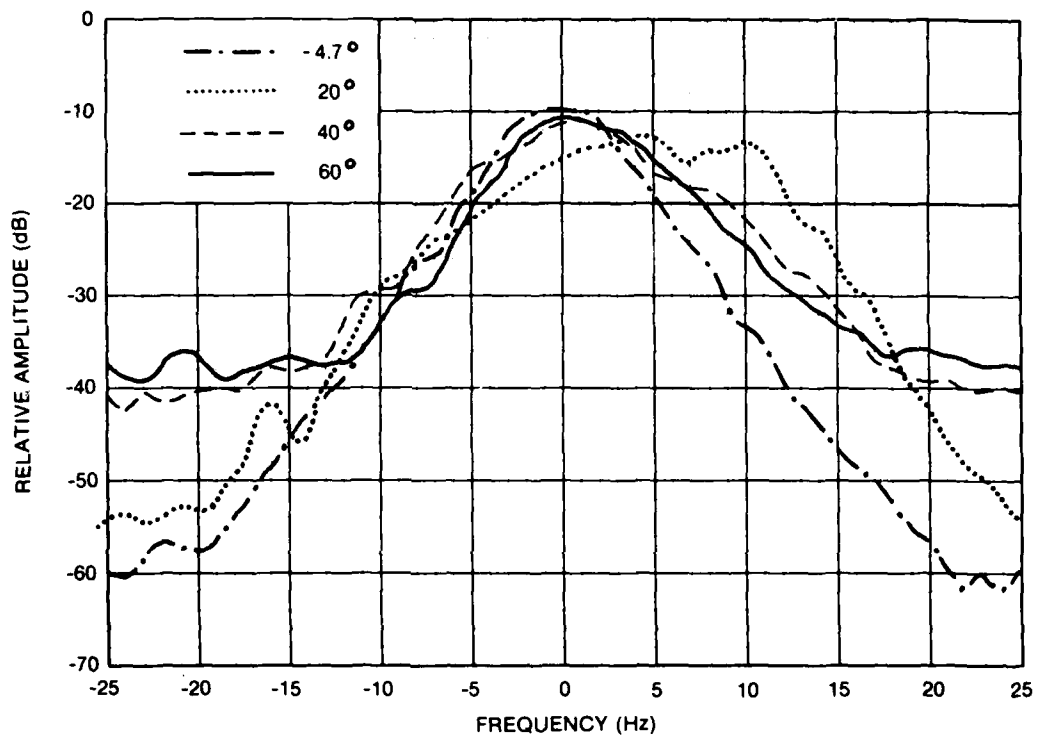


Figure 6-4: Doppler Spectra Obtained at the Four Indicated Incident Angles, and at a Transmitted Frequency of 9 kHz.

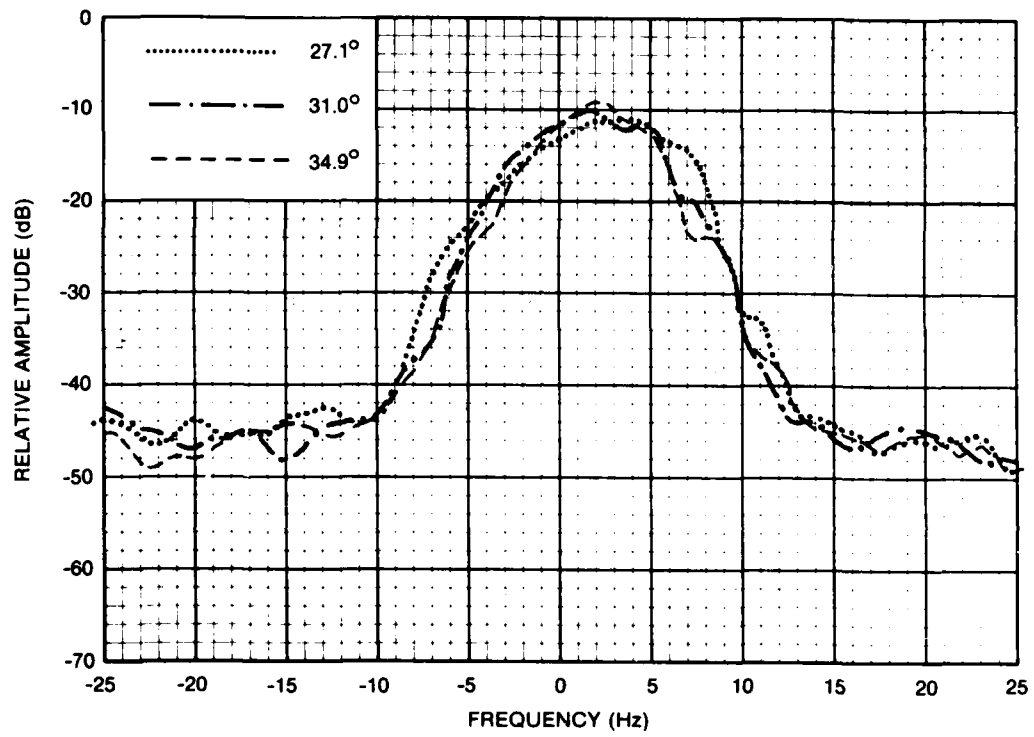


Figure 6-5: Doppler Spectra Obtained at the Three Indicated Scattering Angles, at an Incident Angle of 20° and at a Transmitted Frequency of 5 kHz.

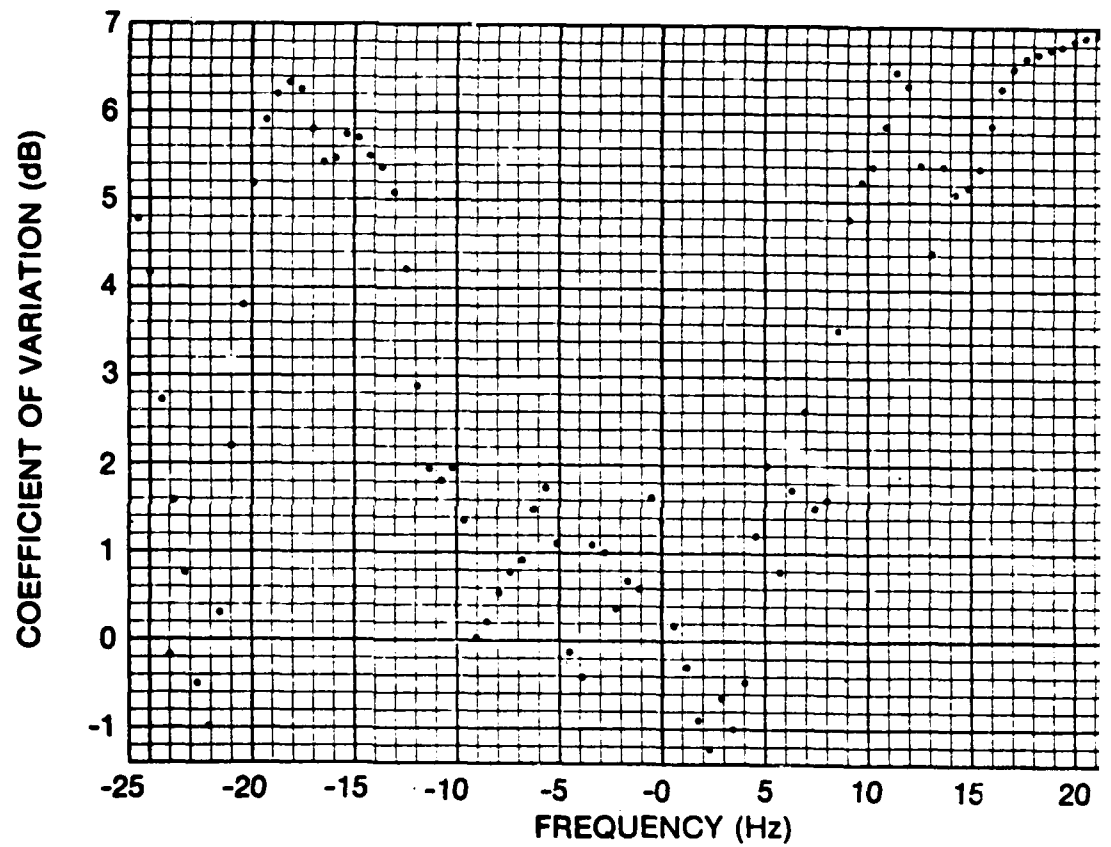


Figure 6-6: Coefficient of Variation ($10 \log CV$) Obtained From Data at an Incident Angle of 20° , a Scattering Angle of 34.9° and at a Transmitted Frequency of 7 kHz.

CHAPTER 7

ESTIMATION METHODS FOR DETERMINING THE DIRECTIONAL CHARACTERISTICS OF THE SEA SURFACE FROM A LINE ARRAY OF WAVE HEIGHT SENSORS

7.1 INTRODUCTION

One of the main difficulties in predicting surface-scattered acoustic fields has been due to the inadequacy of information about the pertinent statistics of the sea surface during the acoustic experiment. Often indirect measurements, such as a simple observation of sea state or anemometer readings of wind speed sufficed in indicating the condition of the sea.

Justification for wind speed as an environmental measurement in support of acoustic data was based on the grounds that the turbulent flow of air above the sea generated the surface waves. However, wind speed by itself was only of limited usefulness because the linear extent over which the wind blows (the fetch), and the time for which the wind blows (the duration) also determines whether a sea will fully develop. Furthermore, wind speed can be an erroneous indicator of sea conditions when swell waves have propagated to the measurement area from distant storms.

More recently, acoustic data have been accompanied by surface RMS wave height or one-dimensional power spectral density as environmental support data. The most prevalent measurement technique used capacitive or resistive probes (staffs) to measure time varying wave height at a discrete point on the sea surface. In shallow water the probes were generally mounted to fixed platforms and in deep water to floating buoys. Other sensors include pressure transducers mounted on the ocean bottom, inverted echo sounders, electromagnetics, and accelerometers. All the sensors that measured wave height at a discrete point were omnidirectional; and the measured wave height consisted of the summation of surface waves arriving from various directions.

Although the directional wave spectrum (or an equivalently coordinate transformed spectrum) is a required input to Doppler spectra scattering models [7-1], to my knowledge, the measurements of both reverberation and surface wave directionality have not been performed simultaneously. However, isolated measurements of surface directionality have been obtained, and the most common technique employs an array of sensors that simultaneously measures wave height at a number of discrete points on the surface. Arrays of probes [7-2], pressure transducer arrays [7-3, 7-4], free floating buoys [7-5], and stereo photograph [7-6] have been used to estimate the directional spectrum of the surface.

In this chapter the measurement techniques and estimation methods are described for obtaining the directional spectrum of the surface waves from a sparse line array of wave height sensors. The directionality was computed from a spatial transform of a cross-spectral density matrix obtained from all

combinations of sensor pairs. (The inverse of the spectral matrix was used in the high resolution method.) The cross-spectral densities were computed via FFT techniques with segment weighting and overlapping to reduce frequency leakage and spectral estimate instability. Three methods were used to obtain the directionality of the waves. Two of the methods can be classified as conventional 'delay and sum' techniques which differ by the location of the weights. One of the conventional methods has a spatial weighting of unity at each sensor position; whereas, the other conventional method has a spatial lag weighting of unity at each unique separation distance between sensor positions. The third method is a high resolution technique which was based on a maximum likelihood criterion.

The spatial lag weighting method of obtaining directional estimates has been described by Barber [7-7] for sea surface waves and by Nuttall and Carter [7-8] for the processing of ambient noise. The spatial weighting and the high resolution method have been successfully applied to the processing of seismic waves by Capon [7-9, 7-10].

The wavenumber resolution of both conventional methods is limited primarily by the natural beampattern of the array. However, the resolution of the maximum likelihood method is limited primarily by the signal-to-noise ratio and not simply by the beampattern of the array configuration. For the high signal-to-noise ratios of the wave height data, the estimate of the directional spectrum based on the high resolution method was superior to either of the conventional methods.

Before describing the estimation methods and digital processing procedures, a brief description is given of the acoustic wave height measuring system which is further described in Appendices D and E. The spectral properties of the sea surface waves that are pertinent to the development of the directional wave spectrum is given considerable attention.

7.2 LINE ARRAY SENSOR SPACING AND ORIENTATION

The line array consisted of five upward-looking transducers with sensor spacing and orientation as indicated in Fig. 7-1. The horizontal line array was supported by the tower (see Fig. 2-2) at a depth of 3 m below the mean low tide surface elevation; and oriented on a bearing of 008° with magnetic north.

Each transducer in the array was pulsed and the surface reflected signal was received. The wave height variations above each transducer were extracted from the pulse length modulated waveforms. The transducers were not equi-spaced in the array, but were spaced such that there would be a maximum number of contiguous separation distances between all combinations of sensor pairs. A minimum separation distance of 30.5 cm (1 foot) was chosen between the two closest transducers. Discrete spacings, at multiples of 30.5 cm, were obtained from the array configuration, to a maximum spacing of 274.3 cm. For a five sensor array, the configuration was optimum for obtaining nine contiguous separation distances [7-8].

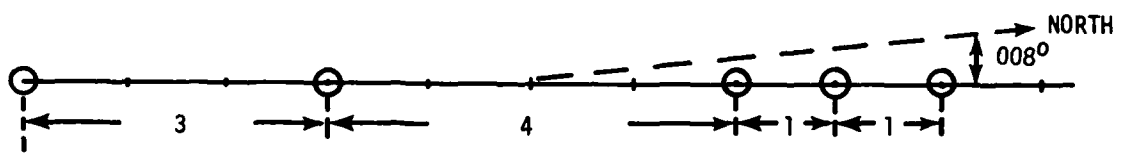


Figure 7-1. Five Sensor Line Array with Separation Distances Given in Units of 30.5 cm. © Designates Sensor Location.

A priori information was required with the line array to determine from which side of the array the surface waves were propagating. The front-to-back ambiguity of the array was resolved by visual observation and by assuming surface wave generation was confined to an angular sector of $\pm\pi/2$ radians of the wind direction. The array was oriented broadside to the most probable wind direction and in a direction with a fetch greater than 45 km.

7.3 ACOUSTIC SURFACE WAVE SENSING SYSTEM

The five upward-looking transducers (inverted fathometers) measured the time varying wave heights simultaneously at five discrete spots on the surface. The transition region from the near-to-far field characteristics of the transducers were used to insonify spot sizes on the surface having cross sectional diameters smaller than the 4 cm diameters of the circular piston transducers.

Each transducer of the wave measuring system was individually and sequentially pulsed with 16 μ sec, 455 kHz, pulses over separate coaxial cables. The first transducer was pulsed, switched to a receive mode, and the surface reflected signal was received. After a delay of 10 msec from the initial transmission, the next transducer was pulsed and the surface reflected signal was received. This procedure continued for each transducer such that the surface was "sampled" at a period of 50 msec above each of the five transducers. A bistable device (flip-flop) was set on each transmitted pulse and reset by the initial reflection from the surface. The bistable output pulse length was modulated by the changing wave height above the transducer. The wave height variations were extracted from the pulse length modulation by a low pass filter having a cut-off frequency of 3 Hz. The Honeywell 5600 tape recorder, described in Section 4.4, was used to record the five low pass filter outputs. The outputs were FM recorded at a tape speed of 7.5 inches/sec.

A prototype acoustic wave measuring system was tested prior to implantment in the Sound. A single transducer measured the wave height of sinusoidal waves generated on the water surface of a tank and the results were compared to wave heights measured with a modified micrometer. The acoustic system was further tested in the Thames River, CT, by comparing wave height measured with a resistive wave staff. The system is described in Appendix D which contains the abstract, text and figures of a paper presented at the Eighty-Fourth Meeting of the Acoustical Society of America [D-1]. Furthermore, the electronic design of the five transducer acoustic wave measuring system, with calibration features, is given in Appendix E.

7.4 SEA SURFACE PROPERTIES

7.41 SOME SPECTRAL PROPERTIES OF SEA SURFACE WAVES

Under constant wind conditions, a fully developed sea can be considered a stochastic process that is both spatially homogeneous (space stationary) and temporally stationary. The randomness is often described by Gaussian statistics such that either the spatial-temporal correlation function or the

directional wave spectrum can completely specify the statistical properties of the surface. Experimentally, MacKay [7-11] and Kinsman [7-12] have shown that if the high frequency components are filtered, the remaining low frequency regime can be described by Gaussian statistics. The departure from normality is usually found in the skewness of the probability density function, i.e., surface waves are not completely symmetrical because the troughs are longer and flatter than the more peaked crests [7-12].

The height $h(x, y, t)$ of a surface with stationary properties has a correlation function that is independent of absolute position (x, y) and time t and can be expressed as an ensemble average by

$$\rho(X, Y, \tau) = \langle h(x, y, t)h(x+X, y+Y, t+\tau) \rangle , \quad (7-1)$$

where $\langle \cdot \rangle$ denotes ensemble average. The correlation function is three-dimensional and dependent on the differences (X, Y, τ) of the spatial and temporal variables. The correlation also has diametrical symmetry,

$$\rho(-X, -Y, -\tau) = \rho(X, Y, \tau). \quad (7-2)$$

It is convenient to view the sea surface as a broadband composition of sinusoidal waves (with random amplitude and phases) propagating in various directions with a directional dependence and mean square wave height that is related to the direction and magnitude of the prevailing winds. The wavenumber-frequency spectrum of the propagating sinusoidal waves can be expressed as a three-dimensional Fourier transform of the correlation function

$$R(k_x, k_y, f) = \iiint_{-\infty}^{+\infty} \rho(X, Y, \tau) \exp[-i2\pi(k_x X + k_y Y + f\tau)] dX dY d\tau, \quad (7-3)$$

and, likewise, the correlation function is the inverse transform

$$\rho(X, Y, \tau) = \iiint_{-\infty}^{+\infty} R(k_x, k_y, f) \exp[i2\pi(k_x X + k_y Y + f\tau)] dk_x dk_y df. \quad (7-4)$$

The spatial frequencies (wavenumber components) k_x, k_y are the number of cycles per unit distance along the respective (x, y) coordinate axis and f is the number of cycles per unit time at a fixed point in space. The spatial frequencies are components of the wavenumber k and have the relationship

$$k^2 = k_x^2 + k_y^2, \quad (7-5)$$

and in polar coordinates (k, ϕ) ,

$$k_x = k \cos\phi, \quad (7-6)$$

$$k_y = k \sin\phi. \quad (7-7)$$

The wavenumber k is the number of cycles per unit distance normal to the direction of propagation and related inversely to the surface wavelength, $k = 1/\Lambda$, and ϕ is the azimuthal angle measured from the x axis.

There is also a unique relationship between spatial frequency and temporal frequency. For small-amplitude gravity waves in deep water, the relationship between a particular frequency f_o and wavenumber k_o is given by the dispersion equation or

$$2\pi f_o^2 = g k_o, \quad (7-8)$$

where g is the acceleration of gravity. The equation is less accurate at the shorter wavelengths because of the oscillatory convection of the short waves by the longer waves [7-13].

From (7-2) and (7-3), the wavenumber-frequency spectrum also has diametrical symmetry

$$R(-k_x, -k_y, -f) = R(k_x, k_y, f). \quad (7-9)$$

Although the three-dimensional wave spectrum is the most general, it is the most difficult to measure experimentally. By integration over the appropriate variables, reduced spectra - two and one-dimensional - can be defined from the three-dimensional. For example, consider a line array along the x axis that measures the spatial-temporal correlation function $\rho(X, \tau)$ for $Y = 0$, then

$$S(k_x, f) = \iint_{-\infty}^{+\infty} \rho(X, \tau) \exp \left[-i2\pi(k_x X + f\tau) \right] dX d\tau, \quad (7-10)$$

where

$$S(k_x, f) = \int_{-\infty}^{+\infty} R(k_x, k_y, f) dk_y. \quad (7-11)$$

Since there is a unique relationship between spatial and temporal frequencies, then,

$$R(k_x, k_y, f) = S(k_x, f) \delta(k_y - k_{yo}), \quad (7-12)$$

and from (7-5) and (7-8)

$$k_{yo} = \pm \sqrt{\frac{4\pi^2 f_o^4}{g^2} - k_{xo}^2}. \quad (7-13)$$

From the measurement along the x axis it is not possible to determine from which side of the axis the waves are propagating; thus the ambiguity in the sign for k_{yo} .

A one-dimensional spectrum can be obtained by measuring the wave height at a discrete point on the surface, and can be defined in terms of the three-dimensional spectrum as

$$P(f) = \iint_{-\infty}^{+\infty} R(k_x, k_y, f) dk_x dk_y, \quad (7-14)$$

or as the transform of the temporal correlation function $\rho(\tau)$,

$$P(f) = \int_{-\infty}^{+\infty} \rho(\tau) \exp[-i2\pi f\tau] d\tau. \quad (7-15)$$

The (auto) spectral density $P(f)$ relates the contributions per unit frequency interval to the mean square wave height σ^2 regardless of the direction of propagation (wavenumber components). Thus,

$$\sigma^2 = \int_{-\infty}^{+\infty} P(f) df, \quad (7-16)$$

and since $\rho(\tau)$ is an even function, then $P(f)$ is also real and symmetric about $f = 0$. It is sometimes convenient to consider positive frequencies so that

$$\sigma^2 = 2 \int_0^{\infty} P(f) df. \quad (7-17)$$

By measuring wave height as a function of time at a number of discrete points on the surface, a cross-spectral density can be obtained from combinations of sensor pairs. For a line array along the x axis, the correlation function $\rho(X, \tau)$ can be expressed as the inverse transform of (7-10), or

$$\rho(X, \tau) = \int_{-\infty}^{+\infty} \exp[i2\pi f\tau] \left\{ \int_{-\infty}^{+\infty} S(k_x, f) \exp[i2\pi k_x X] dk_x \right\} df. \quad (7-18)$$

The bracketed term can be considered the kernel of the temporal-frequency transform, so that

$$\int_{-\infty}^{+\infty} S(k_x, f) \exp[i2\pi k_x X] dk_x = \int_{-\infty}^{+\infty} \rho(X, \tau) \exp[-i2\pi f\tau] d\tau. \quad (7-19)$$

The right side of (7-19) is recognized as the cross-spectrum $A(X, f)$ between two points on the line array separated by a distance X , or

$$A(X, f) = \int_{-\infty}^{+\infty} \rho(X, \tau) \exp[-i2\pi f\tau] d\tau. \quad (7-20)$$

Thus, the two-dimensional directional wave spectrum (wavenumber component-frequency) is the spatial Fourier transform of the cross-spectral density

$$S(k_x, f) = \int_{-\infty}^{+\infty} A(X, f) \exp [-i2\pi k_x X] dX . \quad (7-21)$$

In general, the cross-spectrum is complex. From the symmetries of the correlation function and (7-20) it can be seen that

$$A(-X, f) = A^*(X, f), \quad (7-22)$$

and

$$A(-X, -f) = A(X, f). \quad (7-23)$$

Thus, knowledge of the cross-spectrum in one quadrant suffices in determining the complete function (* denotes complex conjugate).

7.42 SPECTRUM OF A PROPAGATING PLANE WAVE

Consider a monochromatic sinusoidal plane wave of amplitude H propagating on the surface (see Fig. 7-2) in the positive (x, y) direction with spatial frequencies k_{xo} , k_{yo} and temporal frequency f_o expressed by

$$h(x, y, t) = H \cos [2\pi(f_o t - k_{xo} x - k_{yo} y)] . \quad (7-24)$$

From (7-1), the spatial-temporal correlation function is

$$\rho(x, y, \tau) = \frac{H^2}{2} \cos [2\pi(f_o \tau - k_{xo} x - k_{yo} y)] , \quad (7-25)$$

which is also a cosinusoidal periodic function. The mean square wave height is given at $X=Y=\tau=0$, or $\rho(0)=H^2/2$.

For wavefronts propagating parallel to the x axis ($k_{xo} = 0$), the correlation function is independent of X . That is, wavefronts - without delay - "pass over" points on the x axis simultaneously. If the plane wave makes an angle ϕ with the x axis, then the wavefronts pass over each point on the x axis in sequence. The delay in passing over each hypothetical point depends on the arrival angle ϕ , the separation between points X , and the phase speed $C(f)$ of the sinusoid. From (7-25), the correlation function has a peak along the x axis at a temporal delay τ given by

$$\tau = \frac{k_{xo} X}{f_o} + \frac{n}{f_o} , \quad n = 0, \pm 1, \pm 2, \dots , \quad (7-26)$$

and using (7-6),

$$\tau = \frac{X \cos \phi}{C(f_o)} + \frac{n}{f_o} , \quad (7-27)$$

where

$$C(f_o) = \frac{f_o}{k_o} . \quad (7-28)$$

The phase speed is known from the dispersion equation for gravity waves (7-8). For those points on the x axis with known separation, the angle of arrival can be determined from (7-27) and (7-28). The time interval between crests at a fixed point in space is the period of the sinusoid.

The wavenumber-frequency spectrum, obtained via (7-3) consists of Dirac delta functions concentrated at the spatial and temporal frequencies (k_{xo} , k_{yo} , f_o) and is given by

$$R(k_x, k_y, f) = \frac{H^2}{4} \left\{ \delta(f + f_o) \delta(k_x - k_{xo}) \delta(k_y - k_{yo}) \right. \\ \left. + \delta(f - f_o) \delta(k_x + k_{xo}) \delta(k_y + k_{yo}) \right\} . \quad (7-29)$$

The wavenumber component spectrum is shown in Fig. 7-3. The mean square wave height $H^2/2$ is obtained by summing contributions per unit frequency interval.

The wavenumber-frequency spectrum can also be obtained by a spatial Fourier transform of the cross-spectral density. From (7-20), the cross-spectrum, in three-dimensions, is given by

$$A(X, Y, f) = \frac{H^2}{4} \left\{ \exp \left[-2\pi i (k_{xo}X + k_{yo}Y) \right] \delta(f - f_o) \right. \\ \left. + \exp \left[2\pi i (k_{xo}X + k_{yo}Y) \right] \delta(f + f_o) \right\} . \quad (7-30)$$

The symmetries of the correlation function, cross-spectrum, and wavenumber-frequency spectrum can easily be verified from the plane wave results.

7.43 EFFECTS OF TEMPORAL AND SPATIAL WINDOWS ON WAVENUMBER-FREQUENCY SPECTRUM

In the example of the propagating plane wave (Section 7.42), it was assumed that the spatial-temporal correlation function was known for all spatial and temporal lags. The Fourier transform of the correlation function resulted in delta functions at the appropriate spatial and temporal frequencies. However, in a practical situation, the correlation function is not known completely. What is generally available is a limited time history of wave height measured at a number of discrete points on the surface. Thus, the correlation function (and cross-spectrum) are determined from wave height data of finite duration and of finite spatial extent. The effect of viewing the surface through finite length temporal and spatial windows is to smear the power in frequency with a distribution that is related to the transform of the window shapes.

Assume that the correlation function is not known for all spatial and temporal lags, but has values at X, Y, τ specified by the spatial-temporal window $w(X, Y, \tau)$ so that a modified correlation function is given by

$$\hat{\rho}(X, Y, \tau) = \rho(X, Y, \tau)w(X, Y, \tau). \quad (7-31)$$

Denoting the Fourier transform of the three-dimensional window function by

$$W(k_x, k_y, f) = \iiint_{-\infty}^{+\infty} w(X, Y, \tau) \exp \left[-i2\pi(k_x X + k_y Y + f\tau) \right] dX dY d\tau, \quad (7-32)$$

then the estimated wavenumber-frequency spectrum is the convolution (see 7-8)

$$\hat{R}(k_x, k_y, f) = R(k_x, k_y, f) \otimes W(k_x, k_y, f). \quad (7-33)$$

For the case of the plane wave propagating on the surface, the estimated wavenumber-frequency spectrum is

$$\begin{aligned} \hat{R}(k_x, k_y, f) = \frac{H^2}{4} & \left| \begin{array}{l} W(k_x - k_{x_0}, k_y - k_{y_0}, f + f_0) \\ + W(k_x + k_{x_0}, k_y + k_{y_0}, f - f_0) \end{array} \right| . \end{aligned} \quad (7-34)$$

The true spectrum (7-29), which consists of delta functions, is spread over k_x, k_y, f space according to the nature of the frequency window $W(k_x, k_y, f)$. It is desired to have the power concentrated as close as possible to the spatial-temporal frequencies surrounding (k_{x_0}, k_{y_0}, f_0) , and without high sidelobes. This requires the window $w(X, Y, \tau)$ to observe values spread out in space and time. Actually, $W(k_x, k_y, f)$ is a measure of the resolving power of the wave height sensing system. The frequency window appears in (7-32) as the transform of $w(X, Y, \tau)$, and depending on the lag window shape, can take on negative as well as positive values. Thus, the wavenumber-frequency spectrum can show negative power under some circumstances.

The effects of windowing are slightly different if the wavenumber-frequency spectrum is computed via a spatial transform of the cross-spectrum. For example, if the cross-spectrum is computed directly from the time varying wave height by forming the product of the wave height transform and conjugate transform, then the temporal frequency window appears through its magnitude squared,

$$A(X, f) \otimes |W(f)|^2, \quad (7-35)$$

where

$$W(f) = \int_{-\infty}^{+\infty} w(t) \exp(-i2\pi ft) dt, \quad (7-36)$$

and $w(t)$ is the temporal window. Defining the cross-spectrum over the spatial lag window $w(X)$ results in a wavenumber component-frequency spectrum via (7-21) as

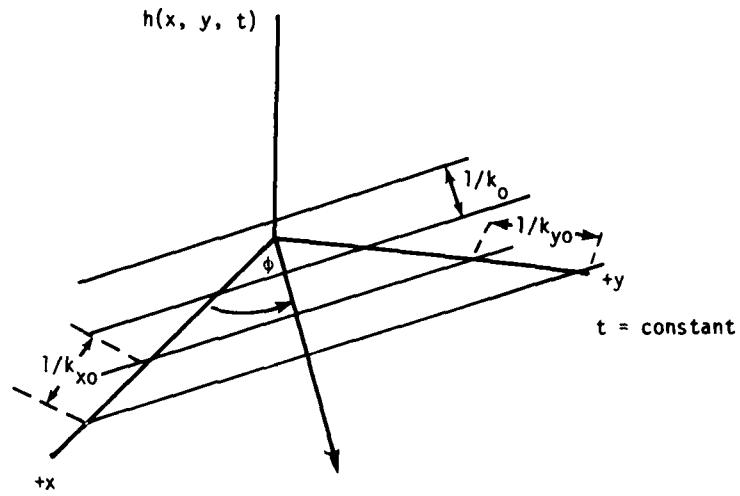


Figure 7-2. Wavefronts of a Plane Wave Propagating on a Surface Frozen in Time.

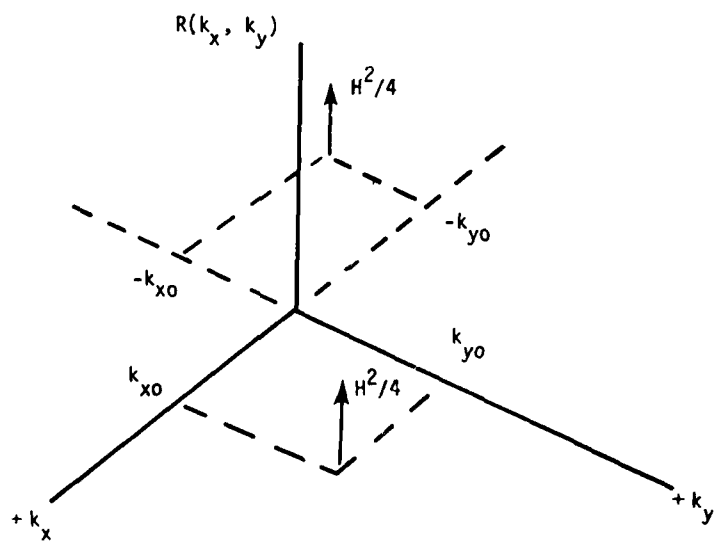


Figure 7-3. Wavenumber Spectrum of a Plane Wave Propagating with Wavenumber Components k_{x0} and k_{y0} .

$$S(k_x, f) \otimes |W(f)|^2 * W(k_x), \quad (7-37)$$

and where

$$W(k_x) = \int_{-\infty}^{+\infty} w(x) \exp(-i2\pi k_x x) dx. \quad (7-38)$$

The spatial frequency window does not appear through its magnitude squared; and depending on window shape, the wavenumber-frequency spectrum can have negative power.

7.44 DETERMINATION OF SURFACE WAVE DIRECTIONALITY FROM A LINE ARRAY OF SENSORS

The surface wave dispersion equation (7-8) provides the unique relationship between frequency and wavenumber that permits the use of a line array to determine the directionality of the surface waves.

Directionality of sea surface waves is usually expressed in terms of a directional wave spectrum $D(\phi, f)$ which relates the density of wave power with respect to direction of wave propagation ϕ and temporal frequency f . The directional wave spectrum can be obtained from the wavenumber component-frequency spectrum $S(k_x, f)$ by an appropriate transformation of coordinate variables.

For a line array along the x axis, the cross-spectral density can be expressed (7-21) as a Fourier transform of the two-dimensional wavenumber component-frequency spectrum. However, it is necessary to resolve the 'front-to-back' ambiguity of the line array. The ambiguity can be resolved in most instances from wind direction, array orientation and visual observation. From the inverse transform of (7-21) and from (7-6) and (7-8), the cross-spectral density can be expressed in terms of the directionality of the surface waves projected onto the array axis, or

$$A(x, f) = \frac{2\pi f^2}{g} \int_0^\pi \left(S \left(\frac{2\pi f^2}{g} \cos\phi, f \right) \exp \left[i2\pi \left(\frac{2\pi f^2}{g} \cos\phi \right) x \right] \sin\phi d\phi \right). \quad (7-39)$$

The directional spectrum $S(\phi, f)$ of the surface waves measured along the x axis of the array is related to the directional wave spectrum by

$$D(\phi, f) = \frac{2\pi f^2}{g} \sin\phi S(\phi, f). \quad (7-40)$$

The one-dimensional power spectrum $P(f)$ can be obtained from $D(\phi, f)$ or $S(\phi, f)$ by summing the contributions to the directionality per unit angle

$$P(f) = \int_0^\pi D(\phi, f) d\phi,$$

or similarly,

$$P(f) = \frac{2\pi f^2}{g} \int_0^\pi S(\phi, f) \sin\phi d\phi. \quad (7-41)$$

It has been assumed that the wave power is confined to the sector defined by the integration limits.

In the remaining sections of this chapter, the directionality of the surface waves $S(\phi, f)$ measured from the five sensor line array is computed from the three estimation methods.

7.5 ESTIMATION OF WAVENUMBER COMPONENT-FREQUENCY SPECTRUM FROM A LINE ARRAY USING CONVENTIONAL METHODS

The wavenumber component-frequency spectrum can be estimated from the spatial transform of the cross-spectrum defined by (7-21). Assume the array consists of K sensors that are oriented along the x axis and the separation distance X between the j^{th} and l^{th} sensor is

$$X = x_j - x_l, \quad j, l = 1, \dots, K, \quad (7-42)$$

where x_j , x_l are the distances measured to the sensor locations from a convenient origin. The cross-spectrum is denoted as

$$A(X, f) \equiv A_{jl}(f), \quad (7-43)$$

and can be estimated directly using FFT techniques. The cross-spectral estimation is based on overlapped processing of windowed data from each sensor output. The windowing reduces the frequency leakage (sidelobes) and the overlapped segment averaging reduces statistical variability in the spectral estimates [7-14]. The estimated cross-spectrum is

$$\hat{A}_{jl}'(f) = \frac{1}{M} \sum_{m=1}^M B_{jm}(f) B_{lm}^*(f), \quad j, l = 1, \dots, K, \quad (7-44)$$

where $B_{jm}(f)$ is the discrete Fourier transform of the windowed data at the j^{th} sensor of the m^{th} segment, and $*$ denotes complex conjugate. The number of segments M is dependent on the percentage overlap, the segment length, and the available record length. The values of f are spaced $1/N\Delta t$, where N is the number of data points in the segment and Δt is the sampling interval.

To equalize any differences in sensor gain, the cross-spectrum is normalized by the power (auto) spectrum in each sensor, or

$$\hat{A}_{j1}(f) = \frac{\hat{A}_{j1}(f)}{\sqrt{\hat{A}_{jj}(f) \hat{A}_{11}(f)}}. \quad (7-45)$$

The normalized cross spectrum defined by (7-45) is referred to as the estimated complex coherence function $\gamma_{j1}(f)$. Techniques for estimating the (magnitude-squared) coherence function using FFT techniques on weighted overlapped segments is given by Carter et al. [7-14].

In estimating the wavenumber-frequency spectrum of ambient noise, Nuttall and Carter 7-8 use FFT techniques to evaluate the spatial transform indicated in (7-21). Firstly, the sensor locations in the array are chosen such that an optimum number of contiguous separation distances can be obtained from relatively few sensors. That is $\{x_j - x_1\}_1^k$ takes on values at 0, $\pm d$, $\pm 2d$, . . . , $\pm Pd$, where d is the closest separation between two sensors and P is as large as possible. The closest separation determines the minimum surface wavelength before spatial aliasing occurs. For the five sensor array used in this experiment, the closest spacing was 30.5 cm and contiguous spacings were obtained to a maximum separation of 274.3 cm.

The wavenumber component-frequency spectrum estimated from (7-21) is

$$\hat{S}(k_x, f) = \sum_{n=-P}^{+P} w_n \hat{A}(nd, f) \exp \left[-i2\pi k_x nd \right], \quad (7-46)$$

where w_n are the weights to control the shape of the wavenumber window. If the spatial frequency is evaluated at discrete values given by

$$k_x = \frac{1}{Ld}, \quad l=0, 1, \dots, L, \quad (7-47)$$

then the spectrum can be evaluated using FFT techniques, that is

$$\hat{S}\left(\frac{l}{Ld}, f\right) = \sum_{n=-P}^{+P} w_n \hat{A}(nd, f) \exp \left[-i2\pi \frac{ln}{L} \right]. \quad (7-48)$$

The value of L determines the spacing between estimates of the spatial frequency and can be greater than $2P+1$ if it is desired to have closer spatial estimates (see e.g. Section 5.21). The transform (7-48) must be evaluated at each frequency of interest.

In the analysis of seismic waves, Capon [7-9] also estimated the wavenumber-frequency spectrum via a transform of the cross-spectral density between sensor pairs. For a line array oriented along the x axis, the wavenumber component-frequency spectrum from [7-9] can be expressed as

$$\hat{S}'(k_x, f) = \frac{1}{K^2} \sum_{j=1}^K \sum_{l=1}^K w_j w_l * \hat{A}_{jl}(f) \exp \left[-i2\pi k_x (x_j - x_l) \right], \quad (7-49)$$

AD-A090 042

NAVAL UNDERWATER SYSTEMS CENTER NEWPORT RI
DOPPLER SPECTRA OF BISTATIC REVERBERATION FROM THE SEA SURFACE. (U)
MAY 79 W I RODERICK

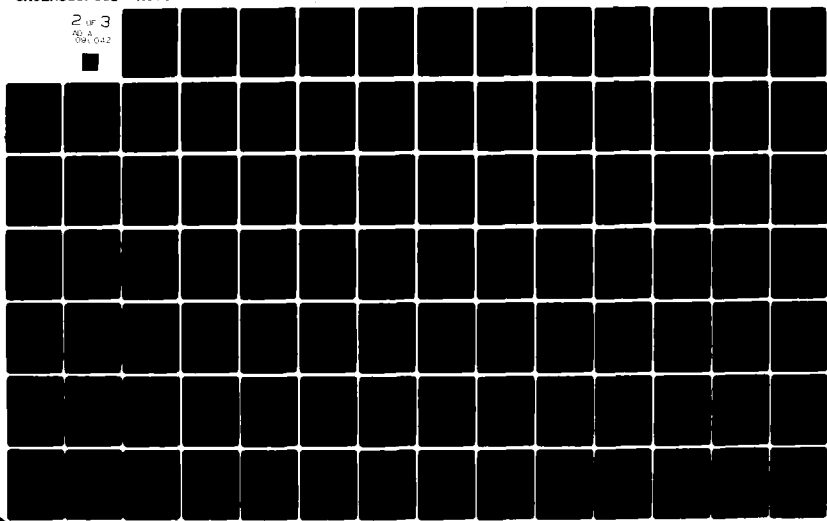
F/6 20/1

UNCLASSIFIED

NUSC-TR-6031

NL

2 of 3
AB A
001 042



where w_j are the (complex) weights applied to the spatial position of the sensors. The estimate $S'(k_x, f)$ is a summation, with the appropriate spatial weighting and array steering, of the cross power spectral densities between all combinations of sensor pairs. There are K^2 terms in the summation, whereas, in the estimate based on (7-46), the number of terms is less $((2P+1) < K^2)$ since only cross-spectral densities at unique separation distances are included.

The differences between the wavenumber-frequency estimates given by (7-46) and (7-49) can be highlighted when a line array with contiguous separation distances is examined. The optimally spaced five sensor array used in the measurement serves as an example (Fig. 7-4). It can be seen that the chosen locations $\{x_j - x_1\}_1^k$ take on the contiguous separations 0, $\pm d$,

$\pm 2d, \dots, \pm 9d$, where $9d$ is the maximum possible separation from the five sensor array ($d = 30.5$ cm). Note that when all sensor combinations are used, there are four redundant separations at 0 since $x_j - x_1 = 0$, $j = 1, 2, \dots, 5$ and there is one redundant separation at both $\pm d$ since $x_4 - x_1 = x_5 - x_4 = d$ and, of course, $x_3 - x_4 = x_4 - x_5 = -d$. Thus, there is a total of 6 redundant separations from the array. If in both equations, the original weights were unity $w_n = w_j = 1$, the effect of the redundant terms is to give an effective weighting of five at 0 separation to the auto spectral densities and an effective weighting of two to the cross-spectral densities at $\pm d$. Thus, the redundant terms in (7-49) effect the shape of the wavenumber window by giving nonuniform weightings to a line array with contiguous separation distances.

To avoid confusion in discussing the wavenumber-frequency estimates obtained via (7-46) and (7-49), the estimates have been designated as 'spatial lag weighting' and 'spatial weighting,' respectively. Also, both methods have been referred to as conventional when contrasted to the 'high resolution' maximum likelihood method.

The directional responses (beam patterns) of the five sensor line array were obtained from (7-46) and (7-49) for a plane wave incident broadside ($k_{x0} = 0$) to the array. By assuming unity weighting, the directional response $B(k_x)$ from (7-46) can be expressed as

$$B(k_x) = \sum_{n=-P}^{+P} \exp [-i2\pi k_x n d], \quad (7-50)$$

which can be reduced to the form

$$B(k_x) = \frac{\sin \left[\frac{(2P+1)}{2} (2\pi k_x d) \right]}{(2P+1)\sin(\pi k_x d)}, \quad (7-51)$$

where the peak value has been normalized to a value of unity. From (7-51), it can be seen that the first zero crossings occur at the angle

$$\phi = \cos^{-1} \left(\frac{1}{(2P+1)dk} \right). \quad (7-52)$$

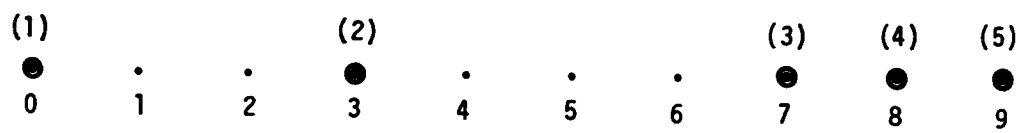


Figure 7-4. Line Array of Five Sensors Positioned on x Axis with Sensor Locations Shown in Units of 30 cm. ● Designates Sensor Location.

The directional response from (7-49) can be written in a form similar to (7-51) with the addition of the redundant terms.

A comparison between the two directional responses is shown in Fig. 7-5 for a surface wave frequency of 0.83 Hz (wavelength 244 cm). Both responses peak broadside to the array at an angle of 90°. The response with spatial lag weighting has a slightly narrower beamwidth and can give an estimate with negative power (see Section 7.4). The response using spatial weighting always gives a positive estimate. Only 180° of the directional response is shown since the same pattern is repeated. That is, the line array cannot distinguish from which side of the array the wave is propagating.

The beamwidth of the directional response depends on the ratio of the surface wavelength to array length (see (7-52)); and hence, the beamwidth increases as the surface frequency decreases. As an example, the beamwidth between half-power points is approximately 60 degrees for a surface frequency of 0.53 Hz.

Thus, the ability of the array to resolve low frequency surface waves, using conventional methods with either spatial or spatial lag weighting, is limited by the array length (spatial window). The ability to measure high frequencies is limited by the closest sensor spacing. At frequencies higher than 1.6 Hz, the wavelengths are less than 60 cm and spatial aliasing occurs. If the five sensors in the array had been equispaced instead of the nonuniform spacing for contiguous lags, then the array length would have been 122 cm and the resolution would have decreased further. A comparison of the directional responses is shown in Fig. 7-6 for an equispaced line array and the five sensor array with contiguous lags. The comparison is made with the estimates with spatial lag weighting for a surface frequency of 0.53 Hz. The poorer resolution of the equispaced array is obvious.

7.6 ESTIMATION OF WAVENUMBER COMPONENT-FREQUENCY SPECTRUM FROM A LINE ARRAY USING A HIGH RESOLUTION MAXIMUM LIKELIHOOD METHOD

The estimations based on either the spatial lag weighting or the spatial weighting methods have spatial resolutions that are limited by the shape of the respective wavenumber-frequency window. The shape of the wavenumber spectrum is basically fixed by the beampattern of the array of sensors.

Capon [7-9] developed a high resolution method that has a wavenumber window whose shape changes with the wavenumber under analysis. The high resolution method requires that the spectral matrix $\hat{A}_{jl}(f)$, obtained from all combinations of sensor pairs, be inverted to form a new matrix $\hat{q}_{jl}(f)$. For a line array with sensors along the X axis, the high resolution wavenumber component-frequency estimate is defined as

$$\hat{p}(k_x, f) = \left\{ \sum_{j=1}^K \sum_{l=1}^K q_{jl}(f) \exp[-i2 k_x (x_j - x_l)] \right\}^{-1} . \quad (7-53)$$

Capon et al., in an earlier paper [7-15], show that the cross-spectral matrix is nonnegative-definite and nonsingular; because in practice, there is always some incoherent noise between sensor pairs.

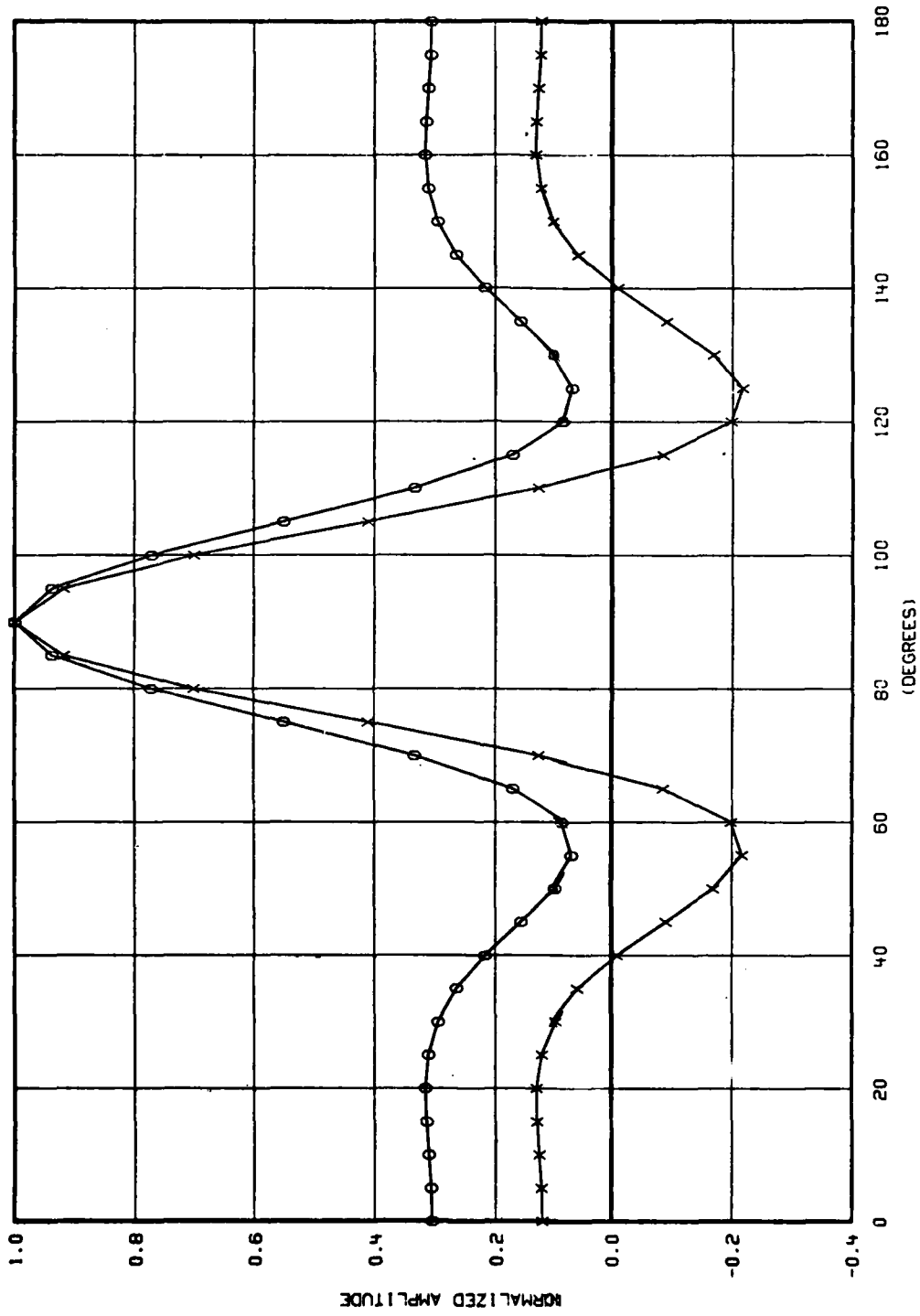


Figure 7-5. Comparison of the Directional Responses Obtained from Conventional Spatial Weighting (000) and Spatial Lag Weighting (XXX) Methods for a Surface Wavelength of 244 cm (0.83 Hz).

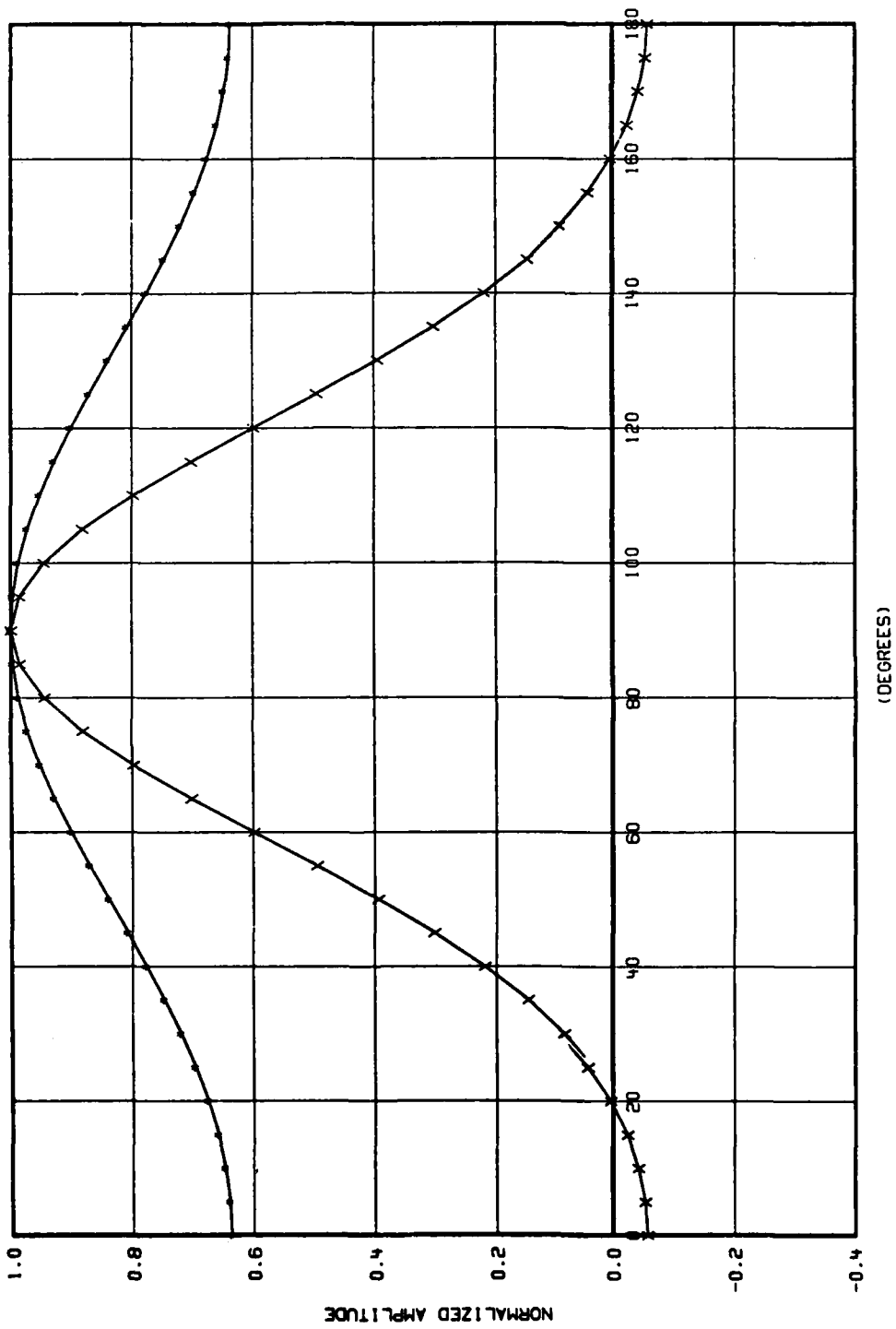


Figure 7-6. Comparison of Directional Responses for a Five Sensor Equispaced Line Array (***)
and a Five Sensor Array Optimally Spaced (XXX) for Contiguous Lags. Responses Based on a Spatial
Lag Weighting Method for a Surface Wavelength of 548 cm (0.53 Hz).

In a comparison of conventional and data adaptive spectral analysis, Lacoss [7-16] applies the high resolution method to the estimation of the power spectral density of time series data. A derivation of an equation similar to (7-53) shows that the estimate gives the power from a filter designed to pass a particular frequency undistorted and to reject all other frequencies in an optimal manner. The rejection of all frequencies is based on a filter designed to have a minimum output variance with the constraint that the filter weights be chosen to pass the input frequency, and to reject the noise.

To show that the high resolution method is superior to the conventional, Capon computes and compares the wavenumber-frequency estimates based on (7-49) and (7-53). Assume a plane wave propagating across the array with a cross-spectral matrix defined as

$$A_{jl}(f_o) = \delta_{jl}(R) \exp [-i2\pi k_x(x_j - x_l)], \quad (7-54)$$

where

$$\delta_{j1}(R) = 1, \quad j = 1$$

and

$$\delta_{j1}(R) = 1 - R, \quad j \neq 1. \quad (7-55)$$

The noise component is assumed incoherent between sensors; and R is defined as the ratio of the incoherent noise power to the total power in the sensor output. Substituting the cross-spectral density (7-54) into (7-49) gives

$$S'(k_x, f_o) = (1 - R) |B'(k_x - k_{xo})|^2 + \frac{R}{K}, \quad (7-56)$$

where

$$B'(k_x) = \frac{1}{K} \sum_{j=1}^K e^{ik_x x_j}. \quad (7-57)$$

By using an appropriate matrix inversion formula, the high resolution wavenumber-frequency estimate can be expressed as

$$\hat{P}(k_x, f_o) = \frac{\frac{R}{K}}{\frac{1 - R + \frac{R}{K}}{1 - R + \frac{2R}{K} - S'(k_x, f_o)}}. \quad (7-58)$$

For the five sensor line array used in the measurements, a comparison between the conventional spatial weighting estimates (7-56) and the high resolution estimates (7-58) has been made for a plane wave incident broadside to the array at frequencies of 0.53 Hz and 0.23 Hz (Figs. 7-7 and 7-8). The ratio of incoherent noise power to total sensor power (R) was assumed to be .1 and .01, respectively. This corresponds to approximate signal-to-noise ratios of 10 and 20 dB. The superiority of the high resolution method is evident in both comparisons. At the 0.23 Hz surface wave frequency (wavelength 2866 cm)

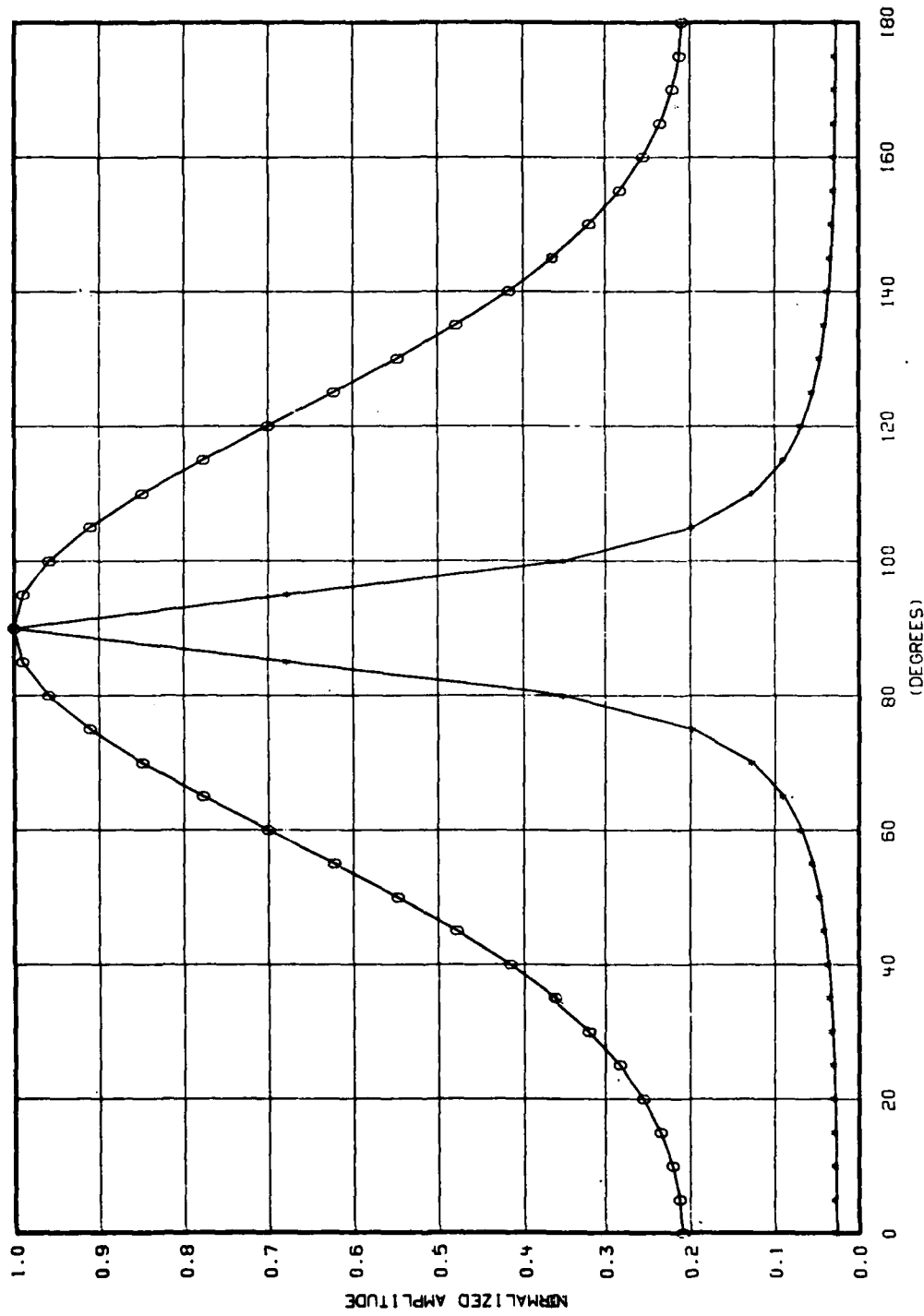


Figure 7-7. Comparison of Directional Responses Obtained from the Conventional Spatial Weighting (000) and the High Resolution (XXX) Methods for a Surface Wavelength of 548 cm (0.53 Hz) and a Signal-to-Noise of Approximately 10 dB.

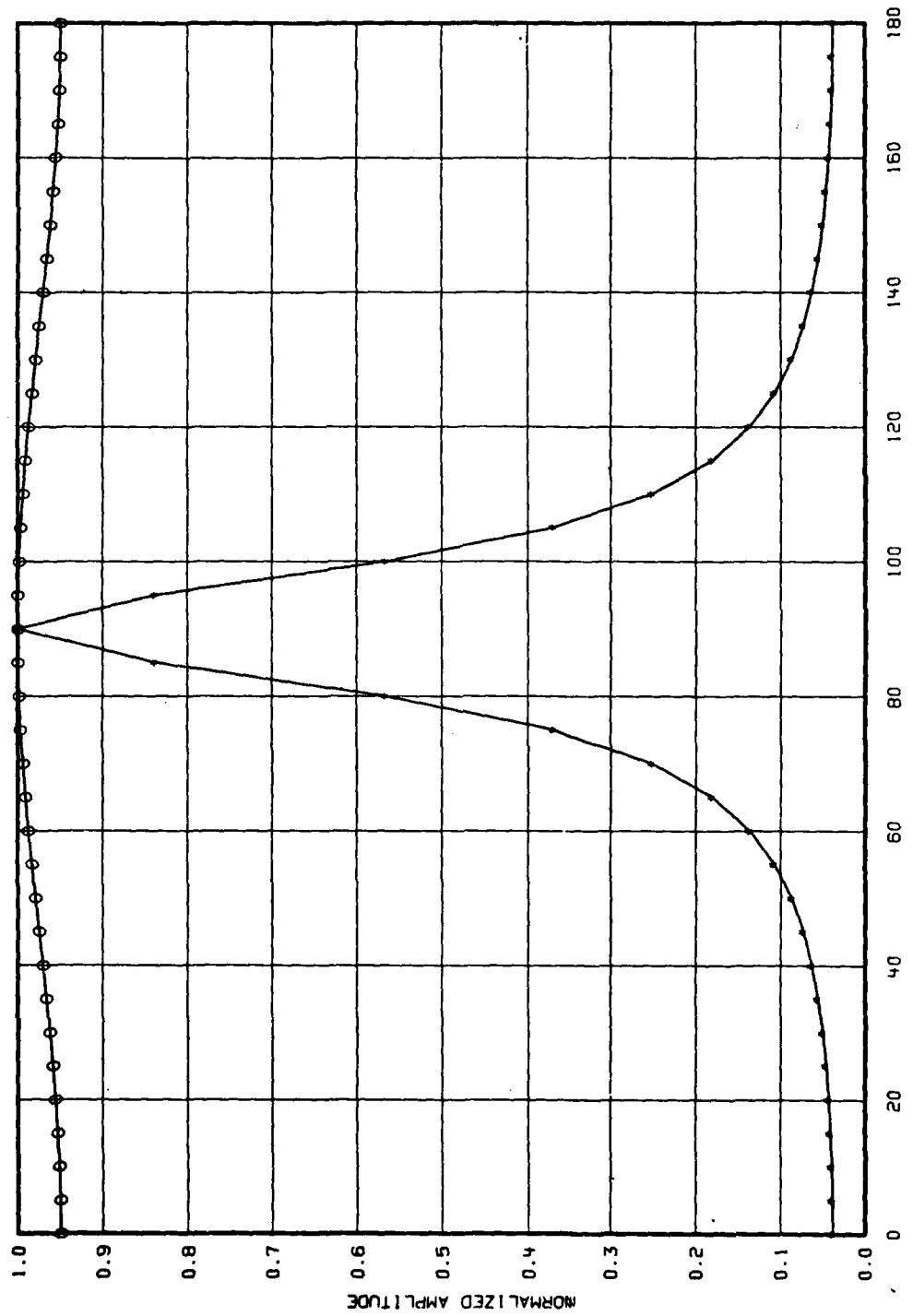


Figure 7-8. Comparison of Directional Responses Obtained from the Conventional Spatial Weighting (000) and the High Resolution (XXX) Methods for a Surface Wavelength of 2866 cm (0.23 Hz) and a Signal-to-Noise of Approximately 20 dB.

the conventional method has basically an omnidirectional response; whereas the high resolution beamwidth (between half-power points) is approximately 15° .

The resolution of the conventional methods are primarily limited by the spatial (lag) windows of the line array, and the high resolution method is limited primarily by the signal-to-noise ratio. For example, the beamwidth of the array response to a 0.23 Hz plane wave increases from 15° to 50° if the signal-to-noise is lowered from 20 dB to 10 dB.

The computation times for the spatial weighting and the high resolution method are basically the same since the additional time to convert the Hermitean spectral matrix is negligible in comparison to the total processing time. The computation time for the conventional spatial lag weighting is the fastest for a line array with contiguous spacings since the wavenumber-frequency spectrum can be evaluated using FFT processing.

7.7 DIGITAL PROCESSING OF WAVE HEIGHT DATA AND ESTIMATION OF NORMALIZED CROSS-SPECTRAL DENSITIES

The normalized cross-spectral densities (complex coherence) between all combinations of sensor pairs were estimated using fast Fourier Transform (FFT) techniques. The estimations were based on a total record length of 13.5 minutes of wave height data obtained from each channel of the five sensor acoustic wave measuring system. Using cross-spectral estimation procedures similar to Carter et al. [7-14], the time series were partitioned into equal overlapped segments, weighted, and transformed.

The desired spectral resolution, sidelobe reduction (frequency leakage), and estimate stability determines the requirements for segment length, weighting function, and the number of segments. That is, the spectral resolution varies inversely with the segment length T , the weighting function $w(t)$ determines the level of sidelobe reduction in the frequency domain, and the bias and variance of the estimates vary inversely with the number of segments M . With a fixed amount of data, these requirements can be conflicting since high resolution requires long segment lengths and good estimate stability requires many segments.

A method of improving estimate stability and maintaining high spectral resolution is to use overlapped segment averaging. If the total record length T_T has a maximum of L disjoint segments of length T , or

$$T_T = LT, \quad (7-59)$$

and if the segments are overlapped by the fraction O_F , the number of overlapped segments is

$$M = \frac{L - O_F}{1 - O_F}, \quad (7-60)$$

where

$$\alpha_F = \frac{T - a}{T}, \quad (7-61)$$

and a is the shift each adjacent weighting function undergoes (see Fig. 7-9).

It can be shown that the equivalent degrees of freedom increases linearly with the number of disjoint segments until overlap occurs. However, with overlap, the degrees of freedom continue to increase, but at a slower rate due to the statistical dependence of the segments [7-17]. A point of diminishing returns is reached where increasing the overlap does not return an increase in estimate stability.

To estimate digitally the normalized cross-spectral density between sensor pairs, the wave measuring system's low pass filter outputs were analogue-to-digital converted at a rate of 16 samples/sec. The sampled data were divided into segment lengths of 30 seconds. Prior to applying Hanning (cosine) weights to the sampled data, the mean value (dc offset) was removed from each segment. With Hanning weights, the first and second order sidelobes were -31.5 and -41.5 dB, respectively. The spectral resolution, between half-power points, of the weighted 30 second segments was .048 Hz.

As a compromise between computational efficiency and estimate stability, a 50 percent ($\alpha_F = .5$) overlap was chosen. In the 13.5 minutes of data there were 53 overlapped segments (or 27 disjoint segments). In [7-14] it was shown that the bias and variance of the magnitude-squared coherence MSC estimate using disjoint segments can be reduced considerably (about 50 percent) when overlapped segment processing is substituted. For a large number disjoint segments L the bias and variance depend on the value of the MSC. Both the bias and variance are zero when the MSC is unity. The bias is greatest $1/L$ when MSC is zero and the variance is greatest $(2/3)^3/L$ when MSC is $1/3$.

The normalized cross-spectral densities were estimated from (7-44) and (7-45) using FFT techniques. Denote the cross-spectral density of the m^{th} zero mean weighted segment of the j^{th} sensor output at frequency f_n as obtained from (7-44) by

$$\hat{A}_{jl}^*(f_n) = \frac{1}{M} \sum_{m=1}^M B_{jm}(f_n) B_{lm}^*(f_n), \quad (7-62)$$

where $j, l = 1, \dots, 5$, and $M = 53$. The frequency spacings are given by

$$f_n = \frac{n}{N\Delta t}, \quad n = 0, 1, 2, \dots, 479, \quad (7-63)$$

where Δt is the sampling interval (1/16 seconds) and N is the number of data points (480) in the segment. Thus, the frequency spacing was 1/30 Hz.

The normalized cross-spectral density was estimated as

$$\hat{A}_{jl}(f_n) = \frac{\hat{A}_{jl}^*(f_n)}{\sqrt{\hat{A}_{jj}^*(f_n) \hat{A}_{ll}^*(f_n)}}. \quad (7-64)$$

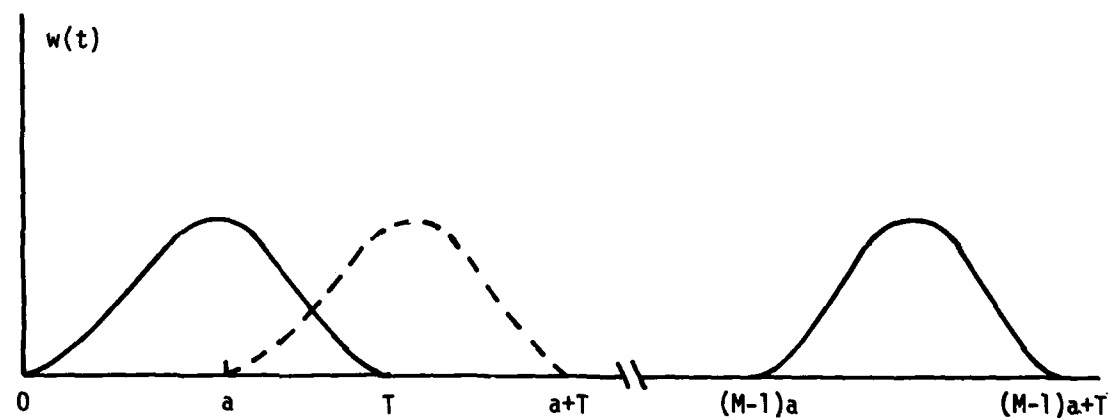


Figure 7-9. Overlapped Weighting Functions.

The cross-spectral density is a complex quantity that can be expressed in terms of a cospectrum $C_{j1}(f)$ and a quadrature spectrum $Q_{j1}(f)$, or

$$\hat{A}_{j1}(f_n) = \hat{C}_{j1}(f_n) + i\hat{Q}_{j1}(f_n). \quad (7-65)$$

The magnitude and argument of the spectrum are

$$|\hat{A}_{j1}(f_n)| = \sqrt{\hat{C}_{j1}^2(f_n) + \hat{Q}_{j1}^2(f_n)}, \quad (7-66)$$

and

$$\hat{\theta}_{j1}(f_n) = \tan^{-1} \left(\frac{\hat{Q}_{j1}(f_n)}{\hat{C}_{j1}(f_n)} \right). \quad (7-67)$$

7.8 ESTIMATION OF DIRECTIONAL SPECTRA FROM CROSS-SPECTRAL DENSITY ESTIMATES

Using the normalized cross-spectral density estimates obtained via (7-64), the wavenumber component-frequency spectra were estimated using the conventional spatial lag weighting (7-46) and spatial weighting (7-49) methods, and the high resolution method (7-53).

The high resolution estimates required an inversion of a 5×5 cross-spectral density matrix which was evaluated at each frequency of interest. The matrix was nonsingular due to the finite amount of noise in each sensor output. The matrix is Hermitian, i.e.,

$$\hat{A}_{1j}(f_n) = \hat{A}_{j1}^*(f_n), \quad (7-68)$$

and various matrix inversion techniques are available for complex matrices that take advantage of the complex symmetry [7-18].

For computational efficiency, advantages were taken of the cosine form of the equations by combining terms involving $\exp -i2\pi k_x(x_j - x_1)$ and $\exp +i2\pi k_x(x_j - x_1)$ and also by making use of the symmetries (7-68) of the cross-spectral densities.

By substituting for the wavenumber component

$$k_{xm} = \frac{2\pi f_n^2}{g} \cos\phi_m, \quad (7-69)$$

directional spectrum $G(\phi_m, f_n)$ were computed as a function of the azimuthal angle at discrete values of the temporal frequency. The function $G(\phi_m, f_n)$ represents the directional spectrum that has been projected onto the axis of the array and estimated from among the three methods. From (7-40), the relationship between $G(\phi_m, f_n)$ and the directional wave spectrum $D(\phi_m, f_n)$ is given by

$$\hat{D}(\phi_m, f_n) = \frac{2\pi f_n^2}{g} \sin\phi_m \hat{G}(\phi_m, f_n). \quad (7-70)$$

The two-dimensional directional estimates were obtained in $5\pi/180$ radian increments of ϕ and $1/30$ Hz spacings in frequency f . The directional spectra were normalized by a factor $1/2\pi P$, where P is the value of the peak spectral estimate in each spectrum. The one-dimensional power spectrum (7-41) can be computed from the directional spectrum estimates via

$$\hat{P}(f_n) = \frac{2\pi f_n^2}{g} (2\pi P) \Delta\phi \sum_{m=0}^M \sin\phi_m G(\phi_m, f_n). \quad (7-71)$$

That is, the integral expressed in (7-41) was approximated by a rectangular summation over the angular sector $M\Delta\phi=\pi$, where $M=36$. The power spectrum was defined as the ensemble average of the five sensor autopower spectral density given by

$$\hat{P}(f_n) = \frac{1}{K} \sum_{j=1}^K \hat{A}_{jj}(f_n), \quad (7-72)$$

where $\hat{A}_{jj}(f_n)$ was the auto-spectral density (7-62) of the j^{th} sensor output.

CHAPTER 8

SEA SURFACE DIRECTIONALITY AND OTHER SPECTRAL ESTIMATES

8.1 INTRODUCTION

Immediately prior to the initiation of the acoustic reverberation measurements, oceanographic information was obtained by simultaneously measuring the time varying wave heights at five points on the sea surface. During the oceanographic and acoustic measurement periods, the wind speed averaged approximately 5 m/sec and the winds were from a westerly sector ($270\text{--}290^\circ$). The wind measurements were made at the Block Island facility at an altitude of about 10 m above sea level. The facility is approximately 2 km east of the experimental site.

The acoustic wave measuring system was oriented on a bearing of 008° relative to magnetic north. Broadside to the array also faced in the same direction (278°) as the maximum response axis of the parametric array. Directional spectra were computed with respect to the counterclockwise rotation of the azimuthal angle between the array and the normal to the approaching wavefront. An azimuthal angle of 0° corresponds to waves approaching at 008° relative to magnetic north and waves approaching broadside to the array have an angle of 90° with respect to the array and 278° with respect to magnetic north. Thus, an angle of 90° corresponds to surface waves propagating in the opposite direction to the acoustic waves launched by the parametric array. From visual observations of the sea surface and wind direction monitoring, the wave power has been assumed to be distributed between $\pm 90^\circ$ of broadside to the array.

This chapter presents auto- and cross-spectra, and directional spectra estimated from the conventional 'delay and sum' and high resolution methods. It will be seen that the high resolution method, under conditions of high signal-to-noise ratio, out-performs both conventional methods. In Appendix F, directional spectra have been presented for the high resolution method for the frequency band 0.1 to 1.2 Hz at frequency spacings of 0.033 Hz.

8.2 ONE-DIMENSIONAL WAVE SPECTRUM

One-dimensional wave spectra were computed from the time varying wave heights measured at the outputs of each sensor. An example is shown in Fig. 8-1 of a one-dimensional spectrum measured from the wave height data at the output of sensor 5. There are approximately 98 equivalent degrees of freedom (EDF) in the spectral estimates. The EDF computations were based on a 50% segment overlap with Hanning weights, and for an average of 53 segments [7-17].

The wind wave power spectrum has a peak in the vicinity of 0.267 Hz and there is also some swell wave energy at approximately 0.1 Hz. The swell wave

energy probably resulted from waves propagating to the experimental site from a distant storm.

The power spectral density in the frequency band 0.6 to 2.0 Hz appears to fall off at a rate proportional to f^{-5} . This can be seen more readily from the data displayed in Fig. 8-2. A comparison is shown with the Pierson-Moskowitz spectra predicted for two different wind speeds [8-1]. The predicted spectra were based on wind speeds of 4.0 and 5.1 m/sec and obtained from

$$P(f) = \frac{\alpha g^2}{(2\pi f)^5} \exp\left[-B \left(\frac{f_0}{f}\right)^4\right], \quad (8-1)$$

where $\alpha = 8.1 \times 10^{-3}$, $B = 0.74$, and

$$f_0 = g/2\pi U. \quad (8-2)$$

The acceleration of gravity g and wind speed U are in consistent units (CGS). The winds were selected to (1) match the mean square wave height (75 cm^2) of the measured data (4.0 m/sec), and (2) to match the frequency of maximum energy at 0.267 Hz (5.1 m/sec). From (8-1), the predicted power spectral density of the high frequencies decrease at a rate proportional to f^{-5} , independent of wind speed. Of course, the swell wave spectrum is not predicted by the Pierson-Moskowitz spectrum.

8.3 NORMALIZED CROSS-SPECTRAL DENSITY ESTIMATES

The magnitude and argument of the normalized cross-spectral density (complex coherence function) were computed from (7-64) for all combinations of sensor pairs. As an example, the magnitude and argument for the two closest sensors (sensors 4 and 5) are shown in Figs. 8-3 and 8-4, respectively. The magnitude coherence is nearly unity for frequencies below 0.6 Hz and gradually drops to a value of below 0.5 for frequencies above 1.2 Hz. The surface wavelength is 108 cm at 1.2 Hz which is about 3.5 times the sensor separation distance. It is evident that there is still coherence at the high frequencies by observation of the magnitude coherence and the gradual fluctuations in the argument of the complex coherence. At larger separation distances, it would be expected that the coherence would diminish more rapidly with frequency.

As a further example, the coherence between the two sensors (sensors 1 and 5) with the maximum separation (274.3 cm) falls off rapidly for frequencies above 0.3 Hz (Fig. 8-5). The magnitude is less than 0.5 for frequencies above 0.4 Hz. The surface wavelength at 0.4 Hz is 975 cm, which is also 3.5 times the sensor separation distance. Apparently, for the particular azimuthal angles associated with these wind generated waves, the coherence falls below 0.5 at separation distances on the order of 1/3 of a surface wavelength. The argument of the complex coherence function (Fig. 8-6) shows that there is no spatial coherence for frequencies above approximately 0.4 Hz. Furthermore, the magnitude coherence shows a similar result (i.e., a lack of coherence) since the bias at zero coherence is a maximum [8-2]. The maximum bias for n disjoint segments is given by

$$\text{max bias} \approx 1/2 \sqrt{\pi/n} .$$

With a 50% overlap, a further approximation can be made by replacing the number of disjoint segments with the number of overlapped segments. The bias is approximately .11 for 53 segments. This estimate of bias would be a lower bound; and the upper bound would be .16 for 27 disjoint segments.

From the arguments of the complex coherence, the arrival angles of the surface waves can be estimated. In Fig. 8-7, the arguments are plotted as a function of unique sensor separation distance for a surface wave frequency of 0.233 Hz. There is a linear relationship between argument and distance which indicates that the plane wave temporal delay given by (7-26) is appropriate to predicting arrival angle. The phase delay from (7-26) can be expressed as

$$\theta(f_n) = 2\pi f_n T = 2\pi k_{x_0} X , \quad (8-3)$$

and from (7-6) and (7-8) gives

$$\theta(f_n) = \left(\frac{4\pi^2 f_n^2}{g} \right) \cos \phi \quad X. \quad (8-4)$$

The azimuthal angle for the 0.233 Hz surface wave frequency was determined from (8-4) and the slope of the measured argument $\hat{\theta}_{j1}(f_n)$ versus sensor separation distance was obtained from Fig. 8-7. The estimated arrival angle was 42° which is in good agreement with the high resolution estimate (40°).

8.4 COMPARISON OF DIRECTIONAL ESTIMATION METHODS

Directional spectra, based on the conventional spatial lag weighting and spatial weighting methods, and the high resolution method are shown in Figs. 8-8, 8-9, and 8-10, respectively. The surface wave frequency is 0.233 Hz. As would be expected, the resolution using either of the conventional methods is practically nonexistent for a surface wavelength approximately eleven times the length of the array.

However, the high resolution method is capable of resolving the 0.233 Hz surface wave frequency which has a spectral peak at 40° and a beamwidth of approximately 35° . The spectrum may actually have a beamwidth narrower than that indicated in Fig. 8-10. The resolution of the high resolution method is limited primarily by the signal-to-noise ratio as indicated in (7-58). The beamwidth of the high resolution method at a signal-to-noise ratio of 20 dB was approximately 15° for a surface wave frequency of 0.233 Hz (see Fig. 7-8). The signal-to-noise ratio is not simply related to the wave height signal power to the noise power. The noise must also include how well the sea surface can be modeled as a summation of uncorrelated plane waves propagating in various directions and how well the acoustic wave height sensor can accurately reproduce the wave height variations at a discrete point on the sea surface. Of course, the signal-to-noise ratio will also have a frequency dependence.

It was shown previously (Fig. 8-2) that the swell spectrum peaked at a frequency of 0.1 Hz with a peak power approximately 7 dB lower than the power of the wind wave spectrum. In Fig. 8-11, the directional spectrum of the swell is seen to peak almost broadside to the array. The ratio of the surface wavelength-to-array length is approximately 57 for the 0.1 Hz surface wave.

At higher surface wave frequencies the wavelengths are shorter, and the conventional methods are more capable of resolving the wavenumber component-frequency estimates. Also, the high resolution method is seen to deteriorate due to presumably an increase in noise. The three methods at a surface wave frequency of 0.833 Hz can be compared in Figs. 8-12, 8-13, and 8-14. All three methods show spectral peaks at approximately 135° from the array axis, and secondary peak powers at approximately 80° from the axis. The secondary peak with the high resolution method is shifted about 10° from the conventional method estimates. Also, the ratio of the peak to secondary peak power levels is approximately the same for the high resolution and spatial weighting methods and slightly higher for the spatial lag weighting method. The high resolution still shows a narrower beamwidth than either of the conventional methods.

The directional characteristics are in agreement with the results obtained in other measurements (see [7-2]). Agreement is found in the confinement of the surface waves propagating with angular distributions close to the direction of the prevailing winds (about 290° relative to magnetic north). Also, agreement is found in the broadening of the angular distribution at the higher surface wave frequencies, and the generation of secondary peaks at these frequencies.

Because of the consistently higher performance of the high resolution method in comparison to either of the conventional methods, these estimates are given in Appendix F for the frequency band 0.1 to 1.2 Hz at frequency spacings of 0.033 Hz.

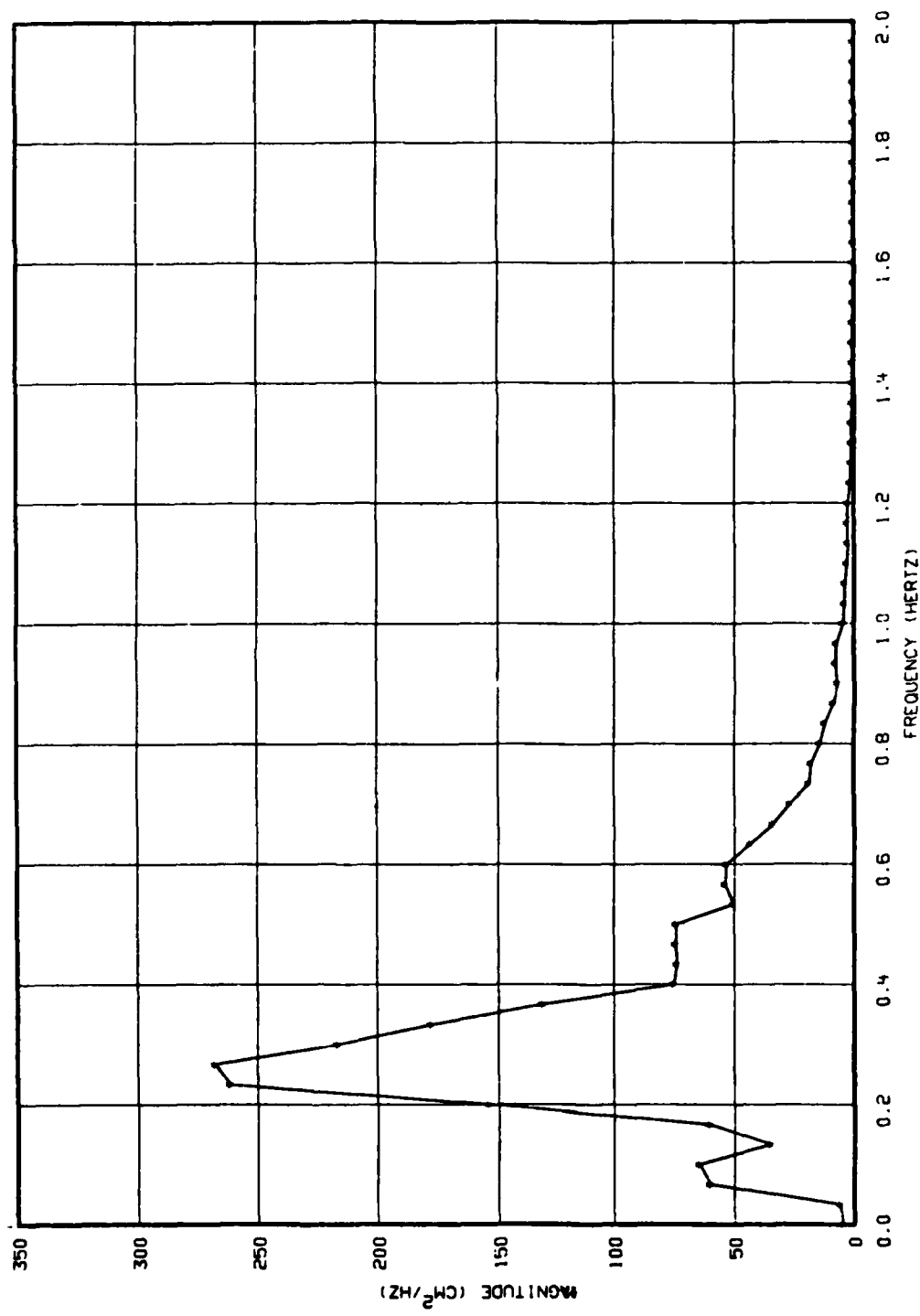


Figure 8-1. One-Dimensional Power Spectrum Obtained from Wave Height Data of Sensor 5.

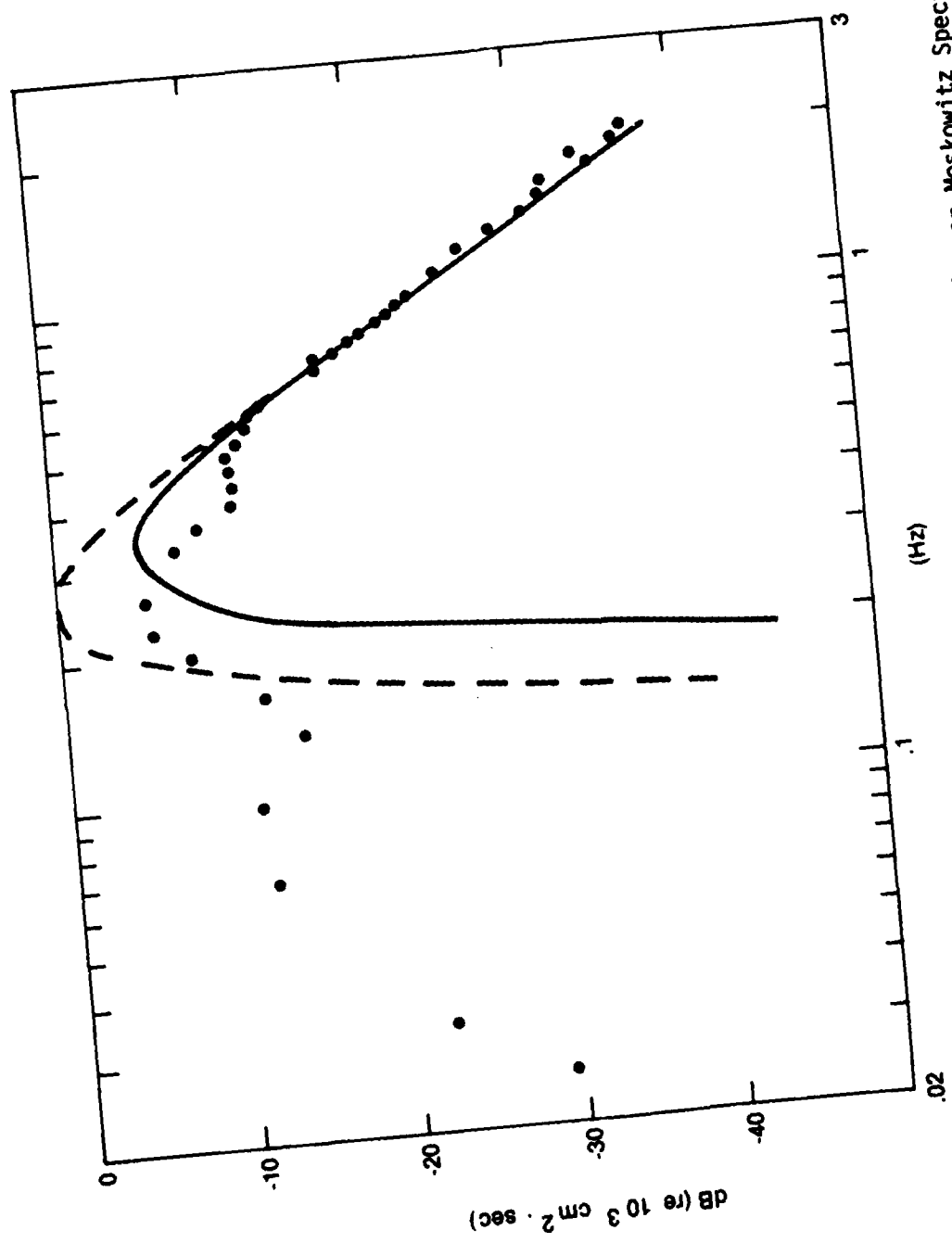


Figure 8-2. Comparisons of One-Dimensional Power Spectrum with Pierson-Moskowitz Spectra Predicted for Wind Speeds of 4.0 (—) and 5.1 (---) m/sec.

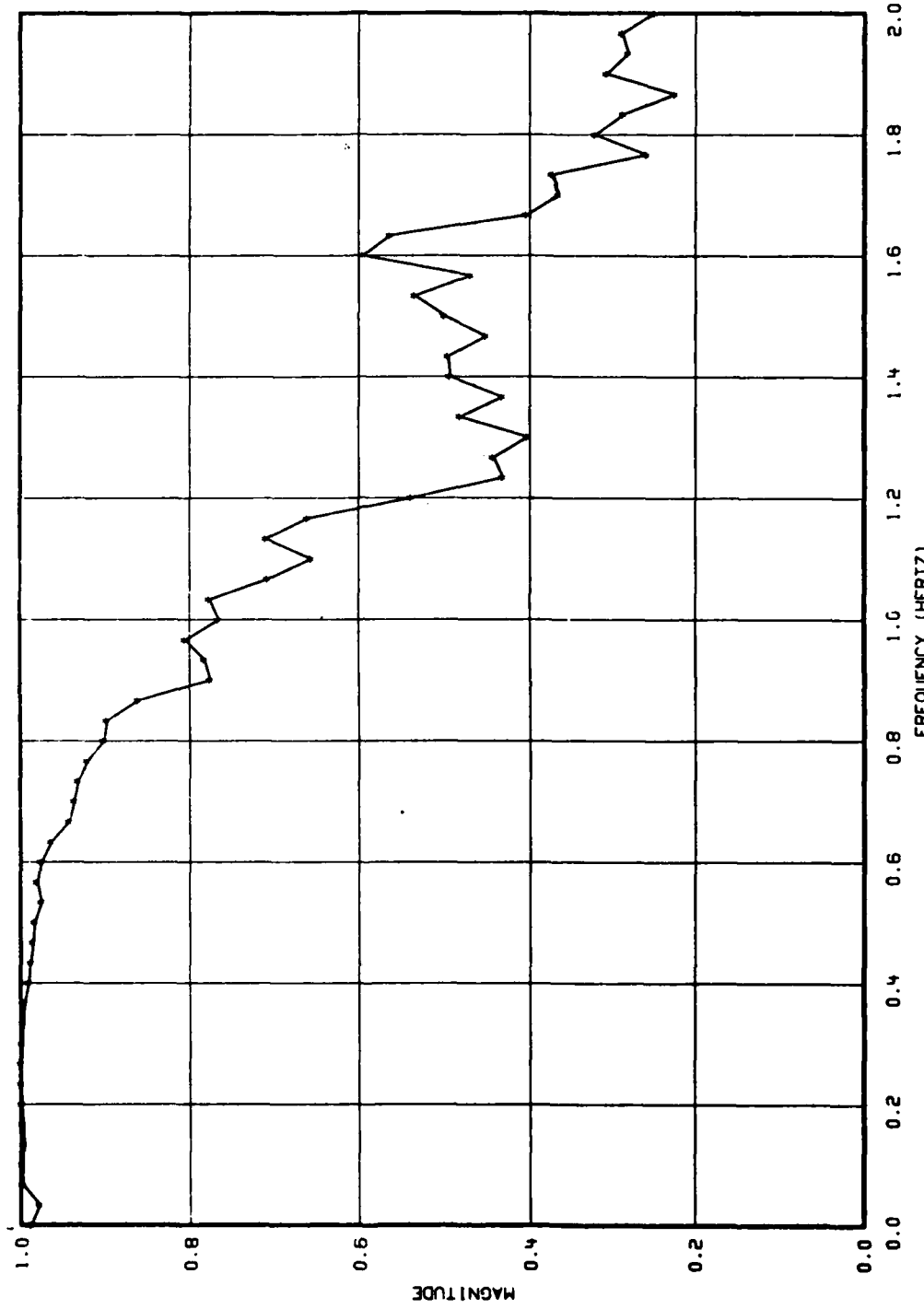


Figure 8-3. Magnitude of Normalized Cross-Spectral Density (Complex Coherence Function) Between the Two Closest Sensors (Sensors 4 and 5).

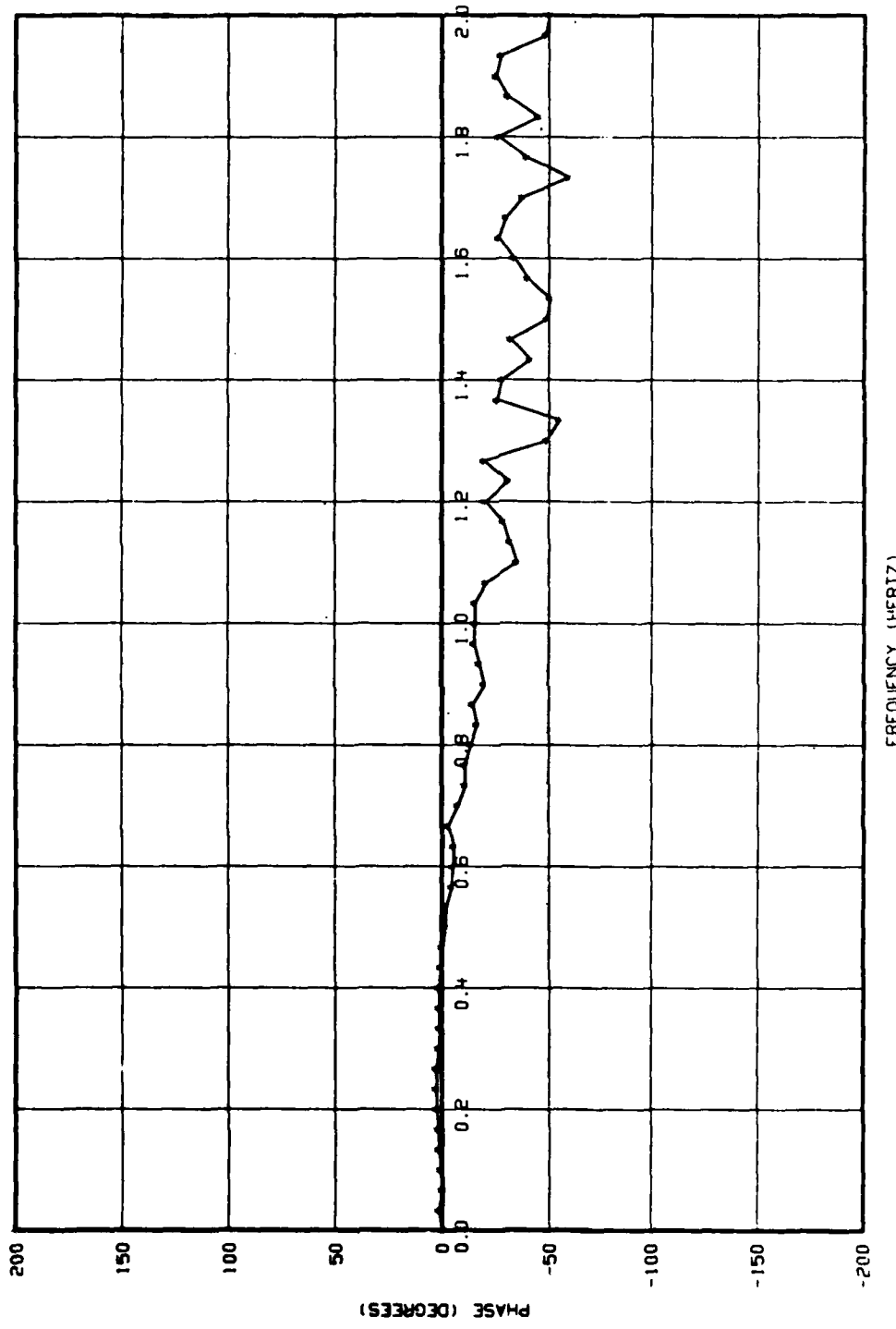


Figure 8-4. Argument of Normalized Cross-Spectral Density (Complex Coherence Function) Between the Two Closest Sensors (Sensors 4 and 5).

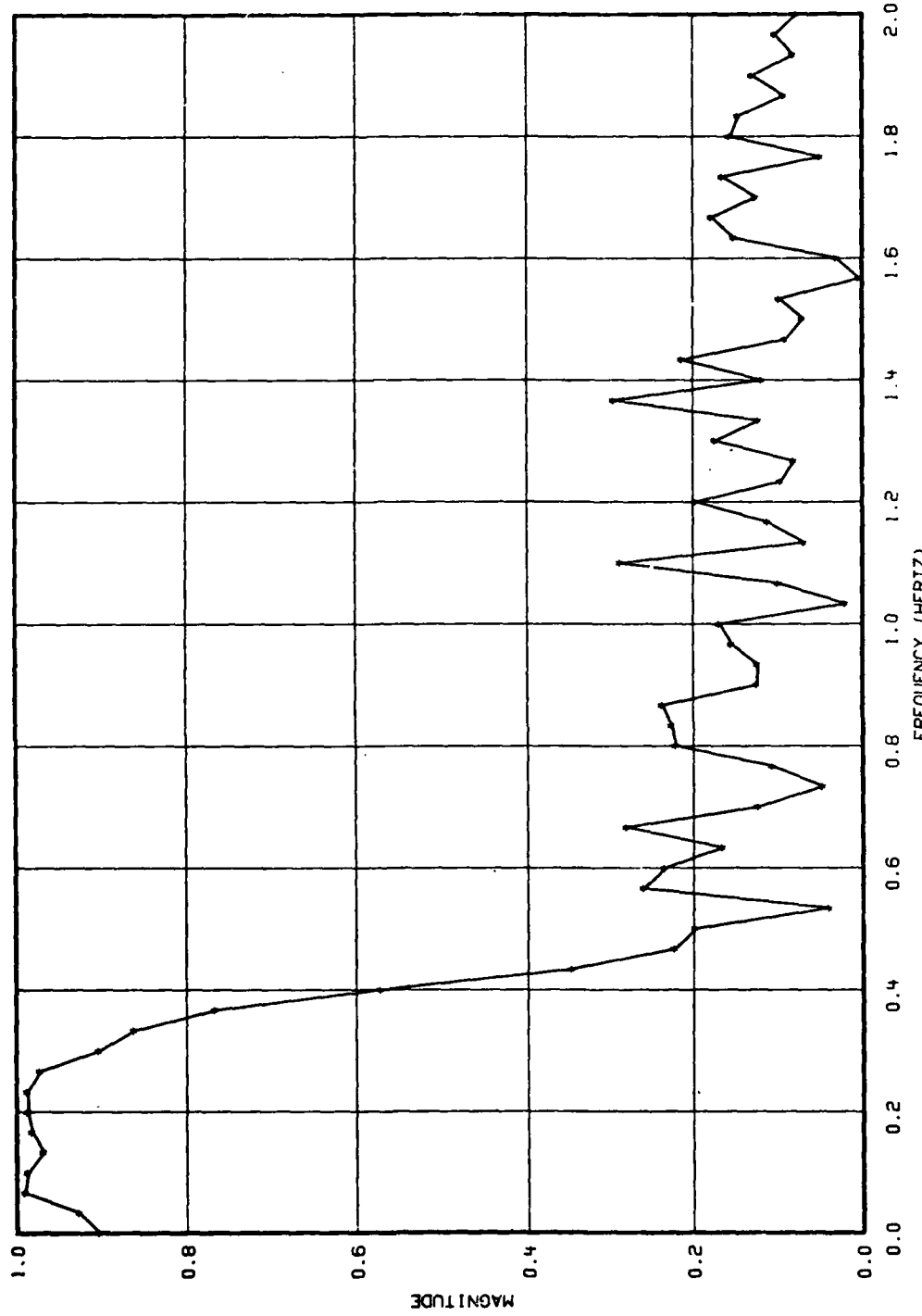


Figure 8-5. Magnitude of Normalized Cross-Spectral Density (Complex Coherence Function) Between the Two Furthest Sensors (Sensors 1 and 5).

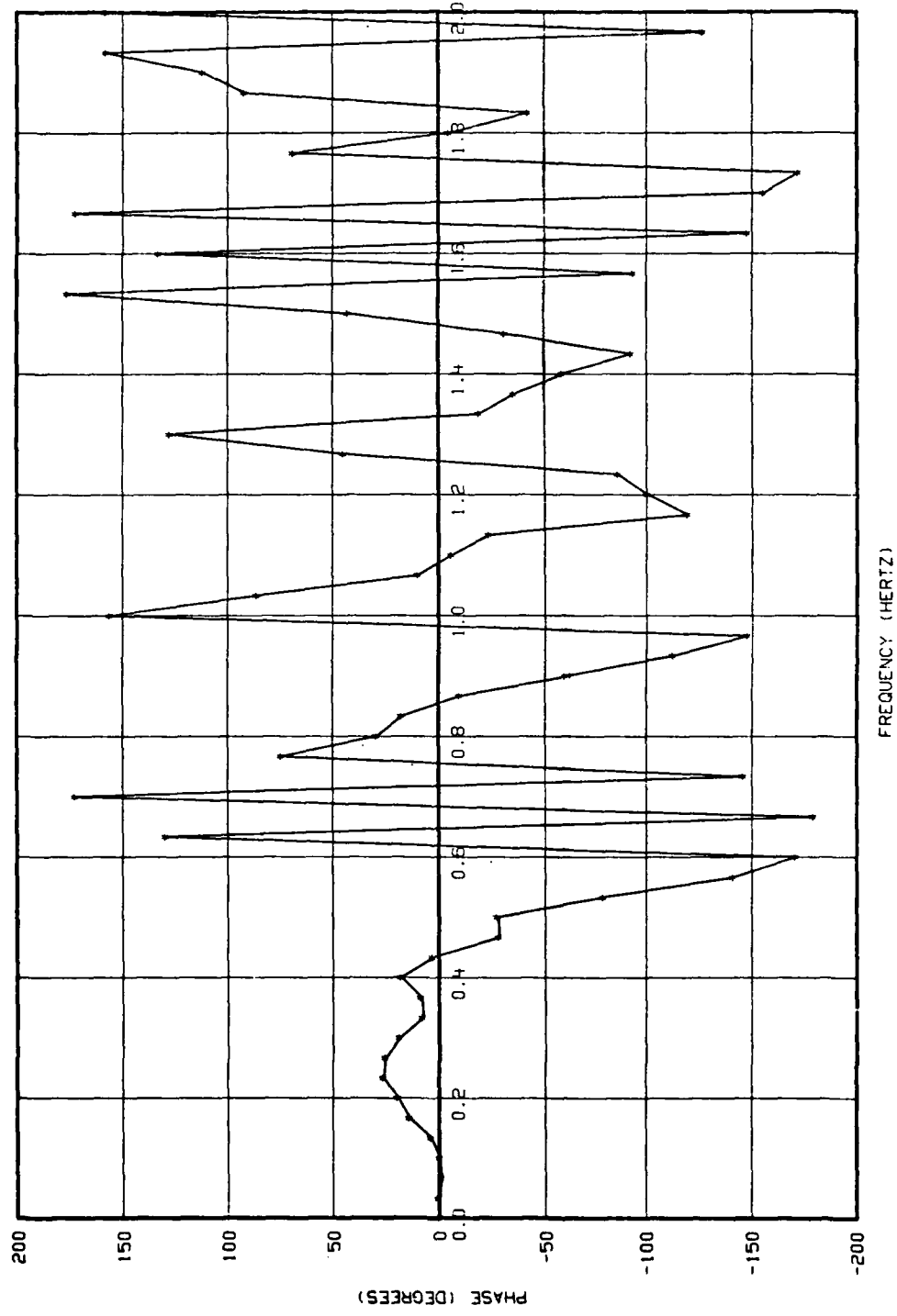


Figure 8-6. Argument of Normalize Cross-Spectral Density (Complex Coherence Function) Between the Two Furthest Sensors (Sensors 1 and 5).

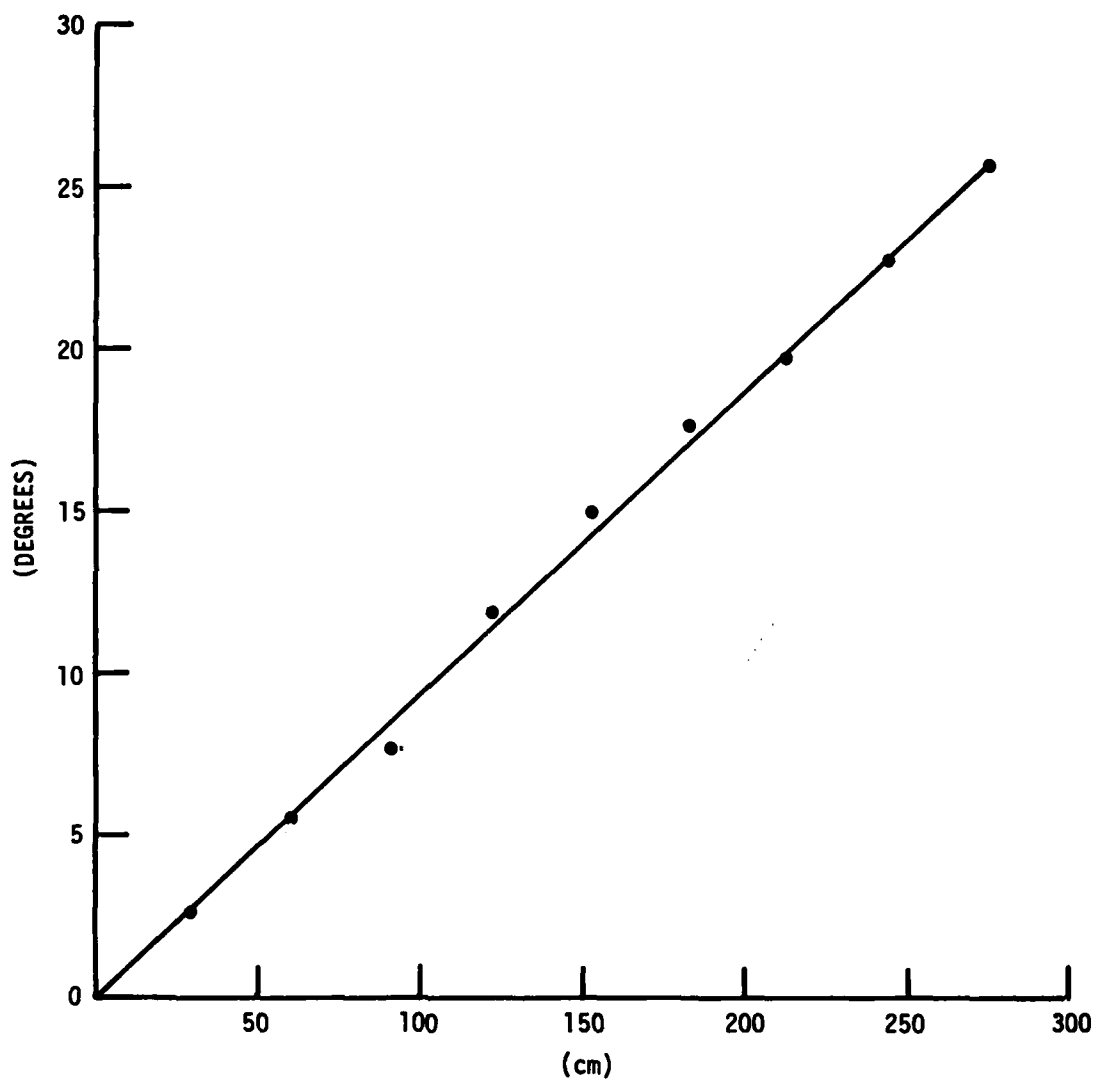


Figure 8-7. Argument of Complex Coherence Function for a Surface Wave Frequency of 0.233 Hz (2866 cm wavelength) Plotted as a Function of Unique Sensor Sensor Separation Distance.

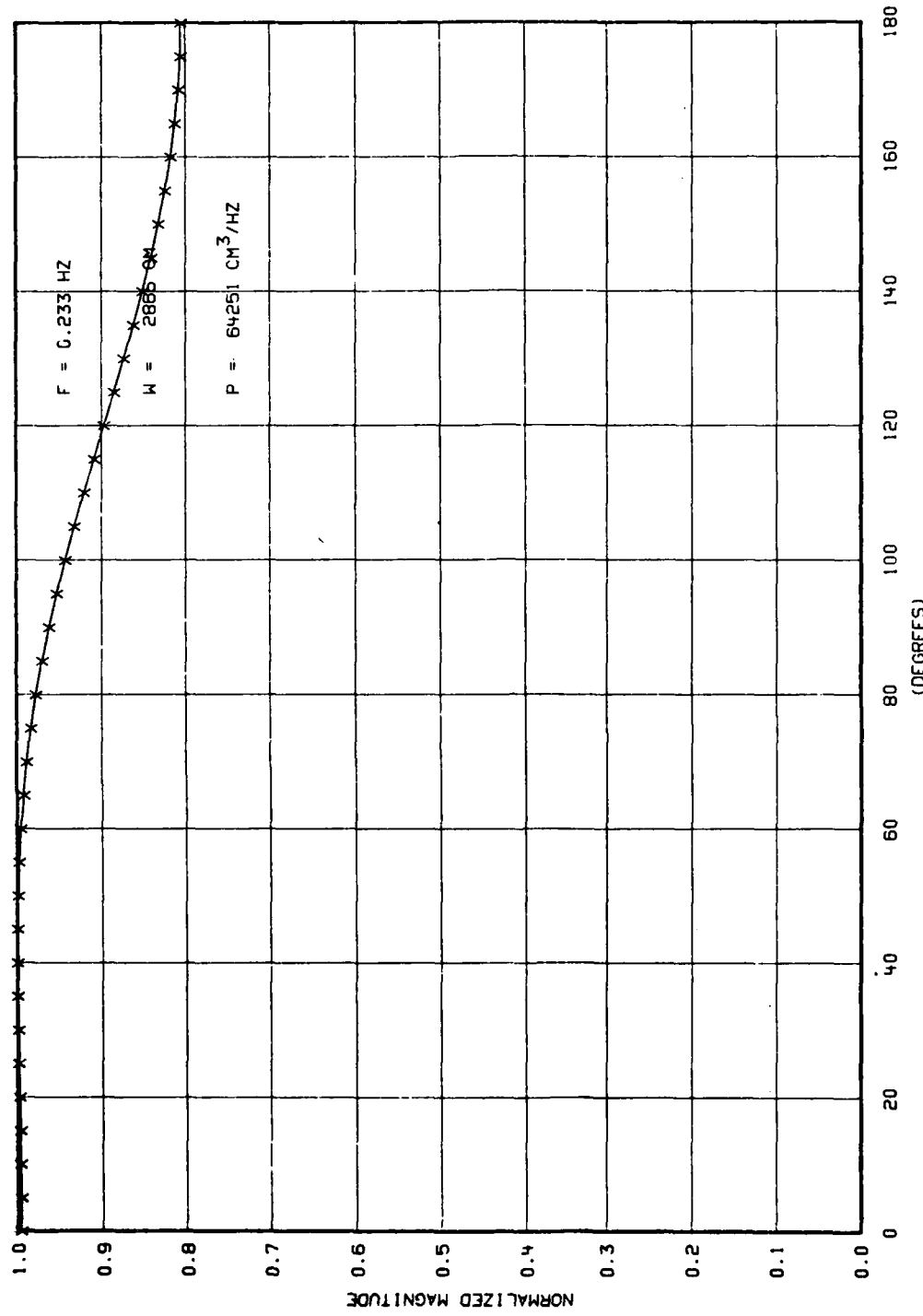


Figure 8-8. Directional Spectrum Based on the Conventional Spatial Lag Weighting Estimation Method for a Surface Wave Frequency of 0.233 Hz.

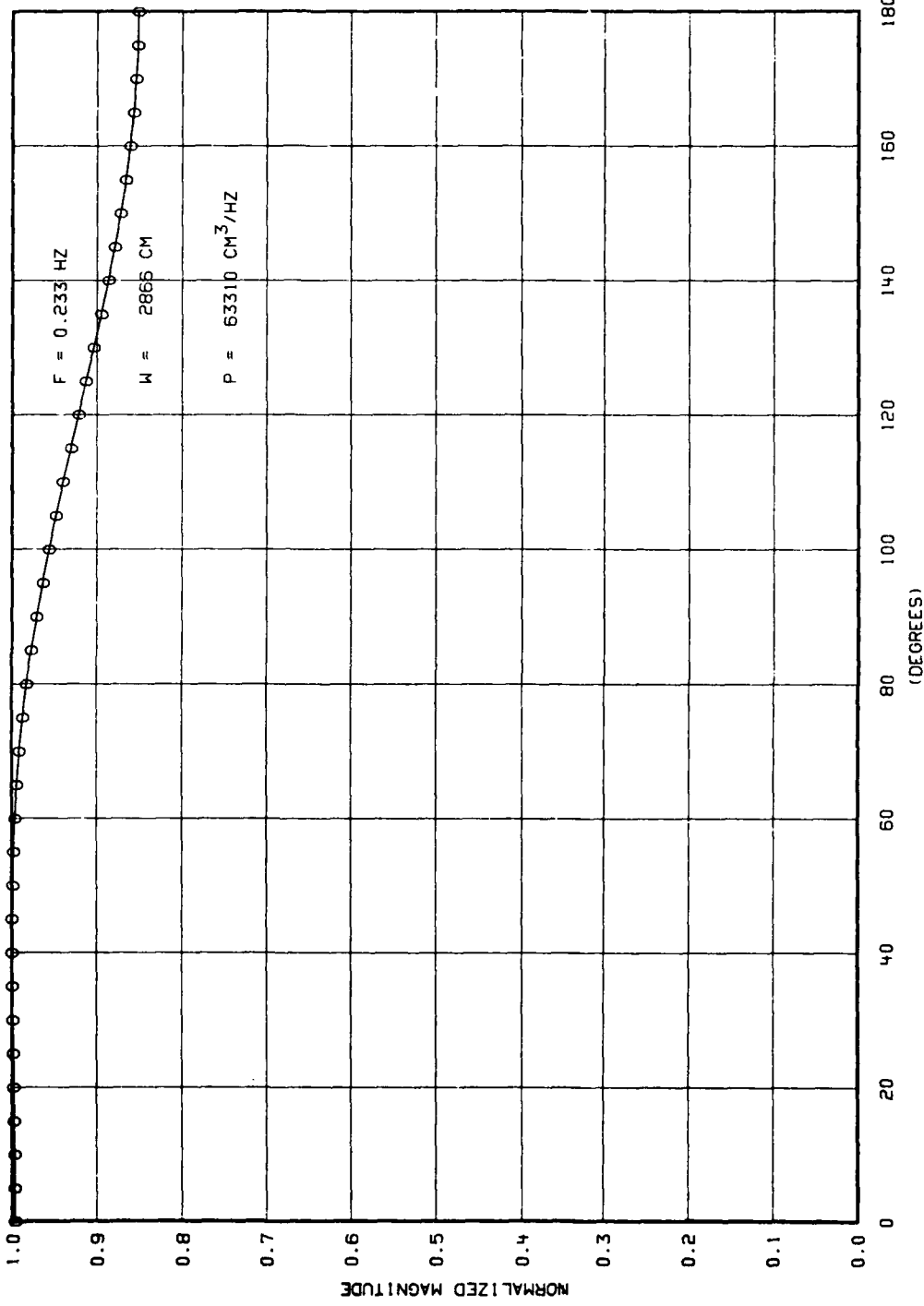


Figure 8-9. Directional Spectrum Based on the Conventional Spatial Weighting Estimation Method for a Surface wave Frequency of 0.233 Hz.

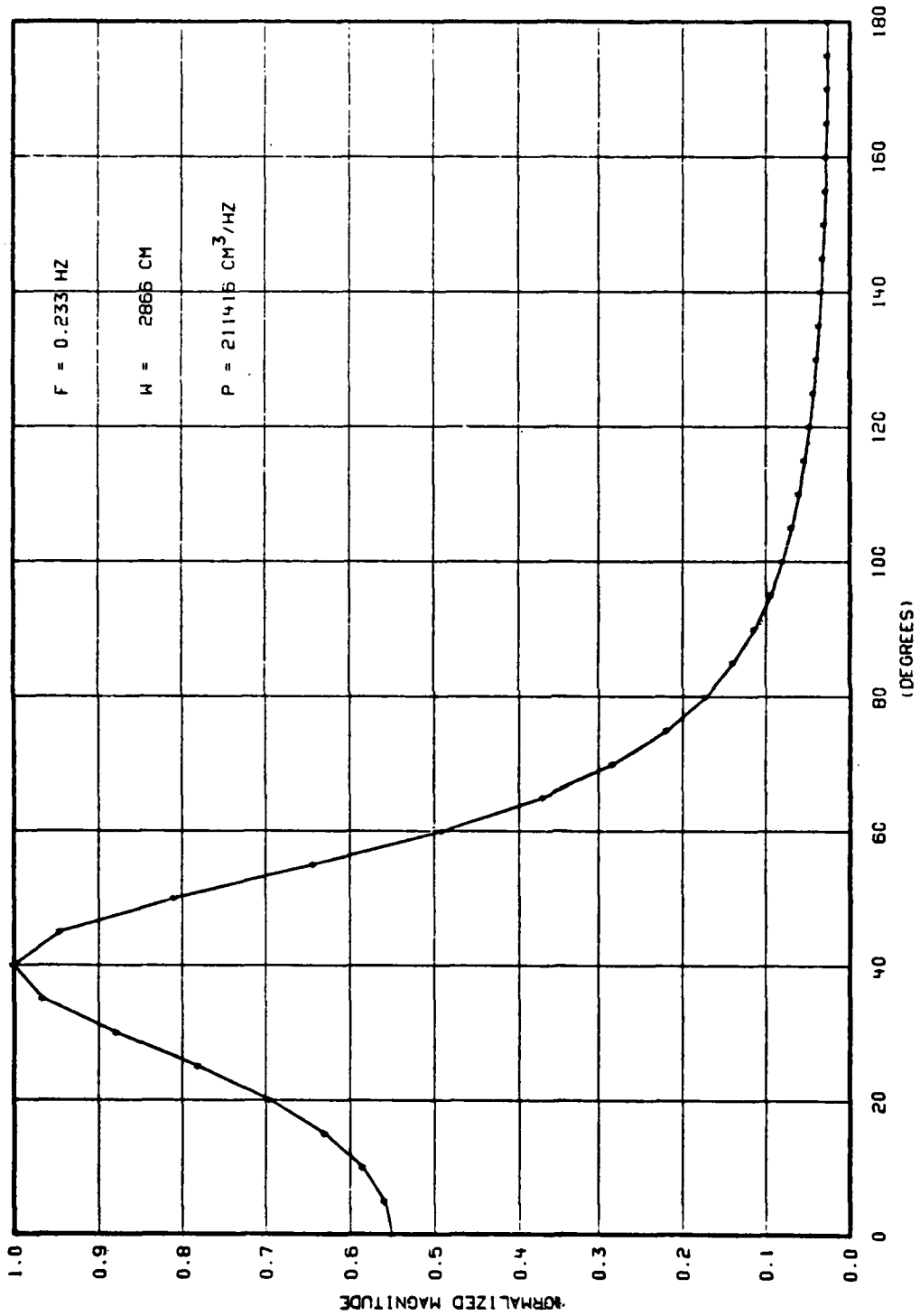


Figure 8-10. Directional Spectrum Based on the High Resolution Estimation Method for a Surface Wave Frequency of 0.233 Hz.

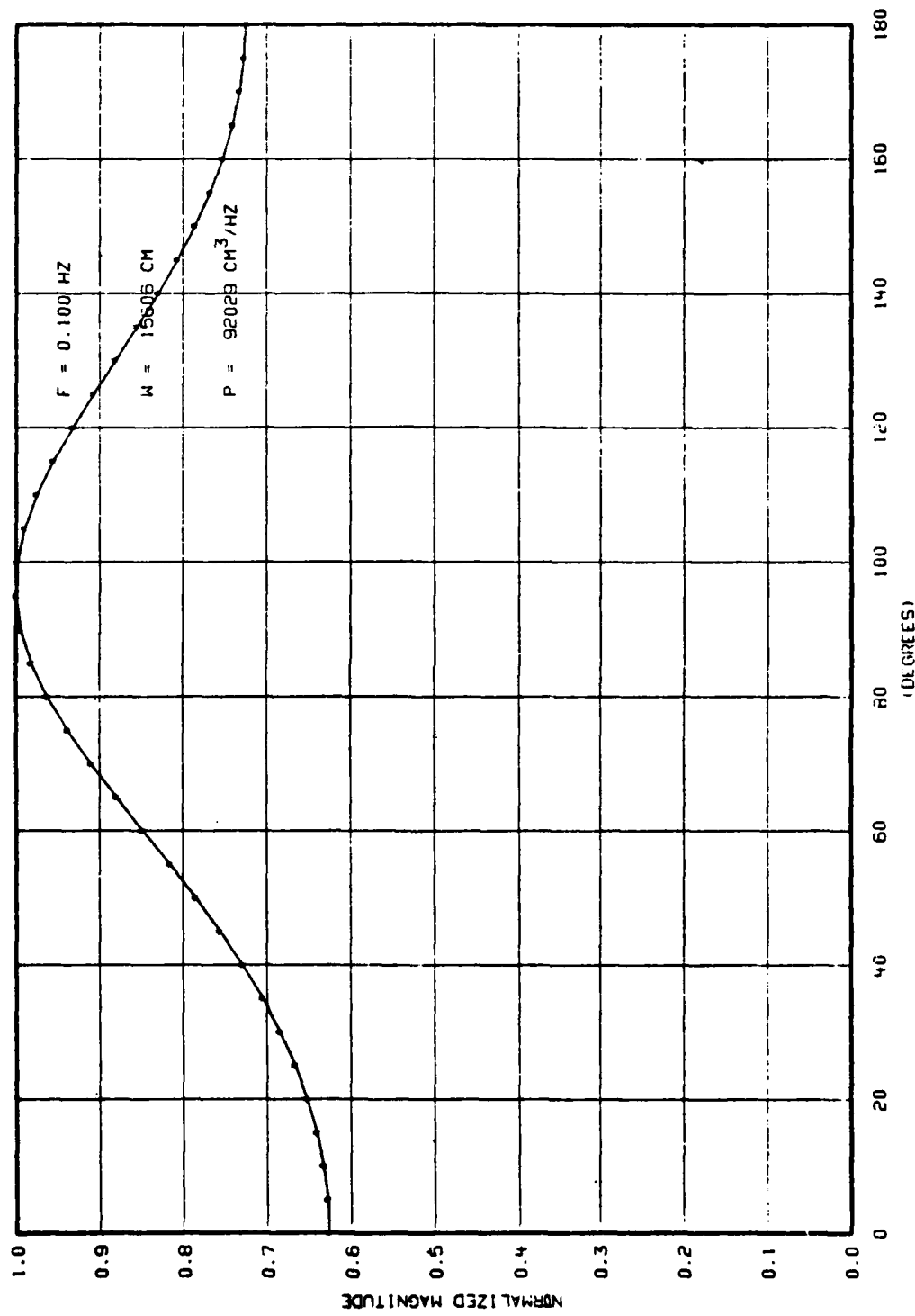


Figure 8-11. Directional Spectrum Based on the High Resolution Estimation Method for a Surface Wave Frequency of 0.1 Hz.

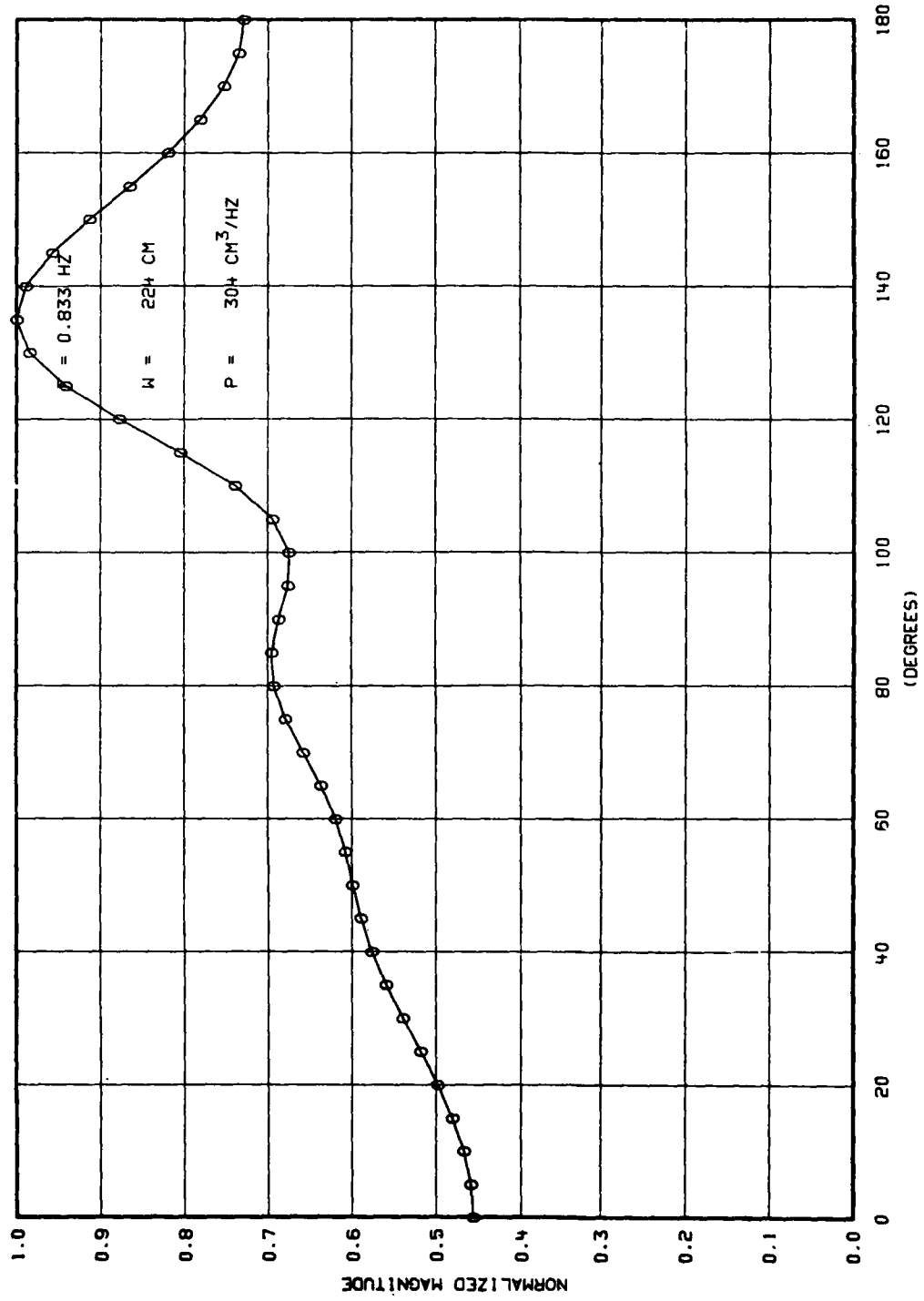


Figure 8-12. Directional Spectrum Based on the Conventional Spatial Weighting Estimation Method for a Surface Wave Frequency of 0.833 Hz.

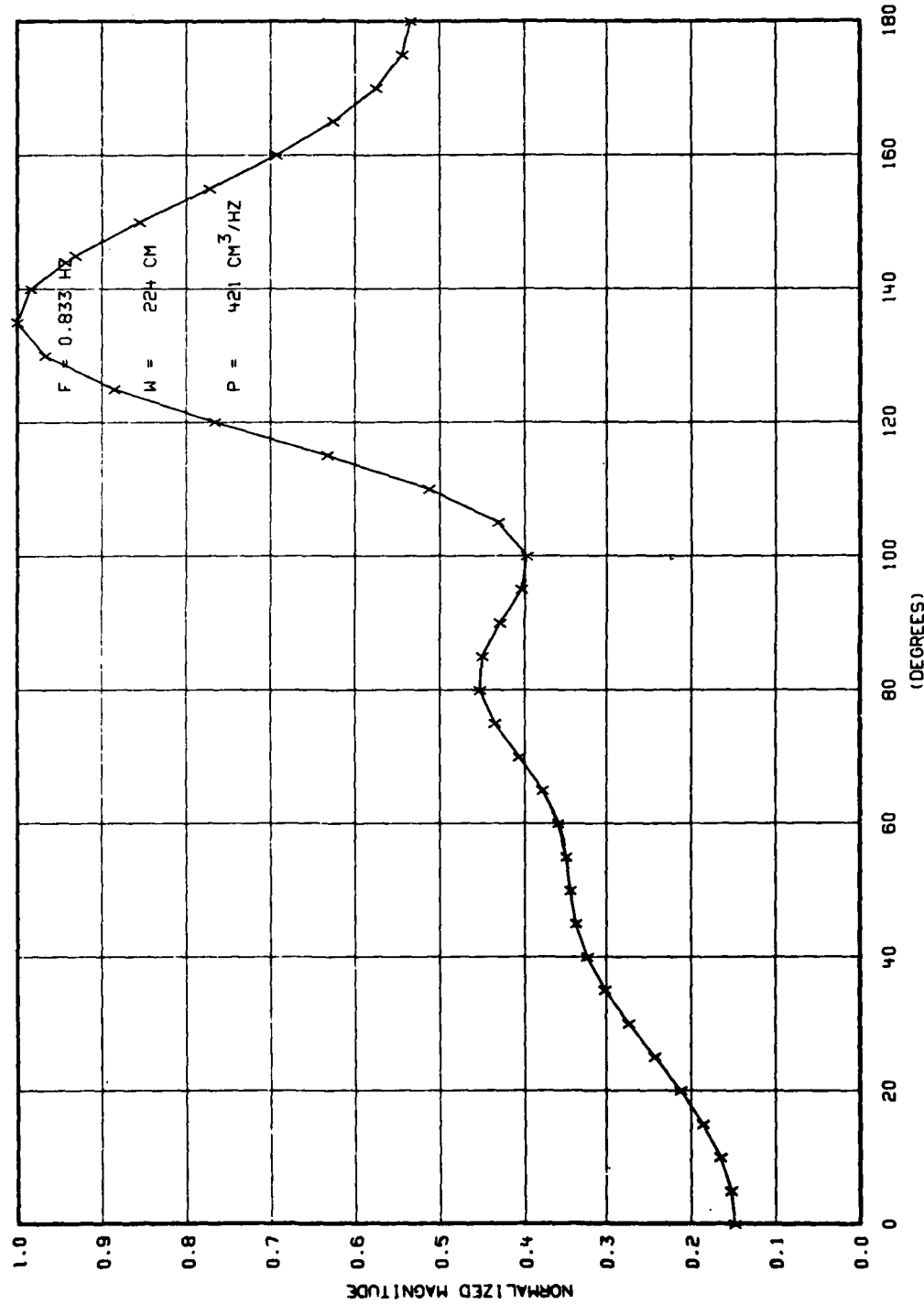


Figure 8-13. Directional Spectrum Based on the Conventional Spatial Lag Weighting Estimation Method for a Surface Wave Frequency of 0.833 Hz.

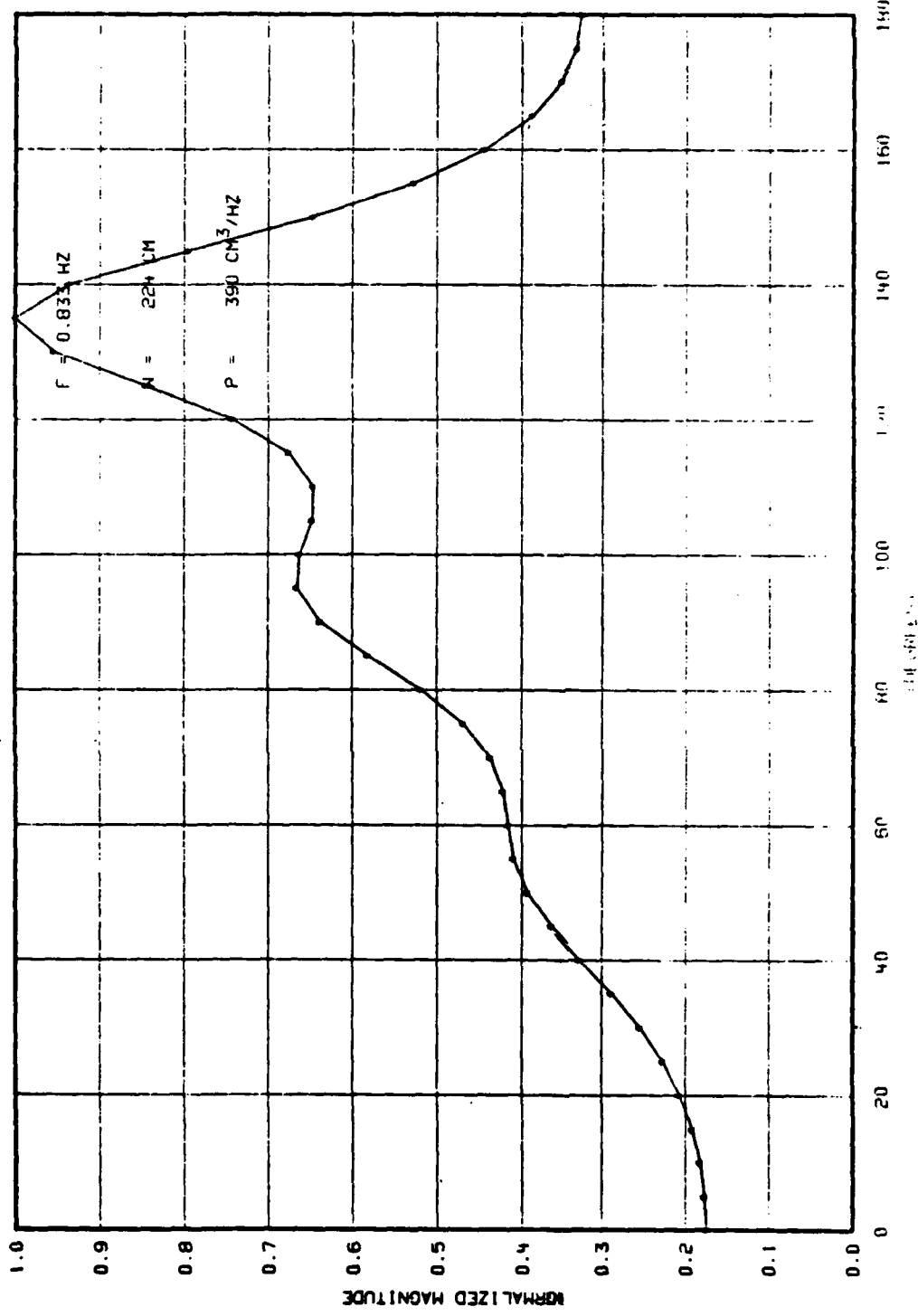


Figure 8-14. Directional Spectrum Based on the High Resolution Estimation Method for a Surface Wave Frequency of 0.833 Hz.

CHAPTER 9

CONCLUSIONS AND RECOMMENDATIONS FOR FUTURE RESEARCH

9.1 EXPERIMENT IN REVIEW

A shallow water reverberation experiment has been performed that measured the spectral properties of surface reverberation. An important adjunct to the reverberation measurements was the measurement of the directional properties of the surface from which the acoustic waves were scattered.

The acoustic and oceanographic measurements resulted in comprehensive and unique data sets. Both data sets were gathered while the sea surface remained statistically stationary. Furthermore, the reverberation data were obtained under isovelocity propagation conditions and when there was no evidence of a near-surface bubble layer to interfere with the scattering from the surface.

Reverberation Doppler spectra were computed from data measured at four angles of incidence, eight angles of scatter, and four acoustic frequencies. Data were obtained at angles that ranged from near-normal to an incidence angle of 60°. The broad bandwidth capability of the parametric array enabled reverberation to be measured at discrete frequencies in a band spanning 3.5 to 9.0 kHz. Also, the parametric array's narrow beamwidth was responsible for confining the insonified surface to a known and analytically describable scattering area. Likewise, the narrow beamwidth and near-absence of sidelobes minimized the effects of multipath interference.

It was not possible to completely eliminate multipaths, particularly direct path and bottom scattered arrivals. As would be expected, interferences were more detrimental at the lower frequencies and higher incidence angles, i.e., at parameters that yielded low surface reverberation levels. An attempt was made to transmit linear frequency modulated (LFM) waveforms with the idea of using the linear time-frequency relationship within the waveform to resolve the multipath. Due to an inadequate time-bandwidth product and arrival time instabilities, the use of a coded waveform did not yield the desired results. However, for the CW data, a digital processing scheme based on a least mean square error criterion was successfully used to remove the interferences from the reverberation data - particularly direct path and electrical pickup. An aftermath of digitally removing the sinusoidal interferences was that reverberation power at frequencies in the vicinity of zero Doppler were also affected. Curve-fitted estimates were provided at the near zero Doppler frequencies.

Surface wave directionality was measured from a sparse line array of five optimumly spaced wave height sensors. Spectral estimates were obtained using two conventional 'delay and sum' methods and a high resolution (maximum likelihood) method. The latter method was superior in estimating the directional spectrum of the surface waves since the array resolving power was not limited

primarily by array length but by signal-to-noise ratio considerations. Directional estimates were computed over a frequency band covering swell wave energy at a frequency of 0.1 Hz (15606 cm wavelength) to a frequency of 1.2 Hz (108 cm wavelength). It was the combination of the high signal-to-noise ratio of the wave height data and the high resolution processing technique that permitted the wave spectrum to be measured over such a broad spectrum of wavelengths.

9.2 SPECTRAL RESULTS IN REVIEW

The time series data obtained from the surface reverberated signals were processed using FFT spectral techniques. The disjoint reverberation segments were windowed, transformed, and Doppler spectra were estimated from the ensemble power spectral densities. The spectra were computed at a frequency resolution of 1.6 Hz and the 90% confidence limits for the estimates were ± 1.5 dB. Coefficients of variation of the spectral estimates were computed to determine the estimate variability.

Similarly, the five sensor wave height data were divided into 50% overlapped segments, windowed, and transformed. Normalized cross-spectral density (complex coherence function) estimates were computed from the ensemble average of 53 cross-spectra. Spectral resolution was 0.048 Hz and the maximum bias of the magnitude estimates was 0.12. Directional estimates were obtained from the cross-spectral density estimates at 5° angular spacings using conventional spatial weighting and spatial lag weighting methods and a high resolution method.

With the parametric array oriented into the direction of the prevailing winds, acoustic signals were reverberated from a sea that consisted mostly of wind generated waves with some swell wave activity. There was a frequency dependence to the surface wave directional distribution. Both the wind wave and swell wave power were concentrated close to the wind direction. Hence, parametric transmission was also into the waves. The surface wave height standard deviation was 8.5 cm and the predominant power in the one-dimensional spectrum peaked near 0.267 Hz. Also, the higher frequency regime of the power spectrum decreased at a rate proportional to f^{-5} . Most of the wind wave power propagated to the experimental site at azimuthal angles between 30 and 60° , relative to the bearing of the parametric array. Although the wind wave power in the higher frequencies was close to the wind direction, the directional distribution was broader and at some frequencies bimodal.

Analyses of the reverberation data revealed considerable spectral broadening in an up-Doppler direction. Qualitatively, a positive shift was in agreement with the directionality of the surface waves. The reverberation spectra exhibited a marked dependence with variations in transmitted frequency and angle of incidence. There was negligible change in reverberation spectral shape or bandwidth with variations in angle of scatter. In general, both the magnitude of the Doppler shifts and the bandwidths decreased with (1) increasing incidence angle and (2) decreasing transmit frequency. The spectral shape was most symmetrical (about the transmitted frequency) at near-normal incidence. This was to be expected since that angle corresponded closely to a specular reflection. The reverberation spectral shape was most asymmetrical

at an incidence angle of 20°. As an example, Doppler shifts and bandwidths of about 6 Hz were measured at an acoustic frequency of 9 kHz. Some of the reverberation spectra exhibited bimodal asymmetry with narrow band secondary peaks displaced about 10 Hz from the transmitted frequency. For instance, this occurred in the high incidence angle data at a frequency of 5 kHz. Coefficient of variation (CV) values showed that the Doppler spectrum estimates were highly variable on the "skirts" of the spectrum with minimum variability at frequencies near the Doppler shift frequency. It was common to have 10 log (CV) values of 0 dB at frequencies in the vicinity of the Doppler shift frequency with values increasing to about 5 dB at frequencies on the skirts of the spectrum.

Using "Bragg" resonance scattering theory as a basis, it was mentioned above that the direction of Doppler shift was in qualitative agreement with the directionality of the surface waves. Quantitatively, however, resonance scattering does not predict the magnitudes of the shift nor the bandwidths of the spectra. This is not surprising since the experimental conditions violated the low roughness assumption imposed on the resonance scattering model. That is, for the Bragg scattering theory to be valid, requires that G (see 6-1) be much less than unity. Or equivalently, the acoustic wavelength must be large in comparison to the apparent surface roughness $2\pi a/\lambda(\cos\theta + \cos\phi)$. For the geometric, acoustic, and oceanographic parameters involved in this experiment, the value of G was larger than unity. For example, at an incident angle of 20° and an acoustic frequency of 9 kHz, the value of G was approximately 6 which clearly violates the low roughness assumption. Thus, resonance scattering theory is not directly applicable, and other scattering models must be considered that account for large surface roughness. This is a subject for future work.

9.3 RECOMMENDATIONS FOR FUTURE RESEARCH

The acoustic and oceanographic data obtained in this experiment provide information for the design and performance prediction of sonar systems operating under reverberation-limited conditions. Although the reverberation measurements encompassed a broad angle of incidence coverage (0-60°), it was not possible to obtain data at higher angles. Reverberation at the higher incidence angles (80-85°) is pertinent to the performance prediction of sonar systems operating in a surface duct mode of propagation. Also, it would have been desirable to have obtained reverberation data at other sea states and at both lower and higher frequencies than that covered in the experiment. To meet these system performance needs, recommendations are made for the continuing development and subsequent validation of reverberation Doppler spectrum models. A further recommendation is made for measurement of surface reverberation at higher incidence angles and other sea states.

From a theoretical viewpoint, the conditions encountered in this experiment require a reverberation model that can accommodate large surface roughness. As an example of a candidate model, the so-called 'composite-roughness surface' (see e.g., 9-1, 9-2) extends the validity of the low roughness resonance scattering theory by assuming the surface is composed of two wave types: low amplitude high frequency (ripples) waves that are responsible for resonance scattering are superimposed on high amplitude low frequency waves.

The low frequency waves are approximated by plane facets whose slopes and motions modify the low roughness Doppler spectrum.

From an experimental viewpoint, data at higher incidence angles requires an acoustic projector with higher source level. The attributes of the parametric array still make this acoustic source attractive for future reverberation experiments. By lowering the acoustic primary frequencies and increasing electrical power, sufficient source level at the difference frequency can be generated. Higher source levels are required to provide adequate reverberation-to-ambient noise levels at high incident angles.

By changing the signal generation and digital processing schemes and conducting the experiment in slightly shallower water, multipath interferences can be virtually eliminated. That is, short CW pulse can be transmitted to resolve the multipath arrivals. The repetition period of the pulses and the number of pulses transmitted would determine the spectral resolution and the statistical confidence in the spectral estimates. Care must be taken that the pulse repetition rate is fast enough (in comparison to the reverberation bandwidth) to avoid aliasing. For the geometries involved in this experiment, this technique was not permissible in the shallow waters of Block Island Sound.

Future reverberation experiments that are supported with surface wave directionality measurements should consider obtaining directional data at higher surface wave frequencies. This can be achieved with a sparse line array with closer sensor spacing. Of course, this requires more sensors. Finally, consideration should be given to increasing the dynamic range of the wave height sensing system by using preemphasis techniques. That is, the frequency response of the receiving system should be arranged so that the low amplitude higher surface wave frequencies are accentuated prior to recording.

APPENDIX A

Removal of Sinusoidal Component From Reverberation Data

In CHAPTER 5 it was mentioned that a least mean error technique was used to eliminate a steady state component - at the transmitted difference frequency - from the reverberation signals. The steady state component was a result from the direct path and/or electrical pickup interferences.

The steady state component was removed by subtracting a sampled sinusoid from each of the reverberation data points. The amplitude and phase of the sinusoid was computed using a least mean square error criterion.

Initially, assume that the transmitted difference frequency f_d is known and define the error $E(A, \phi)$ as

$$E(A, \phi) = \sum_{j=1}^N (x_j - A \cos(2\pi f_d \Delta t j - \phi))^2, \quad (A-1)$$

where x_j , $j=1, \dots, N$ are sampled values of the reverberation return, Δt is the sampling period, and A and ϕ are the unknown amplitude and phase which minimize (A-1). In the computations, 900 data points were used.

Two procedures were examined to determine the best fitting amplitude and phase: the first procedure was a straight forward "brute force" iterative approach. The second, suggested by Nuttall [A-1], involved finding solutions to two simultaneous equations that minimized the error.

In the iterative approach, a value of A was chosen, and held constant, while the phase was incremented. The phase was incremented in two step sizes: a "coarse" size in 18° steps and then in a more refined size in 0.9° steps. After computing the best fitting phase to an accuracy of 0.9° , the amplitude was incremented. In a similar manner, the amplitude was incremented in two step sizes, a coarse size based on one-twentieth of the RMS (root mean square) value of the reverberation data and then a more refined amplitude step size.

Due to tape recorder flutter the recorded and playback frequency was not quite the transmitted difference frequency. Using the reference channel as a frequency reference, the mean square error given by (A-1) could be further reduced by finding the best fitting frequency. The best fitting frequency was also obtained using an iterative technique, where the frequency step sizes were .005 Hz on each side of the transmitted difference frequency. The frequency was incremented 30 times.

In the second procedure, two simultaneous equations were obtained by expressing (A-1) in terms of a trigonometric identity to give

$$E(\alpha, \beta) = \sum_{j=1}^N (x_j - \alpha \cos(2\pi f_d \Delta t j) - \beta \sin(2\pi f_d \Delta t j))^2 , \quad (A-2)$$

where

$$\alpha = A \cos \phi \quad (A-3)$$

$$\beta = A \sin \phi . \quad (A-4)$$

By obtaining the partial derivatives of E with respect to α and β , $\partial E / \partial \alpha$ and $2E / 2\beta$, the results can be set to zero to obtain the best fitting α and β . The optimum values of α and β are solutions of

$$\alpha_0 A_{11} + \beta_0 A_{12} = C_1 \quad (A-5)$$

and

$$\alpha_0 A_{12} + \beta_0 A_{22} = C_2 . \quad (A-6)$$

The values of A_{11} , A_{12} and A_{22} are constants which depend on the number of data points, the frequency and sampling period. Summations are required for the computations of C_1 and C_2 , or

$$C_1 = \sum_{j=1}^N x_j \cos(2\pi f_d \Delta t j)$$

and

$$C_2 = \sum_{j=1}^N x_j \sin(2\pi f_d \Delta t j) .$$

The second technique is superior in both computational time and accuracy in comparison to the iterative technique. However, in both approaches, the effects of tape recorder flutter were removed using an iterative technique. Interference signals with amplitudes 20 dB stronger than the reverberation return could be removed using either of the two techniques.

APPENDIX B

Digital Processing of LFM Reverberation Data

The 1000 msec pulsed CW waveforms were the primary signals for the determination of the reverberation Doppler spectra. Although the pulse length (bandwidth) was sufficient to obtain adequate frequency resolution, the multipath interferences could not be separated in time due to overlap of arrivals. In an attempt to simultaneously resolve the multipath interferences and to determine the reverberation Doppler spectra (with adequate frequency resolution) linear FM pulsed waveforms were transmitted.

The linear FM waveform has the unique property that within the waveform there is a linear relationship between instantaneous frequency and time. Hence, the result from transmitting this waveform is that multipath arrivals not only combine with a time delay difference but also with a frequency difference. Consider the transmission of an LFM waveform $S(t)$ given by

$$S(t) = \cos[2\pi f_0 t + \pi Kt^2], \quad (B-1)$$

where f_0 is the carrier frequency, and K is the slope of the FM. The instantaneous frequency f_i of the waveform is determined by the rate of change of the signal phase which can be expressed as

$$\frac{d(2\pi f_i t)}{dt} = \frac{d}{dt} [2\pi f_0 t + \pi Kt^2], \quad (B-2)$$

or

$$f_i = f_0 + Kt.$$

The sign of K determines the direction in which the frequency is swept (up or down) and the swept bandwidth is given by

$$B = |K|T, \quad (B-3)$$

where T is the pulse length.

Assume that an LFM waveform has been scattered from the sea surface and can be represented by a narrow band signal with time varying envelope $a(t)$ and phase $\phi(t)$, or

$$r(t) = a(t) \cos[2\pi f_0(t-t_1) + \pi K(t-t_1)^2 + \phi(t)], \quad (B-4)$$

where t_1 is the "round-trip" travel time from source-to-surface-to-receiver. If the received surface scattered signal $r(t)$ is multiplied by the transmitted waveform, then for the duration of the overlap (t_1 to T)

$$\begin{aligned}
 y'(t) &= s(t) r(t) \\
 &= \frac{a(t)}{2} \cos[(2\pi Kt_1)t + 2\pi f_o t_1 - \pi Kt_1^2 - \phi(t)] \\
 &\quad + \frac{a(t)}{2} \cos[(2\pi f_o - Kt_1)t + 2\pi Kt^2 - 2\pi f_o t_1 + \pi Kt_1^2 + \phi(t)] .
 \end{aligned} \tag{B-5}$$

The product consists of the summation of low and high frequency signals. An observation of the low frequency band shows that the surface scattered signal has been translated to a lower "carrier frequency" Kt_1 , i.e.,

$$y(t) = \frac{a(t)}{2} \cos[(2\pi Kt_1)t + 2\pi f_o t_1 - \pi Kt_1^2 - \phi(t)] . \tag{B-6}$$

Thus, the surface scattered signal from an LFM waveform has been translated to a lower carrier frequency by the multiplication of the transmitted waveform. Except for the addition of some inconsequential static phase shifts, the Doppler spectra of $y(t)$ would be the same as if a CW waveform had been transmitted at frequency f_o and then the received signal translated to frequency Kt_1 . However, the LFM waveform must be narrowband for this approximation to be valid. It can be seen that if the received signal consisted of other multipath arrivals then

$$z(t) = 1/2 \sum_{j=0}^{P-1} a_j(t) \cos[(2\pi Kt_j)t + 2\pi f_o t_j - \pi Kt_j^2 - \phi_j(t)] , \tag{B-7}$$

where j indexes the travel times and amplitude and phase modulation functions. The translated frequency of each arrival is a function of the linear FM bandwidth and pulse length or

$$f_j = \frac{Bt_j}{T} . \tag{B-8}$$

If the bandwidths of the multipath arrivals are small in relationship to the differences between the translated frequencies then it is possible to separate in frequency the spectra of the arrivals (see Fig. B-1).

In the reverberation experiment, LFM waveforms with 100 Hz bandwidths and 500 msec pulse lengths were transmitted. The frequency translations are given by

$$f_j = 200 t_j \text{ Hz} . \tag{B-9}$$

As an example of the frequency translations at an incident angle of 20° , the direct path, surface scattered and bottom scattered arrivals have respective travel times of approximately 3, 40, and 80 msec which translate to frequencies of 0.6, 8, and 16 Hz.

The product of the reference LFM signal and the hydrophone output signals was accomplished digitally. Starting at approximately 93 msec after transmission, 405 digital samples from the reference and hydrophone signals were multiplied. In a manner similar to the processing of the 1000 msec CW signal

(CHAPTER 5), the product data samples were Hanning weighted. The Hanning weights were applied to reverberation records 396 msec in length which resulted in a frequency resolution (defined between half-power points) of 3.64 Hz. The data samples were padded with an equal number of zeros to obtain a frequency spacing of 1.26 Hz between spectral estimates.

An estimate of the Doppler spectra was obtained by ensemble averaging the power spectral densities of the product of the received reverberation and the reference signal. An example of the Doppler spectra is shown in Fig. B-2 for an incident angle of 40°, a scatter angle of 51.8, and a transmitted frequency of 5 kHz. The Doppler spectra of the surface reverberation peak at approximately 13 Hz and are flanked on both sides by the spectra of the electrical interference which peak at 0 Hz and the spectra of the bottom reverberation which peak at 20 Hz. It is obvious that with the transmitted bandwidth of 100 Hz and the 500 msec pulse length, it was not possible to completely resolve in frequency the Doppler spectra of the surface reverberation. The bottom reverberation peaks up at the translated frequency of 20 Hz and this is in good agreement for the travel time from source-to-bottom-to-receiver. The peak for the surface reverberation is about 2 Hz higher than that predicted by travel time considerations. This difference is due to the Doppler shift in the surface reverberation. The 3 dB bandwidth of the electrical interference is also in good agreement with that predicted for a Hanning spectral window.

Further observations of other Doppler spectra computed from the LFM transmissions show that the surface reverberation spectra are greater in bandwidth than those obtained from the 1000 msec CW transmissions. This is due to the round trip travel time t_1 for the surface reverberation not being constant. That is, t_1 would vary depending on which portion of the insonified surface area contributed to the reverberation. Thus an additional phase modulation (see (B-6)) was introduced into the LFM data which was not present in the CW data.

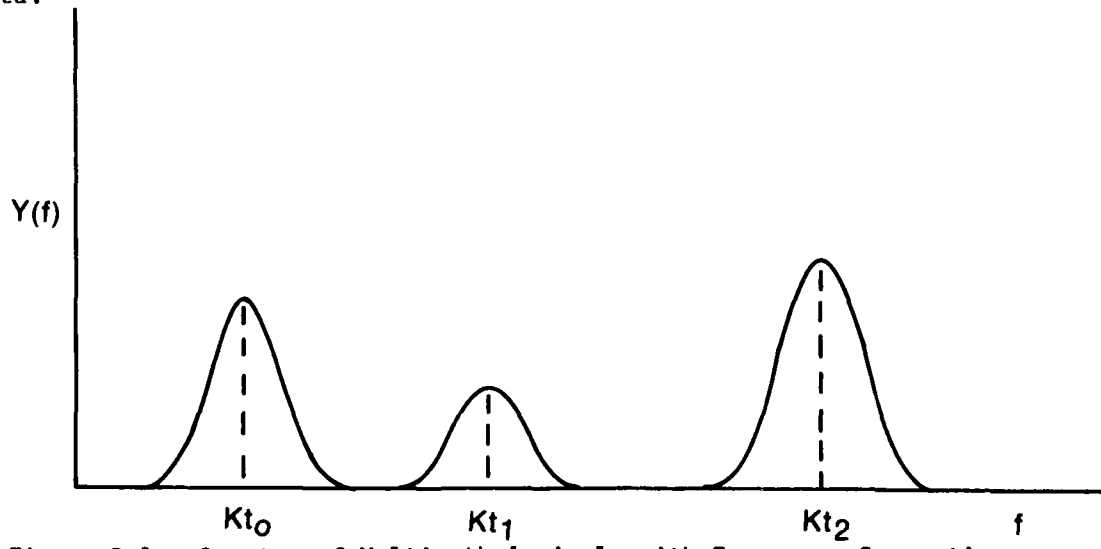


Figure B-1. Spectra of Multipath Arrivals with Frequency Separation Proportional to Travel Time Differences.

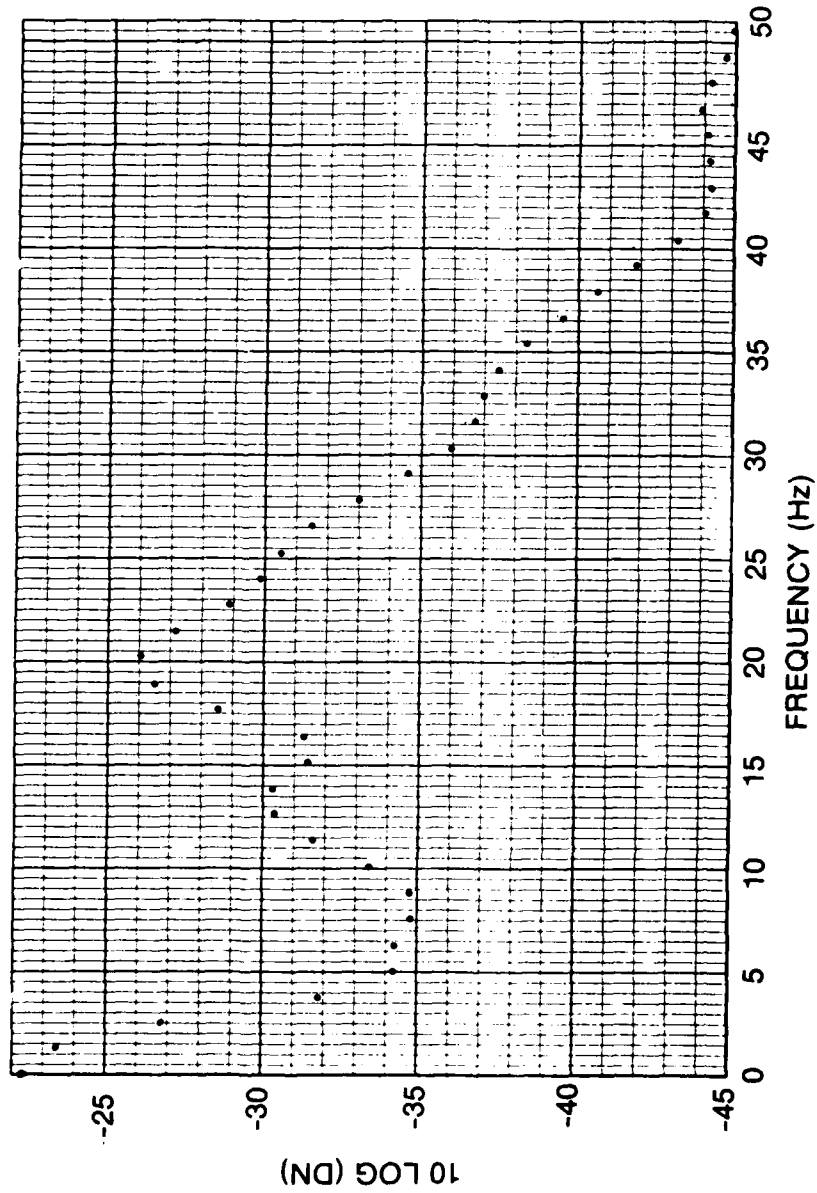


Figure B-2. Power Spectral Density of the Product of the Reference Signal and Received Reverberation for a Transmitted Frequency of 5 kHz, an Incident Angle of 40° and a Scattering Angle of 51.8°

APPENDIX C

EXAMPLES OF DOPPLER SPECTRA ESTIMATED FROM REVERBERATION MEASURED ON TWO HYDROPHONES

This appendix contains examples of reverberation Doppler spectra as measured from data received on hydrophones H1 and H8. (See Fig. 2-2 and Table 2-1 for hydrophone locations and corresponding scatter angles.) The coefficients of variation of the spectral estimates are also presented to show the variability of the estimates. The spectra are displayed as a function of the four transmitted difference frequencies and the four angles of incidence of the parametric array to the sea surfaces.

As mentioned in CHAPTER 6, there is little variation in spectral shape or computed Doppler statistics as a function of scattering angle; therefore, the spectra presented are indicative of the estimates obtained at other scattering angles. The spectral estimates obtained on other hydrophones are readily available from the author upon request.

The digital processing procedures for computing the Doppler spectra and coefficients of variation were described in CHAPTER 5. The spectra were computed by ensemble averaging the power spectral densities of 25 reverberation returns of the 1.0 sec transmitted CW pulses. In the spectra, the transmitted frequency has been referred to a frequency of 0.0 Hz. In the process of removing an interfering sinusoidal component from the reverberation data (SECTION 5.24), the reverberation power at frequencies in the vicinity of zero Doppler shift were adversely effected. The spectral estimates at the transmitted frequency and at the adjacent frequencies have been curve fitted to represent the spectral estimates due to surface reverberation. The curve fitted spectral estimates are symbolized by the open circles. The computed statistics (Doppler shifts and bandwidths) were obtained from the uncorrected estimates.

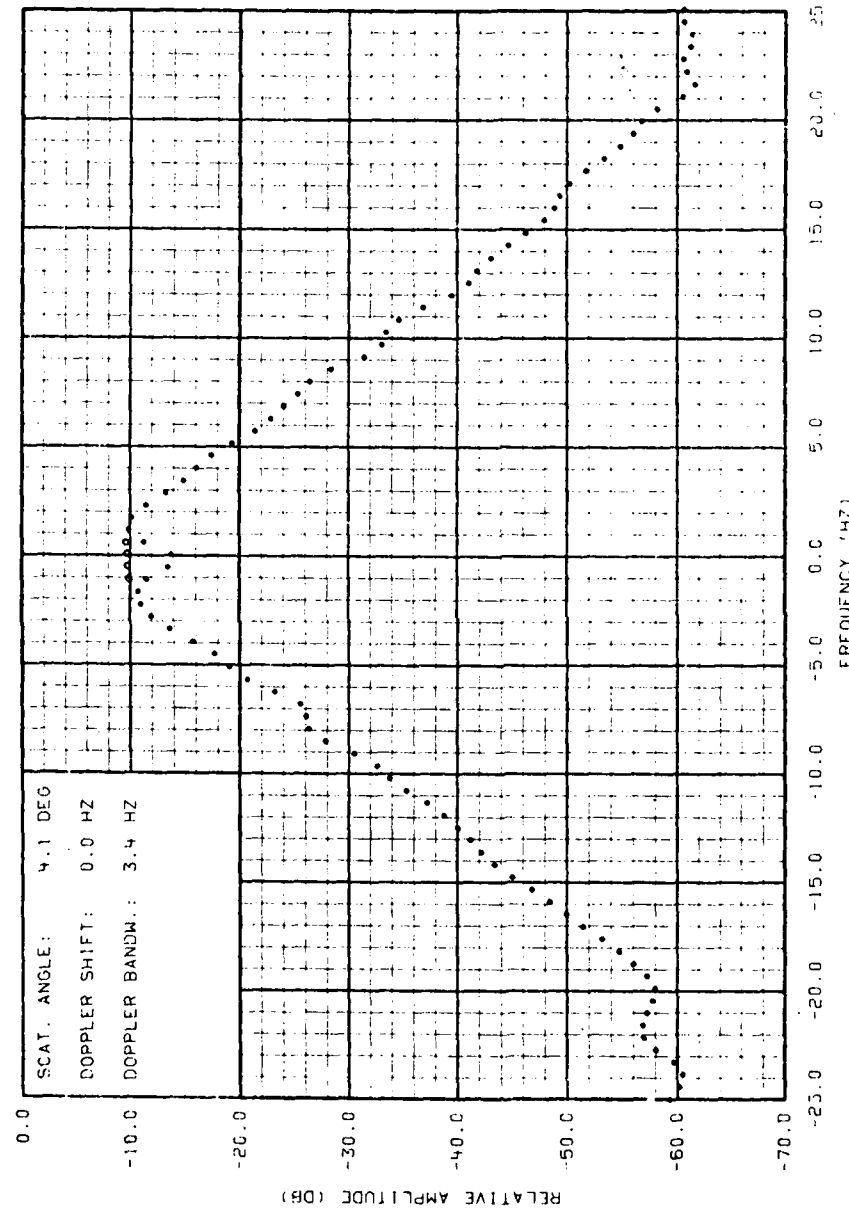


Figure C-1. Doppler Spectrum of Surface Reverberation Obtained at a Transmitted Frequency of 9.0 kHz, an Incident Angle of -4.70, and an Angle of Scatter of 4.10. Corrected Spectral Estimates in the Vicinity of Zero Doppler are Represented by Open Circles.

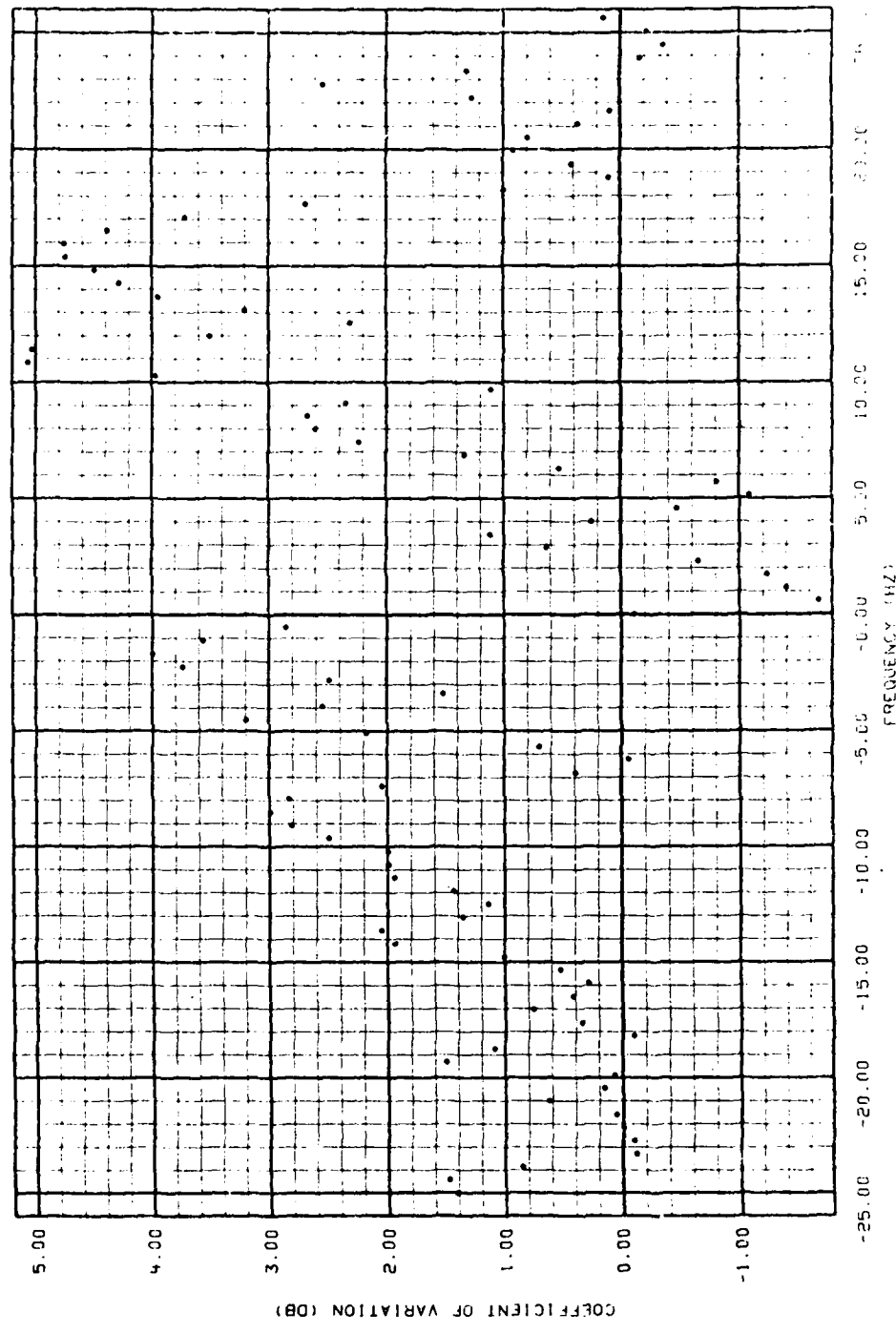


Figure C-2. Coefficients of Variation of the Spectral Estimates Obtained at a Transmitted Frequency of 9.0 kHz, an Incident Angle of -4.7° , and an Angle of Scatter of 4.10° .

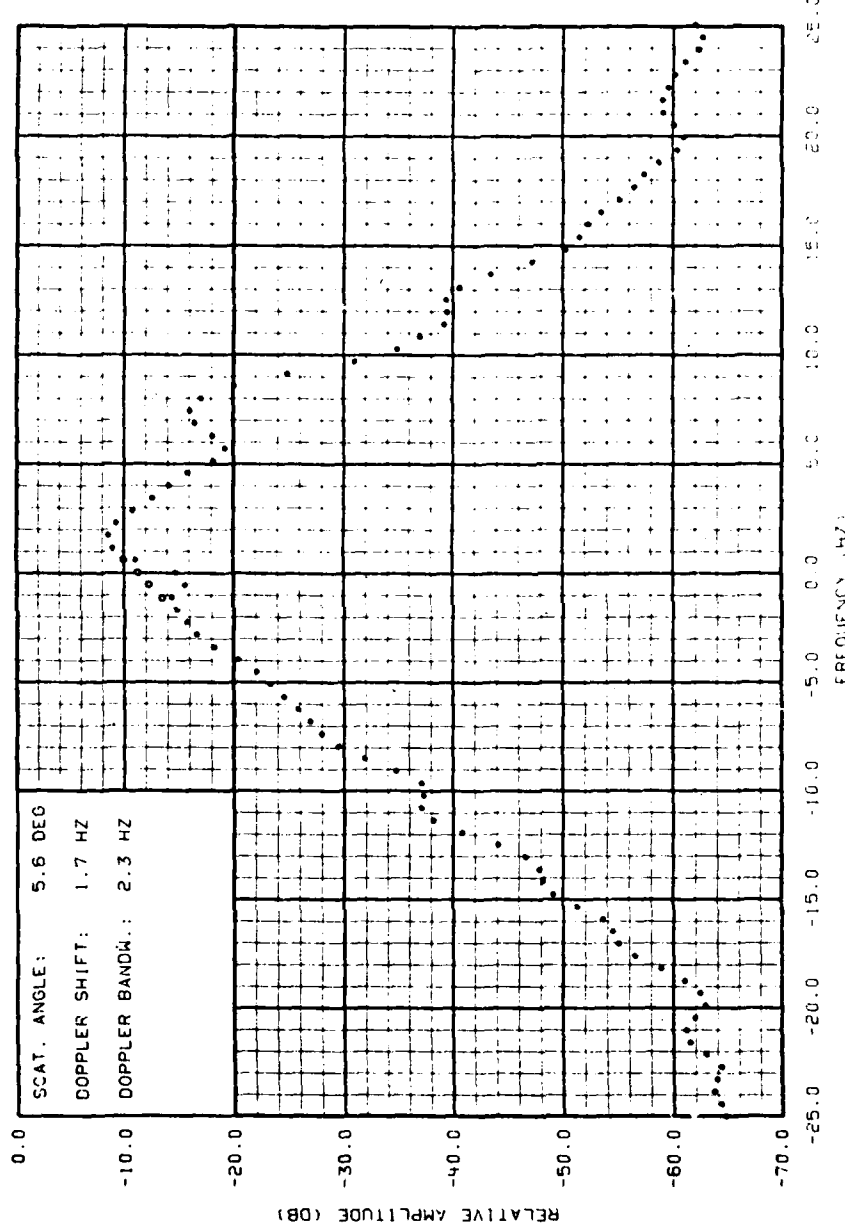


Figure C-3. Doppler Spectrum of Surface Reverberation Obtained at a Transmitted Frequency of 9.0 kHz, an Incident Angle of -4.70° , and an Angle of Scatter of 5.60° . Corrected Spectral Estimates in the Vicinity of Zero Doppler are Represented by Open Circles.

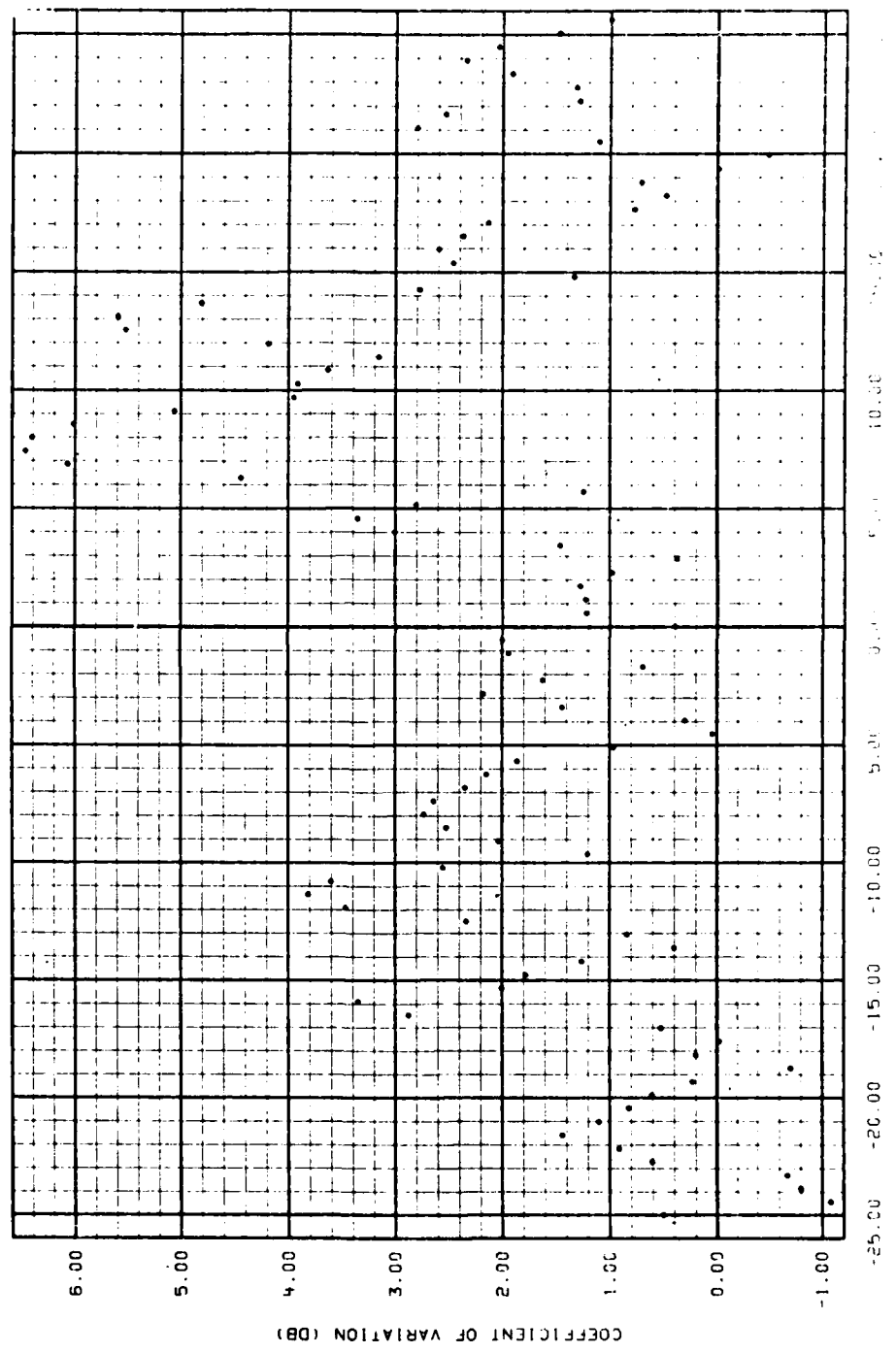


Figure C-4. Coefficients of Variation of the Spectral Estimates Obtained at a Transmitted Frequency of 9.0 kHz, an Incident Angle of -4.70°, and an Angle of Scatter of 5.60°.

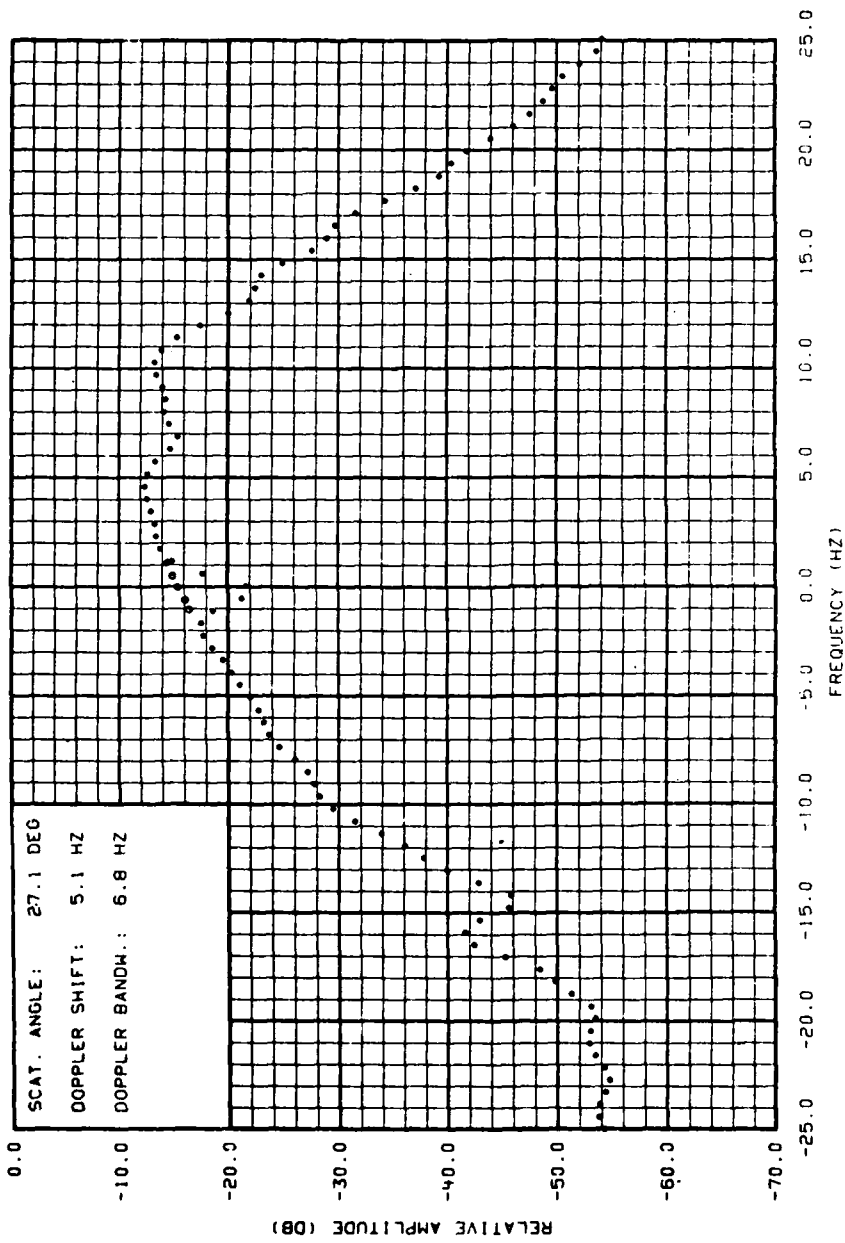


Figure C-5. Doppler Spectrum of Surface Reverberation Obtained at a Transmitted Frequency of 9.0 kHz, an Incident Angle of 20.0°, and an Angle of Scatter of 27.1°. Corrected Spectral Estimates in the Vicinity of Zero Doppler are Represented by Open Circles.

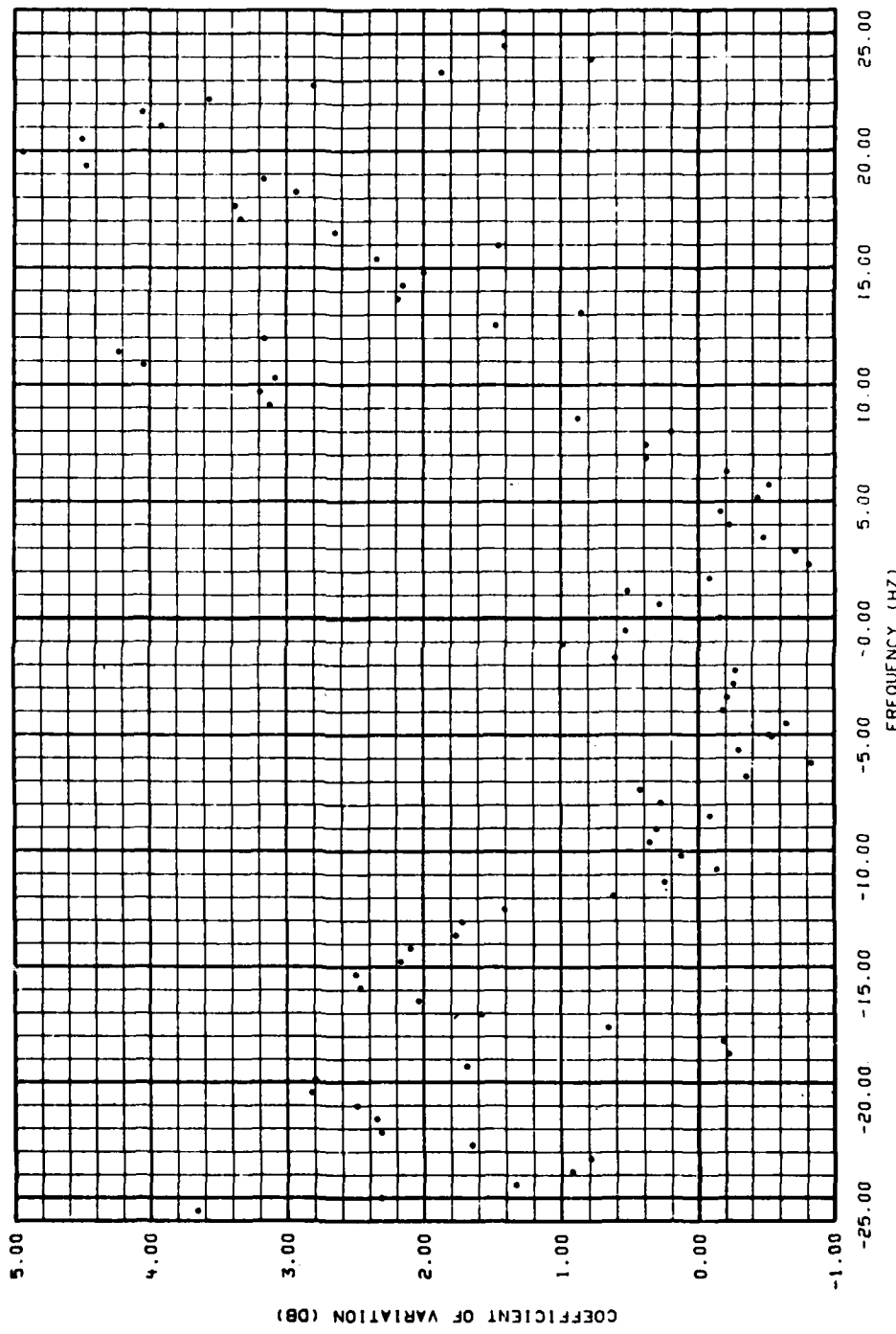


Figure C-6. Coefficients of Variation of the Spectral Estimates Obtained at a Transmitted Frequency of 9.0 kHz, an Incident Angle of 20.00, and an Angle of Scatter of 27.10.

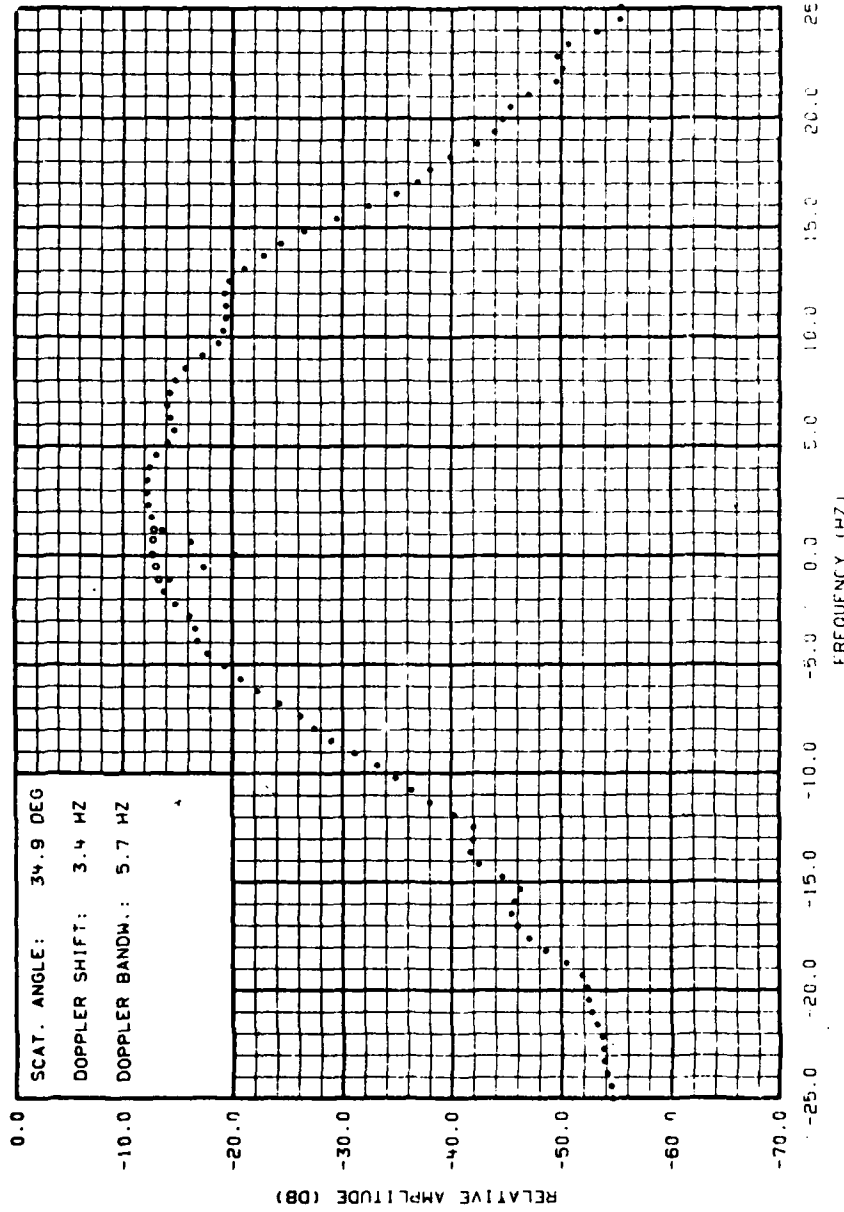


Figure C-7. Doppler Spectrum of Surface Reverberation Obtained at a Transmitted Frequency of 9.0 kHz, an Incident Angle of 20.0°, and an Angle of Scatter of 34.9°. Corrected Spectral Estimates in the Vicinity of Zero Doppler are Represented by Open Circles.

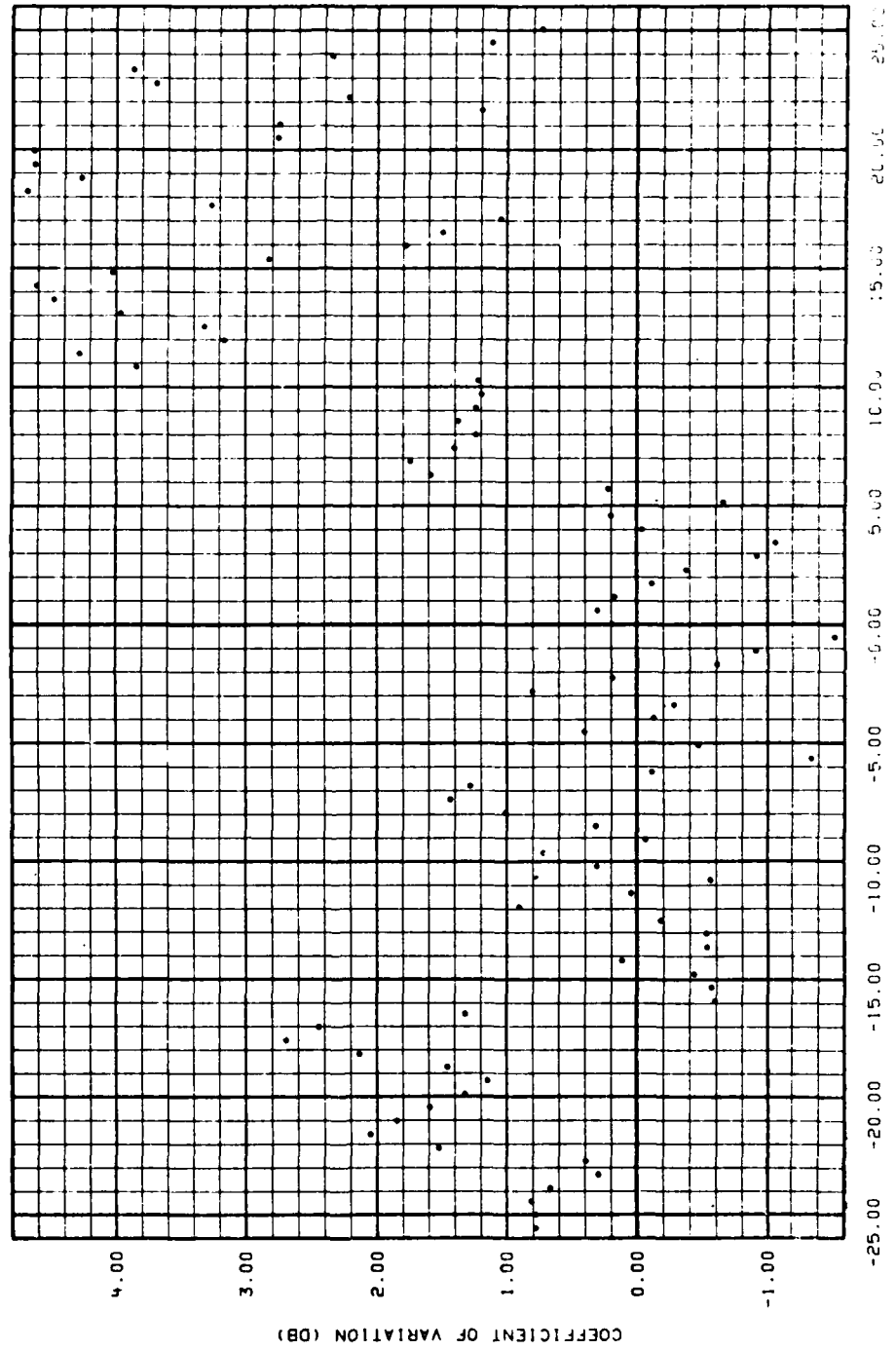


Figure C-8. Coefficients of Variation of the Spectral Estimates Obtained at a Transmitted Frequency of 9.0 kHz, an Incident Angle of 20.0°, and an Angle of Scatter of 34.9°.

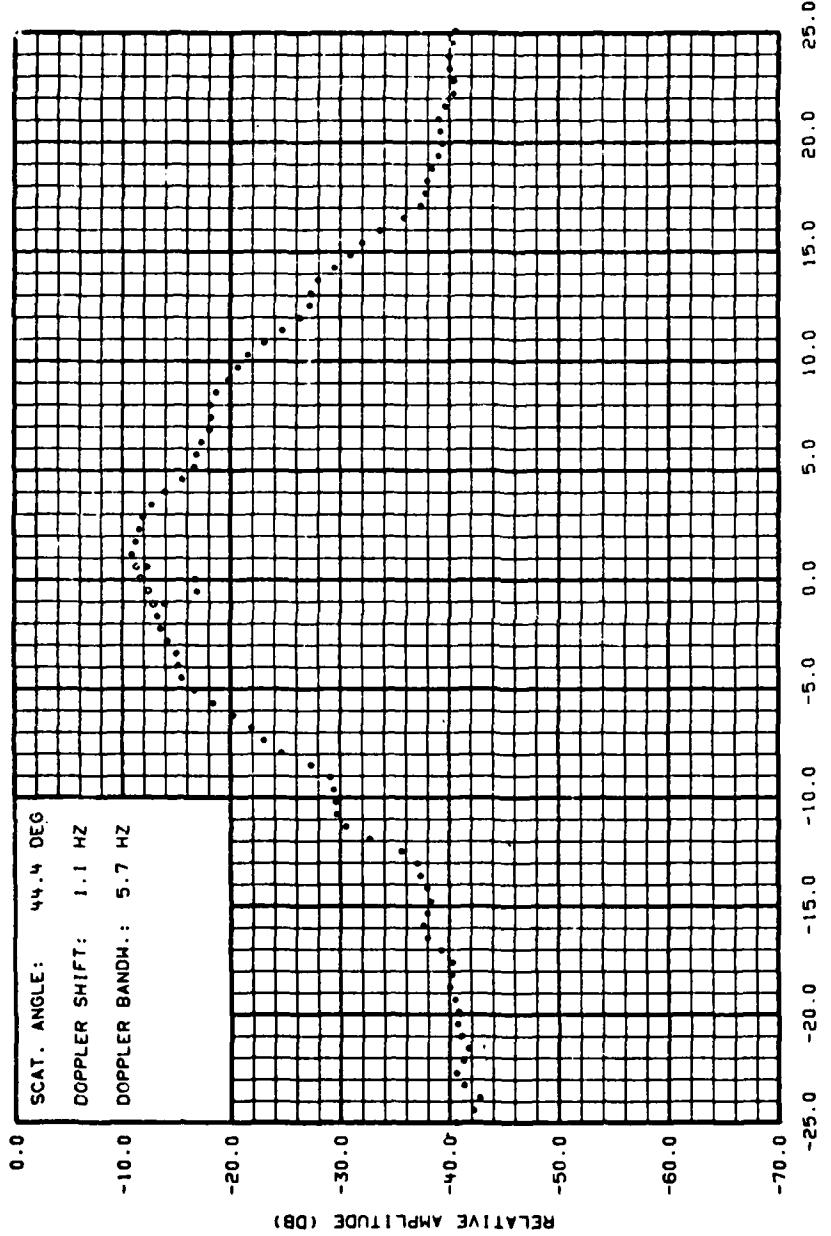


Figure C-9. Doppler Spectrum of Surface Reverberation Obtained at a Transmitted Frequency of 9.0 kHz, an Incident Angle of 40.00, and an Angle of Scatter of 44.40. Corrected Spectral Estimates in the Vicinity of Zero Doppler are Represented by Open Circles.

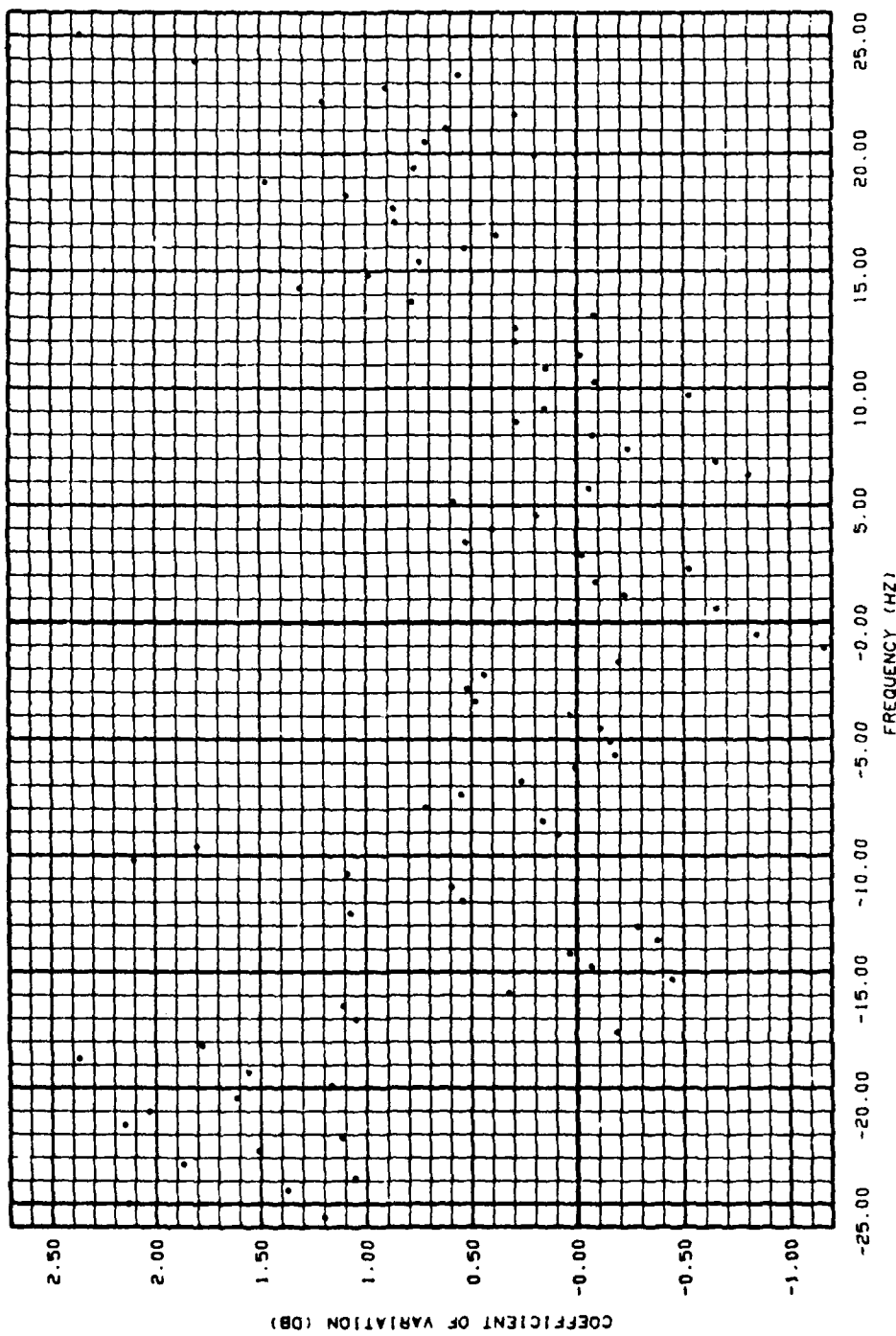


Figure C-10. Coefficients of Variation of the Spectral Estimates Obtained at a Transmitted Frequency of 9.0 kHz, an Incident Angle of 40.00, and an Angle of Scatter of 44.40.

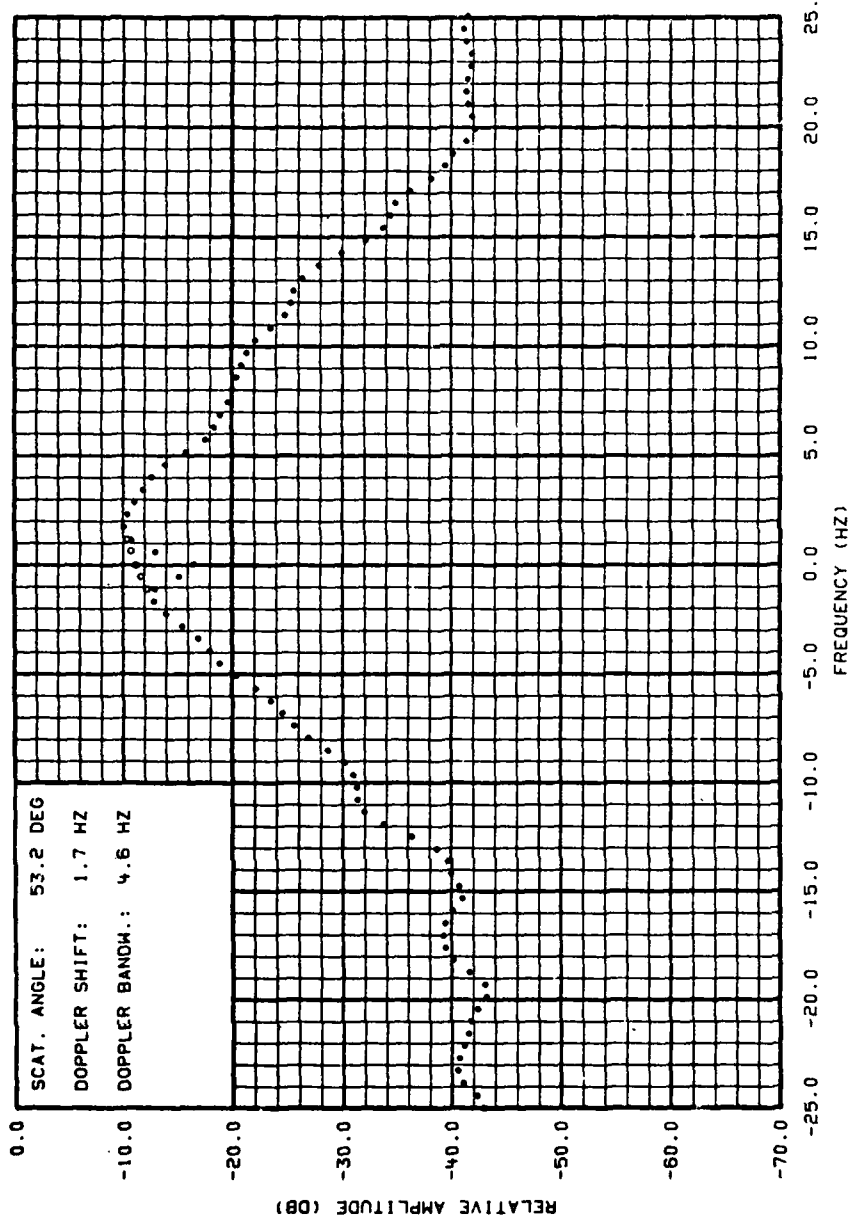


Figure C-11. Doppler Spectrum of Surface Reverberation Obtained at a Transmitted Frequency of 9.0 kHz, an Incident Angle of 40.0°, and an Angle of Scatter of 53.2°. Corrected Spectral Estimates in the Vicinity of Zero Doppler are Represented by Open Circles.

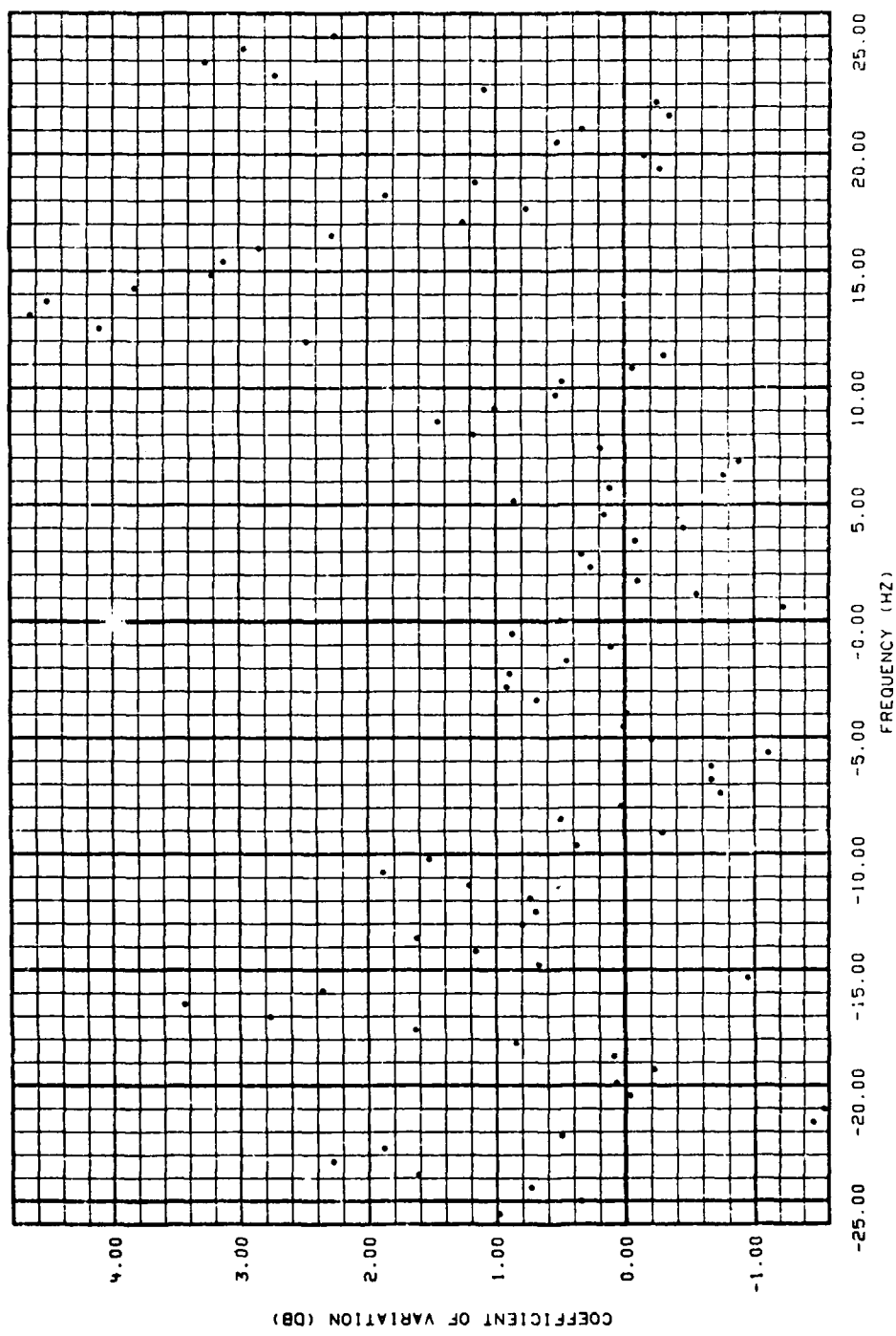


Figure C-12. Coefficients of Variation of the Spectral Estimates Obtained at a Transmitted Frequency of 9.0 kHz, an Incident Angle of 40.0°, and an Angle of Scatter of 53.2°.

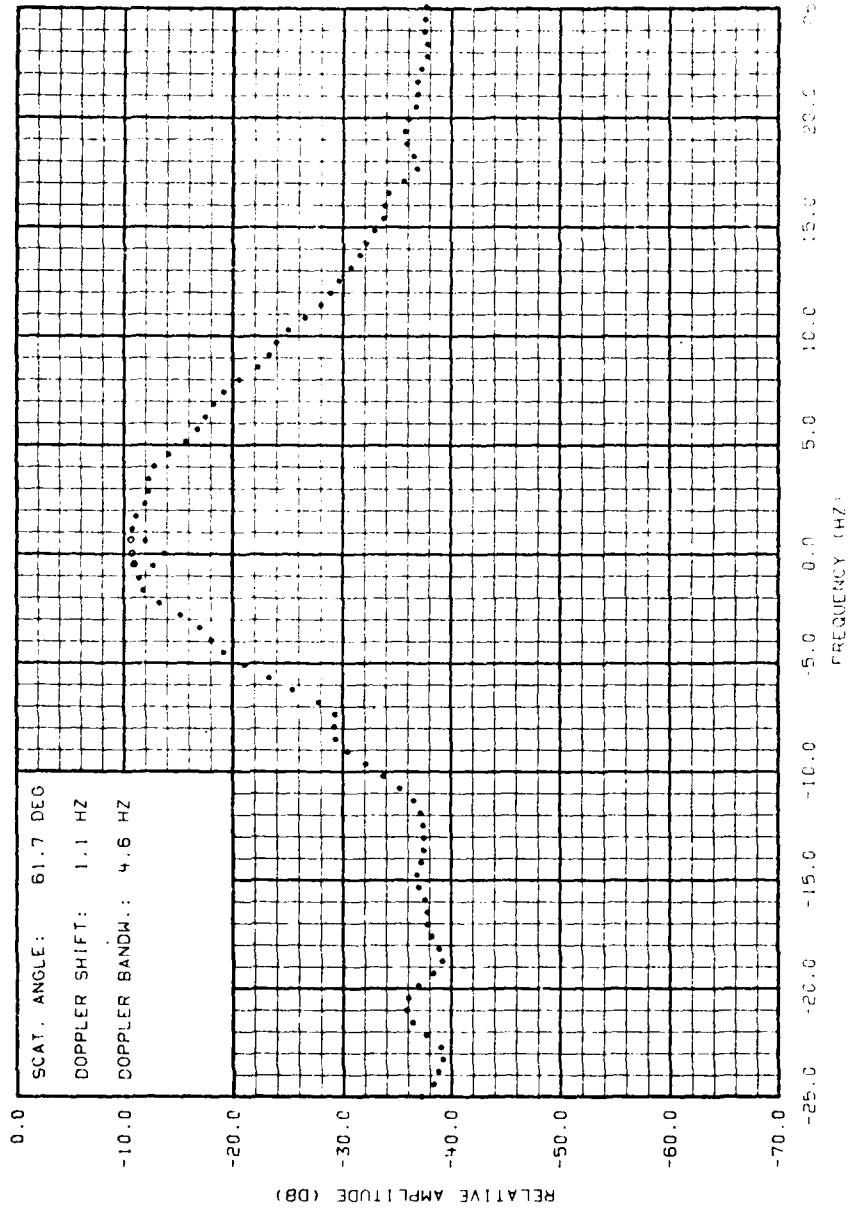


Figure C-13. Doppler Spectrum of Surface Reverberation Obtained at a Transmitted Frequency of 9.0 kHz, an Incident Angle of 60.0°, and an Angle of Scatter of 61.7°. Corrected Spectral Estimates in the Vicinity of Zero Doppler are Represented by Open Circles.

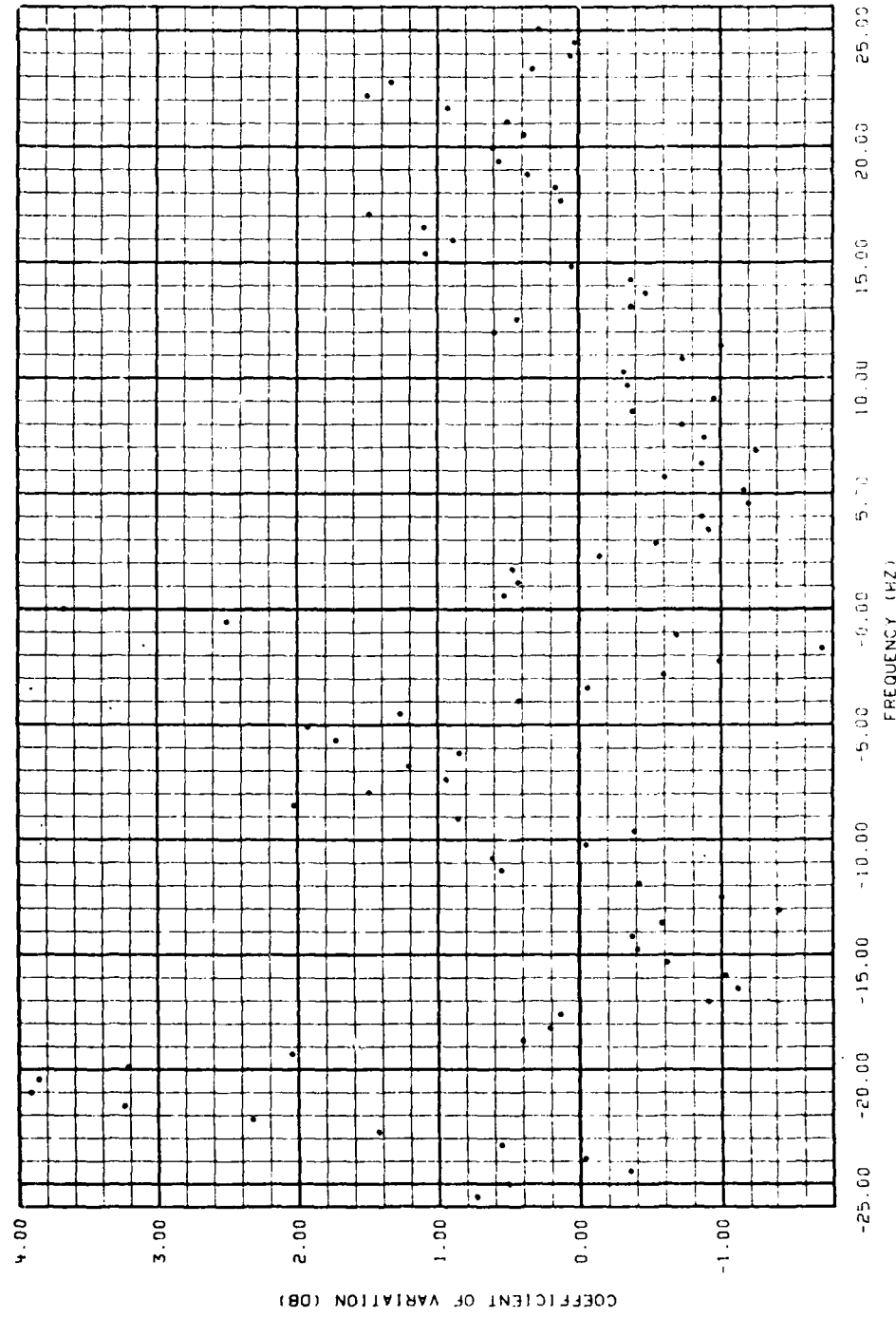


Figure C-14. Coefficients of Variation of the Spectral Estimates Obtained at a Transmitted Frequency of 9.0 kHz, an Incident Angle of 60.0° , and an Angle of Scatter of 61.70° .

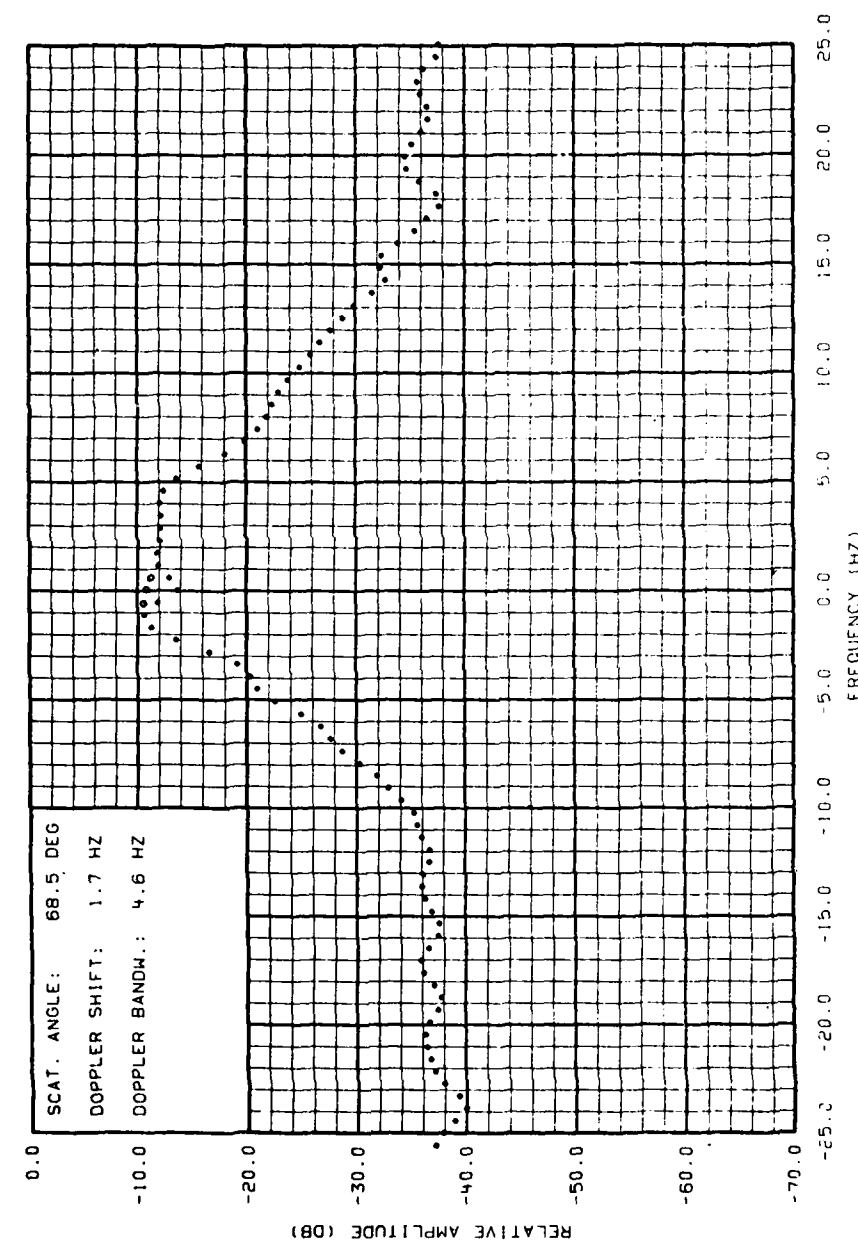


Figure C-15. Doppler Spectrum of Surface Reverberation Obtained at a Transmitted Frequency of 9.0 kHz, an Incident Angle of 60.0°, and an Angle of Scatter of 68.5°. Corrected Spectral Estimates in the Vicinity of Zero Doppler are Represented by Open Circles.

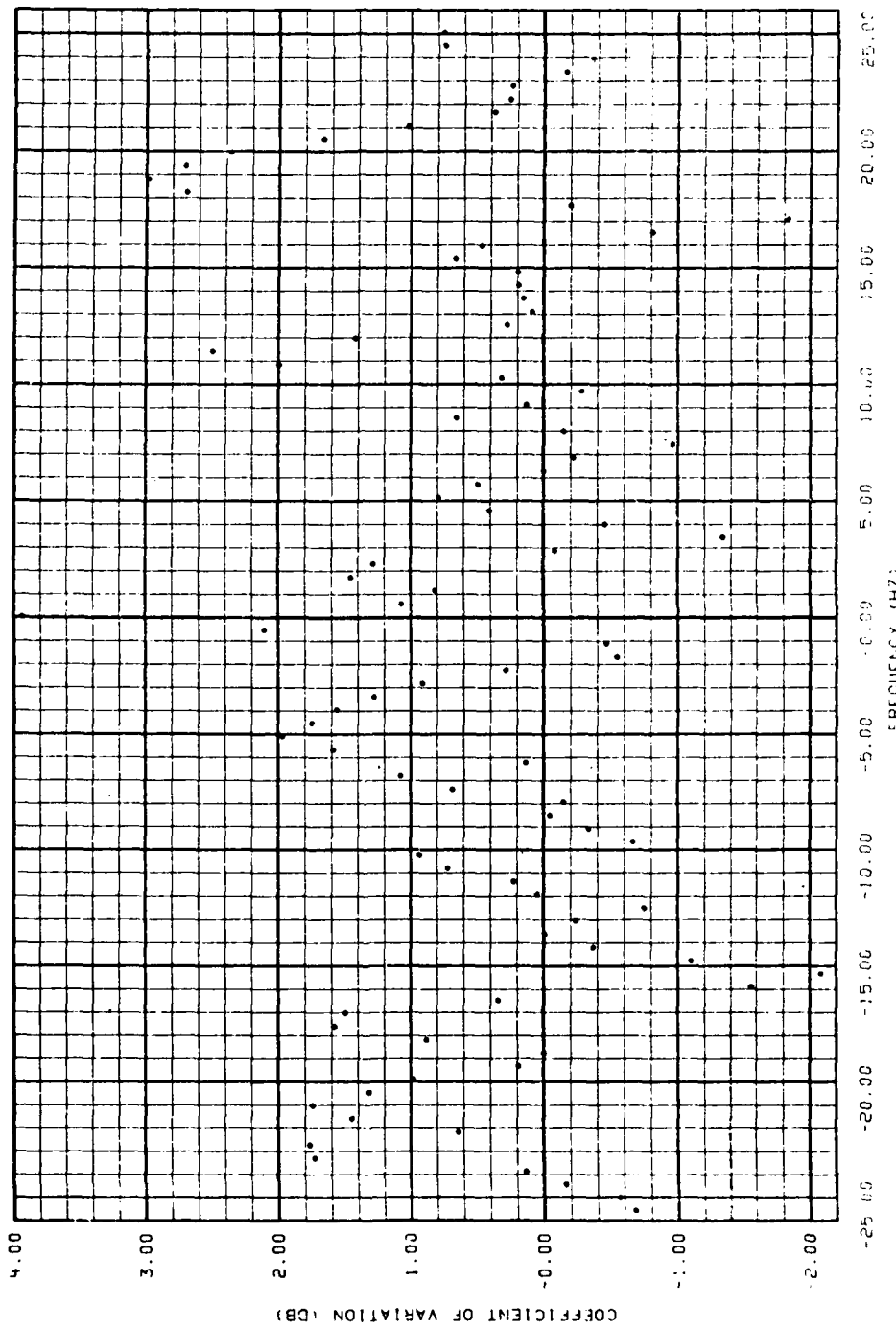


Figure C-16. Coefficients of Variation of the Spectral Estimates Obtained at a Transmitted Frequency of 9.0 kHz, an Incident Angle of 60.0°, and an Angle of Scatter of 68.5°.

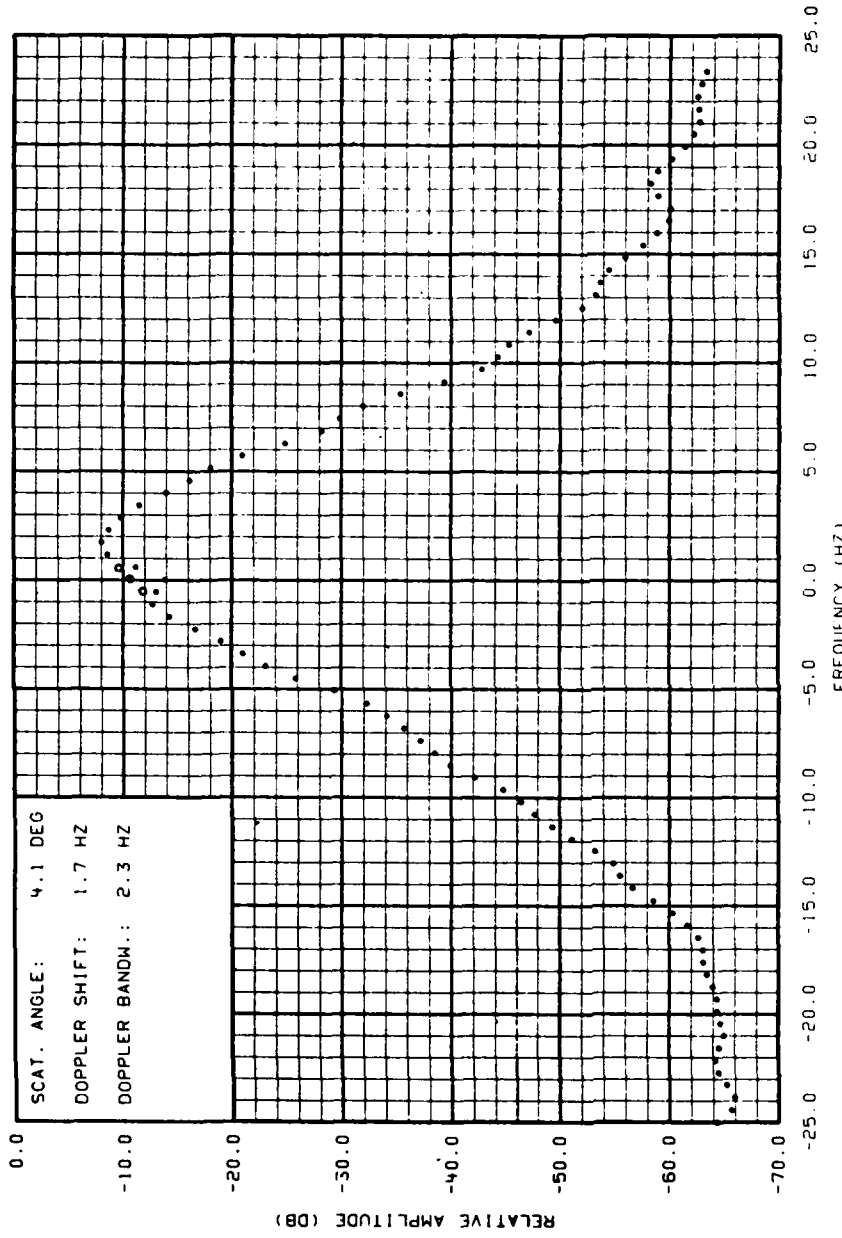


Figure C-17. Doppler Spectrum of Surface Reverberation Obtained at a Transmitted Frequency of 7.0 kHz, an Incident Angle of -4.7°, and an Angle of Scatter of 4.1°. Corrected Spectral Estimates in the Vicinity of Zero Doppler are Represented by Open Circles.

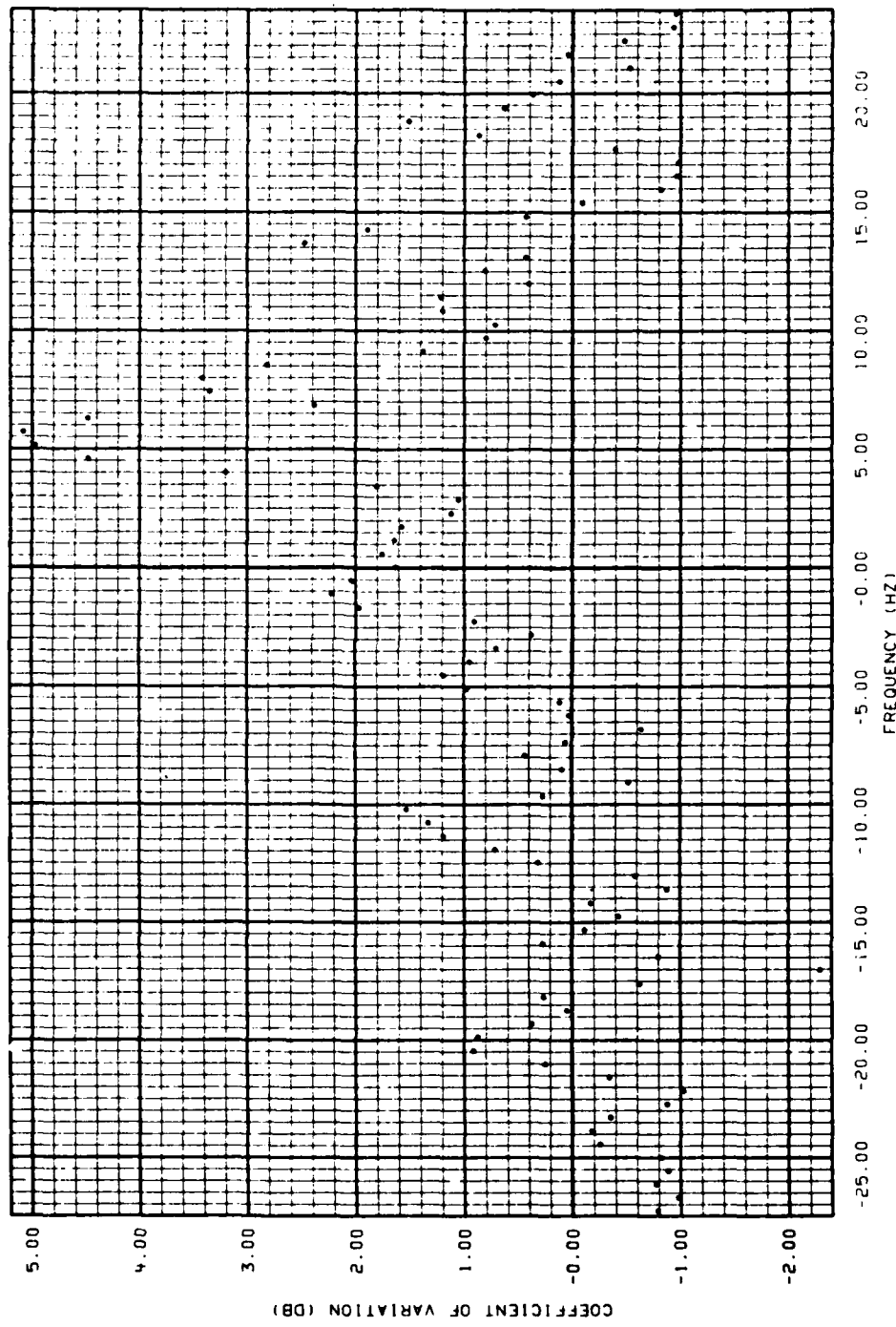


Figure C-18. Coefficients of Variation of the Spectral Estimates Obtained at a Transmitted Frequency of 7.0 kHz, an Incident Angle of -4.7°, and an Angle of Scatter of 4.1°.

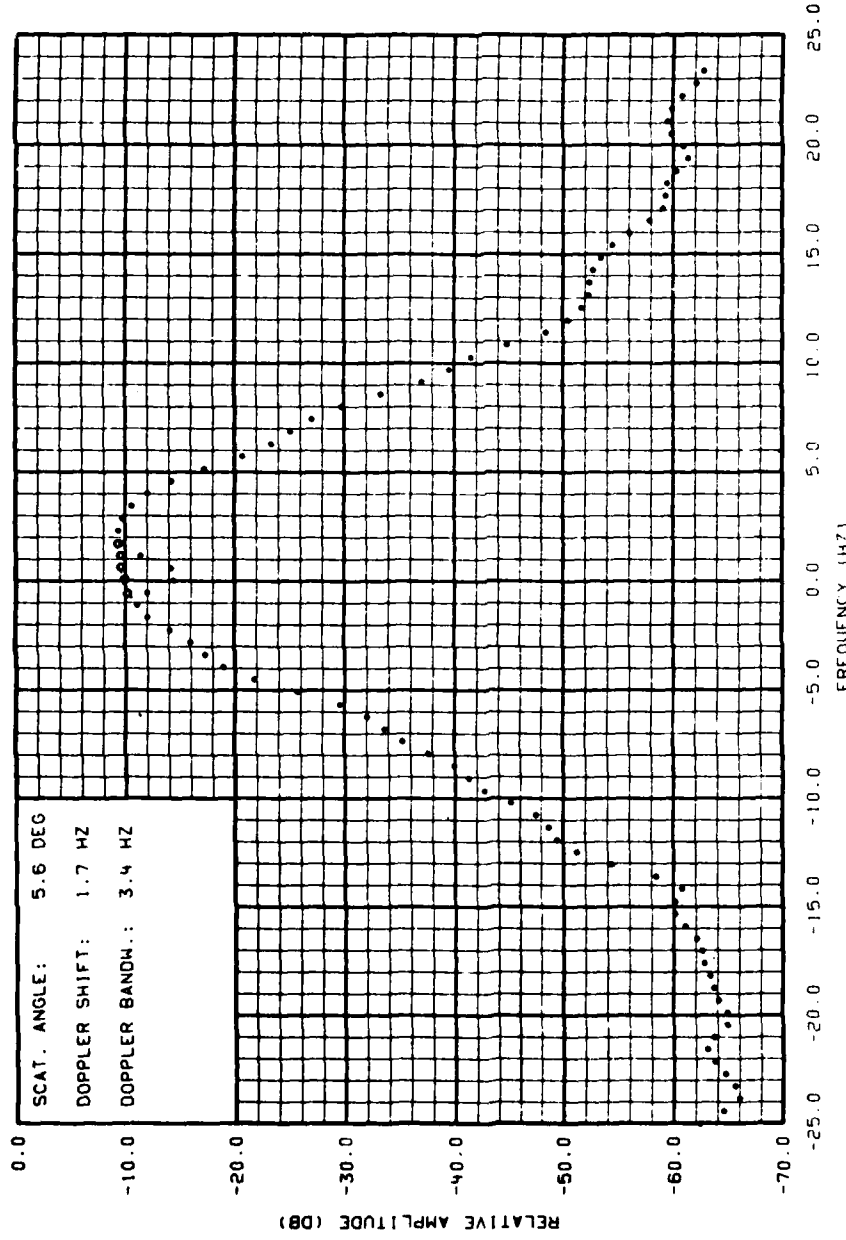


Figure C-19. Doppler Spectrum of Surface Reverberation Obtained at a Transmitted Frequency of 7.0 kHz, an Incident Angle of -4.70, and an Angle of Scatter of 5.60. Corrected Spectral Estimates in the Vicinity of Zero Doppler are Represented by Open Circles.

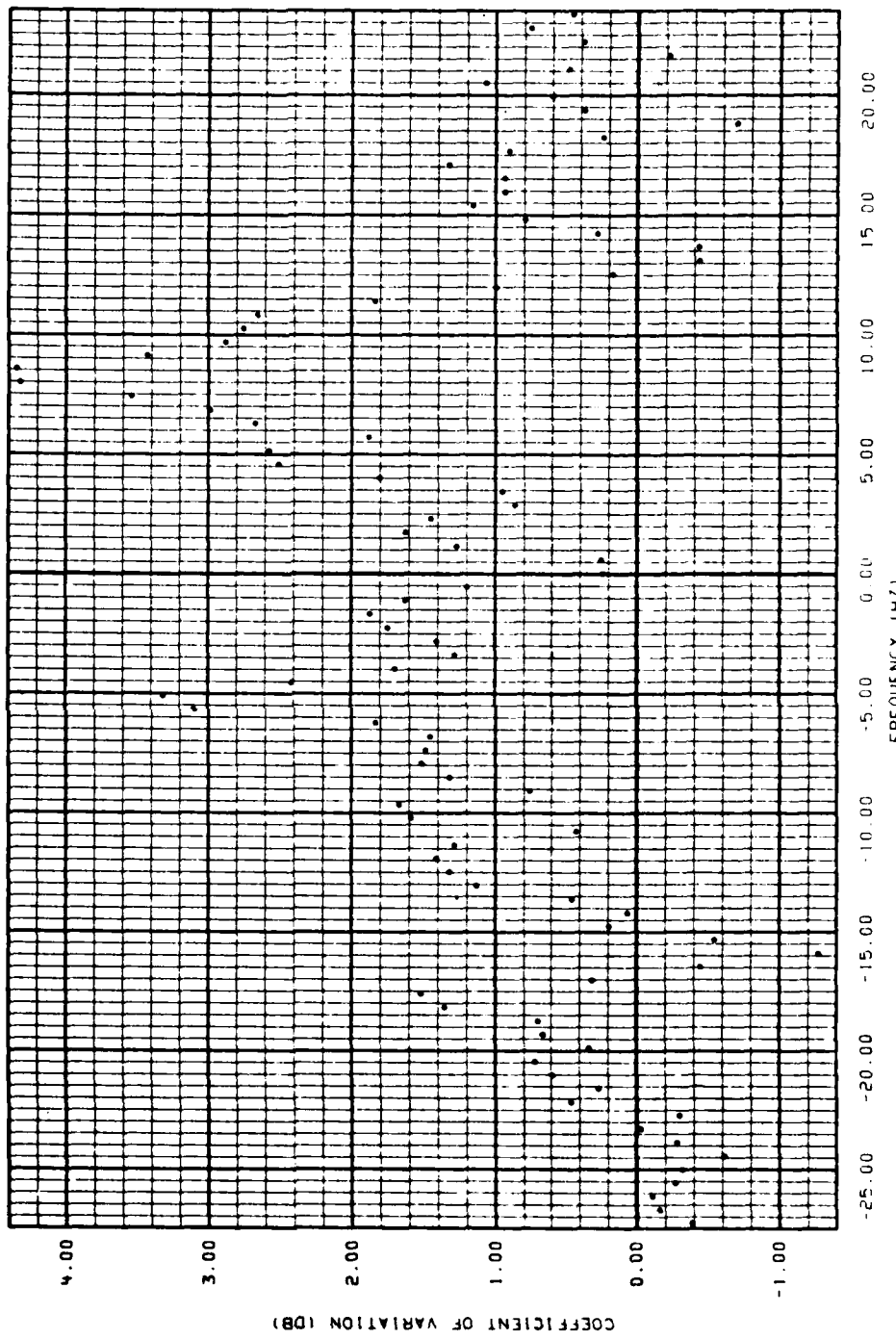


Figure C-20. Coefficients of Variation of the Spectral Estimates Obtained at a Transmitted Frequency of 7.0 kHz, and Incident Angle of -4.7° , and an Angle of Scatter of 5.60° .

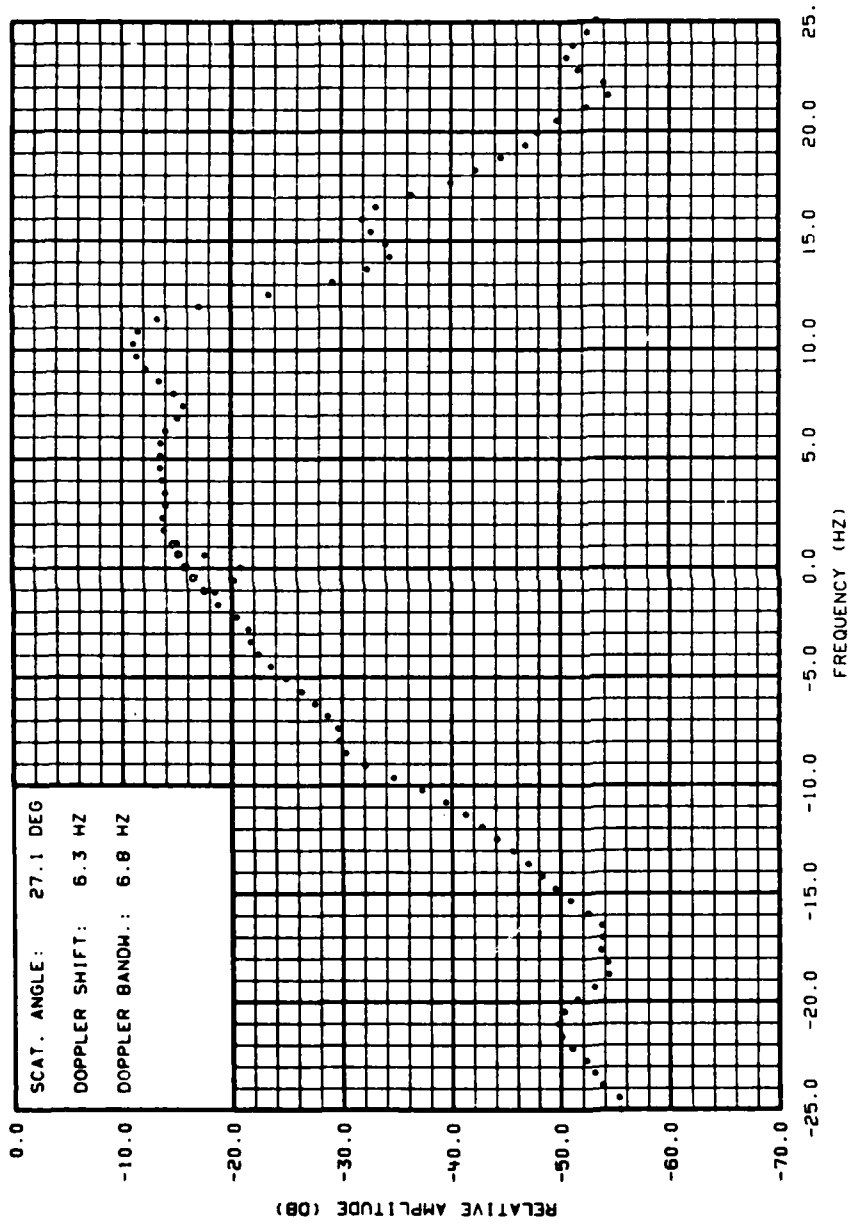


Figure C-21. Doppler Spectrum of Surface Reverberation Obtained at a Transmitted Frequency of 7.0 kHz, an Incident Angle of 20.0°, and an Angle of Scatter of 27.1°. Corrected Spectral Estimates in the Vicinity of Zero Doppler are Represented by Open Circles.

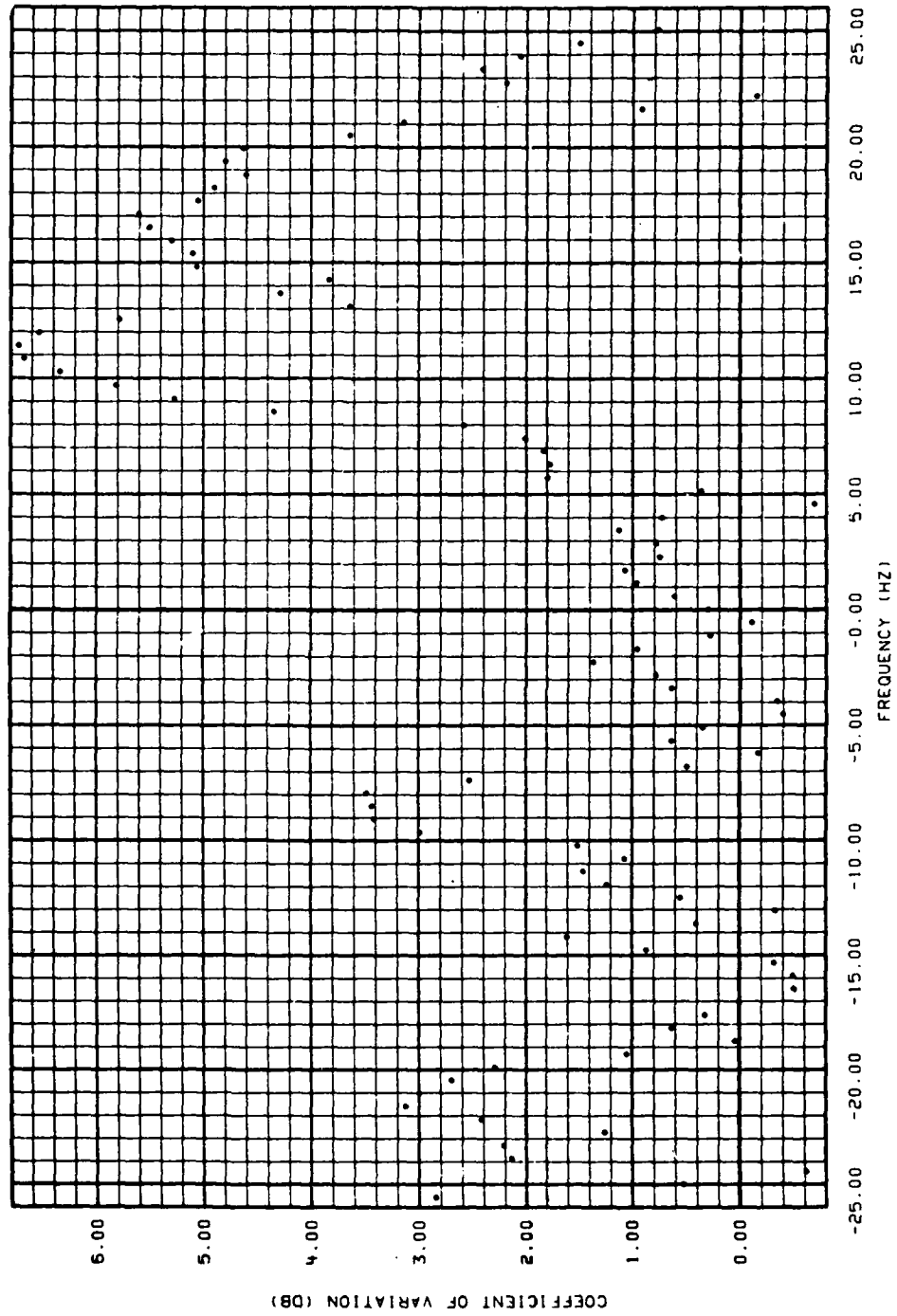


Figure C-22. Coefficients of Variation of the Spectral Estimates Obtained at a Transmitted Frequency of 7.0 kHz, an Incident Angle of 20.00° , and an Angle of Scatter of 27.10° .

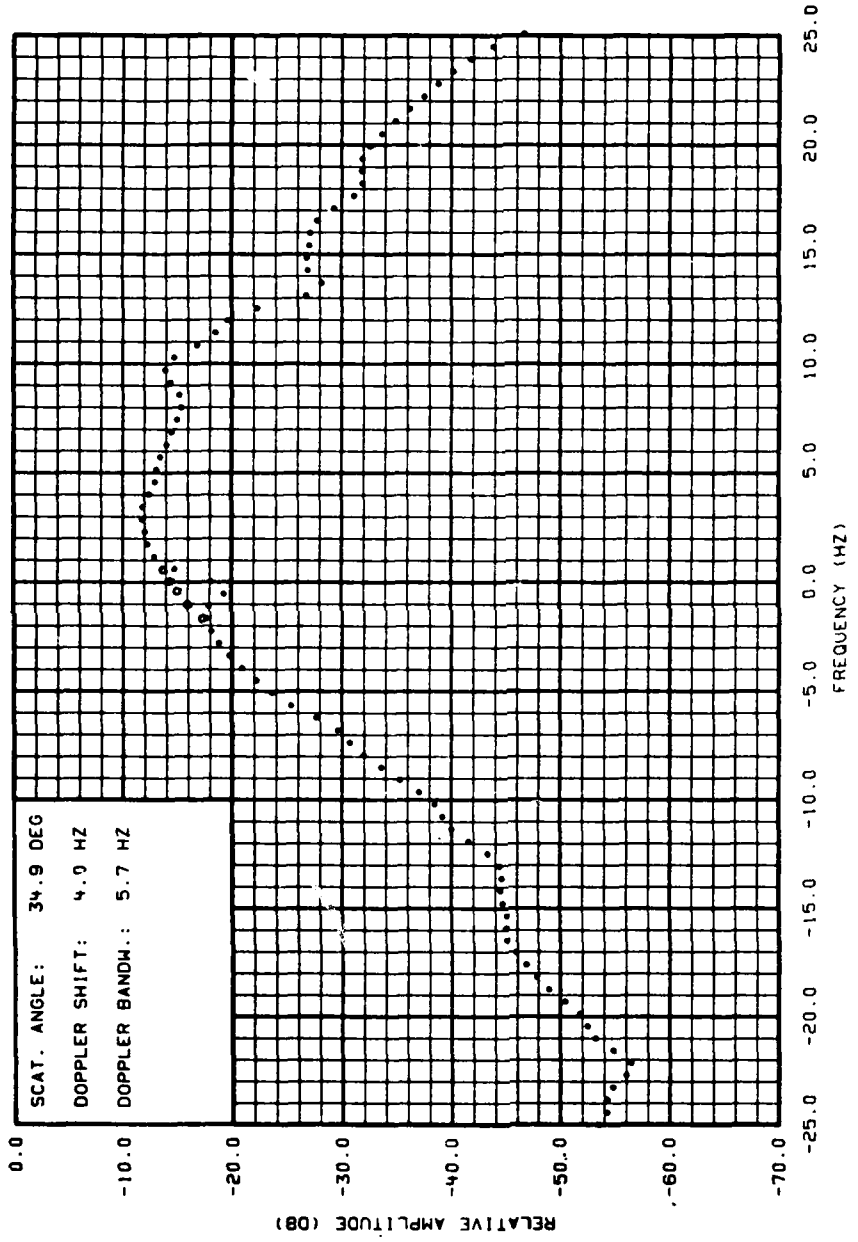


Figure C-23. Doppler Spectrum of Surface Reverberation Obtained at a Transmitted Frequency of 7.0 kHz, an Incident Angle of 20.0°, and an Angle of Scatter of 34.9°. Corrected Spectral Estimates in the Vicinity of Zero Doppler are Represented by Open Circles.

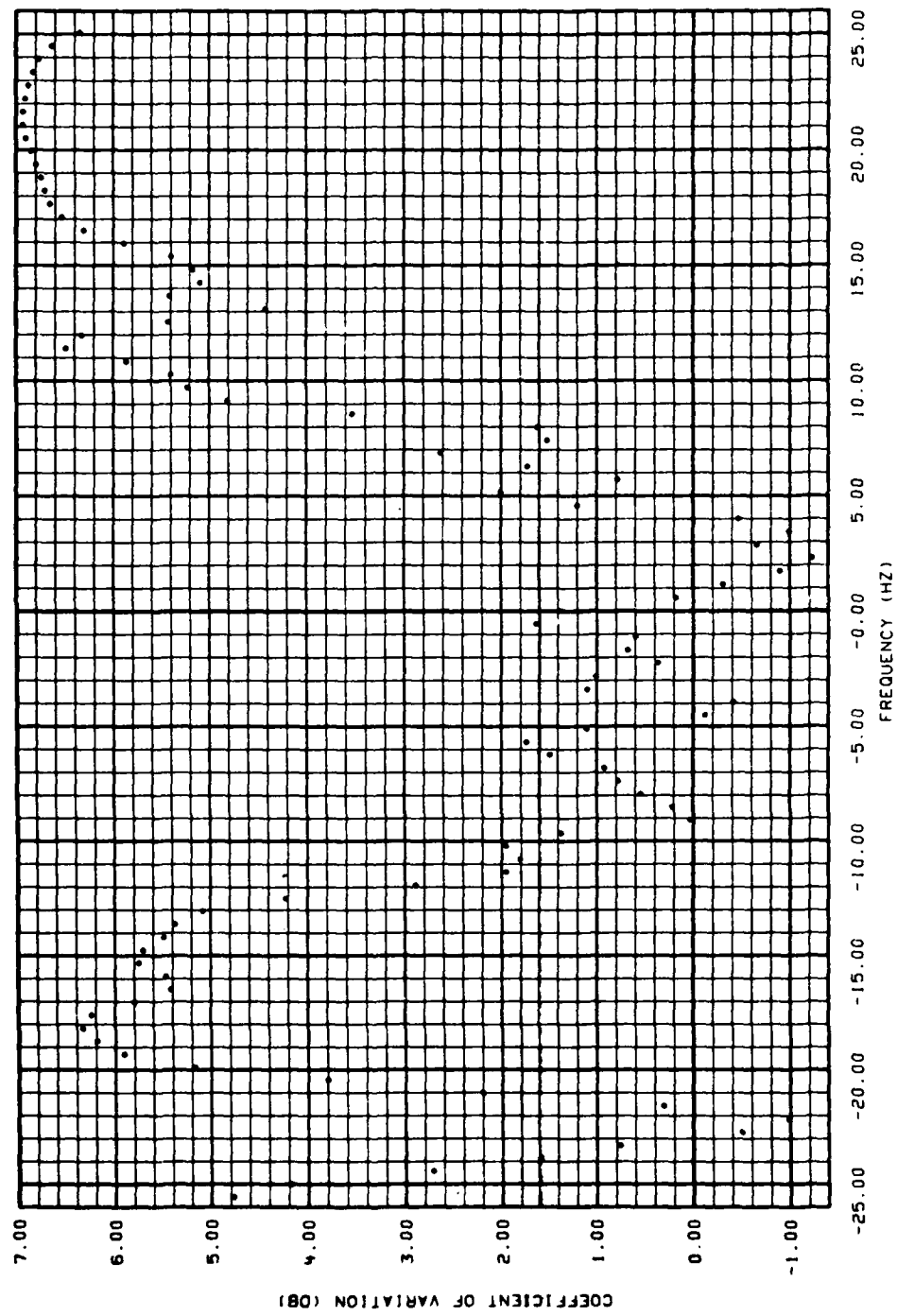


Figure C-24. Coefficients of Variation of the Spectral Estimates Obtained at a Transmitted Frequency of 7.0 kHz, an Incident Angle of 20.0°, and an Angle of Scatter of 34.9°.

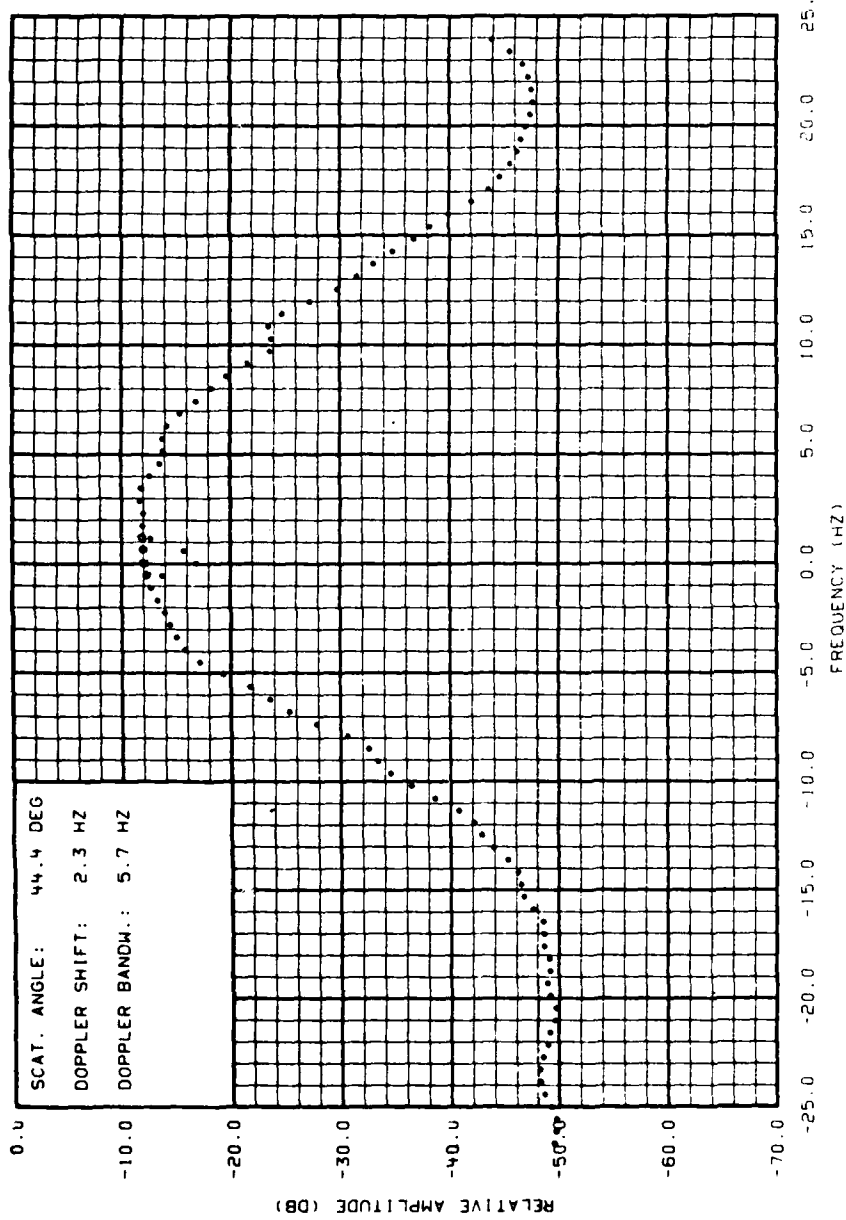


Figure C-25. Doppler Spectrum of Surface Reverberation Obtained at a Transmitted Frequency of 7.0 kHz, an Incident Angle of 40.0°, and an Angle of Scatter of 44.4°. Corrected Spectral Estimates in the Vicinity of Zero Doppler are Represented by Open Circles.

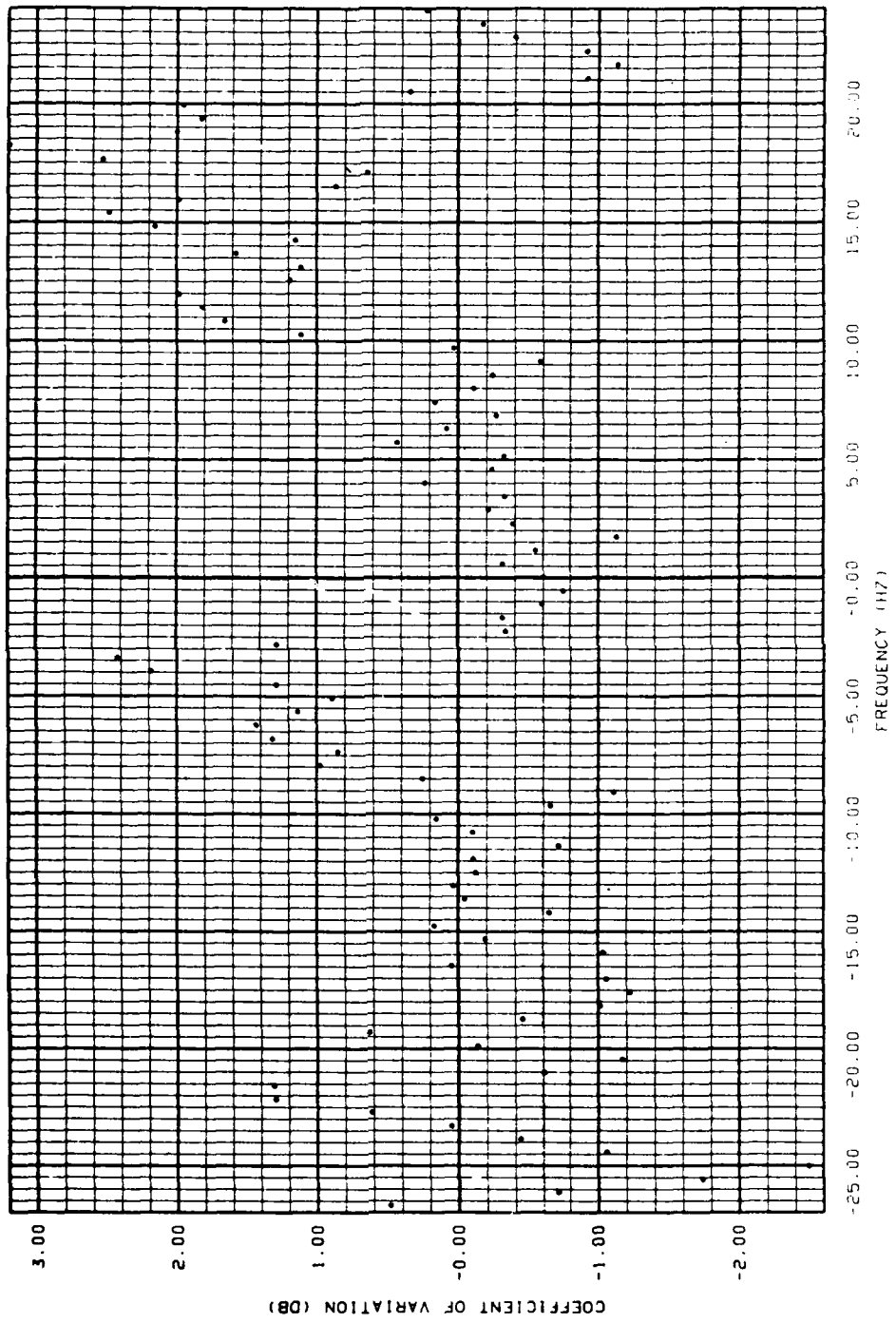


Figure C-26. Coefficients of Variation of the Spectral Estimates Obtained at a Transmitted Frequency of 7.0 kHz, an Incident Angle of 40.0° , and an Angle of Scatter of 44.40° .

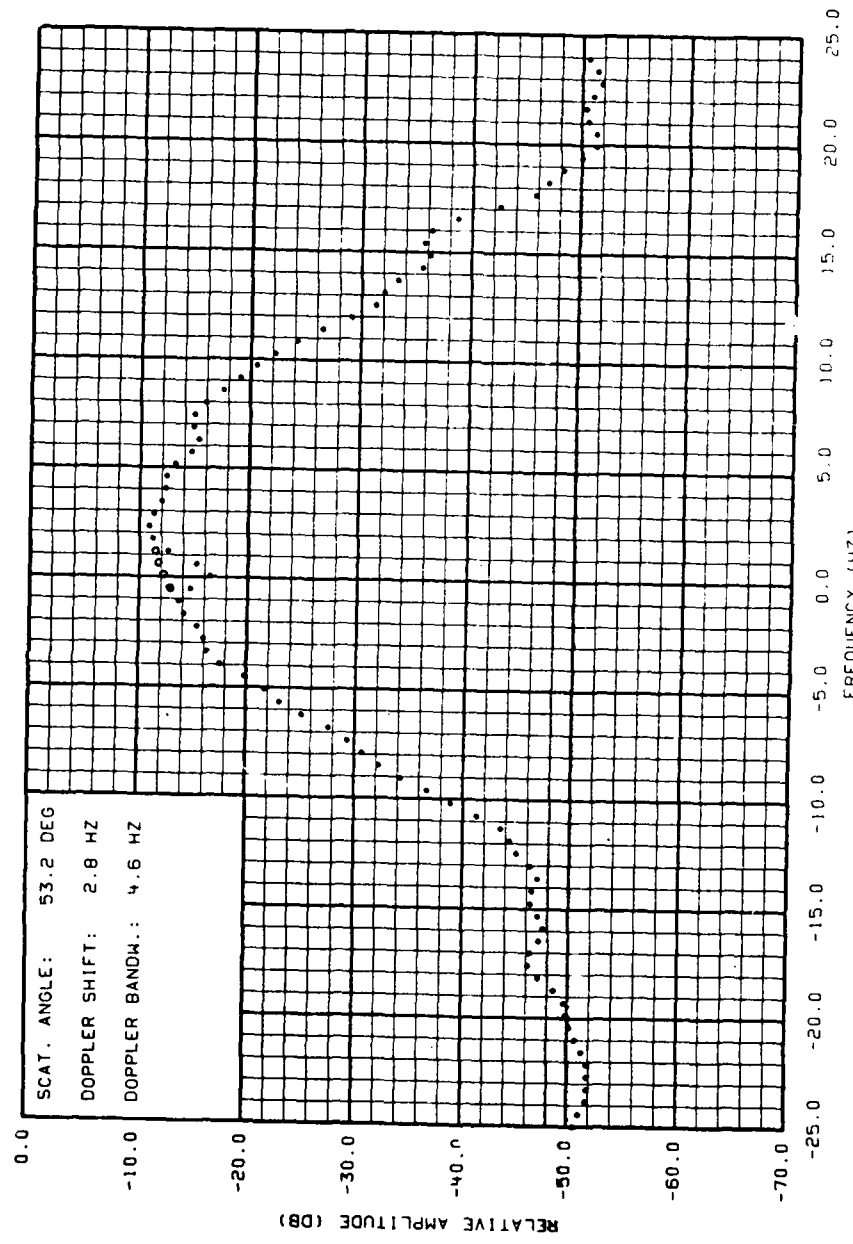


Figure C-27. Doppler Spectrum of Surface Reverberation Obtained at a Transmitted Frequency of 7.0 kHz, an Incident Angle of 40.0°, and an Angle of Scatter of 53.2°. Corrected Spectral Estimates in the Vicinity of Zero Doppler are Represented by Open Circles.

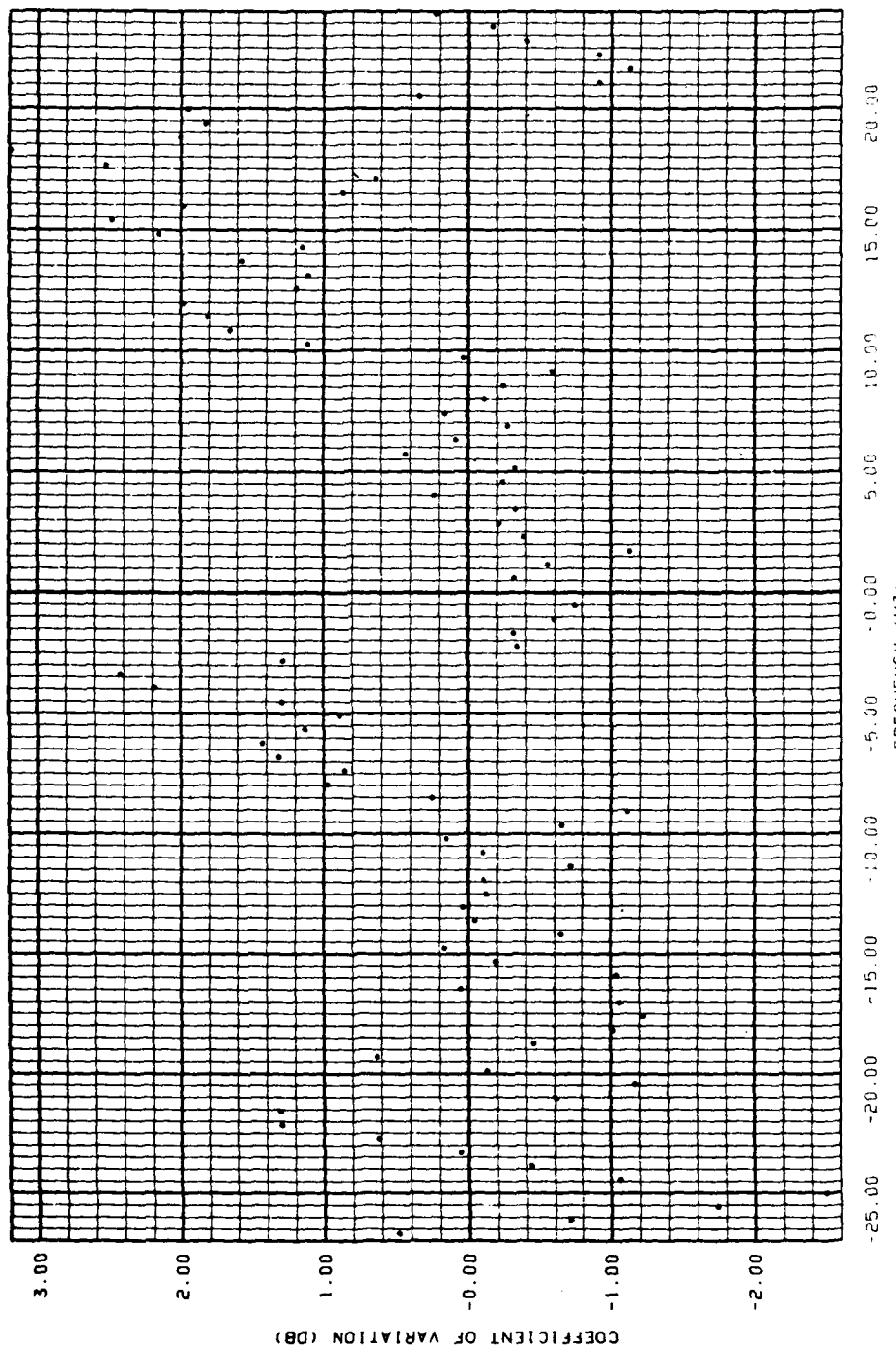


Figure C-26. Coefficients of Variation of the Spectral Estimates Obtained at a Transmitted Frequency of 7.0 kHz, an Incident Angle of 40.0° , and an Angle of Scatter of 44.4° .

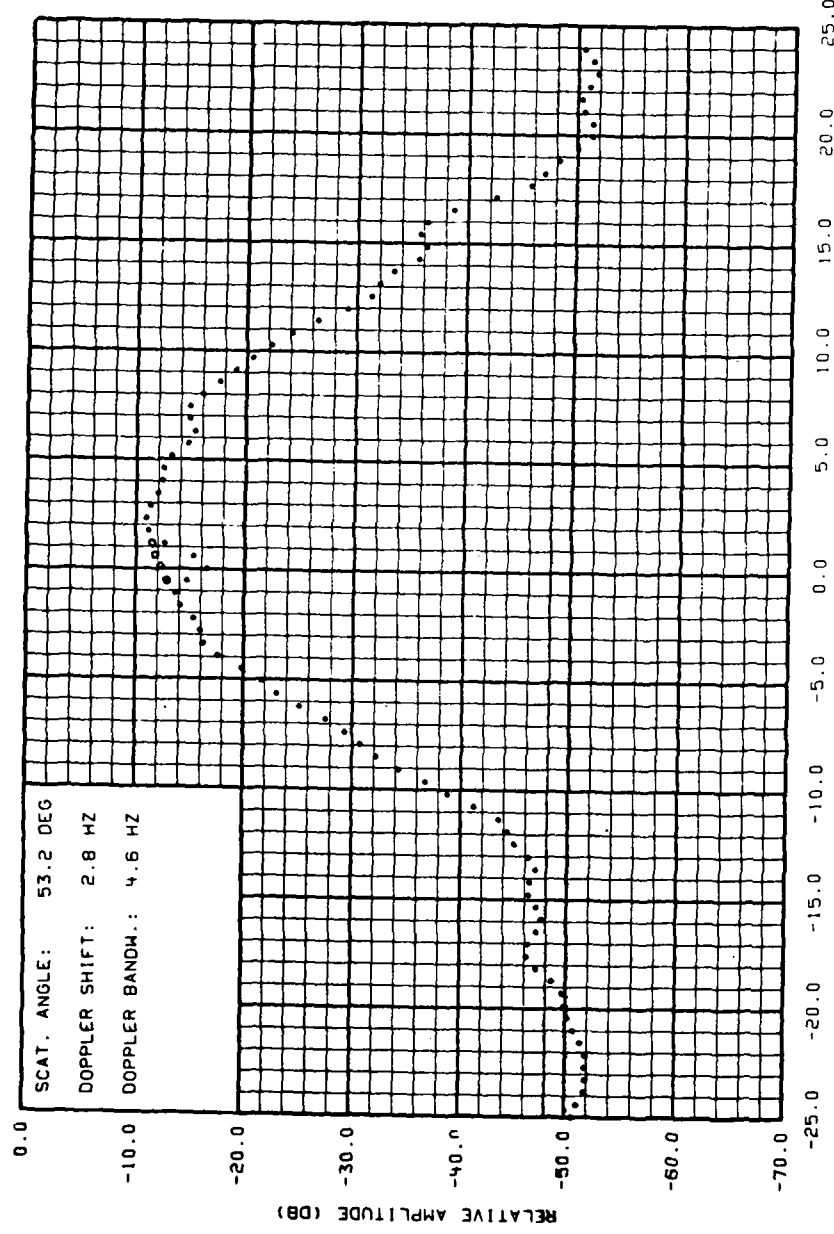


Figure C-27. Doppler Spectrum of Surface Reverberation Obtained at a Transmitted Frequency of 7.0 kHz, an Incident Angle of 40.0° , and an Angle of Scatter of 53.2° . Corrected Spectral Estimates in the Vicinity of Zero Doppler are Represented by Open Circles.

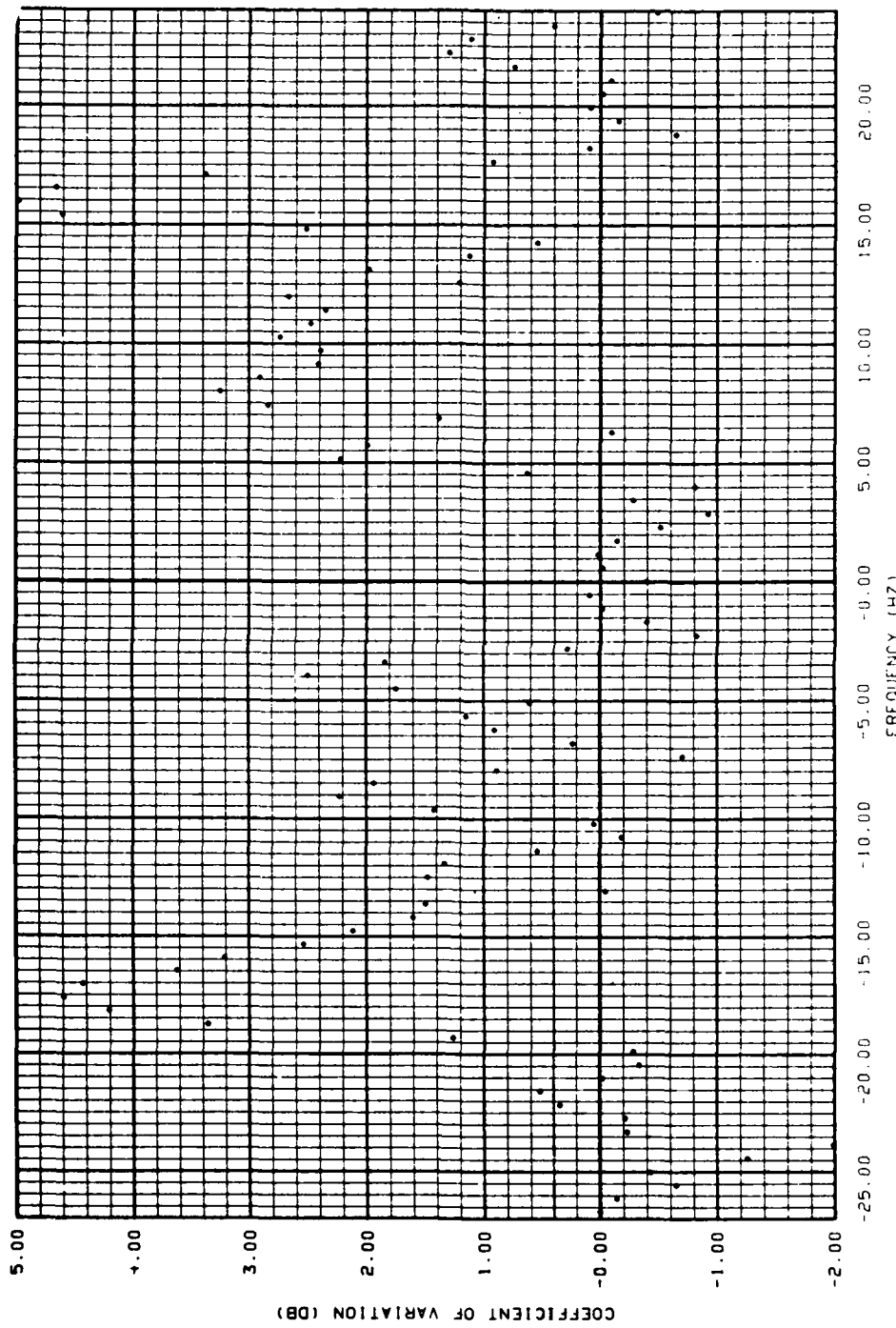


Figure C-28. Coefficients of Variation of the Spectral Estimates Obtained at a Transmitted Frequency of 7.0 kHz, an Incident Angle of 40.00, and an Angle of Scatter of 53.20.

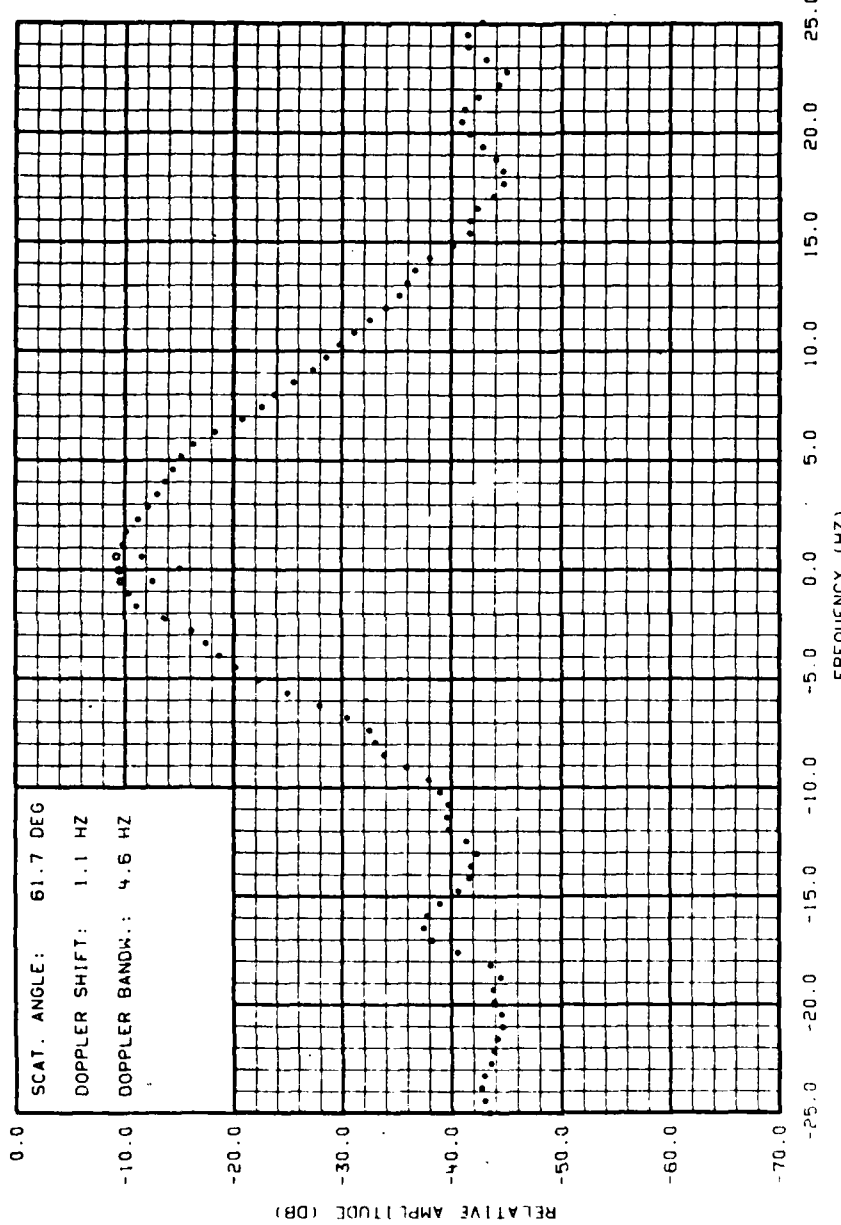


Figure C-29. Doppler Spectrum of Surface Reverberation Obtained at a Transmitted Frequency of 7.0 kHz, an Incident Angle of 60.0°, and an Angle of Scatter of 61.7°. Corrected Spectral Estimates in the Vicinity of Zero Doppler are Represented by Open Circles.

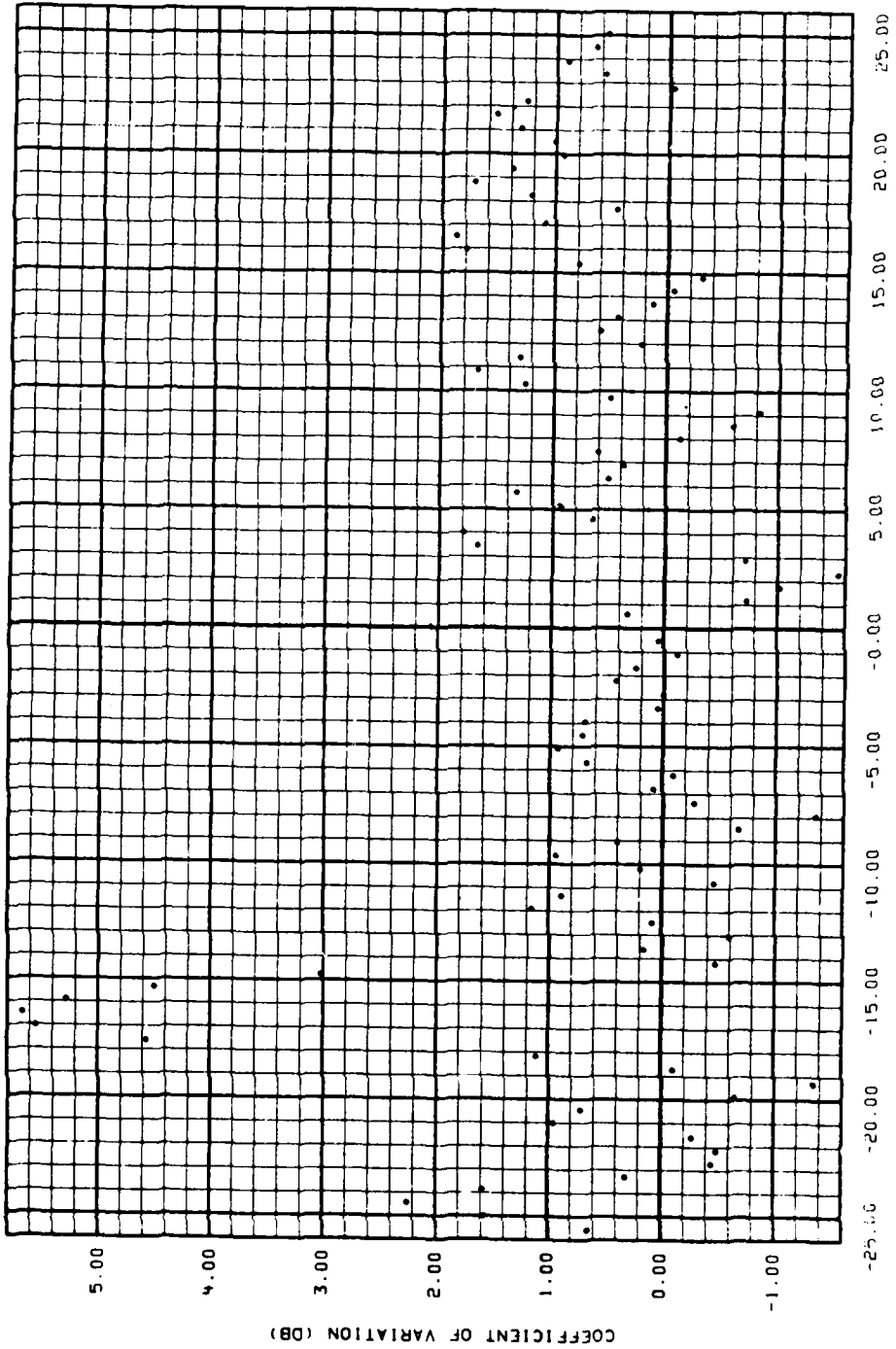


Figure C-30. Coefficients of Variation of the Spectral Estimates Obtained at a Transmitted Frequency of 7.0 kHz, an Incident Angle of 60.00° , and an Angle of Scatter of 61.70° .

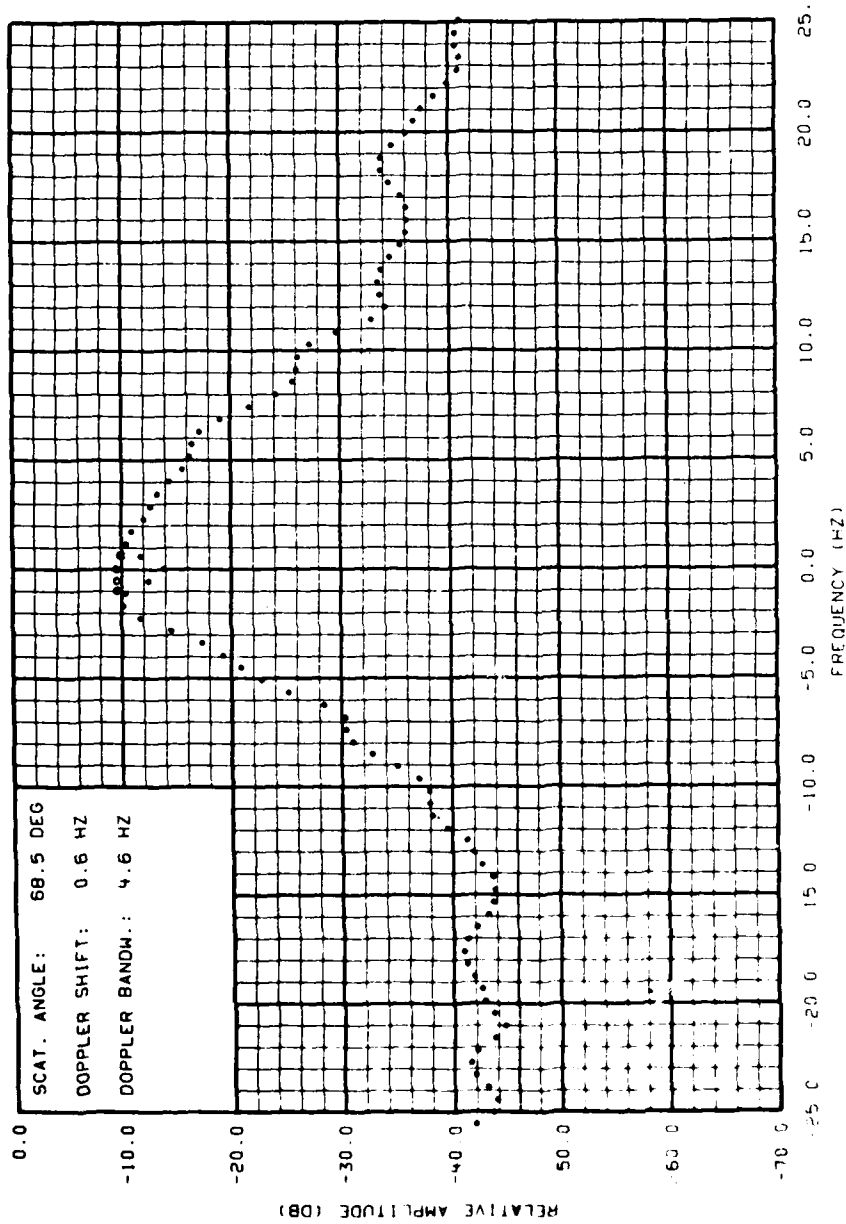


Figure C-31. Doppler Spectrum of Surface Reverberation Obtained at a Transmitted Frequency of 7.0 kHz, an Incident Angle of 60.0°, and an Angle of Scatter of 68.5°. Corrected Spectral Estimates in the Vicinity of Zero Doppler are Represented by Open Circles.

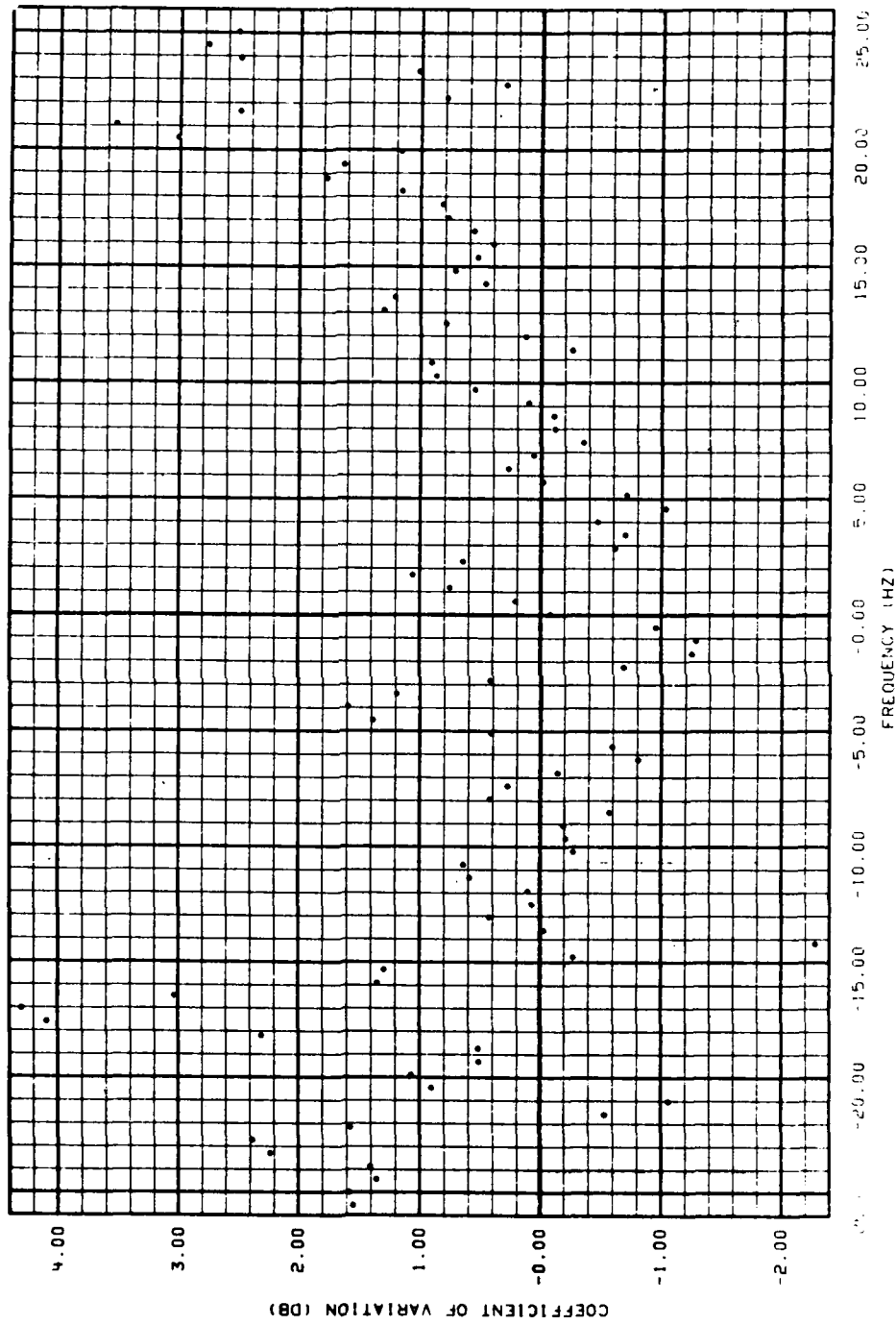


Figure C-32. Coefficients of Variation of the Spectral Estimates Obtained at a Transmitted Frequency of 7.0 kHz, an Incident Angle of 60.00°, and an Angle of Scatter of 68.50°.

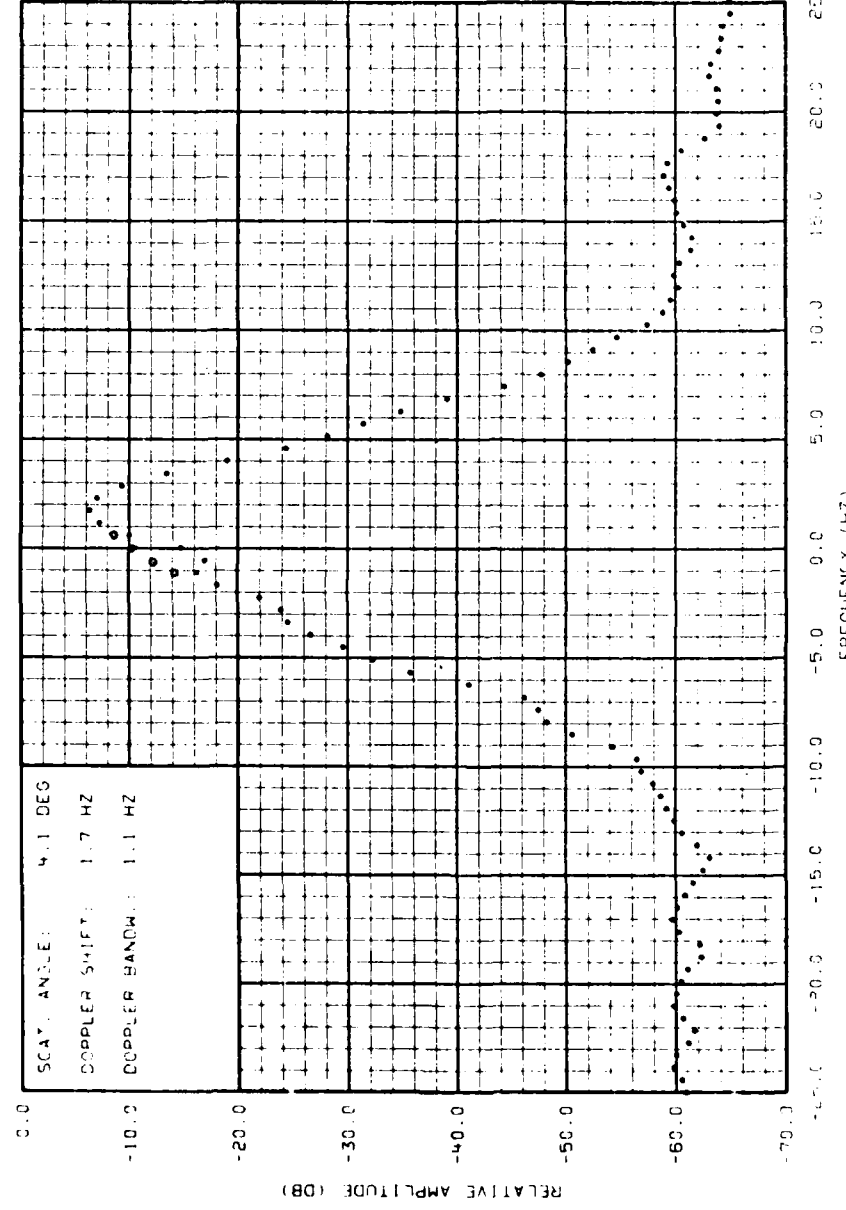


Figure C-33. Doppler Spectrum of Surface Reverberation Obtained at a Transmitted Frequency of 5.0 kHz, an Incident Angle of -4.7° , and an Angle of Scatter of 4.1° . Corrected Spectral Estimates in the Vicinity of Zero Doppler are Represented by Open Circles.

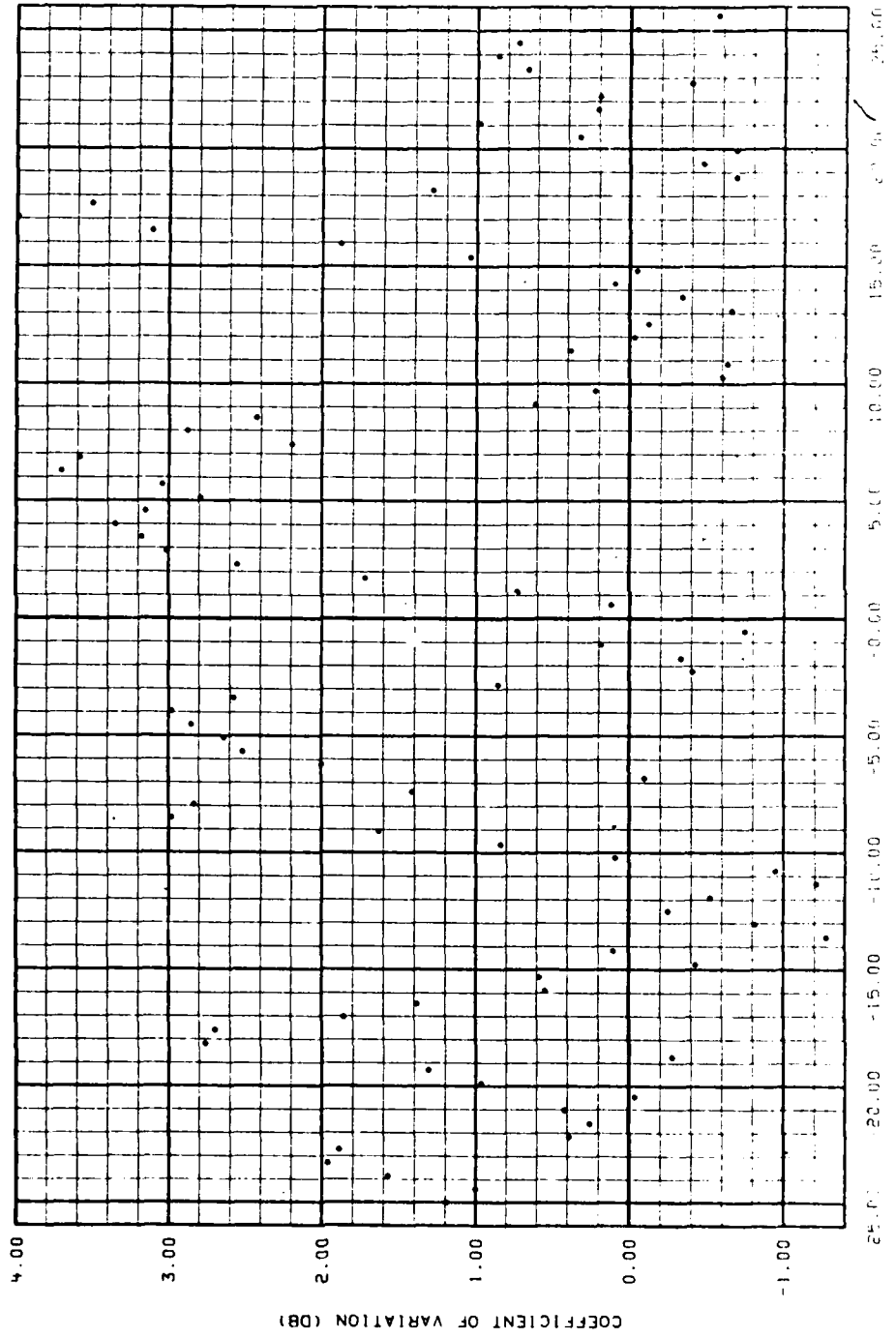


Figure C-34. Coefficients of Variation of the Spectral Estimates Obtained at a Transmitted Frequency of 5.0 kHz, an Incident Angle of -4.7°, and an Angle of Scatter of 4.1°.

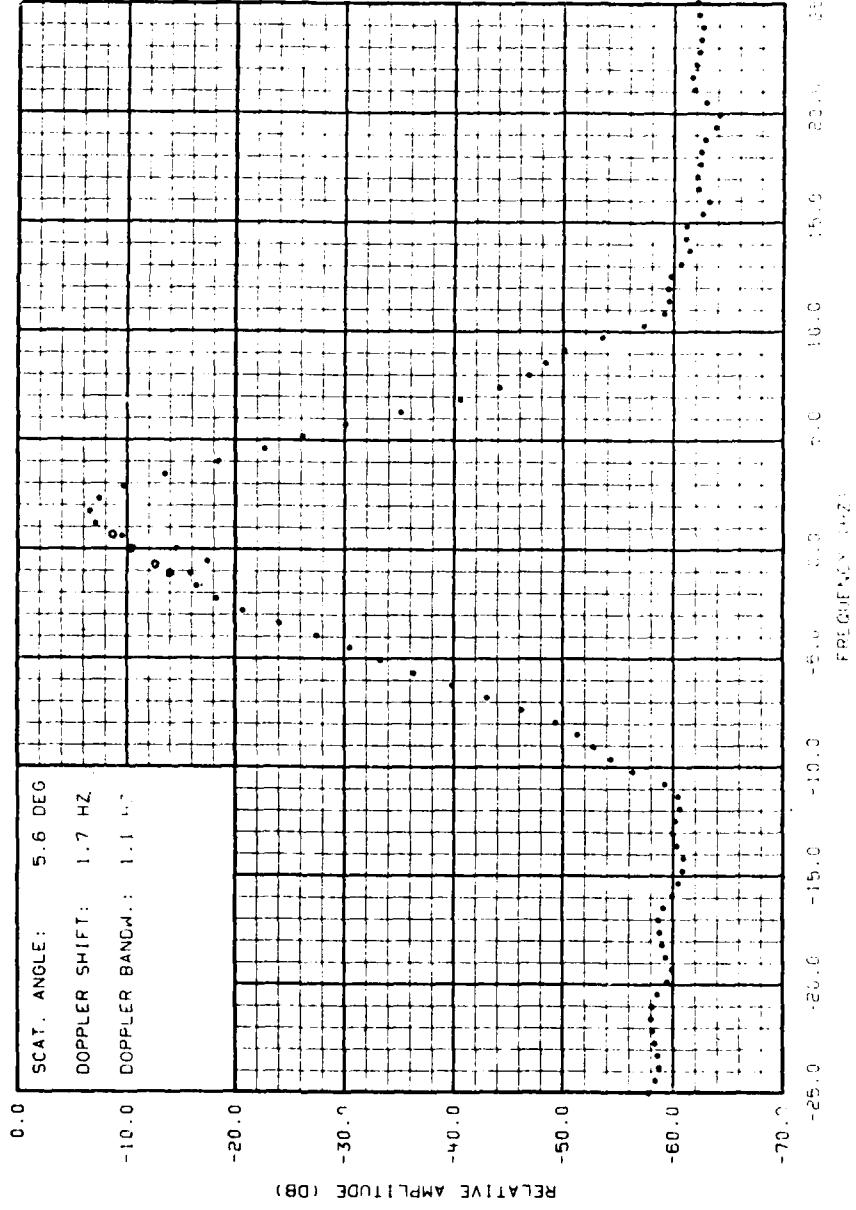


Figure C-35. Doppler Spectrum of Surface Reverberation Obtained at a Transmitted Frequency of 5.0 kHz, an Incident Angle of -4.70° , and an Angle of Scatter of 5.60° . Corrected Spectral Estimates in the Vicinity of Zero Doppler are Represented by Open Circles.

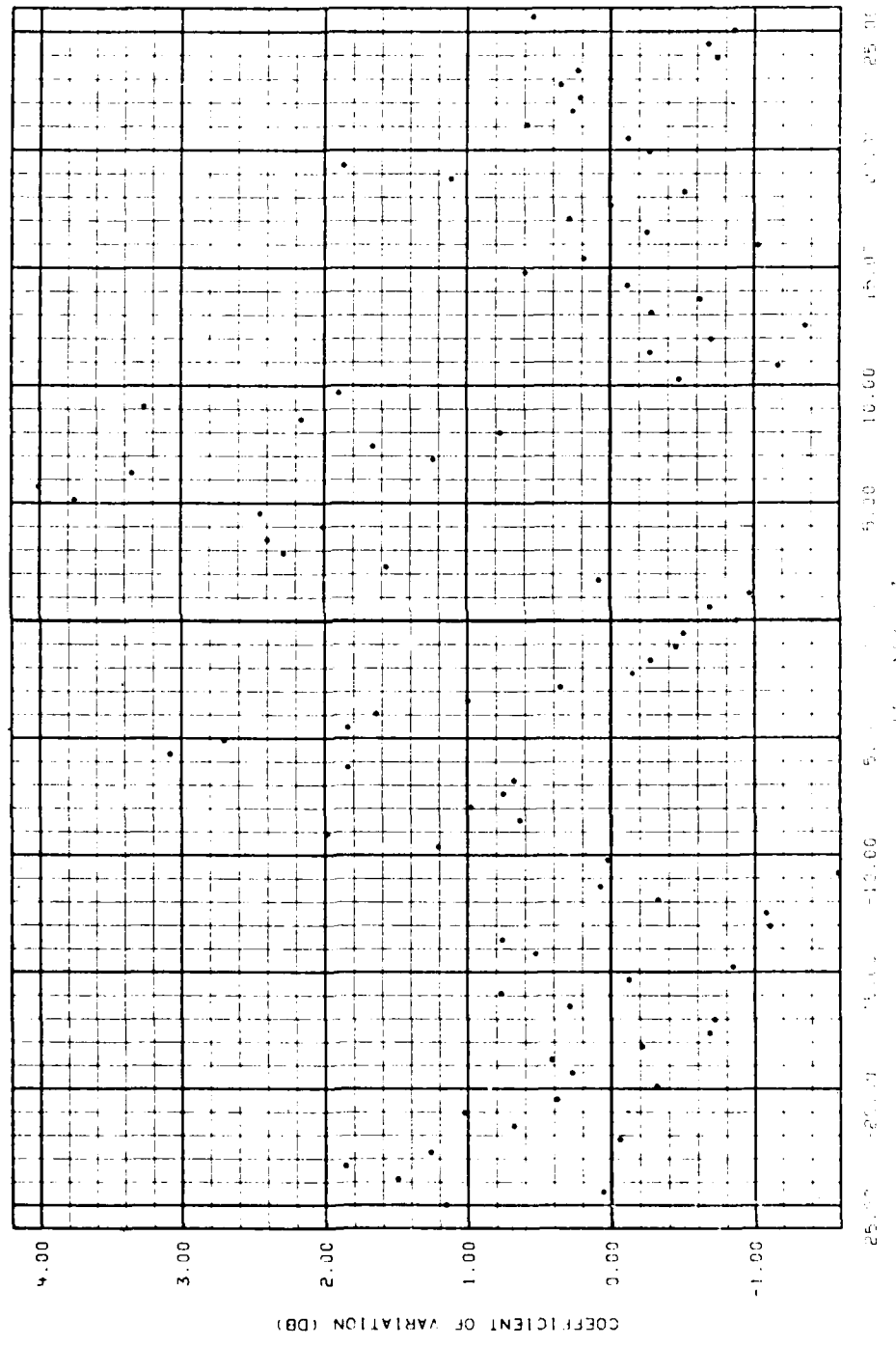


Figure C-36. Coefficients of Variation of the Spectral Estimates Obtained at a Transmitted Frequency of 5.0 kHz, an Incident Angle of -4.70°, and an Angle of Scatter of 5.60°.

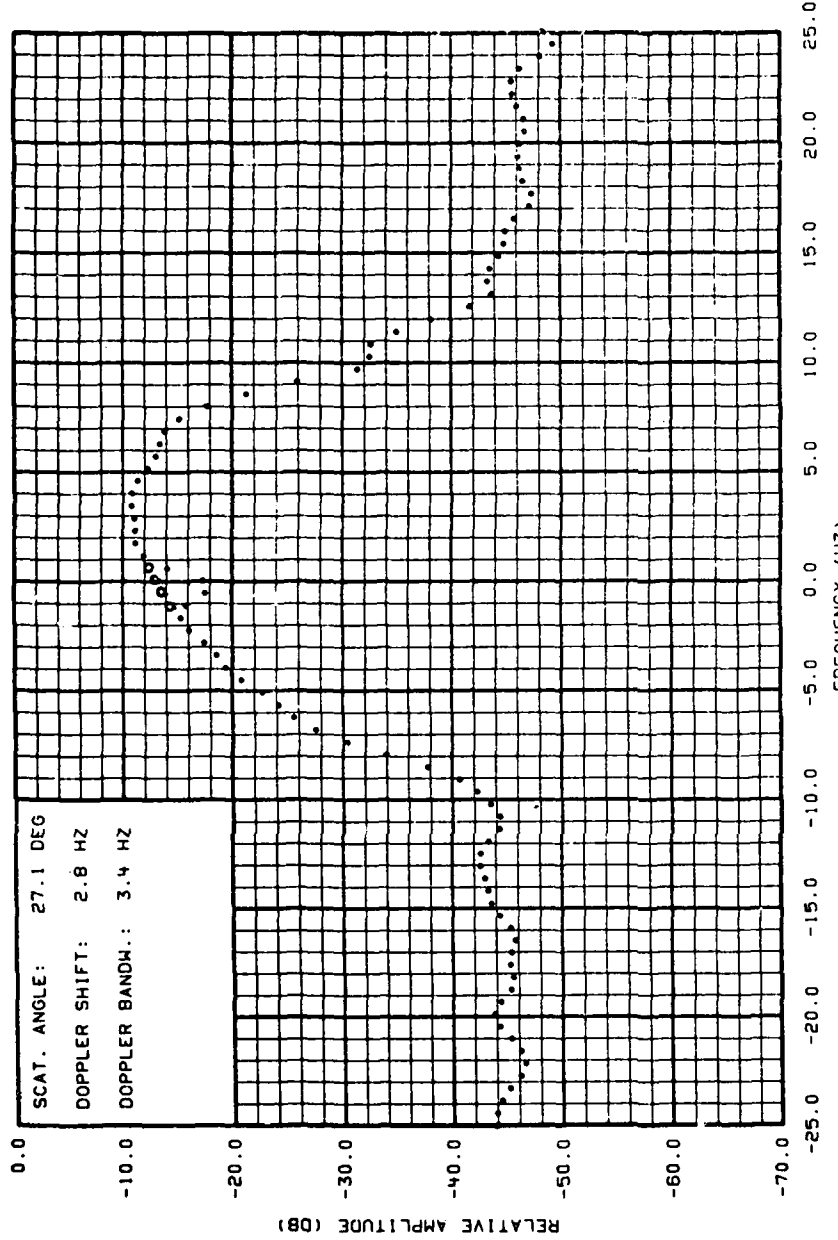


Figure C-37. Doppler Spectrum of Surface Reverberation Obtained at a Transmitted Frequency of 5.0 kHz, an Incident Angle of 20.00, and an Angle of Scatter of 27.10. Corrected Spectral Estimates in the Vicinity of Zero Doppler are Represented by Open Circles.

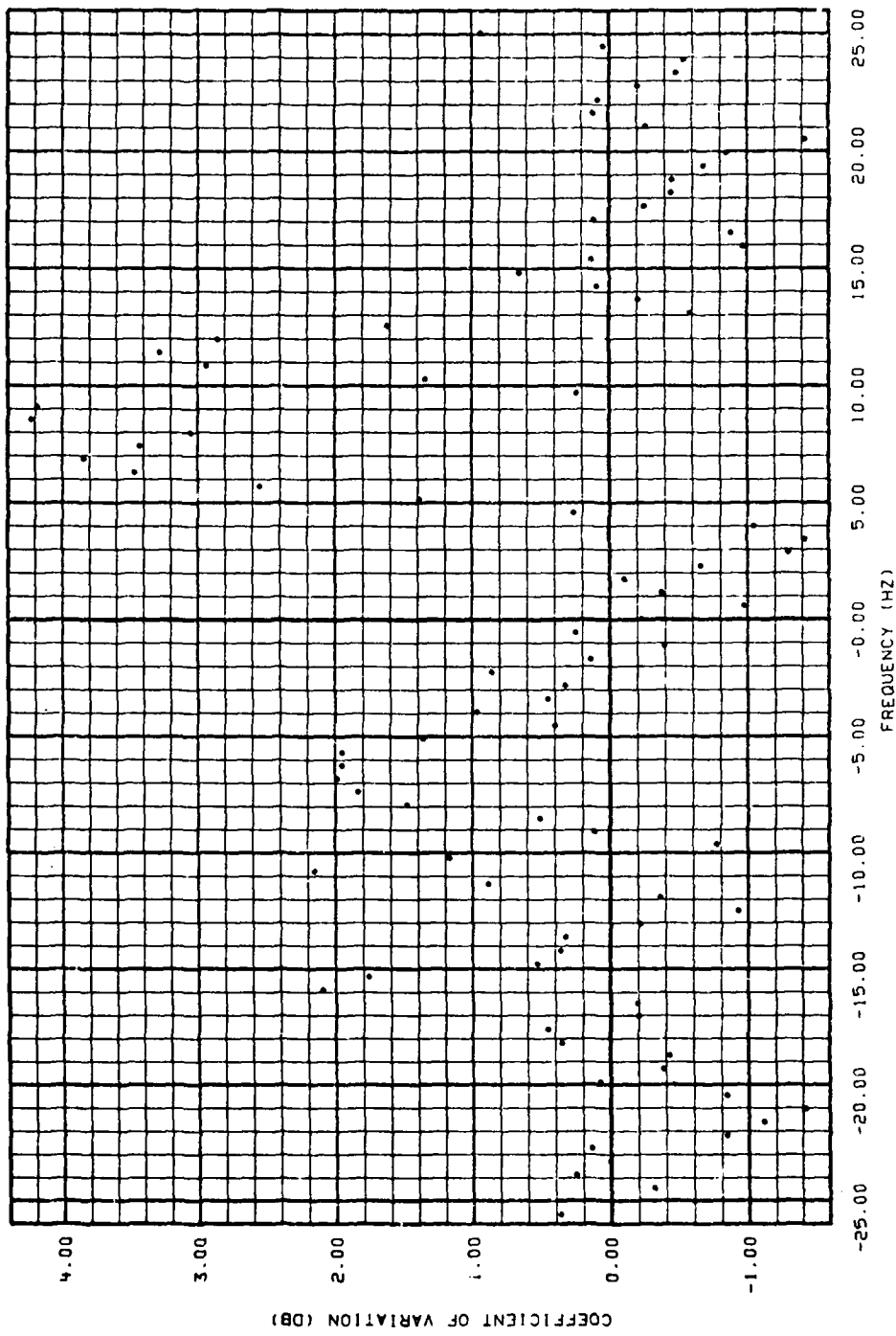
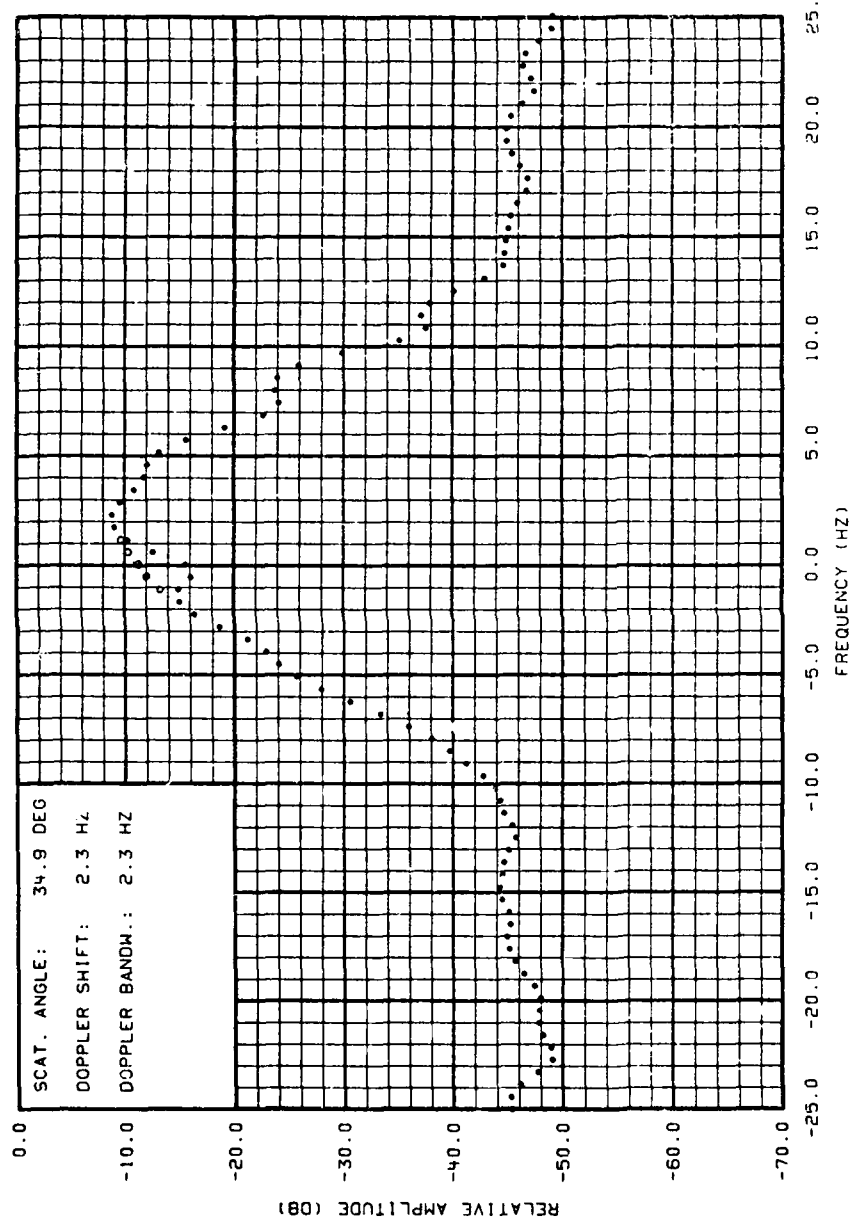


Figure C-38. Coefficients of Variation of the Spectral Estimates Obtained at a Transmitted Frequency of 5.0 kHz, an Incident Angle of 20.00°, and an Angle of Scatter of 27.10°.



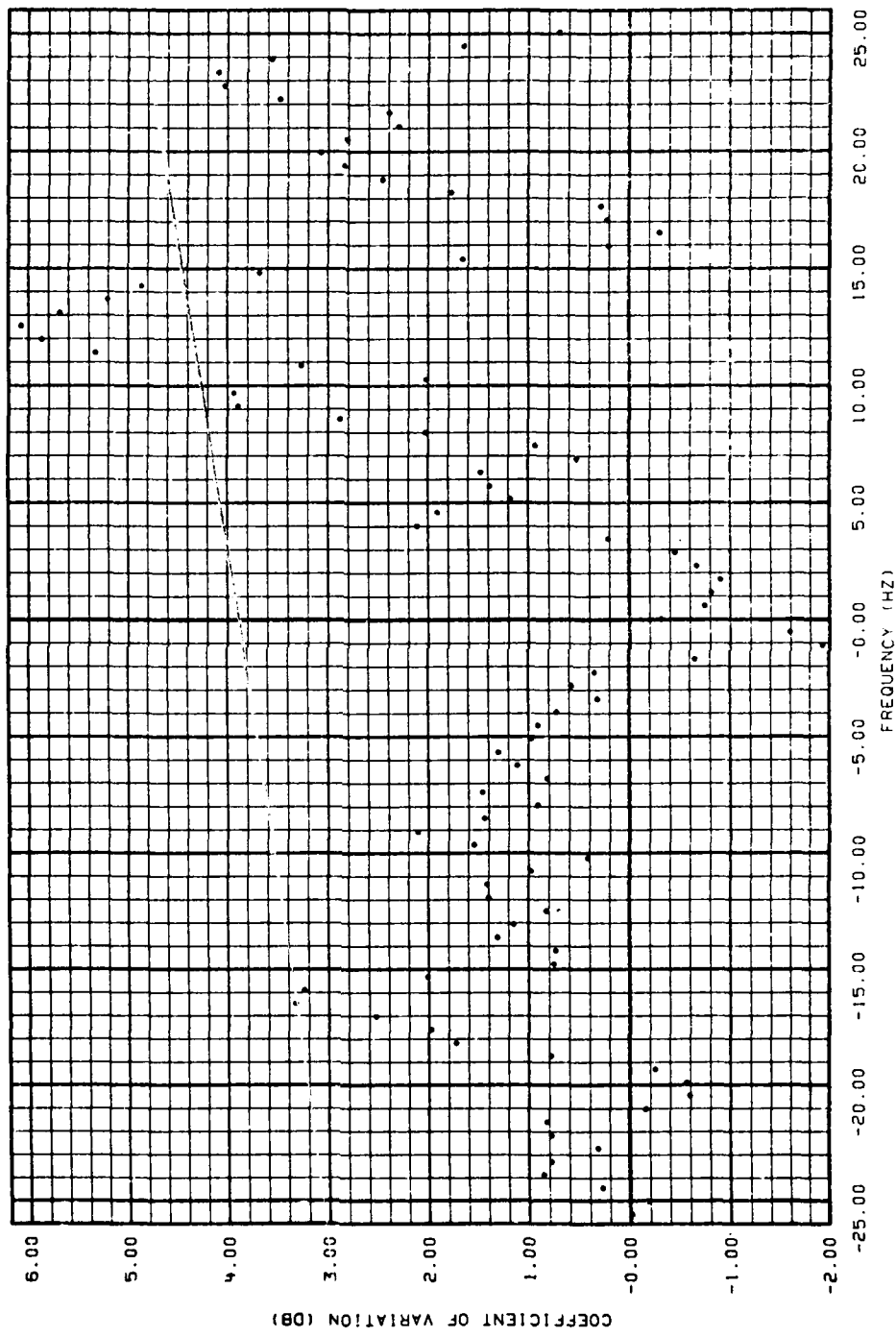


Figure C-40. Coefficients of Variation of the Spectral Estimates Obtained at a Transmitted Frequency of 5.0 kHz, an Incident Angle of 20.0°, and an Angle of Scatter of 34.9°.

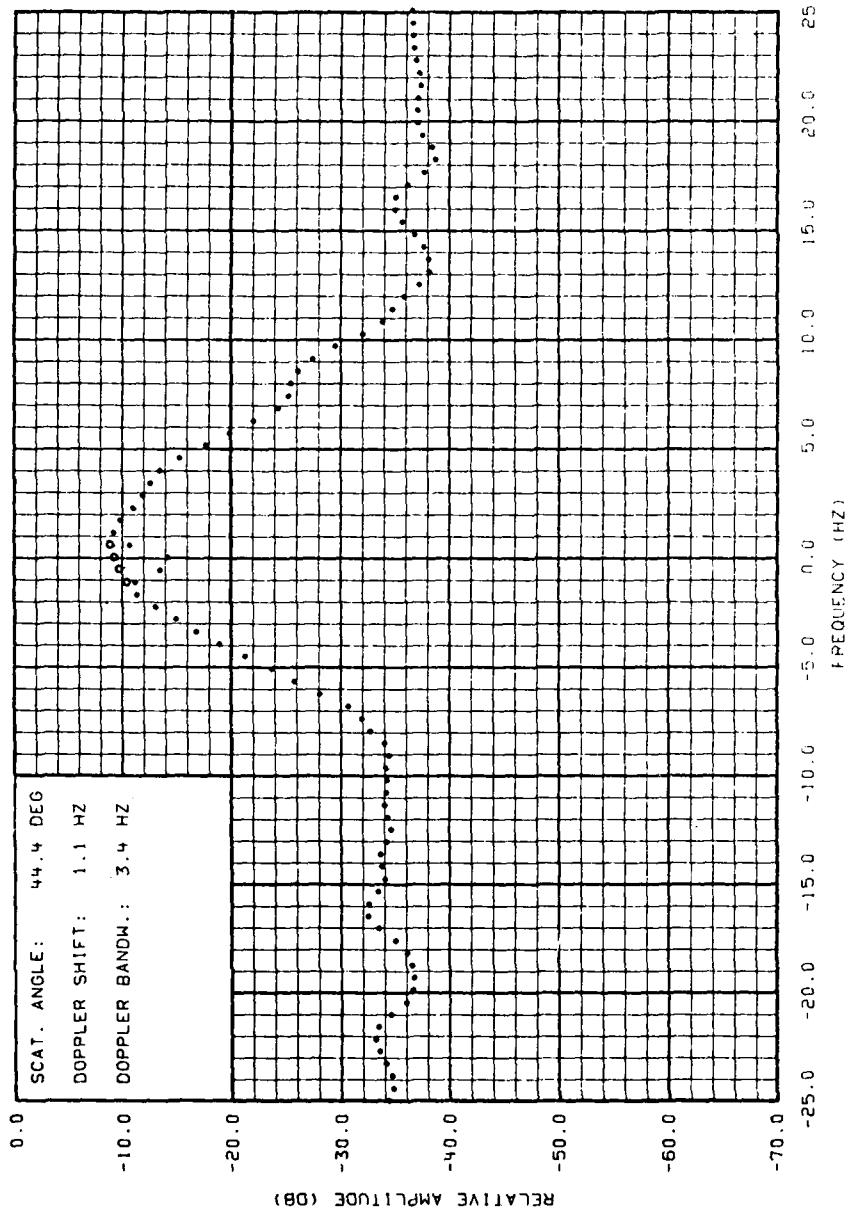


Figure C-41. Doppler Spectrum of Surface Reverberation Obtained at a Transmitted Frequency of 5.0 kHz, an Incident Angle of 40.0°, and an Angle of Scatter of 44.4°. Corrected Spectral Estimates in the Vicinity of Zero Doppler are Represented by Open Circles.

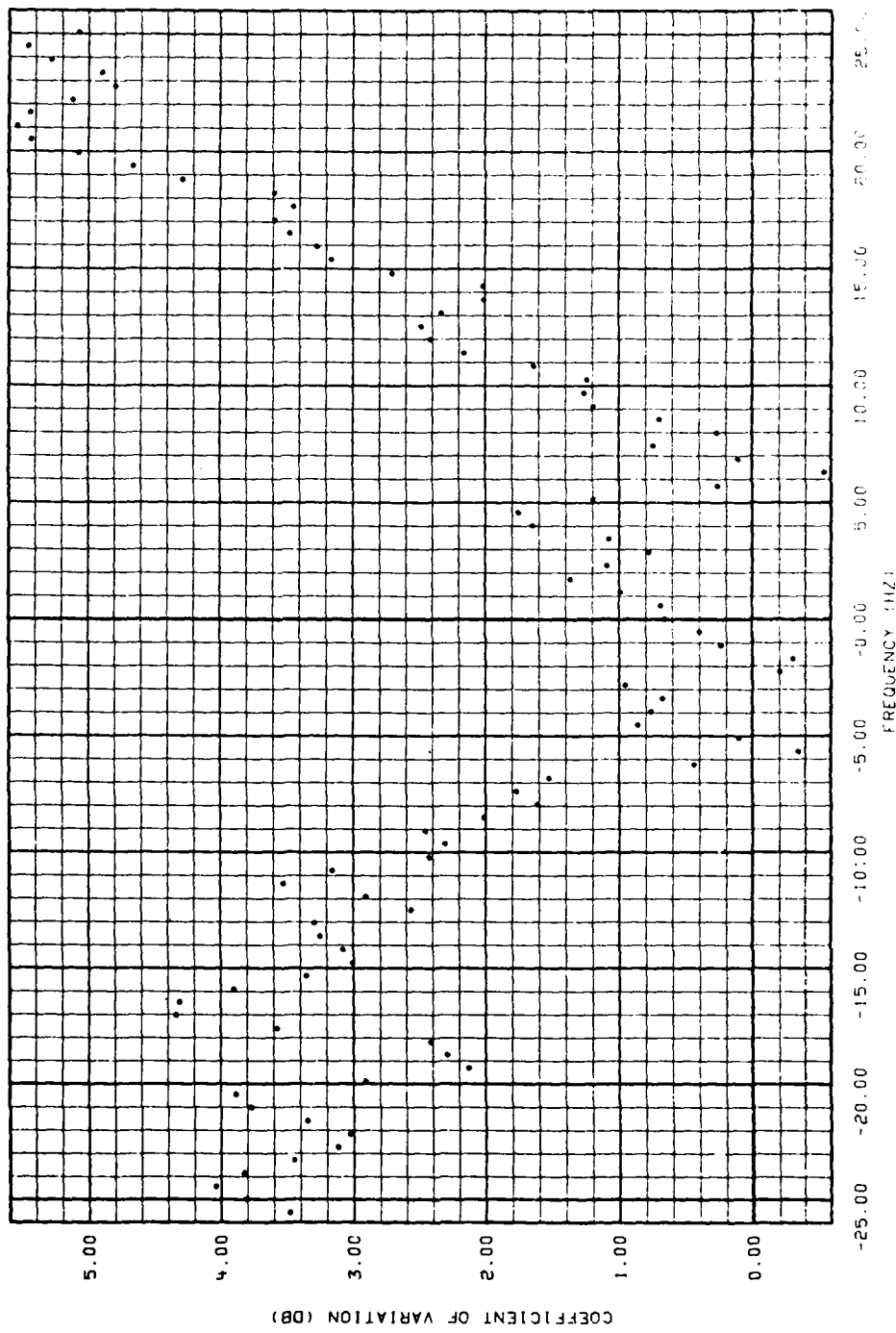


Figure C-42. Coefficients of Variation of the Spectral Estimates Obtained at a Transmitted Frequency of 5.0 kHz, an Incident Angle of 40.0°, and an Angle of Scatter of 44.40.

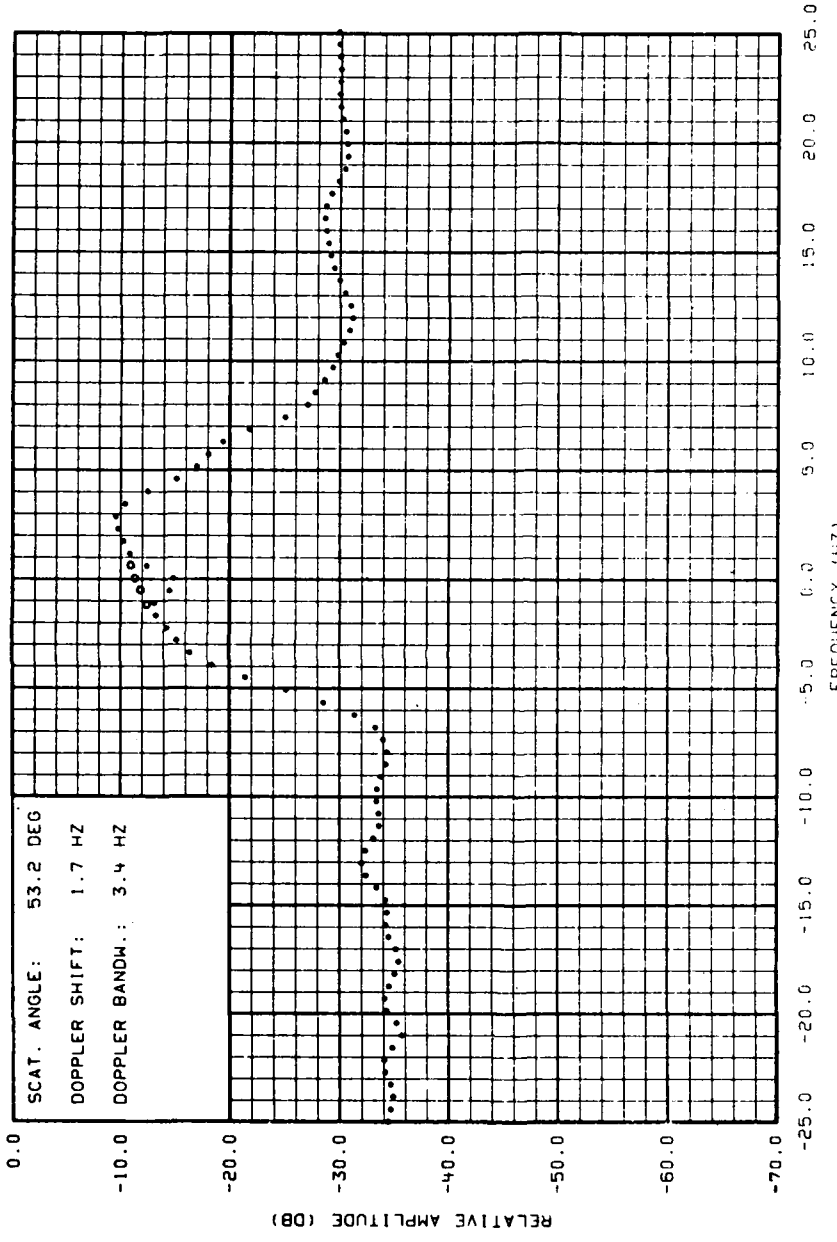


Figure C-43. Doppler Spectrum of Surface Reverberation Obtained at a Transmitted Frequency of 5.0 kHz, an Incident Angle of 40.0° , and an Angle of Scatter of 53.2° . Corrected Spectral Estimates in the Vicinity of Zero Doppler are Represented by Open Circles.

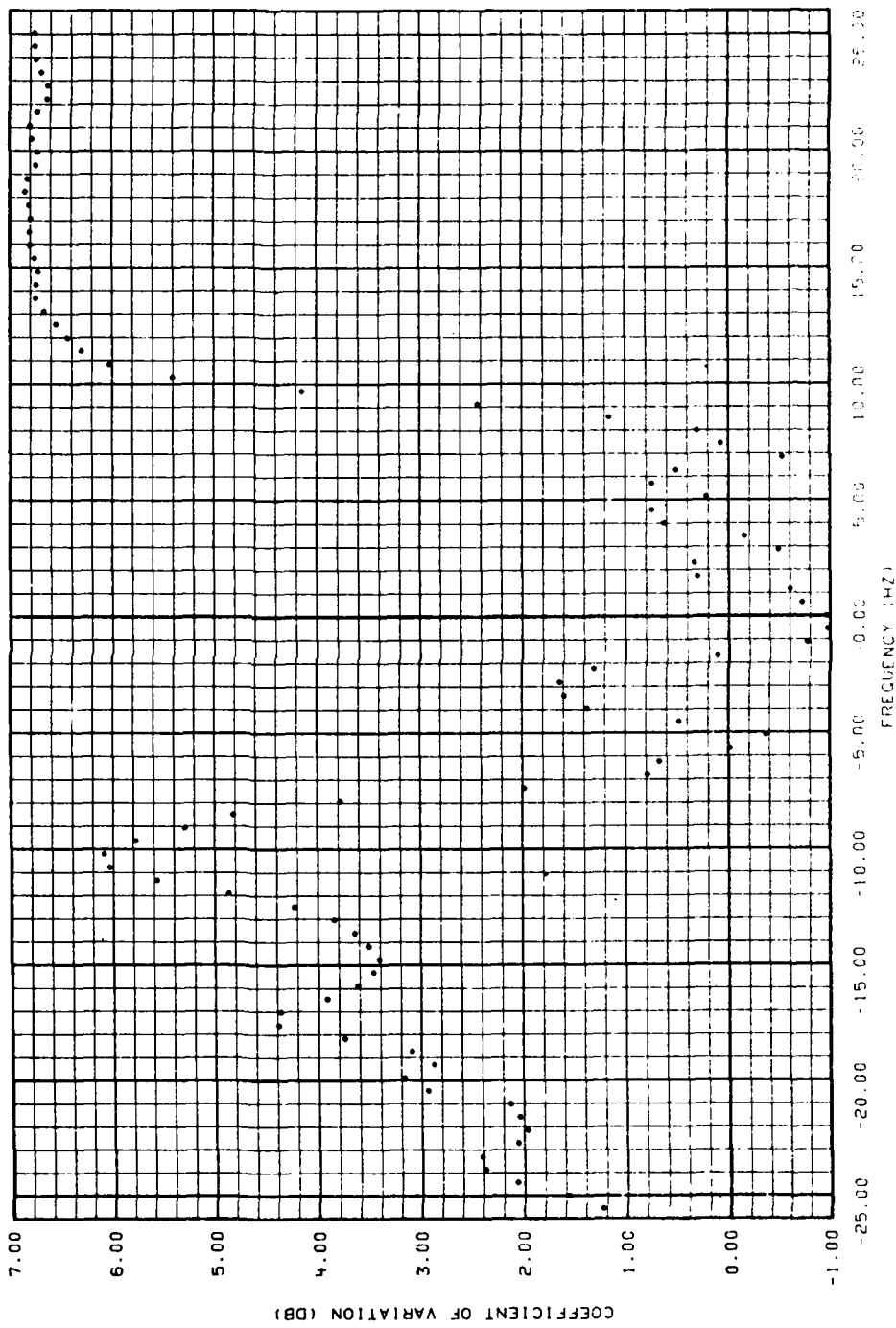


Figure C-44. Coefficients of Variation of the Spectral Estimates Obtained at a Transmitted Frequency of 5.0 kHz, an Incident Angle of 40.0°, and an Angle of Scatter of 53.2°.

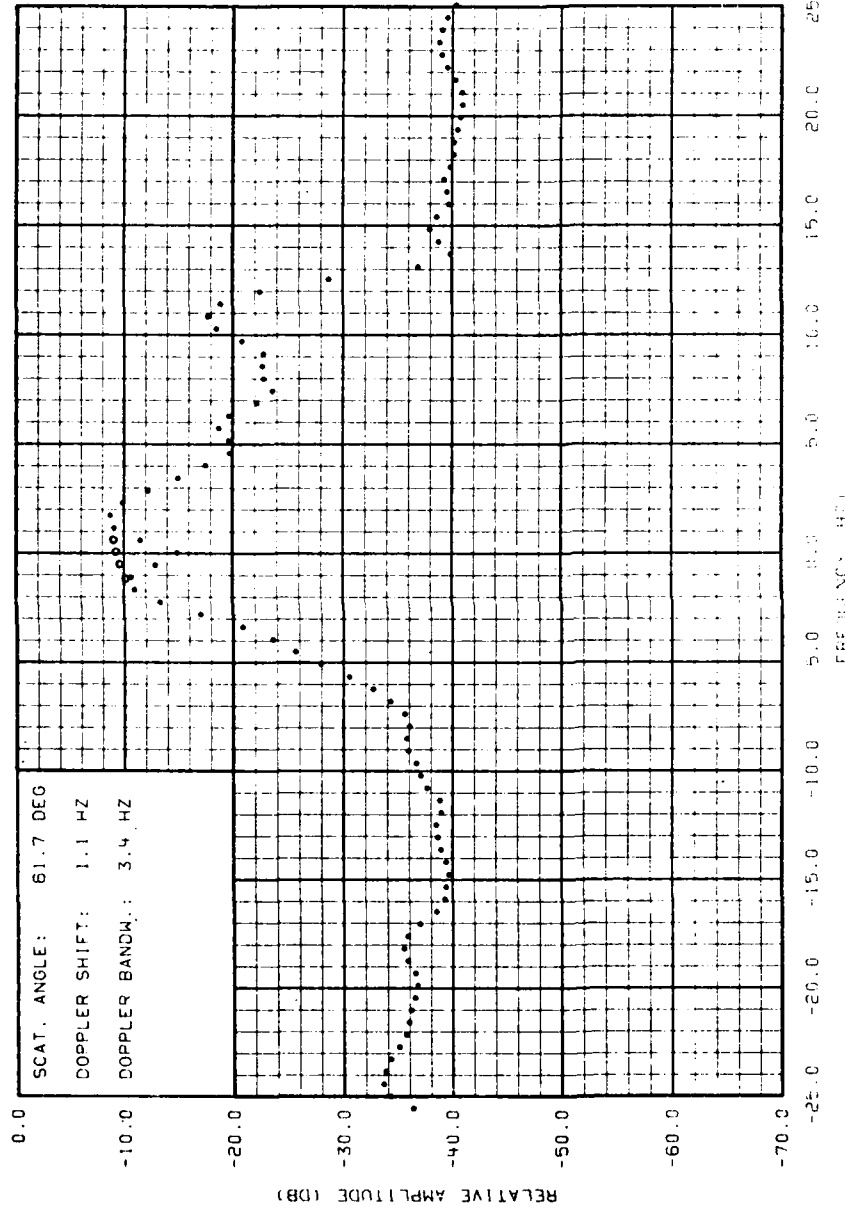


Figure C-45. Doppler Spectrum of Surface Reverberation Obtained at a Transmitted Frequency of 5.0 kHz, an Incident Angle of 60.0°, and an Angle of Scatter of 61.7°. Corrected Spectral Estimates in the Vicinity of Zero Doppler are Represented by Open Circles.

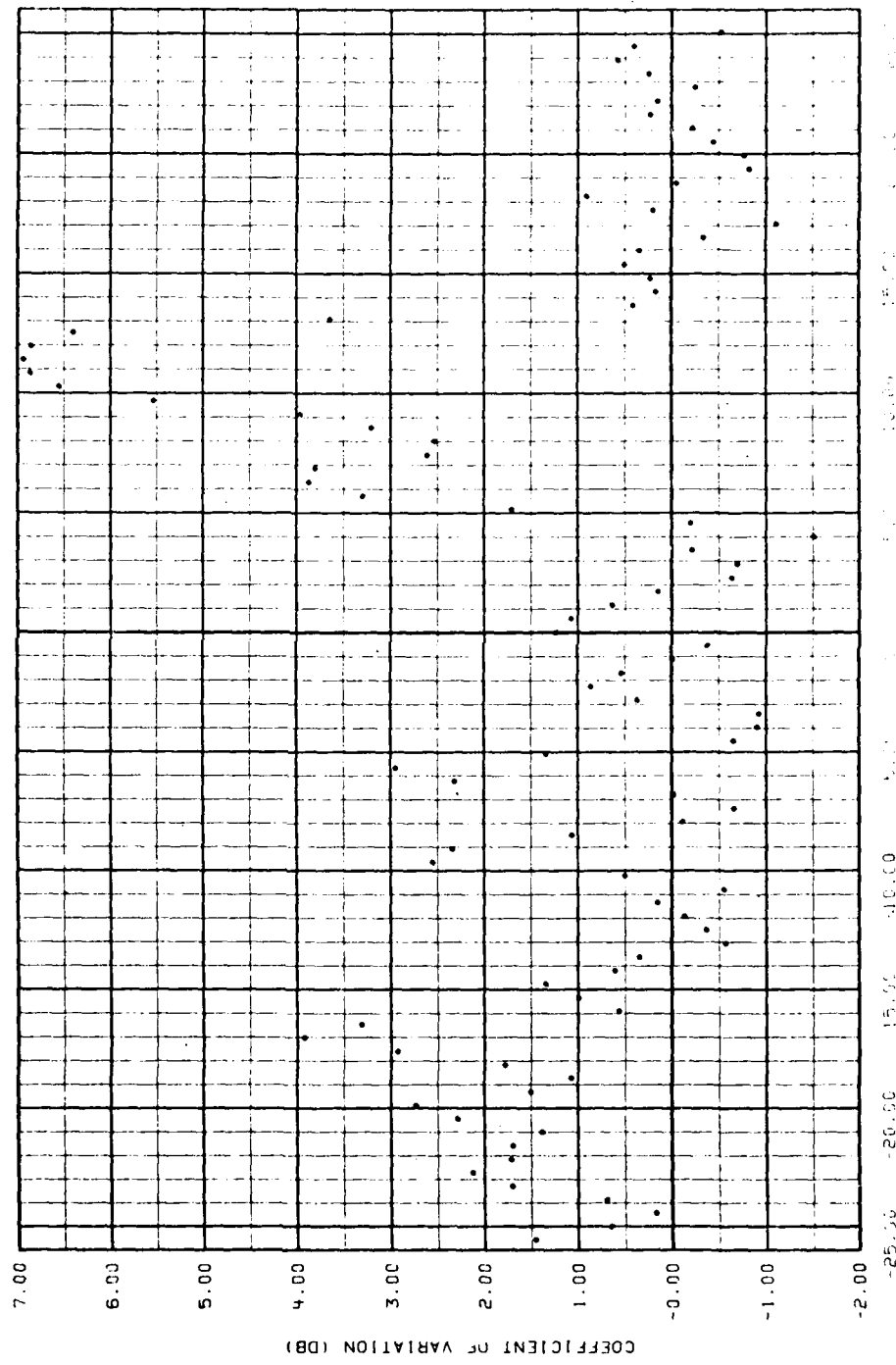


Figure C-46. Coefficients of Variation of the Spectral Estimates Obtained at a Transmitted Frequency of 5.0 kHz, an Incident Angle of 60.0°, and an Angle of Scatter of 61.7°.

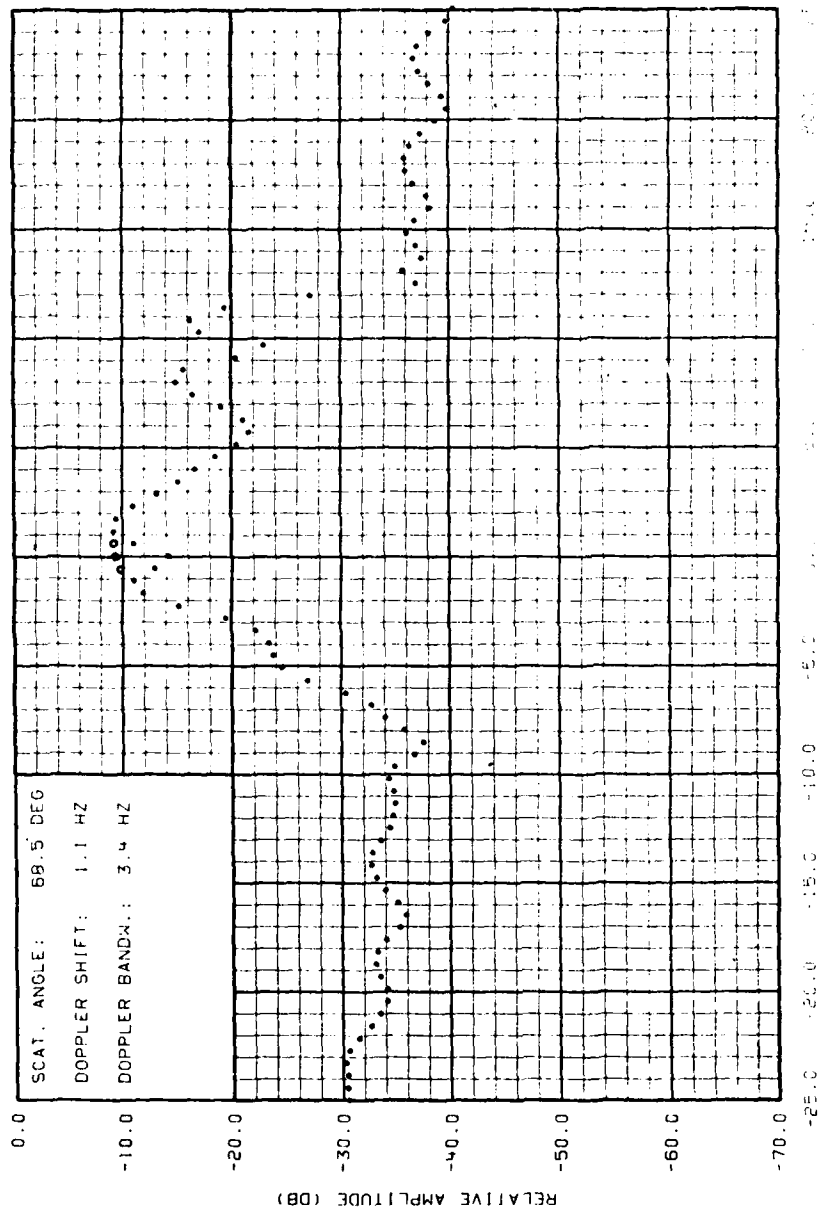


Figure C-47. Doppler Spectrum of Surface Reverberation Obtained at a Transmitted Frequency of 5.0 kHz, an Incident Angle of 60.0°, and an Angle of Scatter of 68.5°. Corrected Spectral Estimates in the Vicinity of Zero Doppler are Represented by Open Circles.

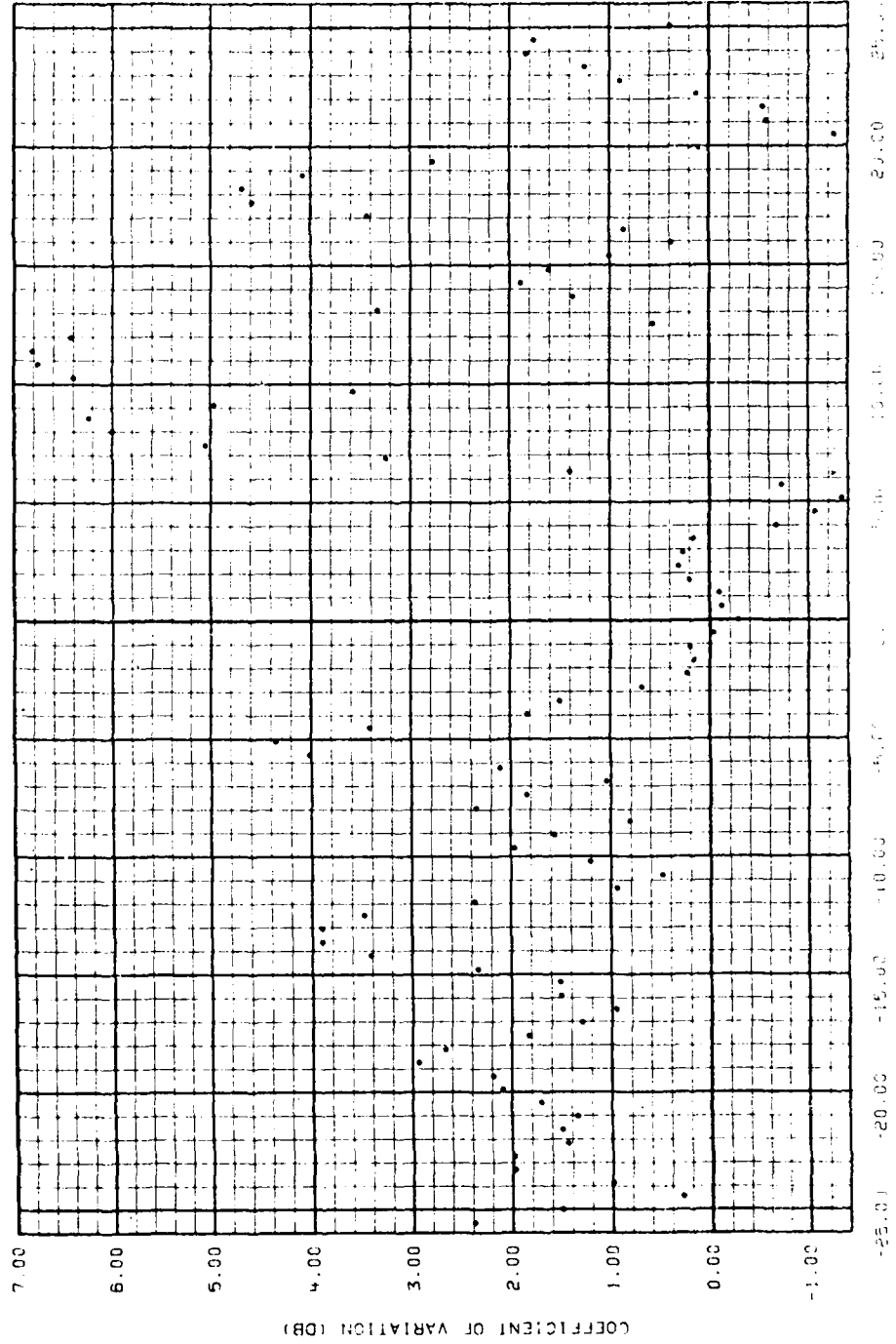


Figure C-48. Coefficients of Variation of the Spectral Estimates Obtained at a Transmitted Frequency of 5.0 kHz, an Incident Angle of 60.0°, and an Angle of Scatter of 68.5°.

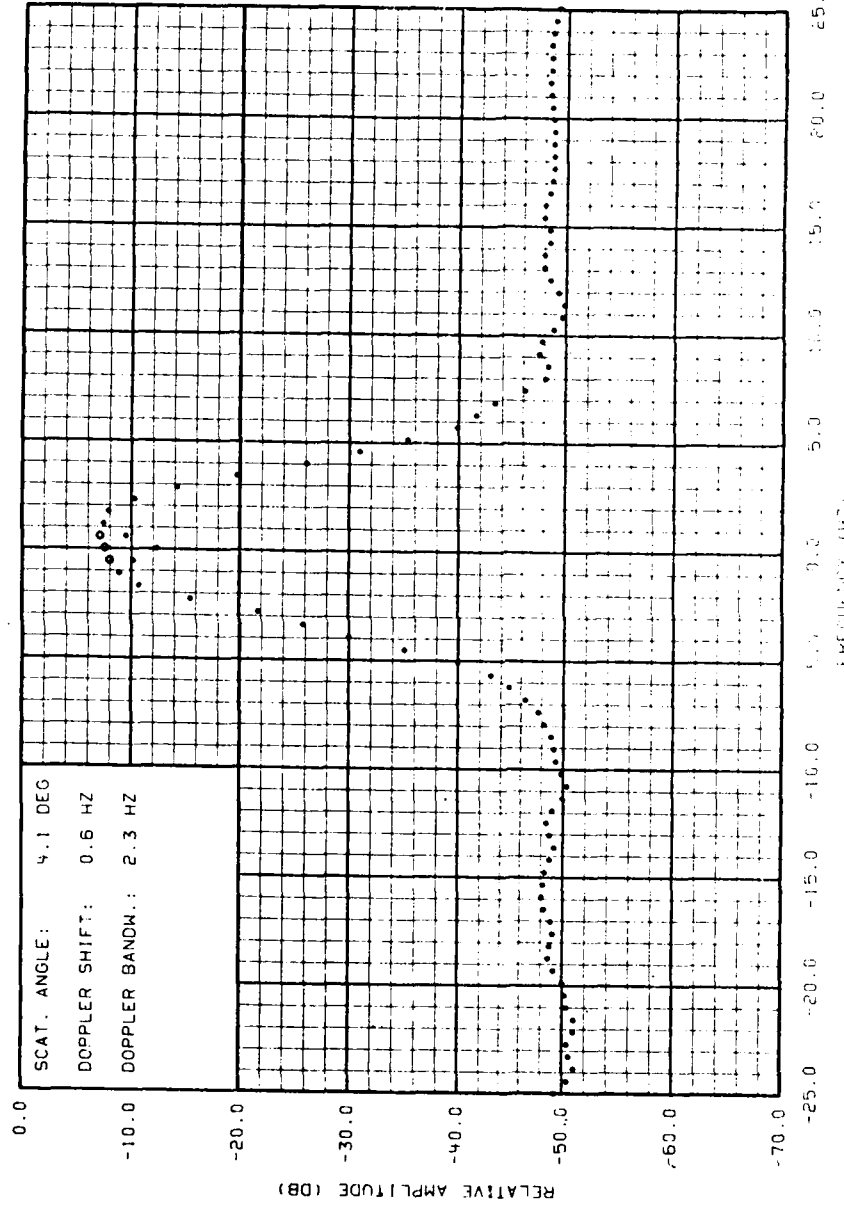


Figure C-49. Doppler Spectrum of Surface Reverberation Obtained at a Transmitted Frequency of 3.5 kHz, an Incident Angle of -4.7°, and an Angle of Scatter of 4.1°. Corrected Spectral Estimates in the Vicinity of Zero Doppler are Represented by Open Circles.

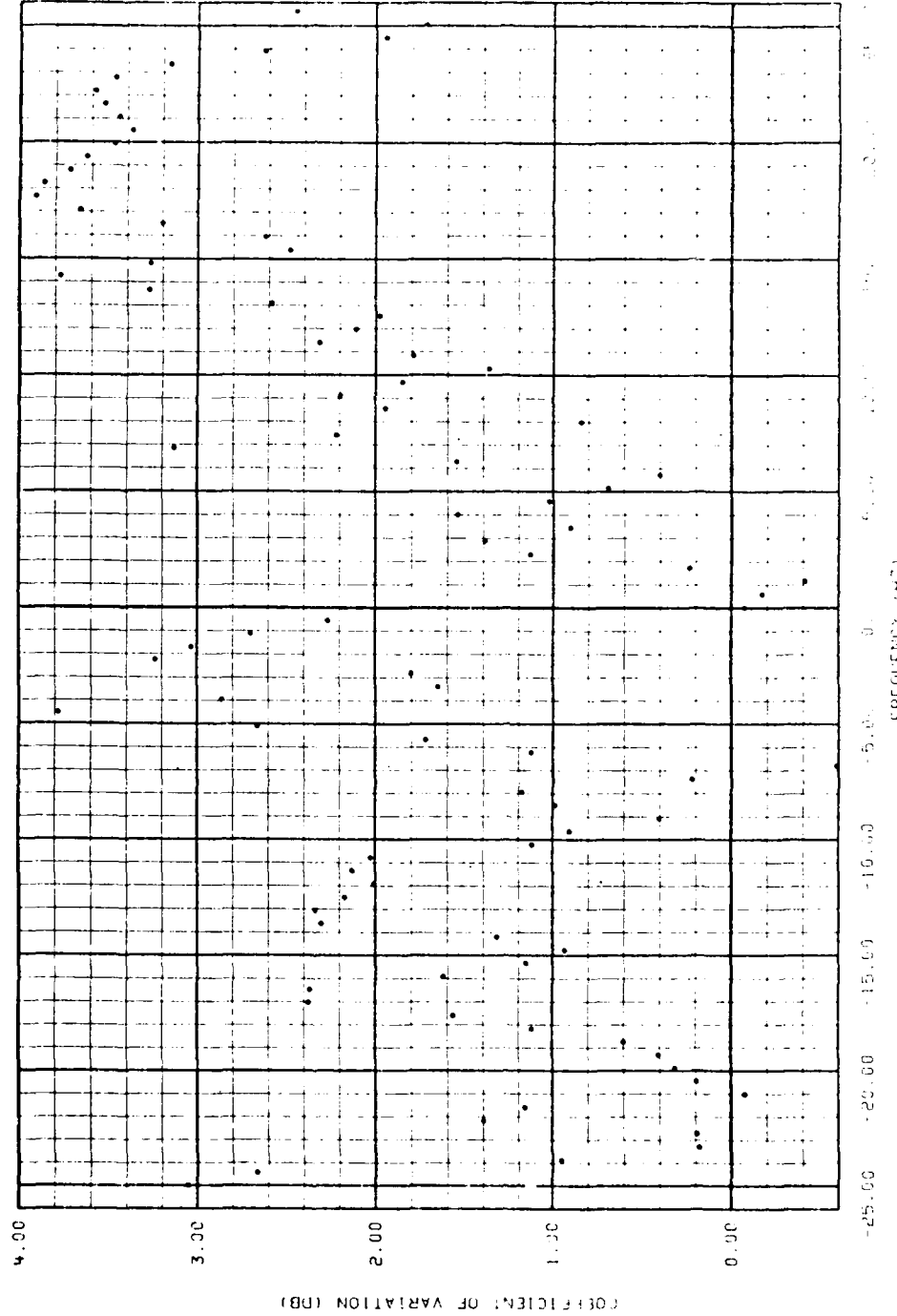


Figure C-50. Coefficients of Variation of the Spectral Estimates Obtained at a Transmitted Frequency of 3.5 kHz, an Incident Angle of -4.7°, and an Angle of Scatter of 4.1°.

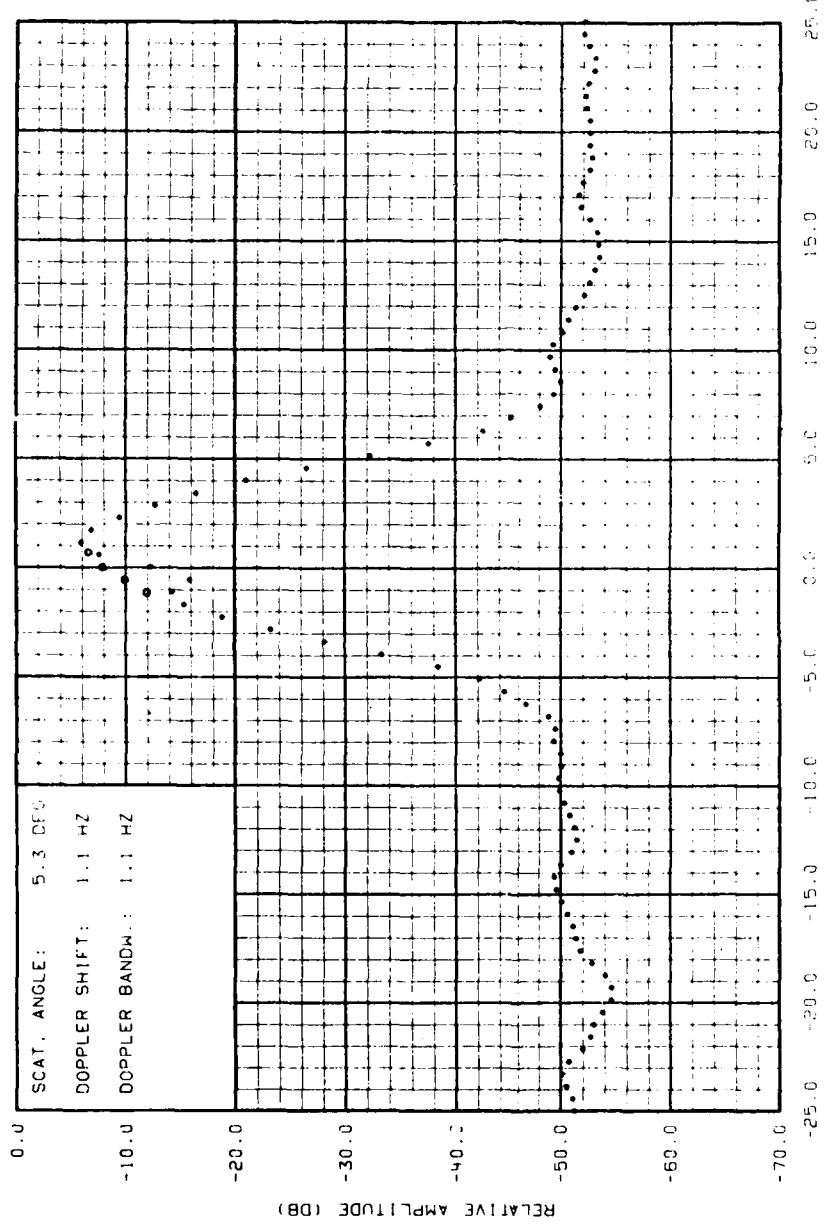


Figure C-51. Doppler Spectrum of Surface Reverberation Obtained at a Transmitted Frequency of 3.5 kHz, an Incident Angle of -4.7°, and an Angle of Scatter of 5.6°. Corrected Spectral Estimates in the Vicinity of Zero Doppler are Represented by Open Circles.

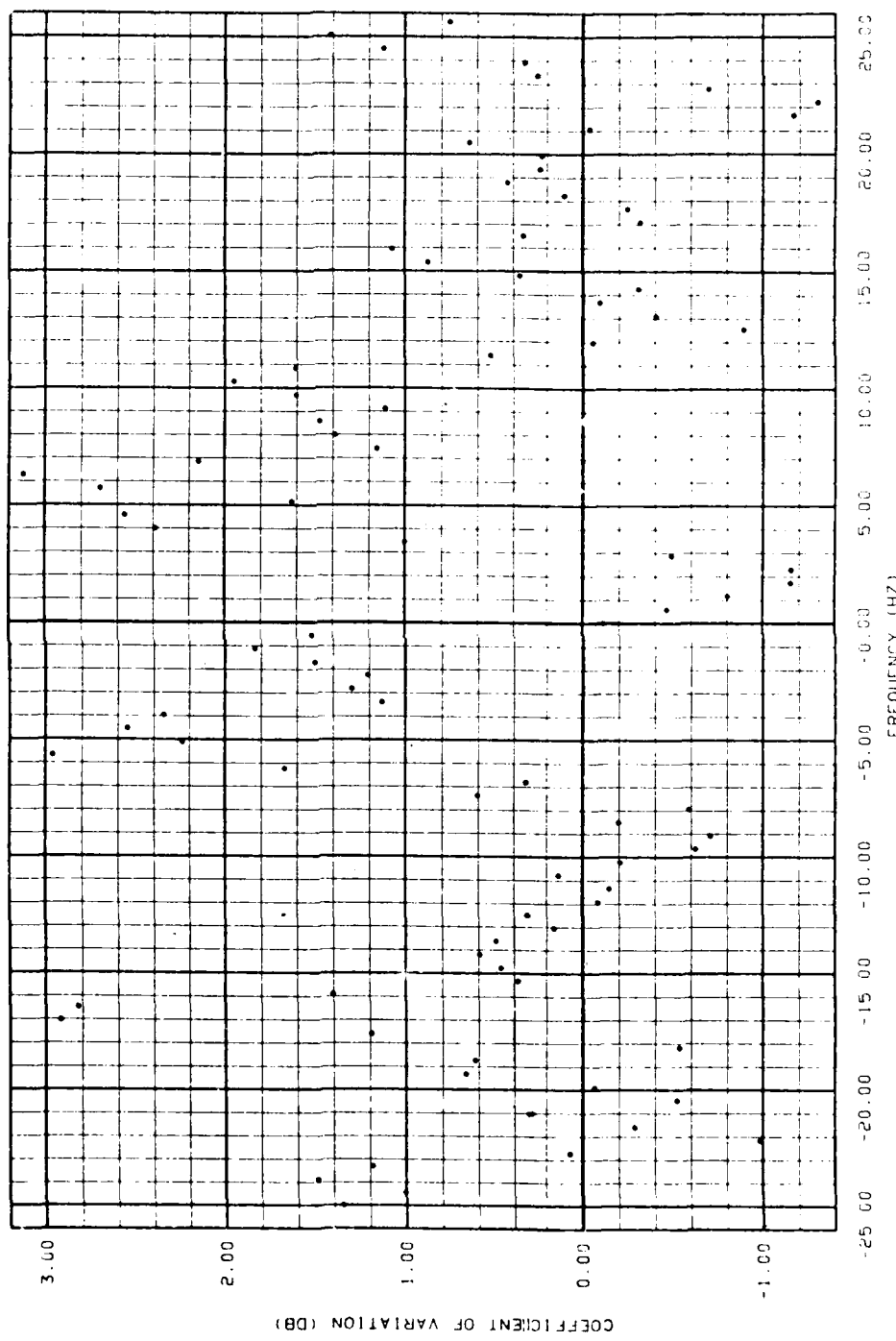


Figure C-52. Coefficients of Variation of the Spectral Estimates Obtained at a Transmitted Frequency of 3.5 kHz, an Incident Angle of -4.70° , and an Angle of Scatter of 5.60° .

AD-A090 042

NAVAL UNDERWATER SYSTEMS CENTER NEWPORT RI
DOPPLER SPECTRA OF BISTATIC REVERBERATION FROM THE SEA SURFACE.(U)

F/6 20/1

MAY 79 W I RODERICK

UNCLASSIFIED

NUSC-TR-6031

NL

3 of 3
AD-A090042

END
1480
DTIC

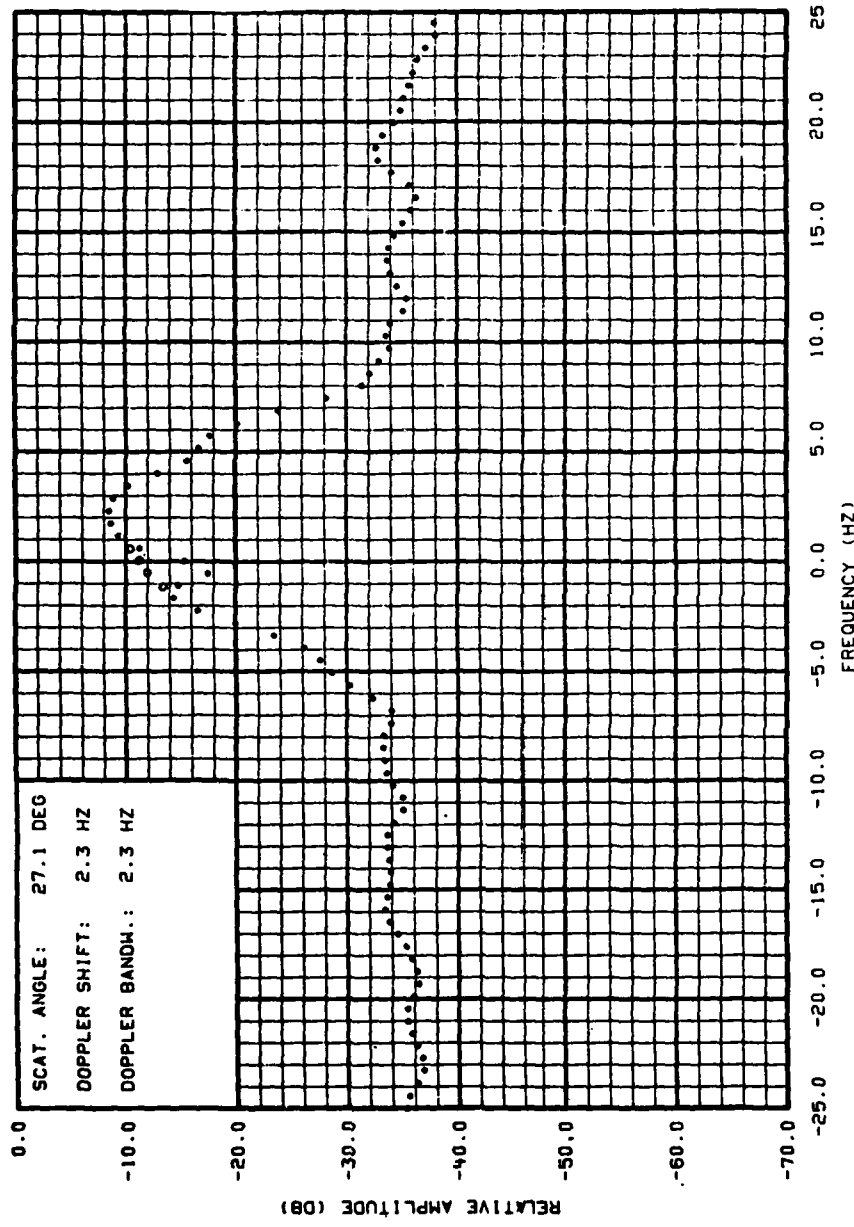


Figure C-53. Doppler Spectrum of Surface Reverberation Obtained at a Transmitted Frequency of 3.5 kHz, an Incident Angle of 20.0°, and an Angle of Scatter of 27.1°. Corrected Spectral Estimates in the Vicinity of Zero Doppler are Represented by Open Circles.

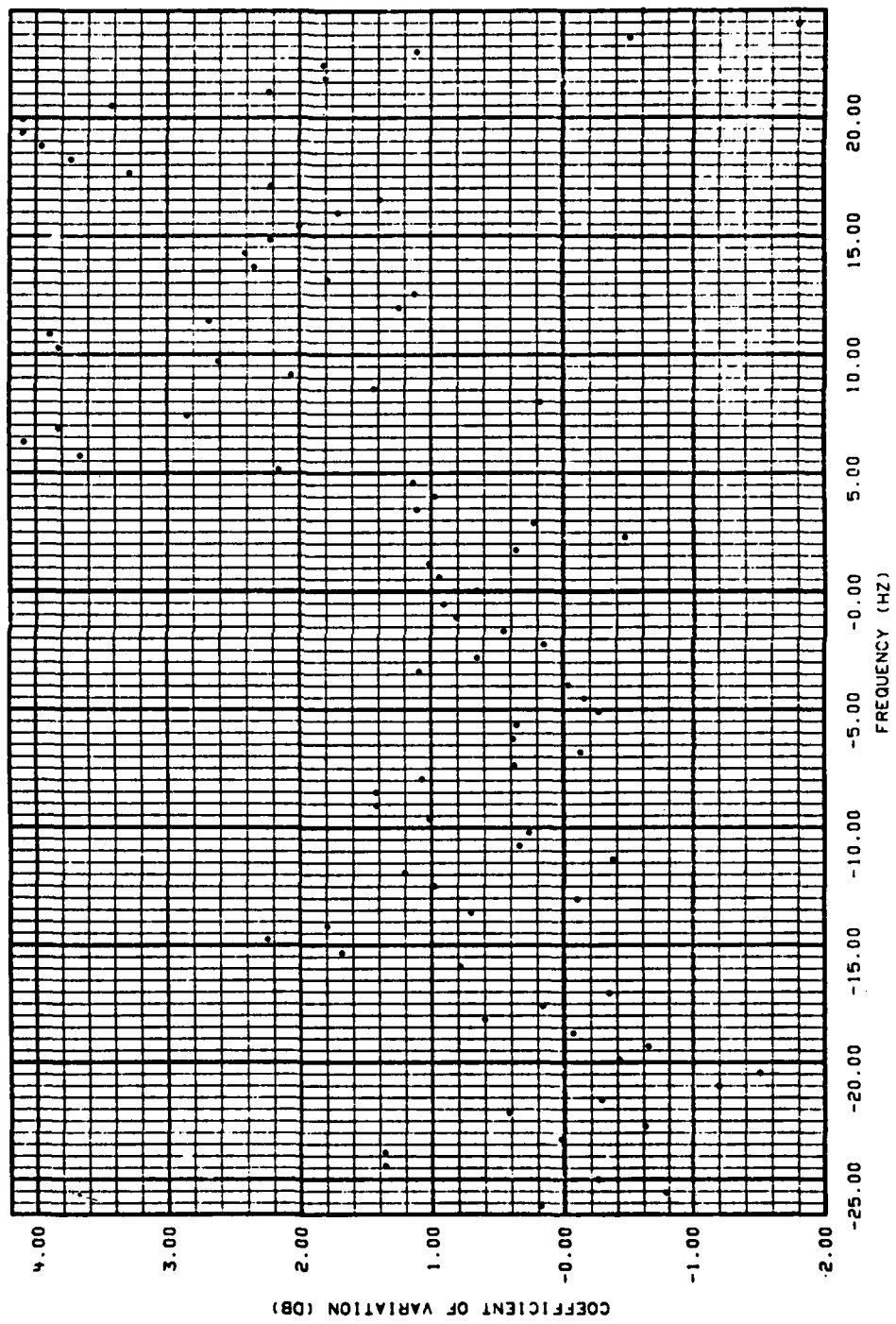


Figure C-54. Coefficients of Variation of the Spectral Estimates Obtained at a Transmitted Frequency of 3.5 kHz, an Incident Angle of 20.00° , and an Angle of Scatter of 27.10° .

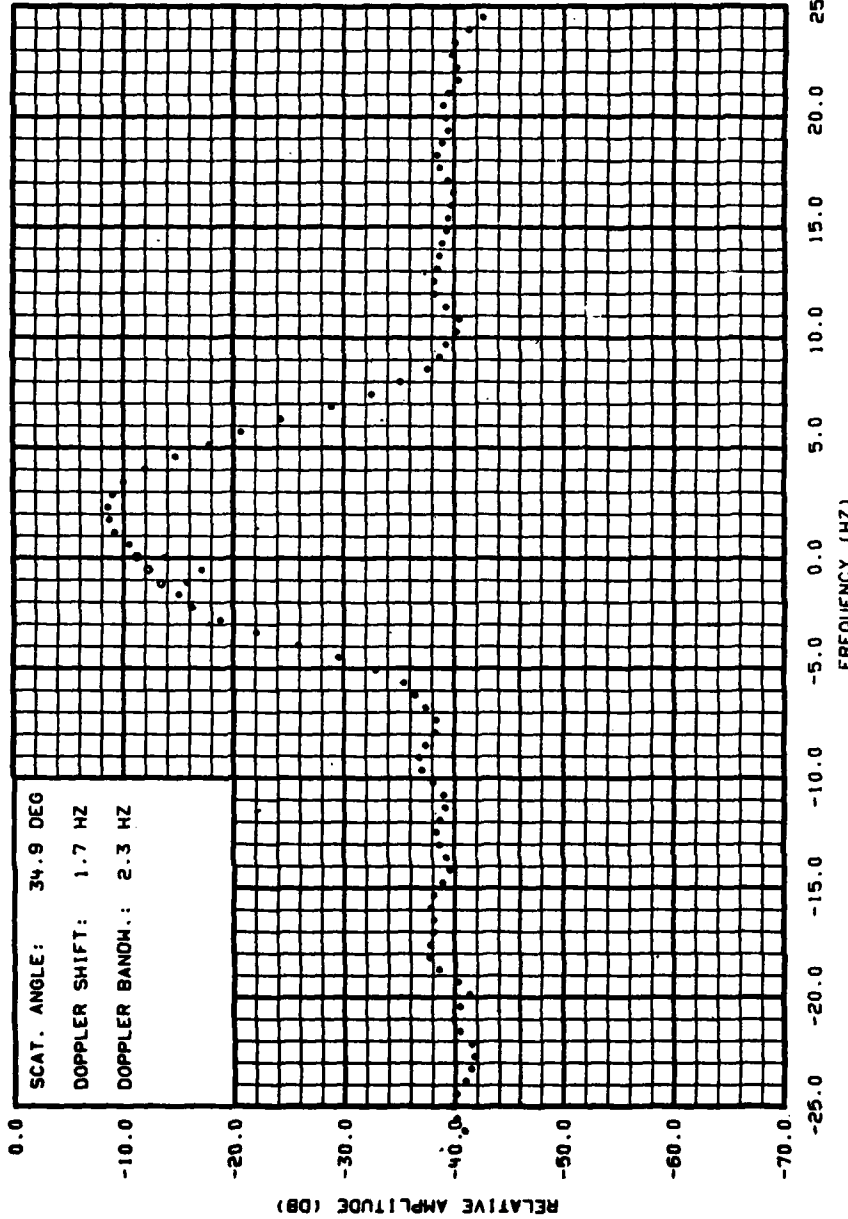


Figure C-55. Doppler Spectrum of Surface Reverberation Obtained at a Transmitted Frequency of 3.5 kHz, an Incident Angle of 20.0°, and an Angle of Scatter of 34.9°. Corrected Spectral Estimates in the Vicinity of Zero Doppler are Represented by Open Circles.

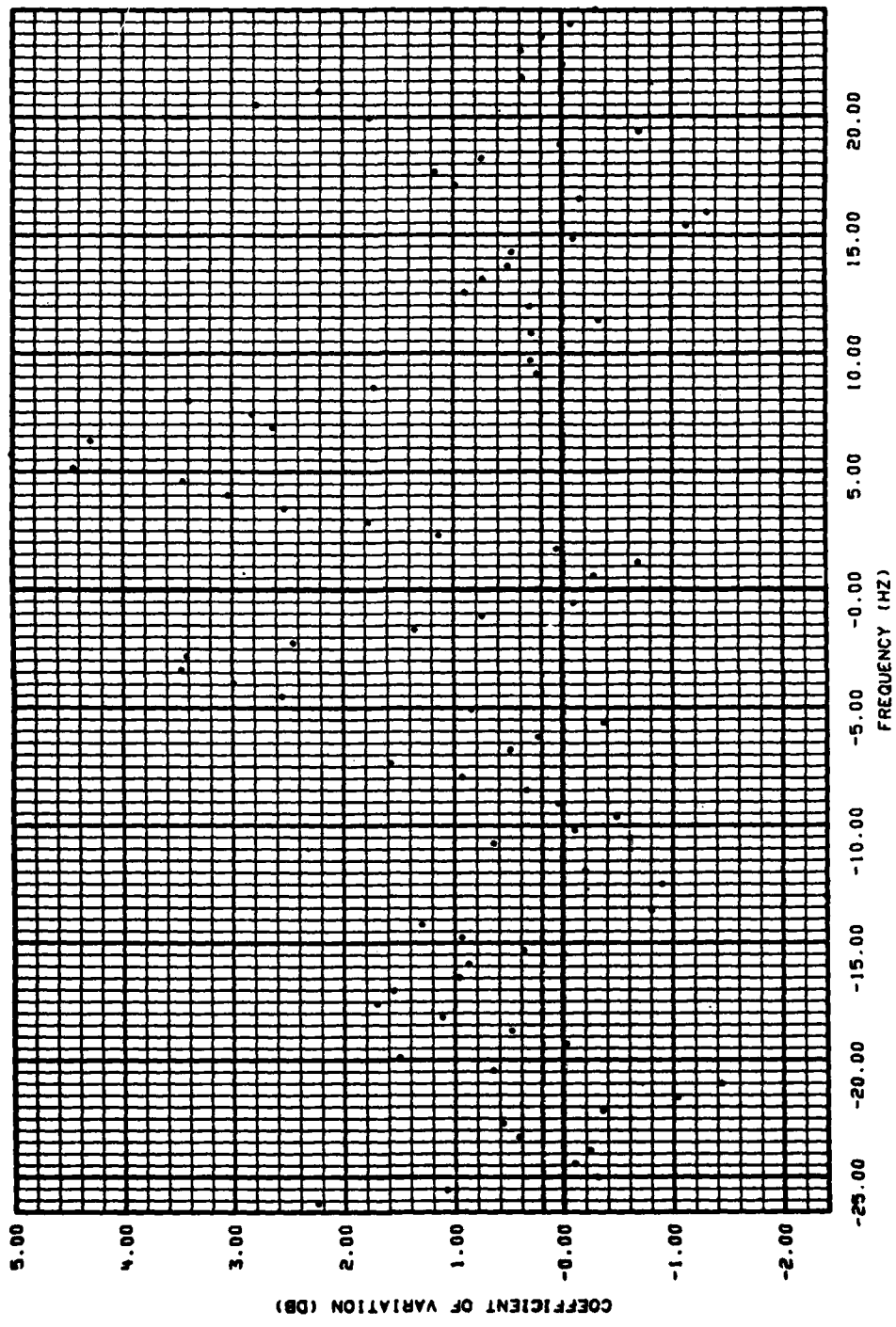


Figure C-56. Coefficients of Variation of the Spectral Estimates Obtained at a Transmitted Frequency of 3.5 kHz, an Incident Angle of 20.0°, and an Angle of Scatter of 34.9°.

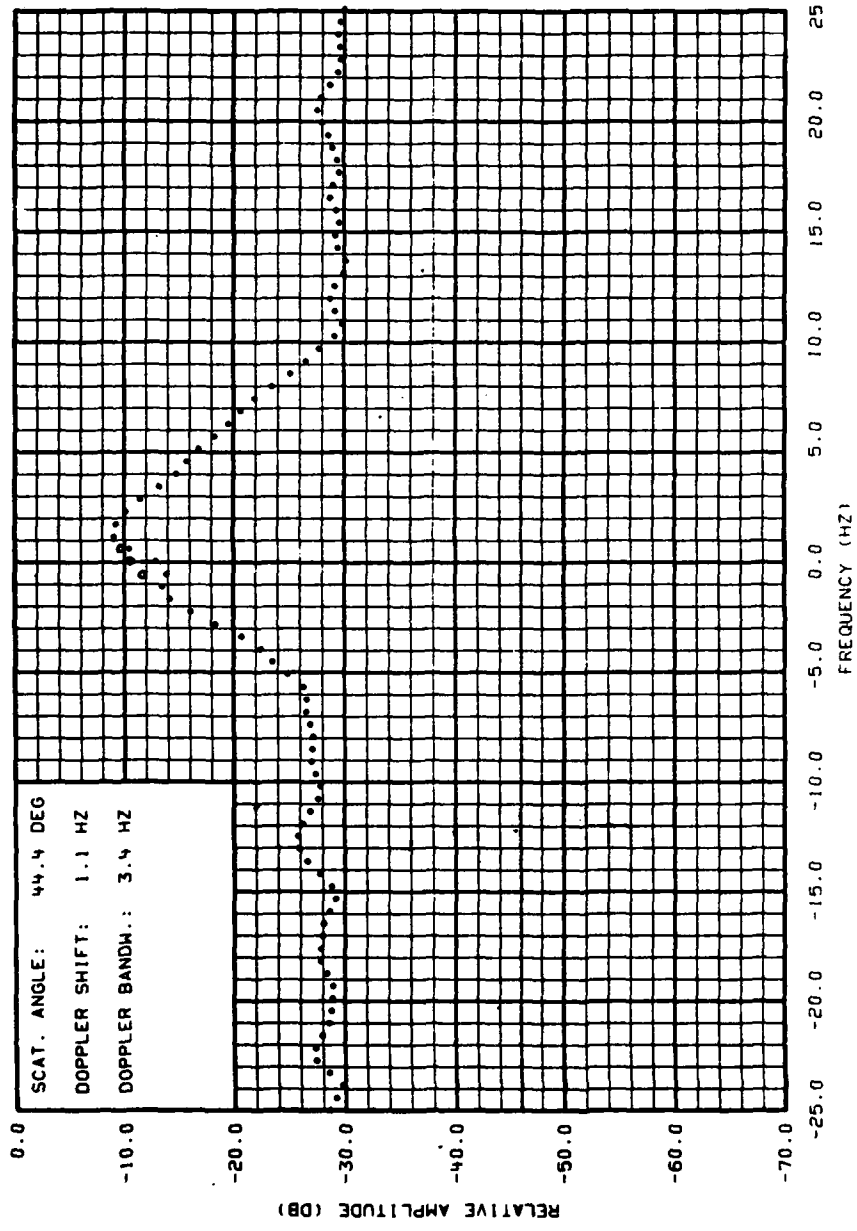


Figure C-57. Doppler Spectrum of Surface Reverberation Obtained at a Transmitted Frequency of 3.5 kHz, an Incident Angle of 40.0°, and an Angle of Scatter of 44.4°. Corrected Spectral Estimates in the Vicinity of Zero Doppler are Represented by Open Circles.

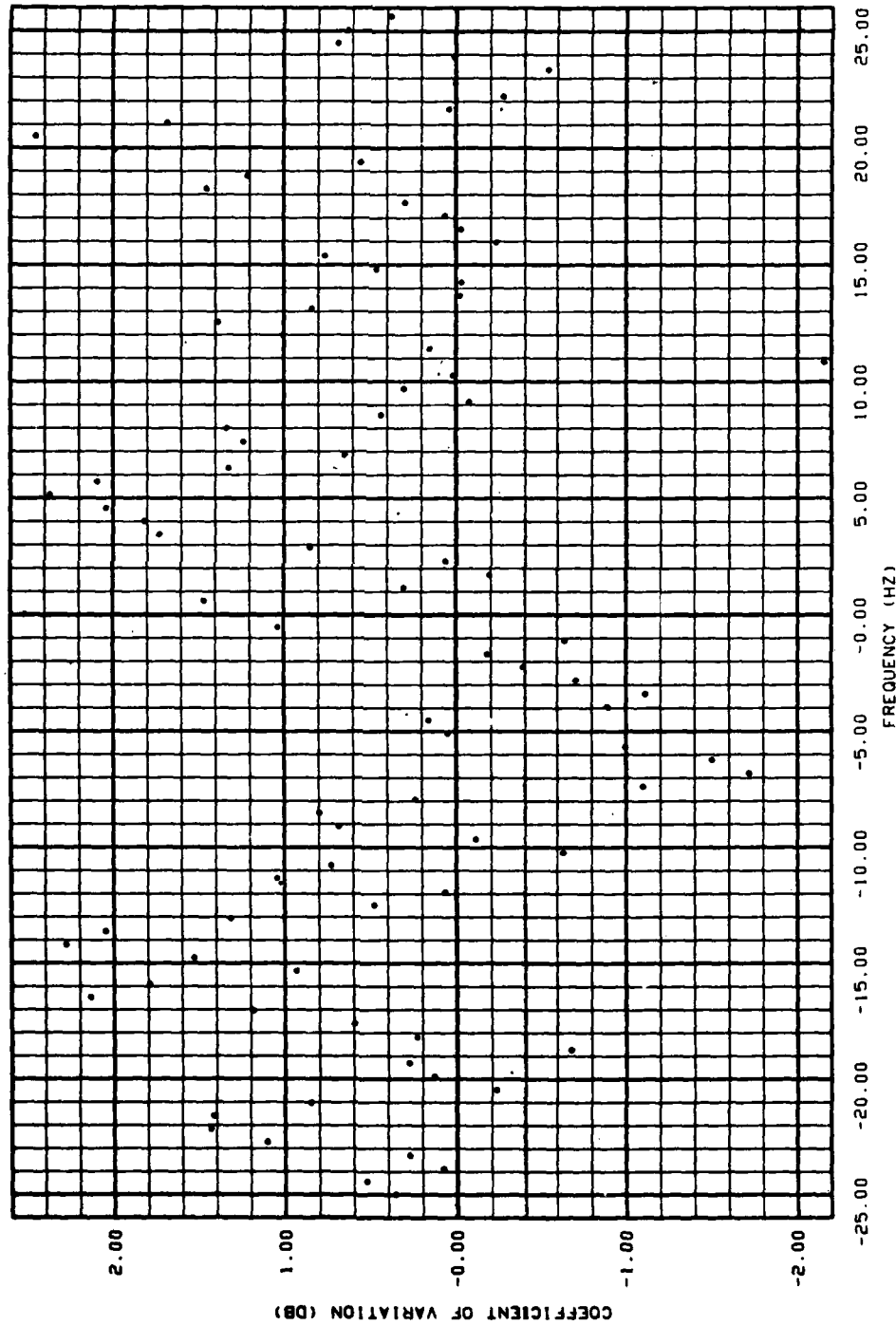


Figure C-58. Coefficients of Variation of the Spectral Estimates Obtained at a Transmitted Frequency of 3.5 kHz, an Incident Angle of 40.00° , and an Angle of Scatter of 44.40° .

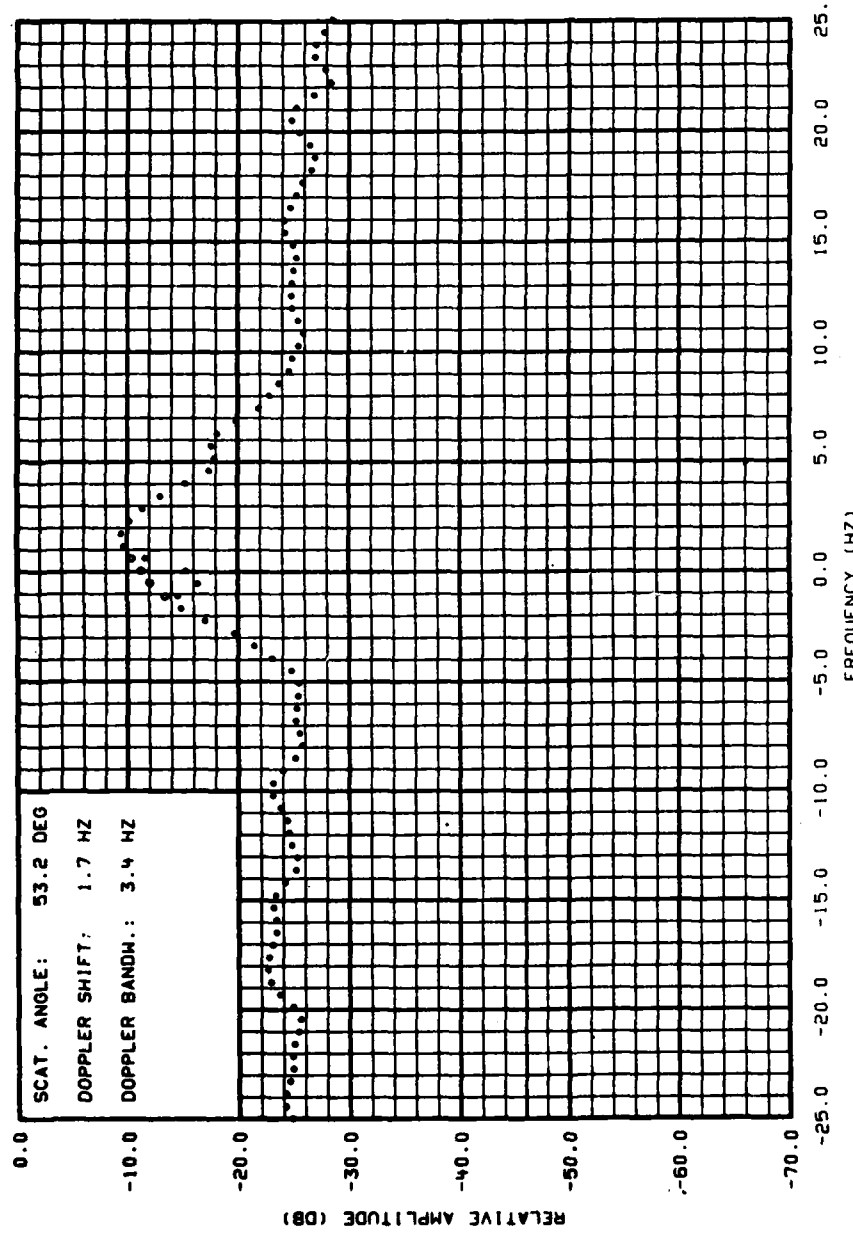


Figure C-59. Doppler Spectrum of Surface Reverberation Obtained at a Transmitted Frequency of 3.5 kHz, an Incident Angle of 40.0°, and an Angle of Scatter of 53.2°. Corrected Spectral Estimates in the Vicinity of Zero Doppler are Represented by Open Circles.

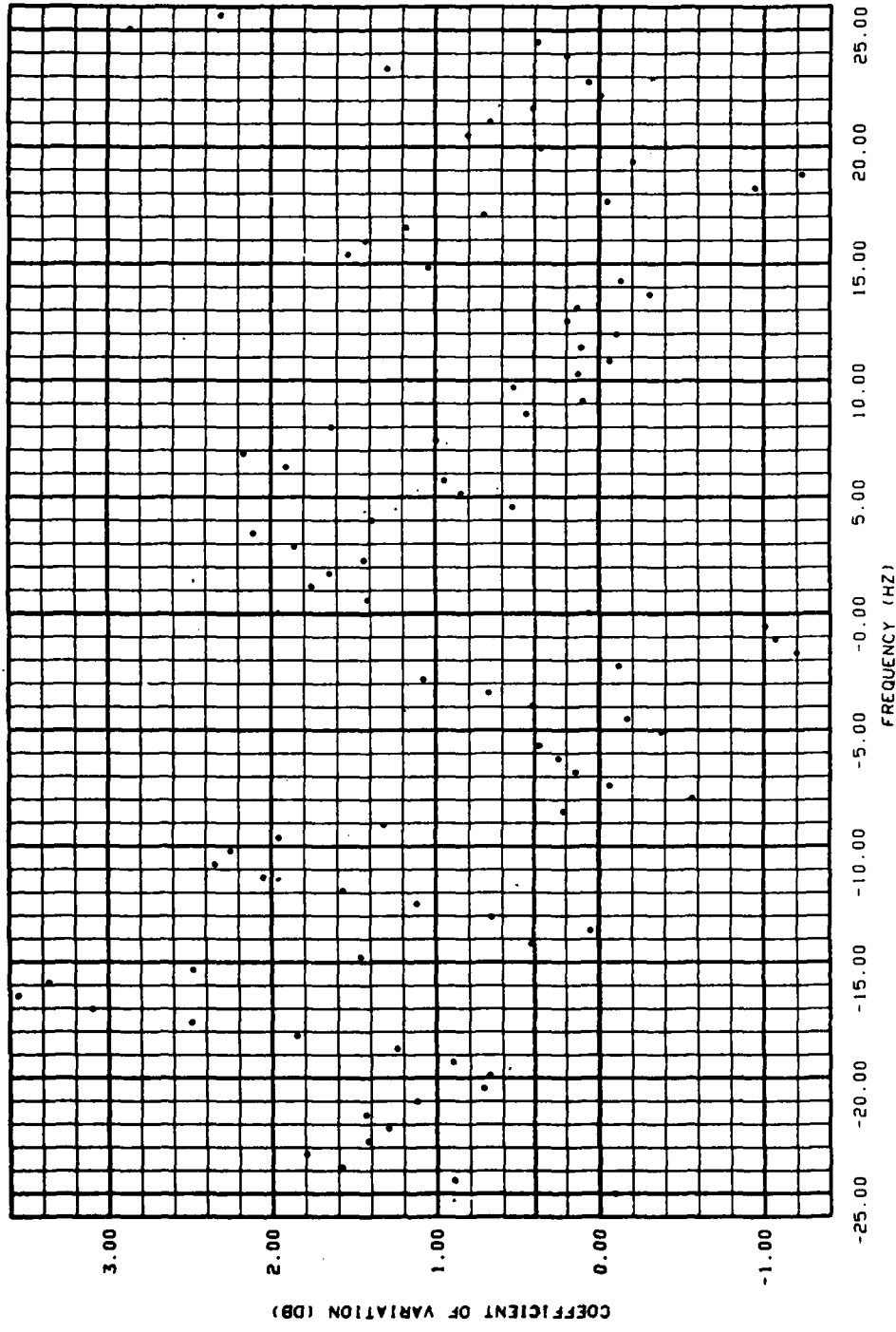


Figure C-60. Coefficients of Variation of the Spectral Estimates Obtained at a Transmitted Frequency of 3.5 kHz, an Incident Angle of 40.0° , and an Angle of Scatter of 53.20° .

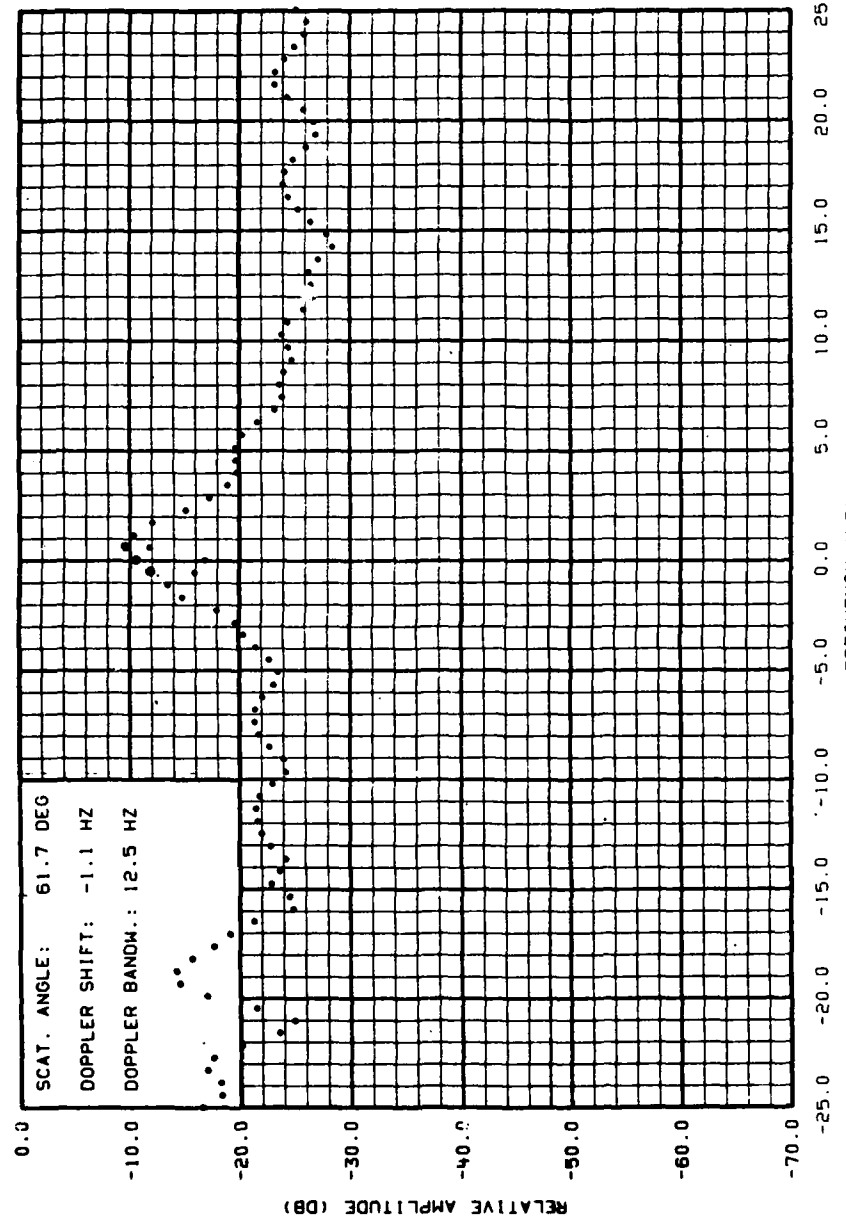


Figure C-61. Doppler Spectrum of Surface Reverberation Obtained at a Transmitted Frequency of 3.5 kHz, an Incident Angle of 60.0°, and an Angle of Scatter of 61.7°. Corrected Spectral Estimates in the Vicinity of Zero Doppler are Represented by Open Circles.

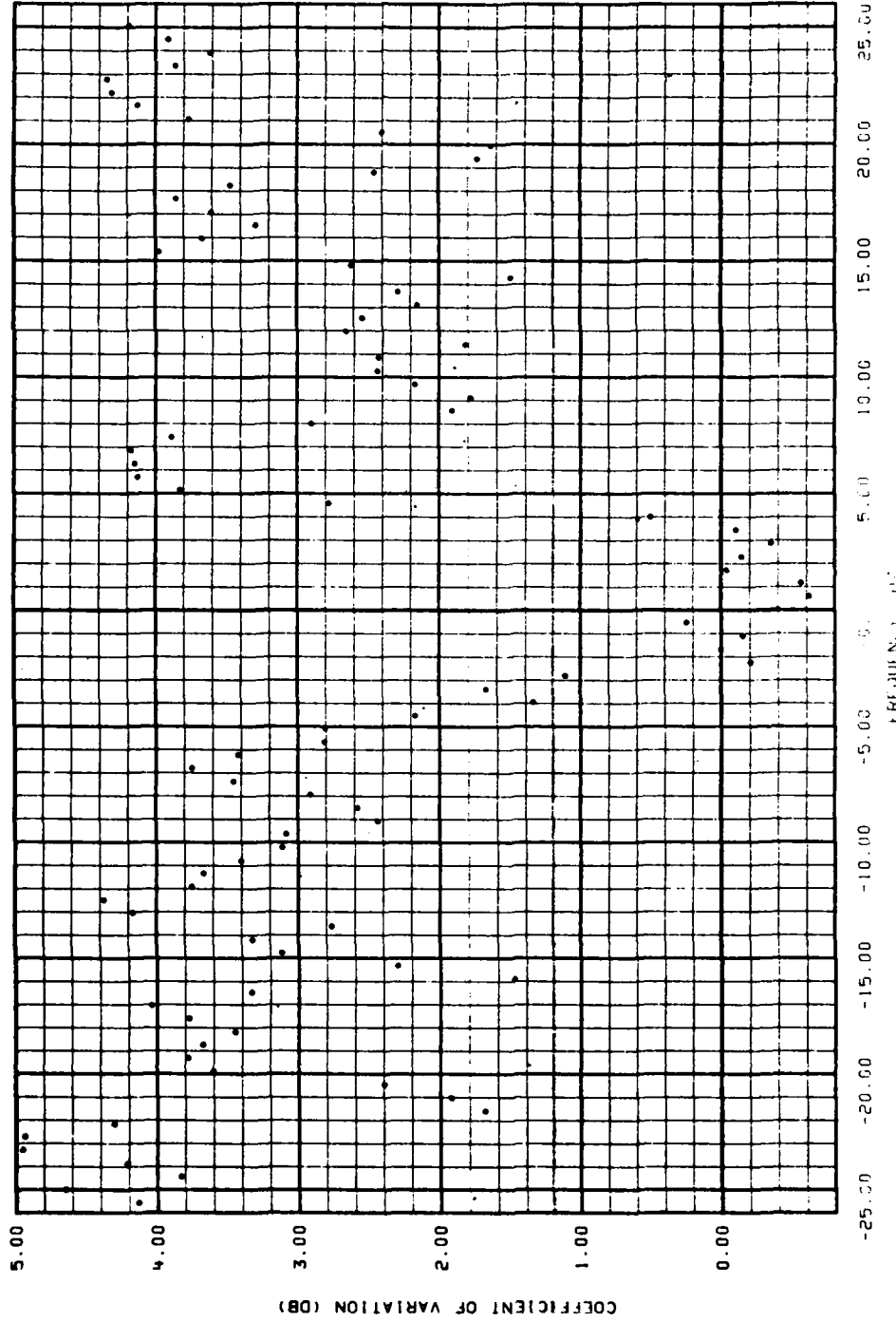


Figure C-62. Coefficients of Variation of the Spectral Estimates Obtained at a Transmitted Frequency of 3.5 kHz, an Incident Angle of 60.0° , and an Angle of Scatter of 61.70° .

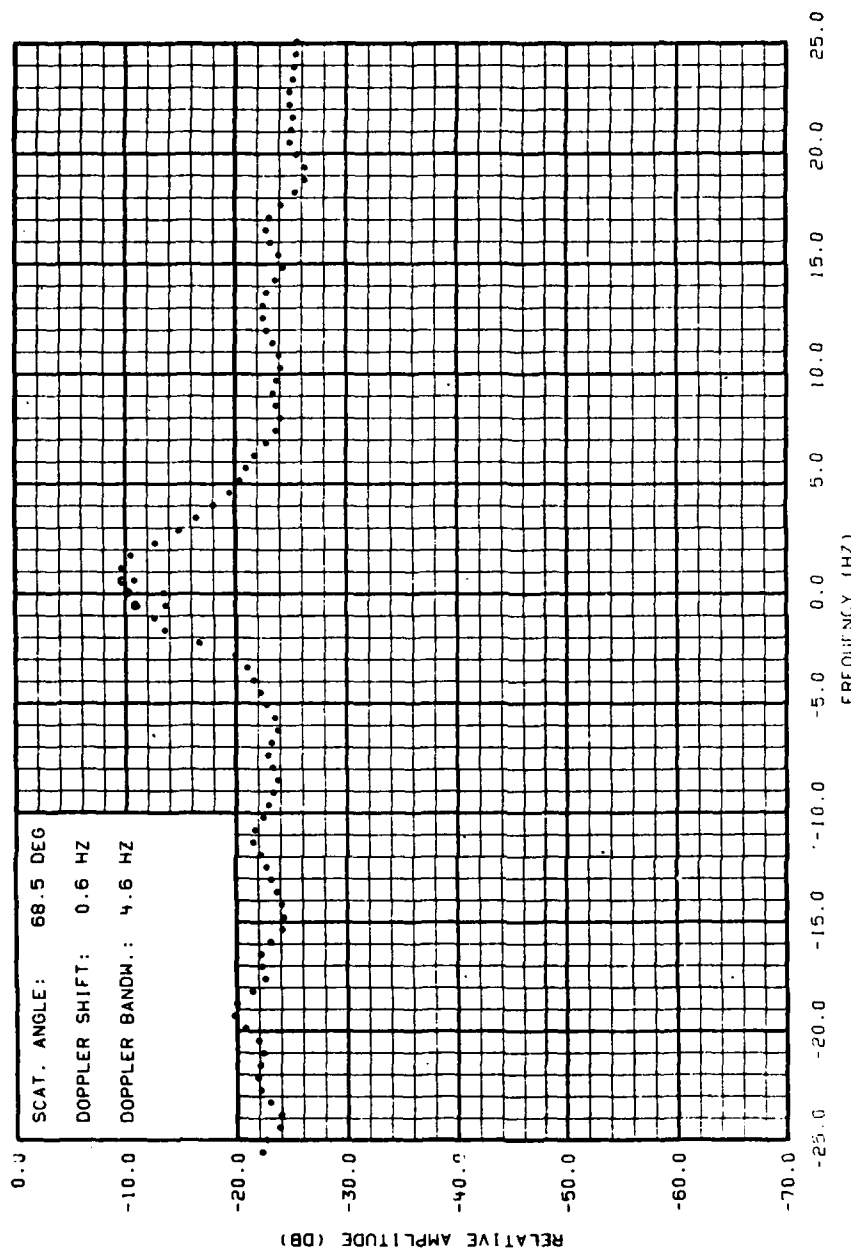


Figure C-63. Doppler Spectrum of Surface Reverberation Obtained at a Transmitted Frequency of 3.5 kHz, an Incident Angle of 60.0° , and an Angle of Scatter of 68.5° . Corrected Spectral Estimates in the Vicinity of Zero Doppler are Represented by Open Circles.

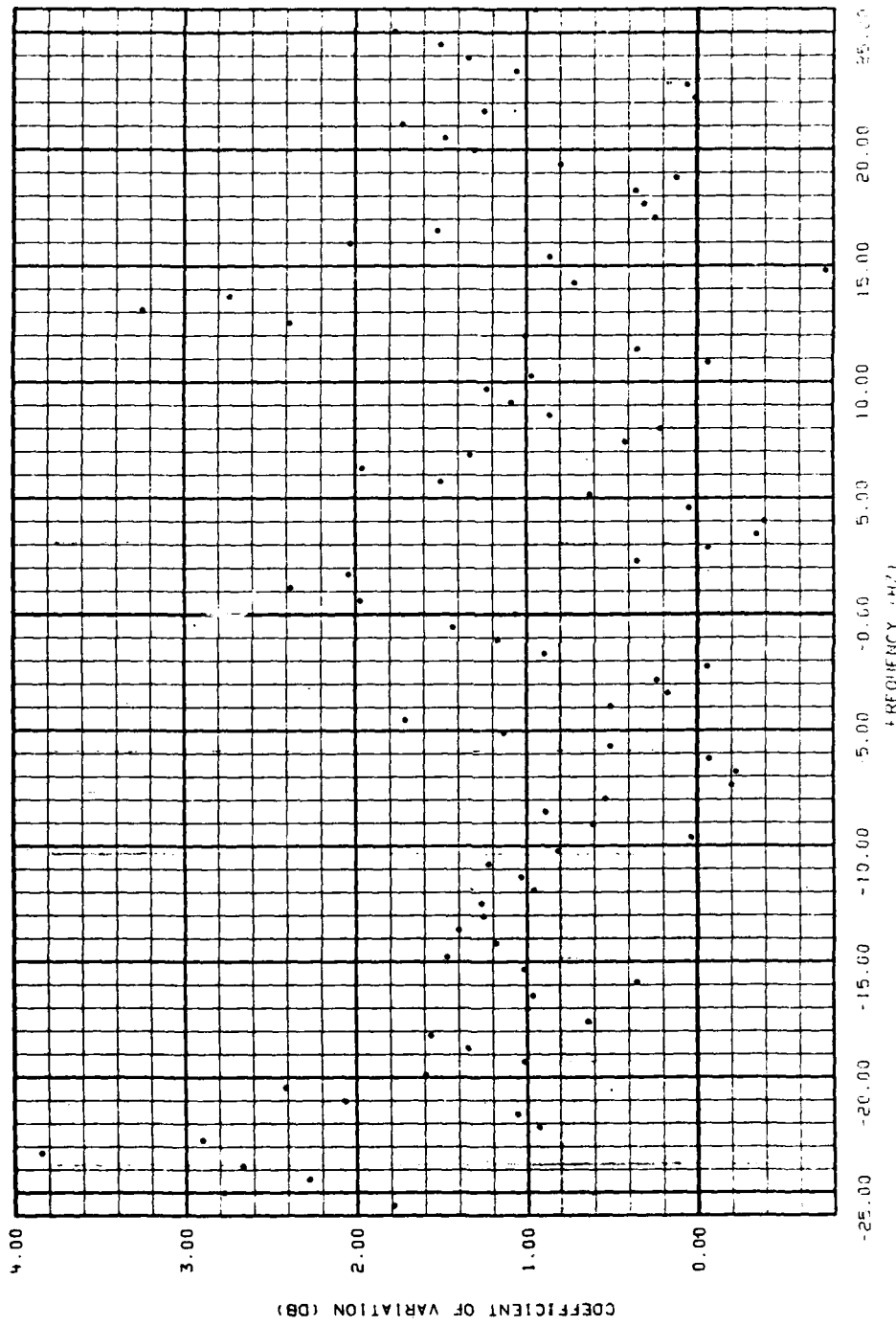


Figure C-64. Coefficients of Variation of the Spectral Estimates Obtained at a Transmitted Frequency of 3.5 kHz, an Incident Angle of 60.0°, and an Angle of Scatter of 68.5°.

APPENDIX D

An Acoustic System for Measuring the Wave Height of Sea Surface Waves¹

ABSTRACT

An upward-looking echo-sounder system has been designed to measure the time varying wave height of sea-surface waves. A narrow beam of pulsed acoustic energy was focused on the sea surface by utilizing the transitional region from the near-to-far field characteristics of a circular piston transducer. The transducer, operating at 360 kHz, was pulsed at 10-msec intervals to sample the wave height. By transmitting short pulse lengths, the wideband characteristics of the transducer were used to discriminate against near-surface bubble reverberation. The system is linear and can presently measure surface wave frequencies below 4.5 Hz. Wave heights as small as .05 inches were measured in a model tank by comparing the echo-sounder results with results obtained from a micrometer. An experiment, conducted in the Thames River, compared the performance of the echo-sounder to a 15-foot resistive wave staff. Comparisons of ensemble-averaged power spectral densities obtained from the wave staff and the transducer, positioned 10 feet below the surface, were excellent for wave frequencies below 4.0 Hz.

INTRODUCTION

Most acoustic measurements of scattering from the sea surface require knowledge of the surface statistics. Depending on the parameters of the surface scattered signals which are being investigated, it may be desired to know either the surface RMS wave height, the one dimensional surface wave spectrum, or more complete information such as the directional wave spectrum.

Presently, there are various techniques used in obtaining sea surface data. Probably the most common and also most incomplete is just a visual observation of sea state. Of the physical measurements, the resistive or capacitive wave staff is the most direct method in obtaining one dimensional data. Other techniques in use include pressure gauges, buoys, accelerometer wave gauges, lasers, and stereophotography. None of the above systems can measure an exact record of the sea surface. The system output is related to the surface waves, but distorted in many ways. The acoustic sensor technique described in this paper also measures a distorted record of the surface waves, but the technique has certain advantages that may find it attractive in your particular surface scattering experiments.

¹ This appendix contains the abstract, text, and figures of a paper presented by the author at the Eighty-Fourth Meeting of the Acoustical Society of America in Miami, Florida on 30 November 1972 [D-1].

These advantages are (1) only a small, light-weight, low power, ultrasonic transducer is required, (2) for most applications no underwater electronics are needed, and (3) an array of transducers can be positioned in a horizontal plane below the surface to measure the directional wave spectrum. At this time the major disadvantage is that a fixed platform is required to support the transducer.

Basically, the acoustic sensor is positioned below the surface at an appropriate depth that is determined by the minimum surface wavelength that is of interest, the acoustic frequency, and the dimensions of the transducer. As with other echo ranging methods, a repetition of short pulses is transmitted. The transducer is gated to receive the echo and the travel time variations are converted to a calibrated voltage that is a linear function of the wave height above the transducer.

ACOUSTIC SENSOR TECHNIQUE

A simplified block diagram of the acoustic sensor's transmit-receiver system is shown in Fig. D-1. A short burst of acoustic energy is transmitted via a transmit-relay. The relay is switched immediately after transmission to the receive mode for reception of the acoustic reflection from the surface. Simultaneously, with the transmitted pulse, a synchronizing pulse is shaped by a Schmitt trigger which is used to set a flip flop. The signal received from the surface is amplified and clipped to permit further amplification. The receiving system must have sufficient gain to overcome a sloped surface. A Schmitt trigger is used as a threshold detector to determine the initial return from the surface and the output is used to reset the flip flop. A low pass filter is used to obtain the time variation of the DC output of the flip flop. The cut off frequency of the low pass filter is 10 Hz such that the frequency spectrum of the surface from 0 to 10 Hz will be received and the spectral lines due to the pulsing at a 10 msec rate will be filtered. The bottom of the figure shows the flip flop output for two typical returns from the surface. R is the range from the transducer to the surface and c is the velocity of sound. The pulse length is simply $2R/c$. If the surface moves to a height $R + \Delta R$, the dc output will change by $2\Delta R/CT$ where T is the repetition pulse period.

It is of prime importance to know what is the effective surface area that contributes to the initial voltage at the receiver. Figure D-2 shows the results for a 360 kHz, 2 inch diameter piston transducer positioned at a depth of 5 ft below the surface. By using the Kirchoff diffraction integral with Fresnel phase approximations it is possible to determine the deviation from geometric acoustics that would be obtained from a finite plane pressure release surface. The actual beam pattern of the transducer in the analysis has been approximated by a Gaussian pattern with the same half power points. The solution from geometric acoustics would predict a pressure magnitude of $1/2 r_{10}$ as the amplitude of a spherical wave reflected from an infinite plane surface, where r_{10} is the depth of the transducer. It can be seen from this graph that the deviation from geometric acoustics has a damped oscillation depending on the number of odd or even Fresnel zones that are insonified on the surface. The radius of the insonified area is approximately 5 inches before the deviation is within 5% of the steady state value $1/2 r_{10}$. Since the

BLOCK DIAGRAM OF
ACOUSTIC WAVE SENSOR

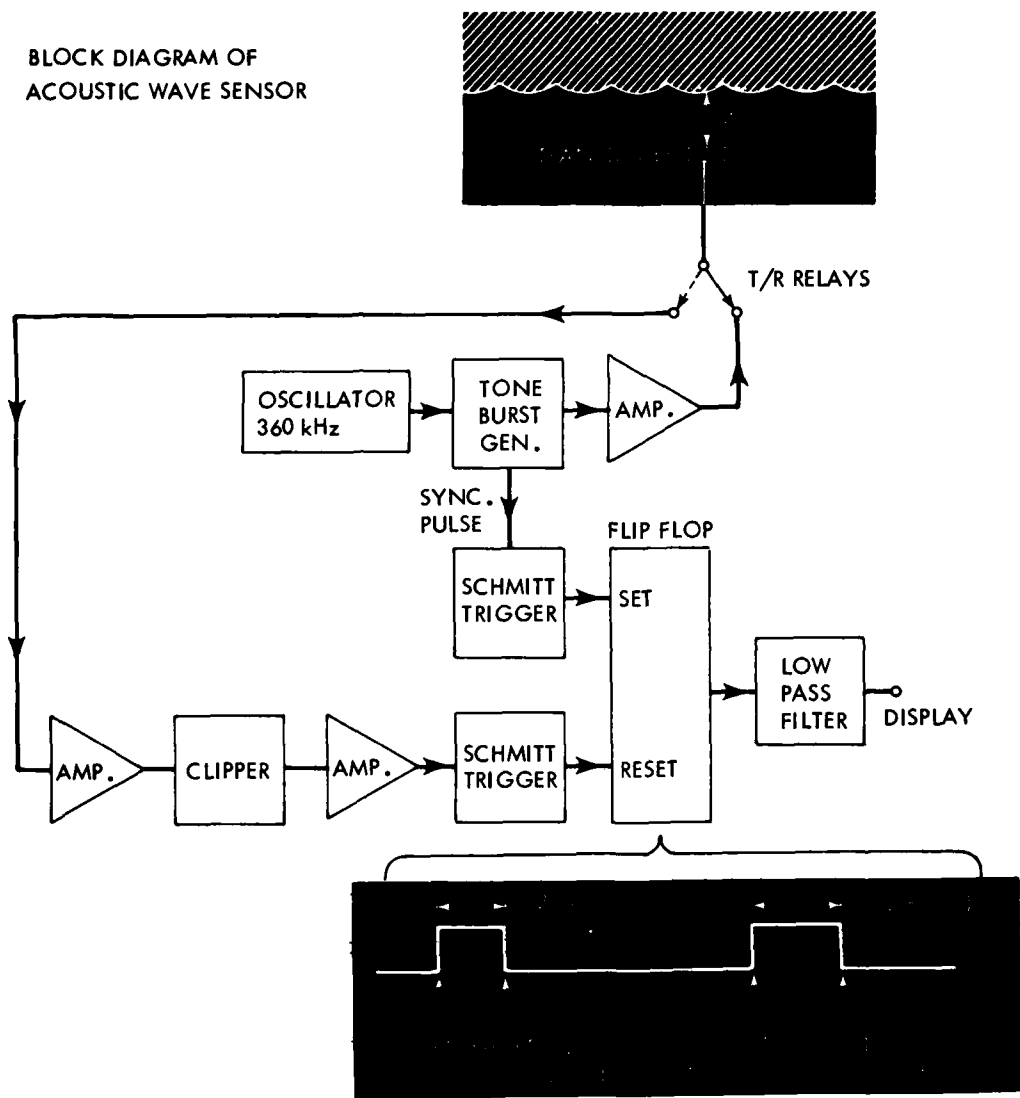


Figure D-1. Simplified Block Diagram of Acoustic Wave Height Sensing System.

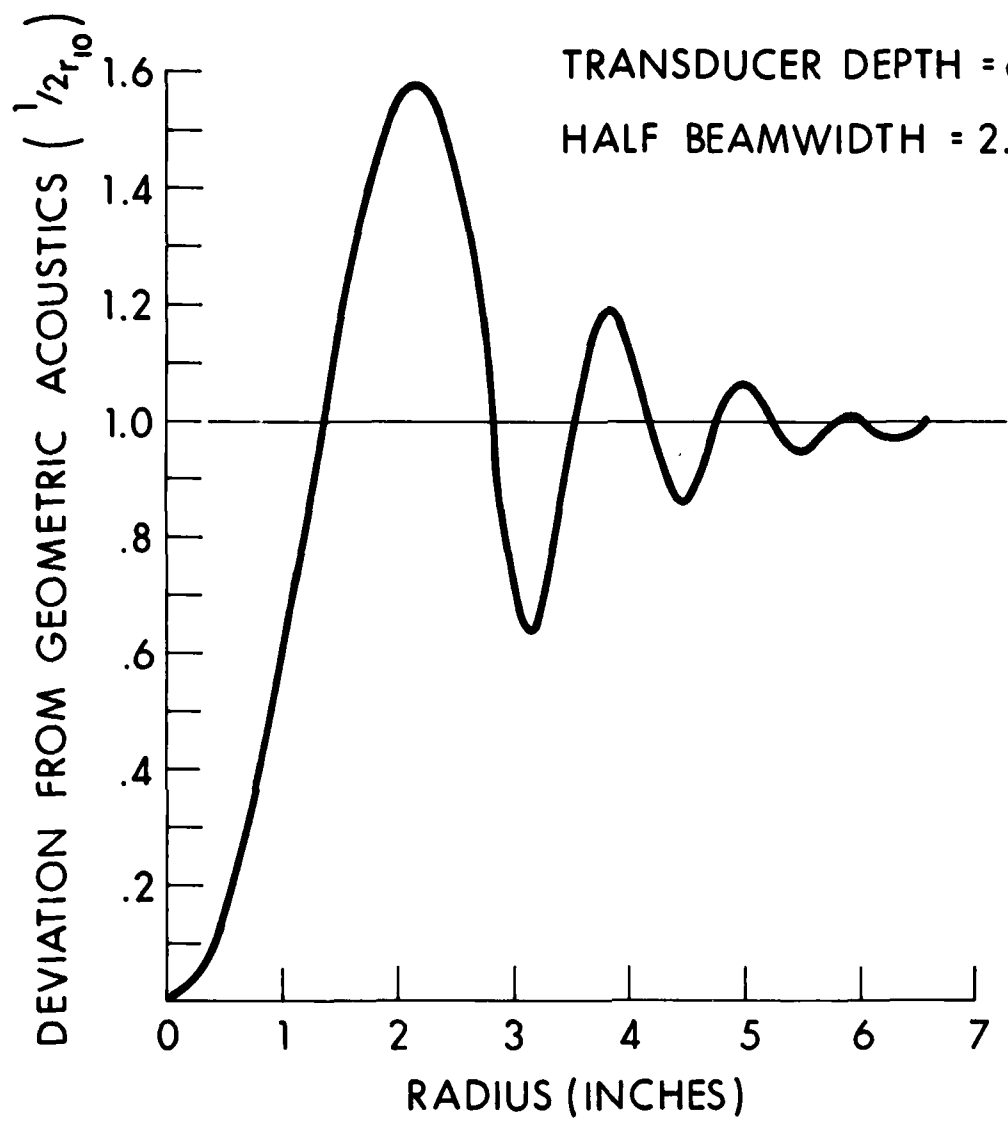


Figure D-2. Deviation of Pressure Amplitude from that Obtained from an Infinite Plane Surface.

threshold detector was set at approximately 1/10 of the steady state value, it is seen that the radius of insonification is less than 1/2 inch.

A narrow beamwidth is desired to eliminate false returns from surface facets off the maximum response axis of the transducer. Also, it is desirable to have a narrow beamwidth and a wideband system frequency response so that reverberation from bubbles will be reduced. Fig. D-3 shows the near to far field characteristics of a circular piston transducer. The figure was reproduced from a January 1971 JASA article by Zemenek. His numerical investigation of the near field region of a vibrating piston showed the interesting result that the -3 dB contour can have a spot size of less than 1/4 the diameter of the piston. Also it was shown that the contour behaves in a regular manner from the far field region to a distance of .75 of a^2/λ from the transducer, where a is the λ radius of the piston and λ is the acoustic wavelength. Therefore, it is possible to insonify an area on the surface with a diameter that is less than the diameter of the piston over a distance that ranges from .75 to 4 of a^2/λ as shown in this figure. Actually, the effective area is much less than this due to the product of the transmit and receive patterns.

MODEL TANK RESULTS

To test the acoustic wave height sensor, an experiment was conducted in a model tank. The crest wave height measurement obtained from the acoustic sensor was compared to the wave height measured from a micrometer. The micrometer was positioned over the insonified area and a micrometer reading from a flat surface was obtained. Waves were then generated from a vibrating plate, and the micrometer was lowered to the surface to obtain a crest height measurement. The upper strip chart recording was obtained from the acoustic sensor. The surface frequency was 3.0 Hz and the input to the vibrating plate generator is shown at the bottom of this figure (Figure D-4). It is evident that the sensor recording is of the same frequency as the generator, however, the crests are narrower than the troughs. This is to be expected because of the trochoidal nature of the surface waves. There is a "knee" in the trough of the surface wave recording. This is thought to be due to the insonified diameter on the surface being only about 1/7 the wavelength of the surface waves. For this recording the micrometer reading of the crest wave height was .28 inches and the acoustic sensor recording was .36 inches. Other comparisons of wave records have been made and closer agreement was found.

WAVE STAFF COMPARISON

The acoustic sensor was then compared to a 15-foot resistive wave staff. The transducer was positioned at a depth of 10 feet below the surface and at a horizontal distance of approximately 1 foot from the suspended wave staff. The experiment was conducted in the Thames Estuary, New London, Connecticut. The purpose of the experiment was to compare wave records. A typical comparison is shown in Fig. D-5. It can be seen there is good correlation between the two system outputs. Data were also recorded on magnetic tape for later processing to compare the power spectral densities of each technique.

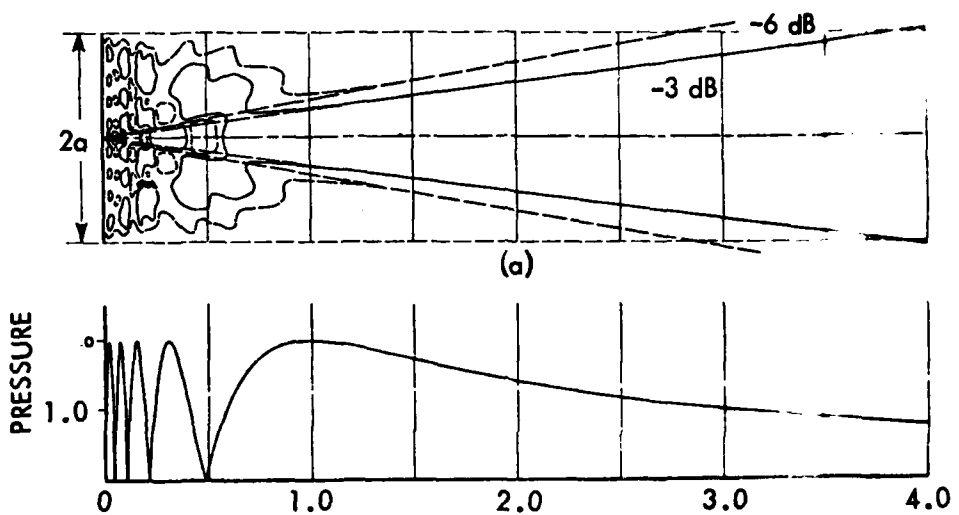


Figure D-3. Near-to-Far Field Characteristics of a Circular Piston Transducer (Taken from J. Zemanek [D-1])

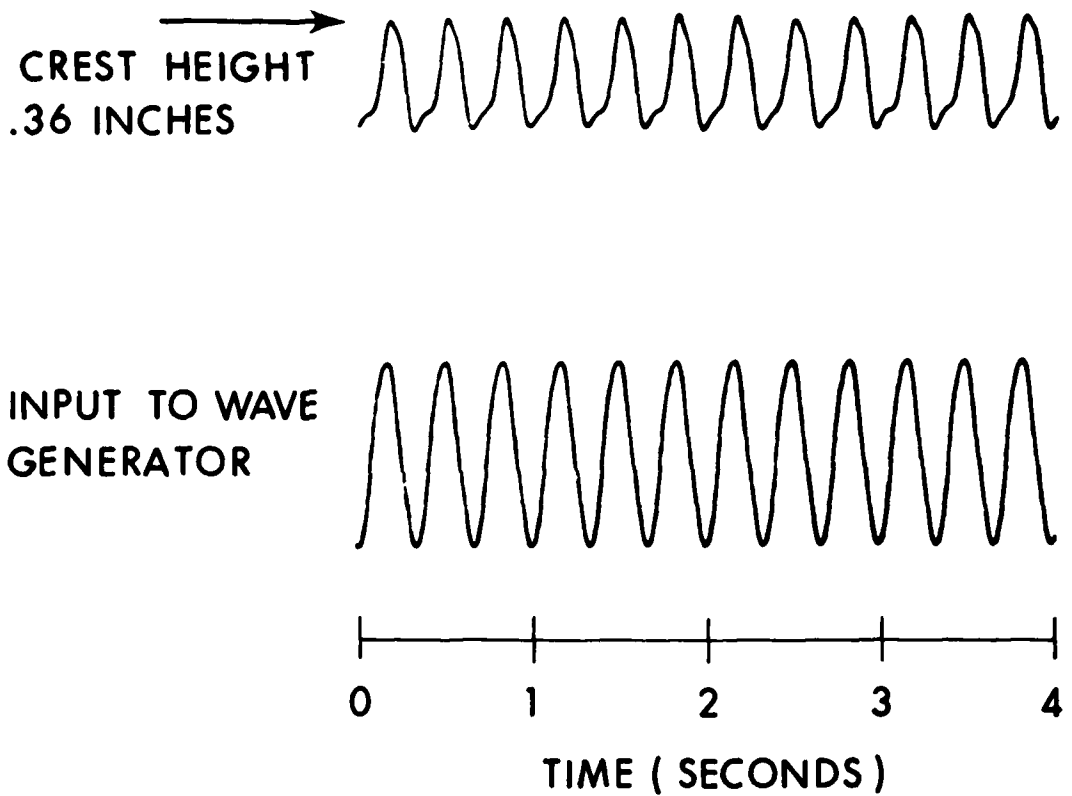


Figure D-4. Wave Height-Versus-Time Output of Acoustic Sensing System.

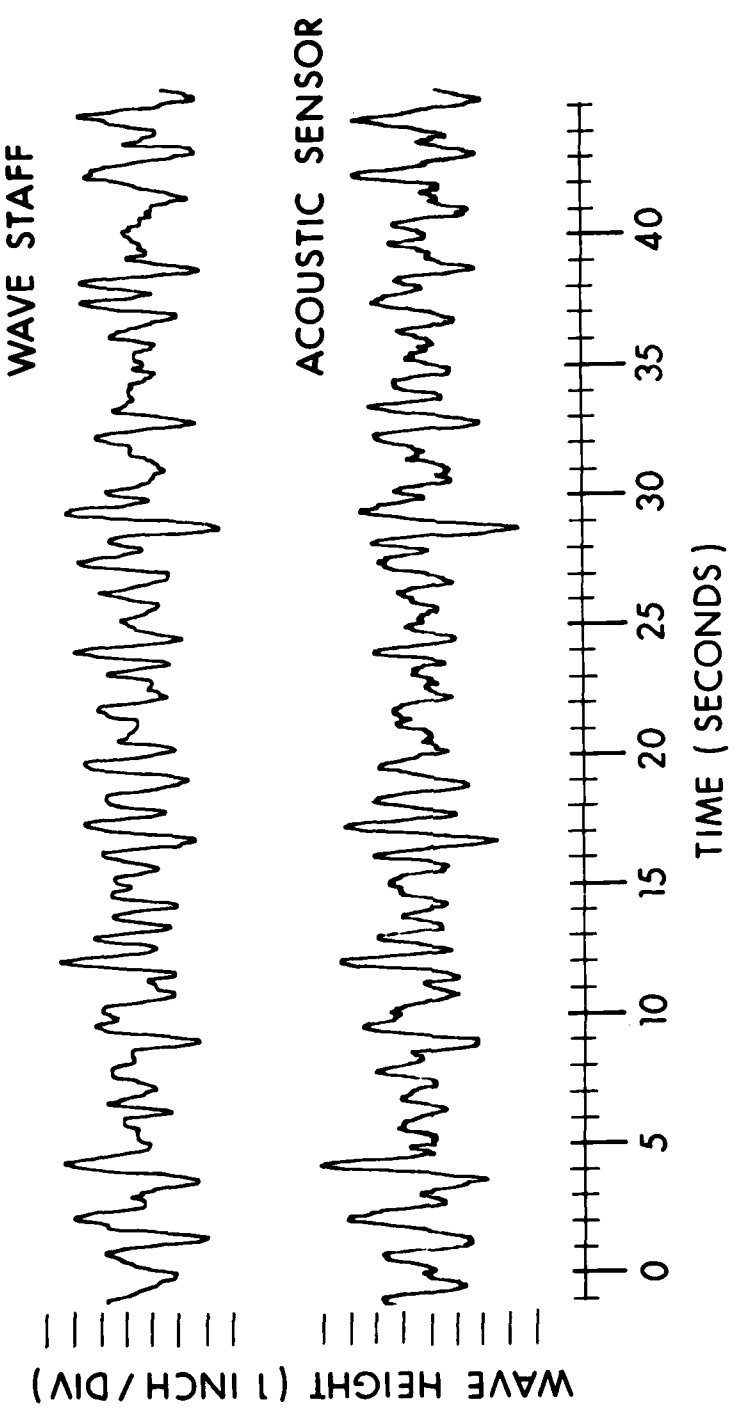


Figure D-5. Comparison of Wave Height Records Measured by Resistive Wave Staff and Acoustic Wave Height Sensing System.

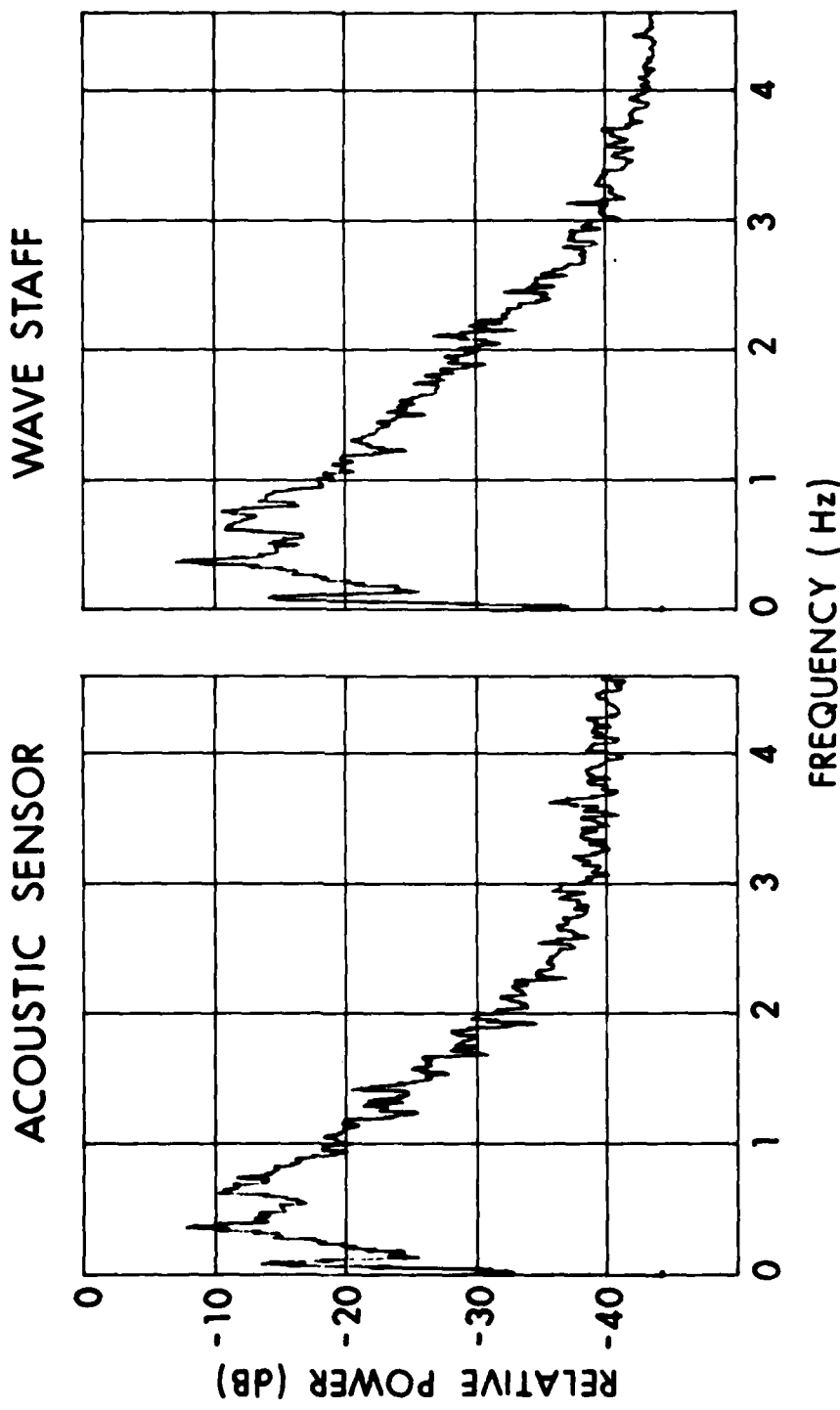


Figure D-6. Comparison of the One-Dimensional Surface Wave Spectrum Obtained from Data Measured by the Resistive Wave Staff and the Acoustic Wave Height Sensing System.

A comparison is shown in Fig. D-6 of the ensemble power spectral densities of surface waves measured in the Thames Estuary. Each of the spectra is represented by an ensemble average of 15 individual spectra obtained from 50 second records. The spectral resolution is .03 Hz and there are 30 degrees of freedom in each ensemble. There is excellent agreement between the two techniques from 0 to 3 Hz. Above 3 Hz, the acoustic sensor shows slightly more energy in the spectra.

There are some general observations that can be made concerning the electrical and acoustical parameters for an acoustic wave measuring system:

- (1) The system must be high gain to overcome tilted surfaces that reflect energy off the maximum response axis of the transducer.
 - (2) The system must be wideband such that short pulses can be transmitted to reduce reverberation from near surface bubbles.
 - (3) The pulse repetition rate must be fast enough to sample the surface at a rate higher than the Nyquist sampling frequency. However, the repetition rate must be slow enough to permit multiple reflections between the transducer and the surface to die out before the next transmission.
- and (4) The choice of transducer dimensions, acoustic frequency, and transducer depth should be based on insonifying a small spot size on the surface. The near to far field characteristics of acoustic transducers should be considered for this purpose.

CONCLUSIONS

An acoustic sensor has been evaluated by comparison with other techniques. The ensemble average power spectra comparison with a wave staff output showed excellent agreement. Plans have been made to use an array of acoustic sensors to obtain the directional wave spectrum of the sea surface. The advantages of using an acoustic wave measuring system should make it an attractive technique for obtaining sea surface statistics.

APPENDIX E

A FIVE SENSOR ACOUSTIC SYSTEM FOR MEASURING SURFACE WAVE DIRECTIONALITY

The previous appendix described the acoustic system for measuring the time varying wave height at a discrete point above the transducer. In this appendix, a description is given of the five sensor acoustic system that measures wave heights at five discrete points.

The directional characteristics of the surface waves were estimated from a horizontal line array of nonlinearily spaced inverted fathometers. The sparse line array was mounted to a tower at a depth of approximately 3 m below the mean low tide level. Five identical EDO Weston (Model 455-5.5) circular piston transducers with 4 cm diameters were used in the array. The transition regions of the near-to-far field characteristics of the transducers were used to insonify spot sizes on the surface-spot sizes that were smaller than the piston diameters.

Each transducer of the wave sensing system was individually and sequentially pulsed at a transmit frequency of 455 kHz over separate coaxial cables. The transducers had electrical-to-acoustical power conversion efficiencies of approximately 55 percent, receiving sensitivities of -183 dB//1 volt/1 μ Pa, and impedances similiar to the 50 ohm characteristic impedances of the coaxial cables. Nominally, 8 cycles of 455 kHz were transmitted at a voltage peak level of 60 volts at the cable input (cable losses were approximately 11 dB/km). The number of cycles transmitted was switchable in binary units and was dependent on the level of bubble (volume) reverberation.

The pulsing sequence began as follows: A transducer was pulsed, switched to a receive mode, and the surface reflected signal was received. After a delay of 10 msec from the initial transmission, the next transducer was pulsed and the surface reflected signal was received. This procedure continued for each transducer such that the surface was 'sampled' at a period of 50 msec above each of the five transducers. A bistable device (flip-flop) was set on each transmitted pulse and reset by the initial reflection from the sea surface. The bistable output pulse length was modulated by the changing wave height above the transducer. The wave height variations were extracted from the pulse length modulation by a low pass filter having a cut-off frequency of 3 Hz. Each of the five low pass filter outputs was FM recorded on the Honeywell tape recorder (see CHAPTER 4).

A simplified block diagram of the five sensor wave measuring system is shown in Fig. E-1. Control signals were required for synchronizing the transmit and receive systems. That is, control signals were used to (1) generate a pulsed 455 kHz carrier with appropriate repetition period and pulse length, (2) close a transmit relay prior to pulse transmission and inhibit activation of other transmit relays, (3) set the main flip-flop coincident with each pulse transmission, (4) close the corresponding receive relay following

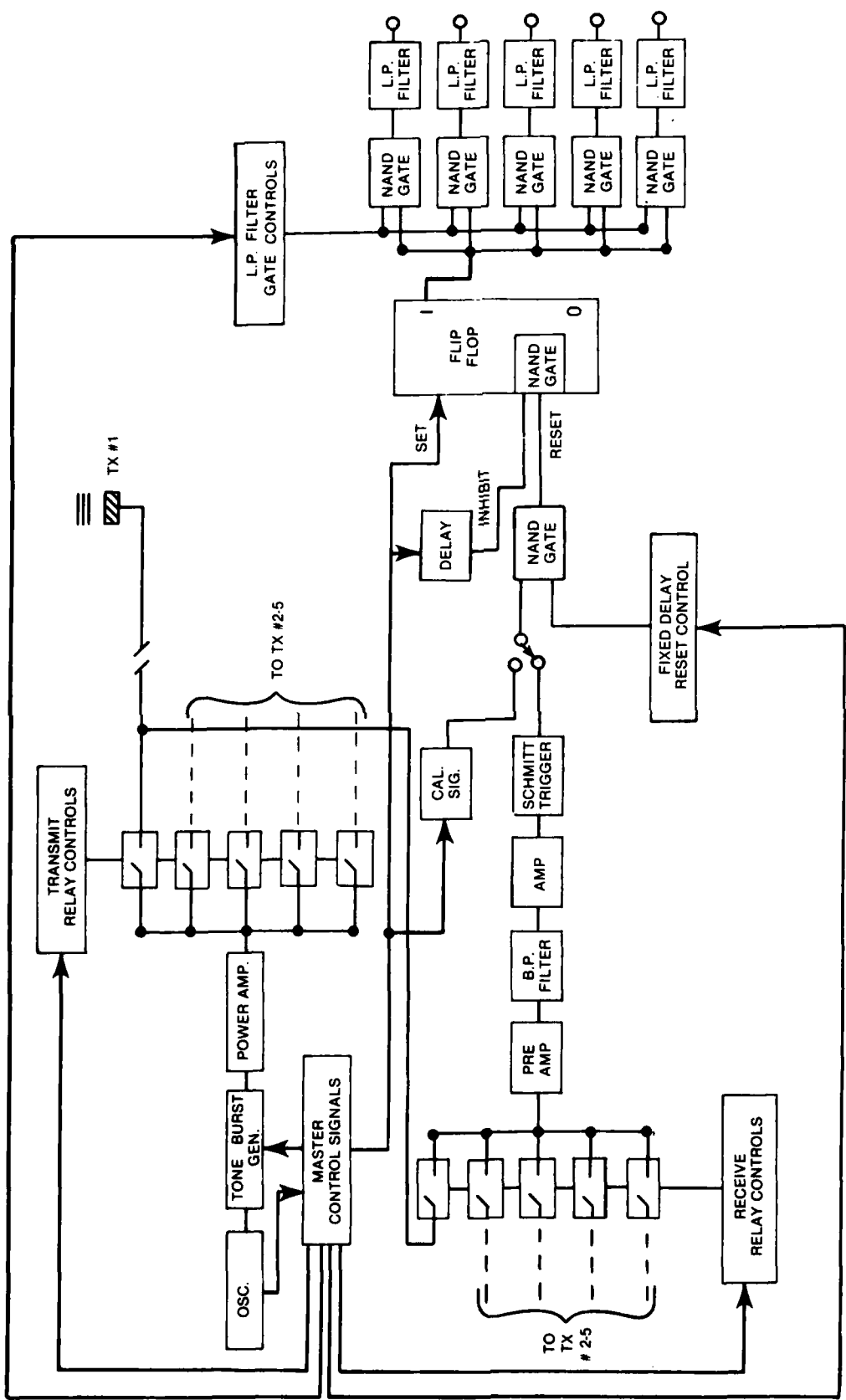


Figure E-1. Simplified Block Diagram of Five Sensor Acoustic Wave Height Measuring System.

transmission, and (5) direct the pulse modulated waveform at the flip-flop output to the appropriate low pass filter via a NAND gate.

The control signals consisted of pulse waveforms having voltage levels of -6 volts (a logic ONE) or 0 volts (a logic ZERO). Computer Control Company (3C) modules were used to generate the required waveforms for the timing and synchronization. The modules consisted of diode-coupled transistor logic circuits (mounted on printed circuit boards) that performed the functions of NAND gates, flip-flops, one-shot multivibrators, solenoid drivers, Schmitt triggers, and dividers. The circuits were compatible such that one circuit could drive another. The modules were fitted into a container with receptacles that form a front panel pinboard arrangement. The modules were interconnected on the pinboard to implement the wave height measuring system.

To generate the outgoing pulses, the master control signal was used to trigger the external timing of the tone burst generator. The trigger signal was obtained by shaping the 455 kHz oscillator signal into pulses compatible with the 3C modules. The shaped oscillator output was frequency divided by two separate networks: a divide by 4560 network determined the (approximate) 10 msec repetition period, and a binary divide (4, 8, ..., 128) determined the number of cycles gated through the tone burst. A rotary switch selected the number of cycles for transmission. The control signal also set the main flip-flop that was subsequently reset by the initial reflection from the sea surface (see APPENDIX D for details). Furthermore, the master control signal provided the appropriate timing for the control of relays, gates, and system calibration.

The tone burst output fed the five transmit relays; however, the transmit relay controls, synchronized to the master control, determined the closing of each relay in sequence. Thus, only one relay was pulsed every 10 msec. Fast switching Dual-Inline magnetic reed relays were used for both transmission and reception. The coils were driven from a modified BCD counter for closing the appropriate transmit and receive relays in sequence. The transmit relay was closed 2 msec prior to pulse transmission to avoid interferences from relay 'actuate and bounce' times.

An inhibit signal of 250 μ sec duration prevented the main flip-flop from being reset by signal leakage into the receiving system during transmit.

The surface reflected signal was amplified, bandpass filtered, further amplified, and the initial return from the surface was detected with a Schmitt trigger. The flip-flop was reset by either the surface return or a 'false return' introduced by a fixed delay reset control signal. The false return was provided to reset the flip-flop in case there was no surface reflected signal.

The pulse length modulated output of the main flip-flop was directed to the appropriate low pass filter output via a NAND gate. Control signals were used at each gate to direct the flip-flop output. The gate signals were synchronized with the receive relay signals. Low pass filters rejected the periodic pulse harmonic frequencies and passed the time varying direct current signal which was proportional to the wave height variations above the transducer.

The wave measuring system could easily be calibrated by positioning a toggle switch into a calibration mode. In this mode, the main flip-flop was reset approximately 6 msec after transmit. This pulse length was compared to the flip-flop output pulse length (8 msec) that was obtained from the 'false return.' The pulse length difference was measured on the delayed-sweep of an oscilloscope and the corresponding change in DC output from the low pass filters was also measured. The change in wave height was obtained by multiplying the change in pulse length by one-half the sound speed. As a final note, the average DC value was removed by providing a DC offset voltage at the filter input.

APPENDIX F

DIRECTIONAL SPECTRUM OF THE SEA SURFACE

High resolution estimates of the directional spectrum of the surface waves are provided in this appendix. For details concerning the computational procedures, refer to Chapter 7.

The spectral estimates are based on wave height data which was measured while the winds were from a westerly sector ($270\text{--}290^\circ$) at an approximate speed of 5 m/sec.

The line array of wave height sensors was oriented on a bearing of 008° relative to magnetic north and broadside to the array was on the same bearing (278°) as the maximum response axis of the parametric source.

Directional estimates are presented with respect to the counterclockwise rotation of the azimuthal angle between the array and the normal to the approaching wavefronts. An azimuthal angle of 0° corresponds to waves approaching at 008° relative to magnetic north and waves approaching broadside to the array have an angle of 90° with respect to the array and 278° with respect to magnetic north. Estimates are provided in angular increments of 5° at discrete frequencies separated by 0.033 Hz over the frequency band 0.1 to 1.2 Hz. The legend at the upper right of each figure contains the surface frequency (F), the surface wavelength (W) and a factor (P) that normalizes the peak value in each spectrum to a value of unity.

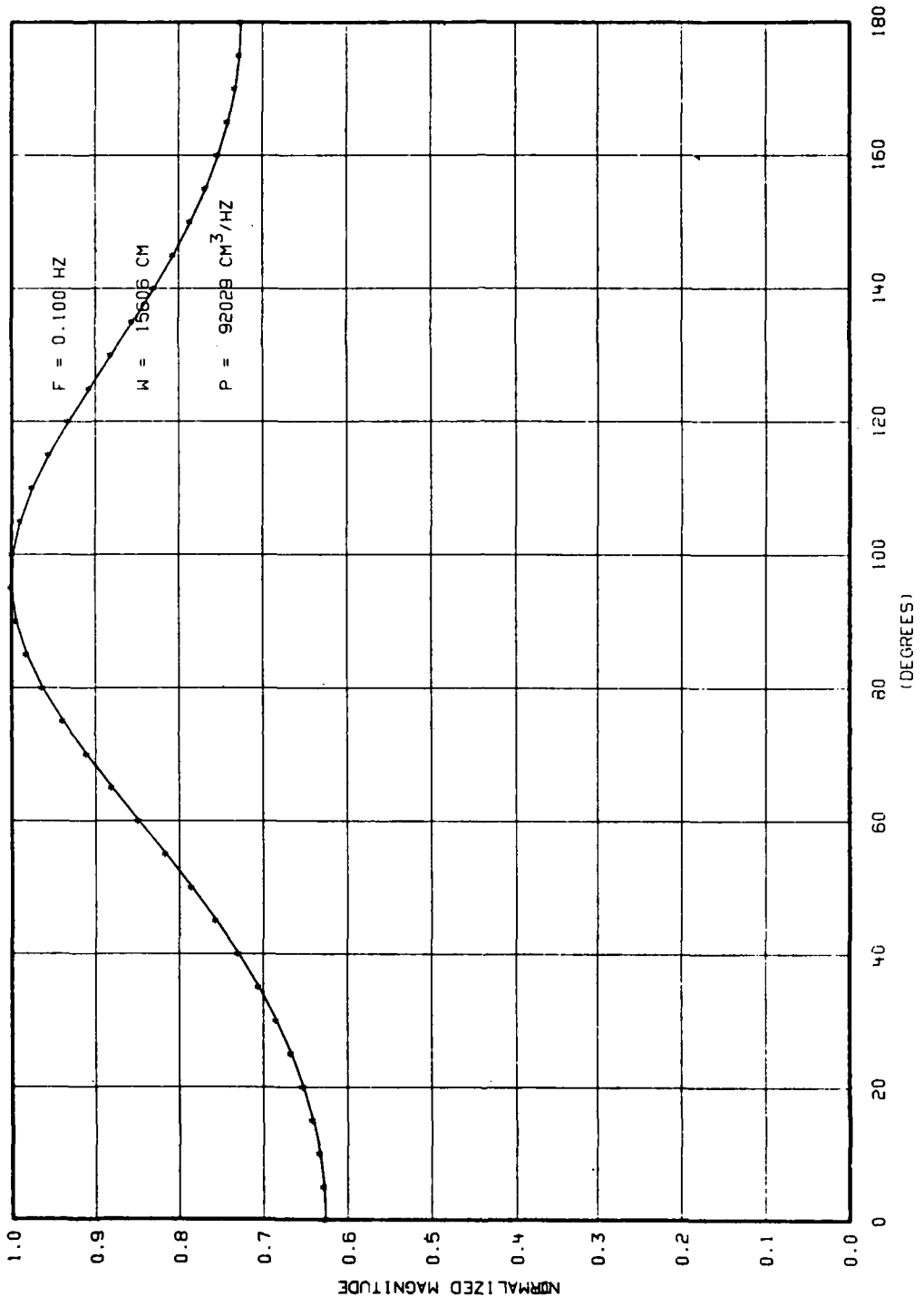


Figure F-1. Directional Spectrum for a Surface Wave Frequency of 0.100 Hz.

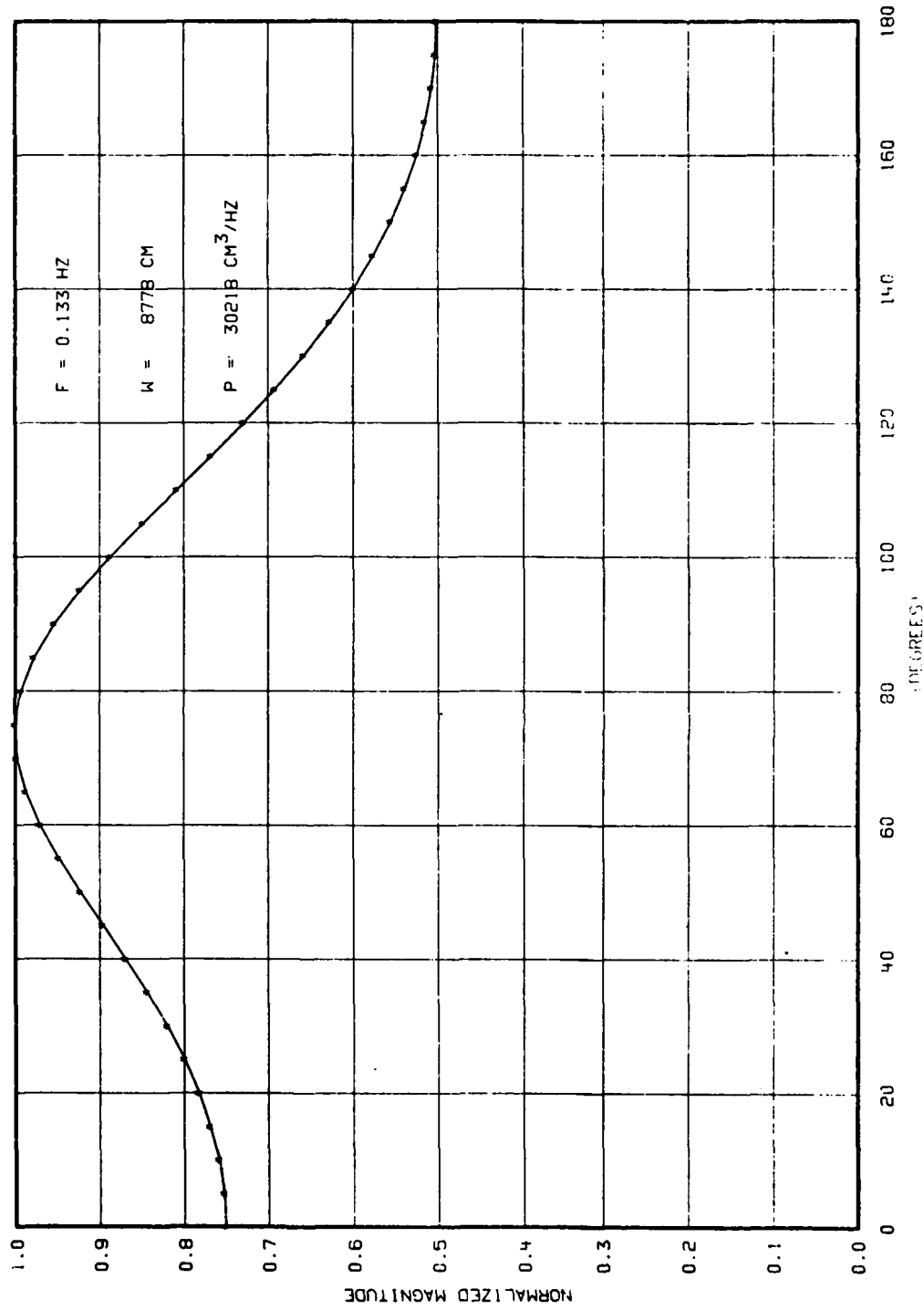


Figure F-2. Directional Spectrum for a Surface Wave Frequency of 0.133 Hz.

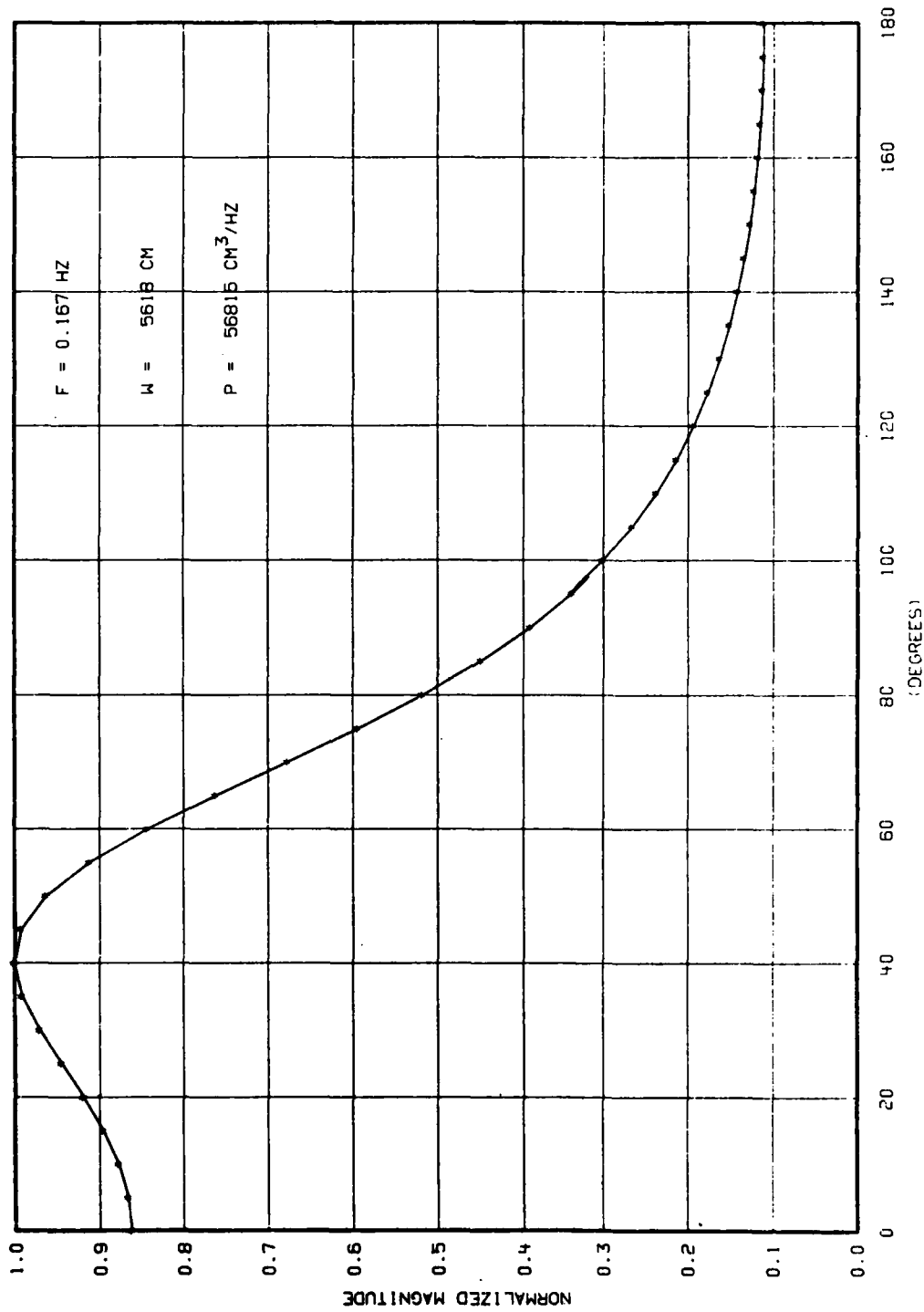


Figure F-3. Directional Spectrum for a Surface Wave Frequency of 0.167 Hz.

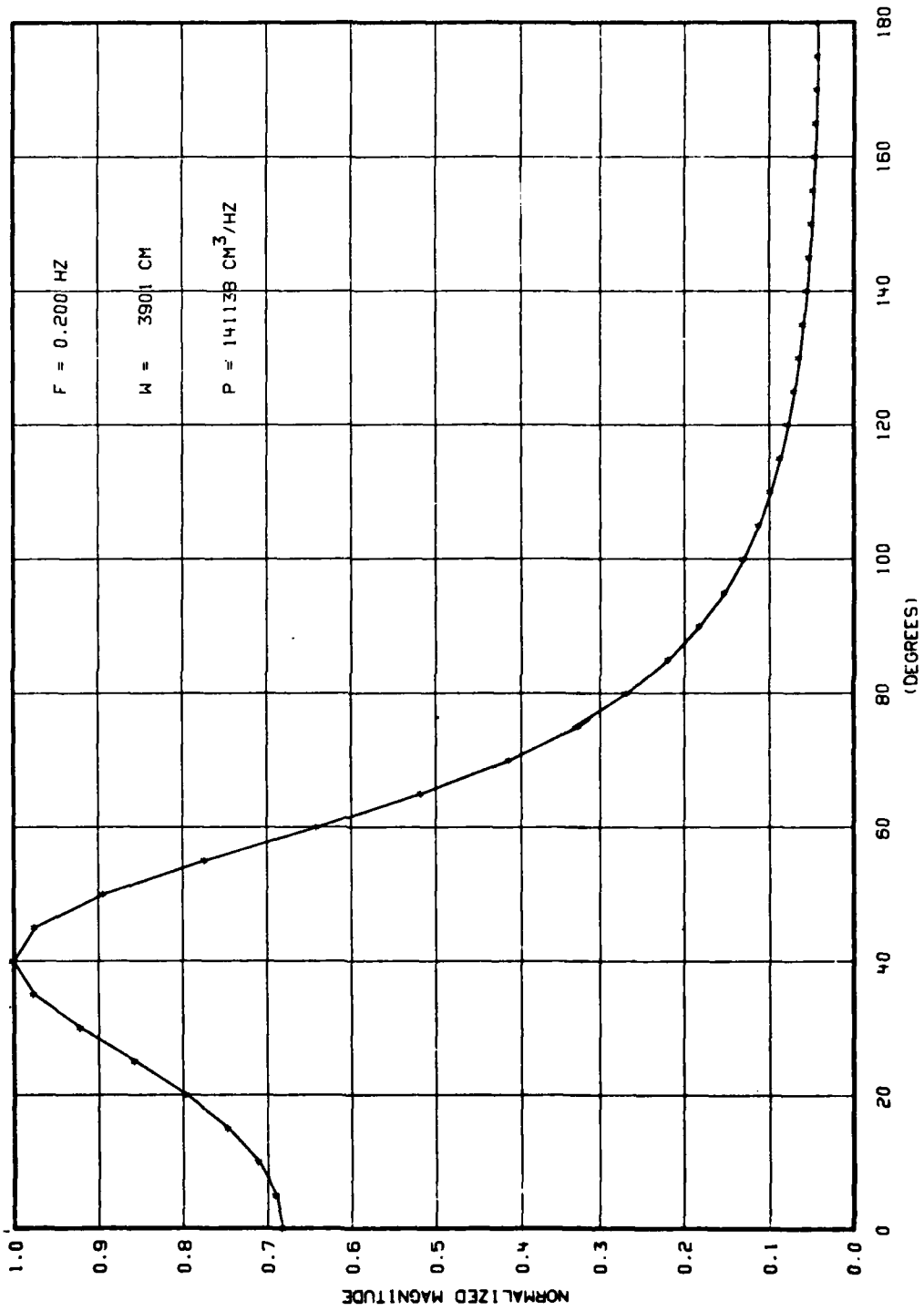


Figure F-4. Directional Spectrum for a Surface Wave Frequency of 0.200 Hz.

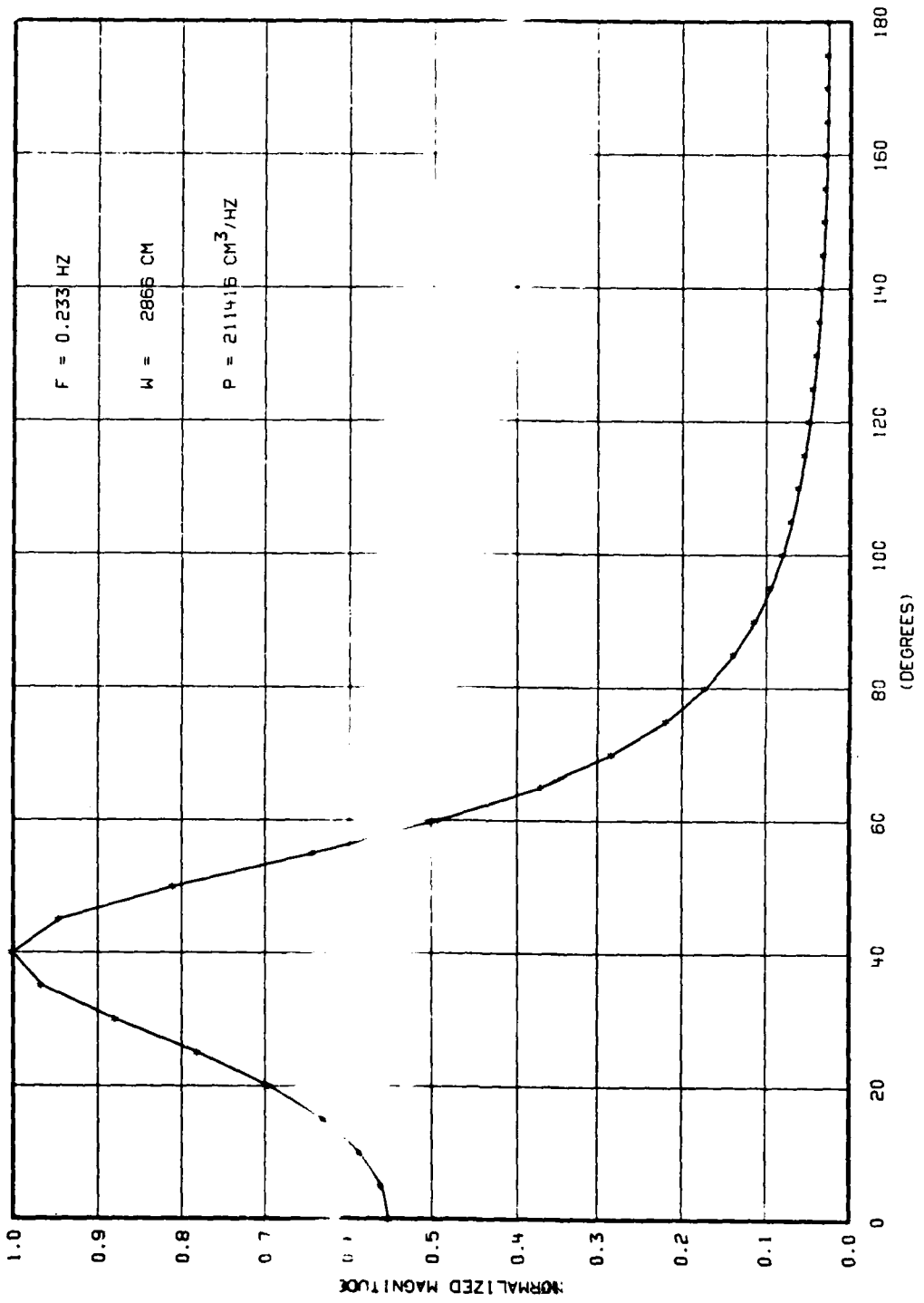


Figure F-5. Directional Spectrum for a Surface Wave Frequency of 0.233 Hz.

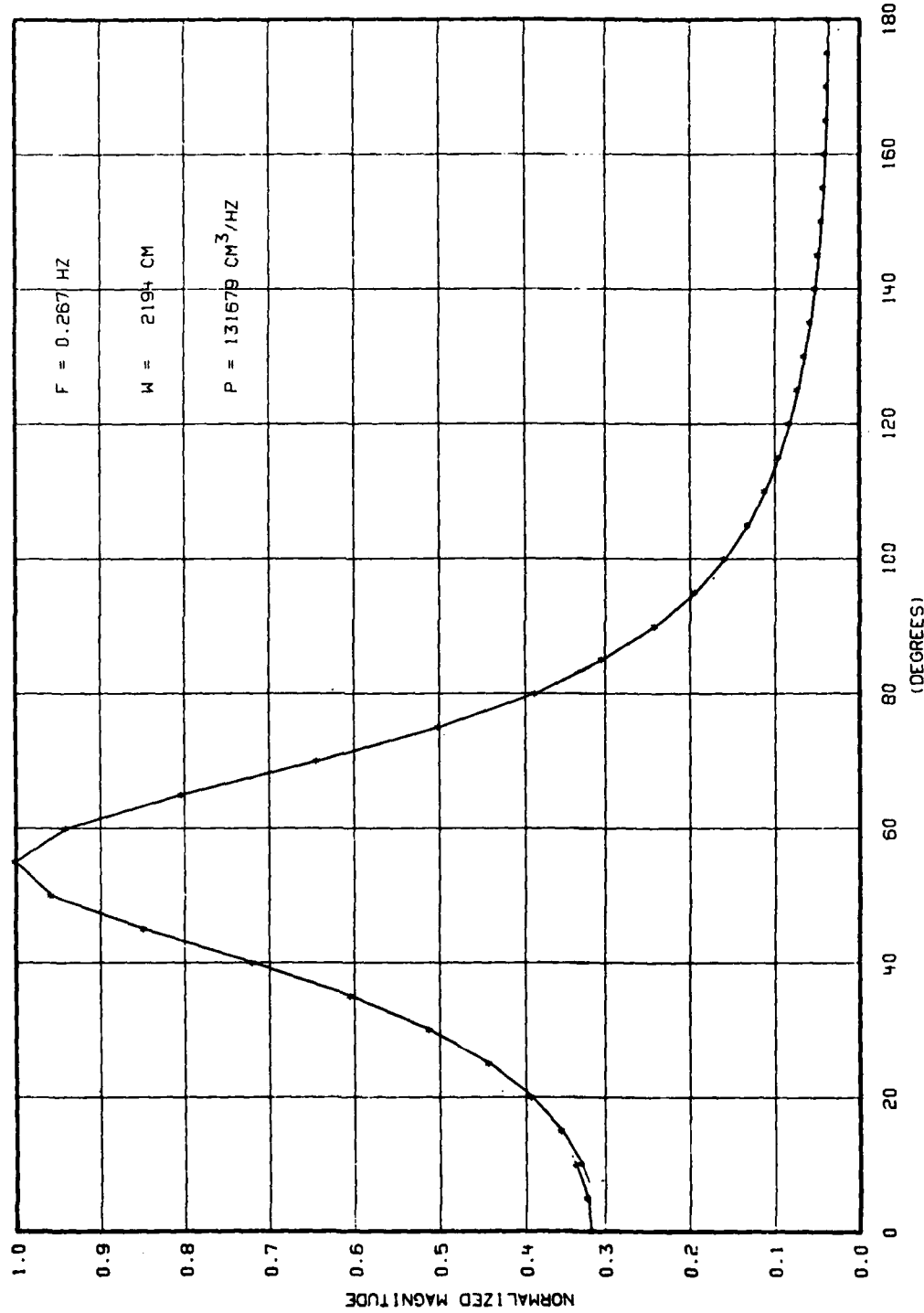


Figure F-6. Directional Spectrum for a Surface Wave Frequency of 0.267 Hz.

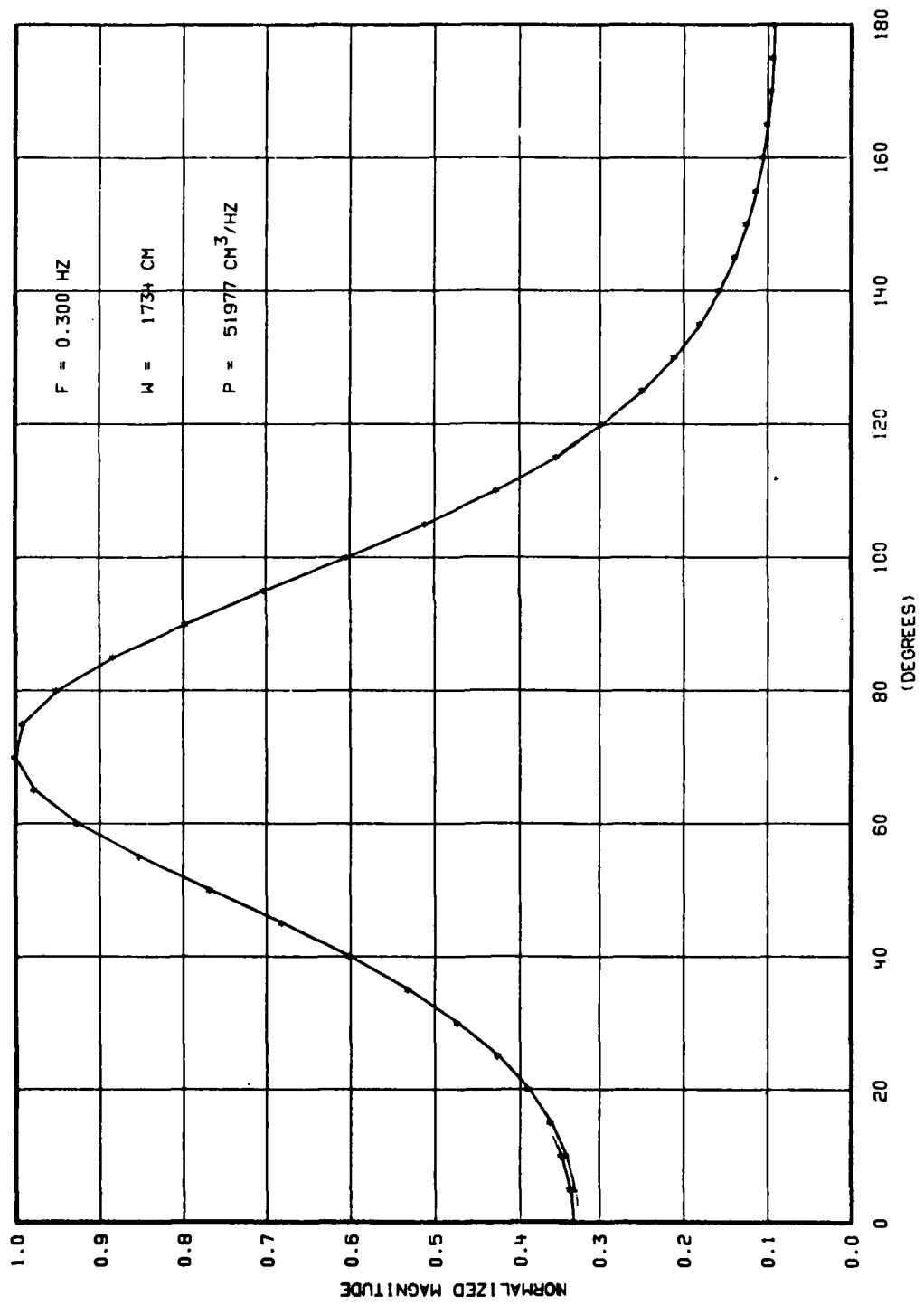


Figure F-7. Directional Spectrum for a Surface Wave Frequency of 0.300 Hz.

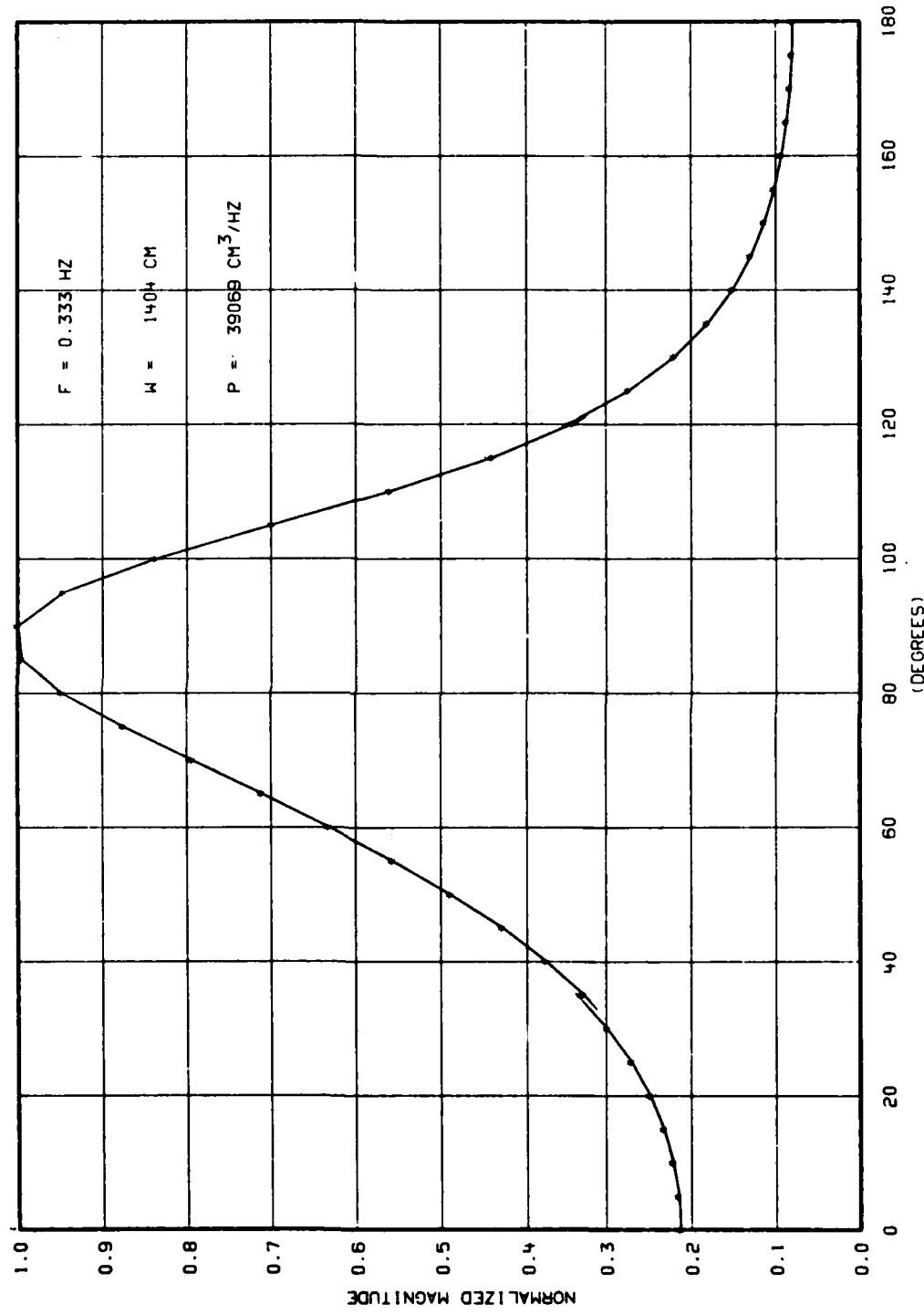


Figure F-8. Directional Spectrum for a Surface Wave Frequency of 0.333 Hz.

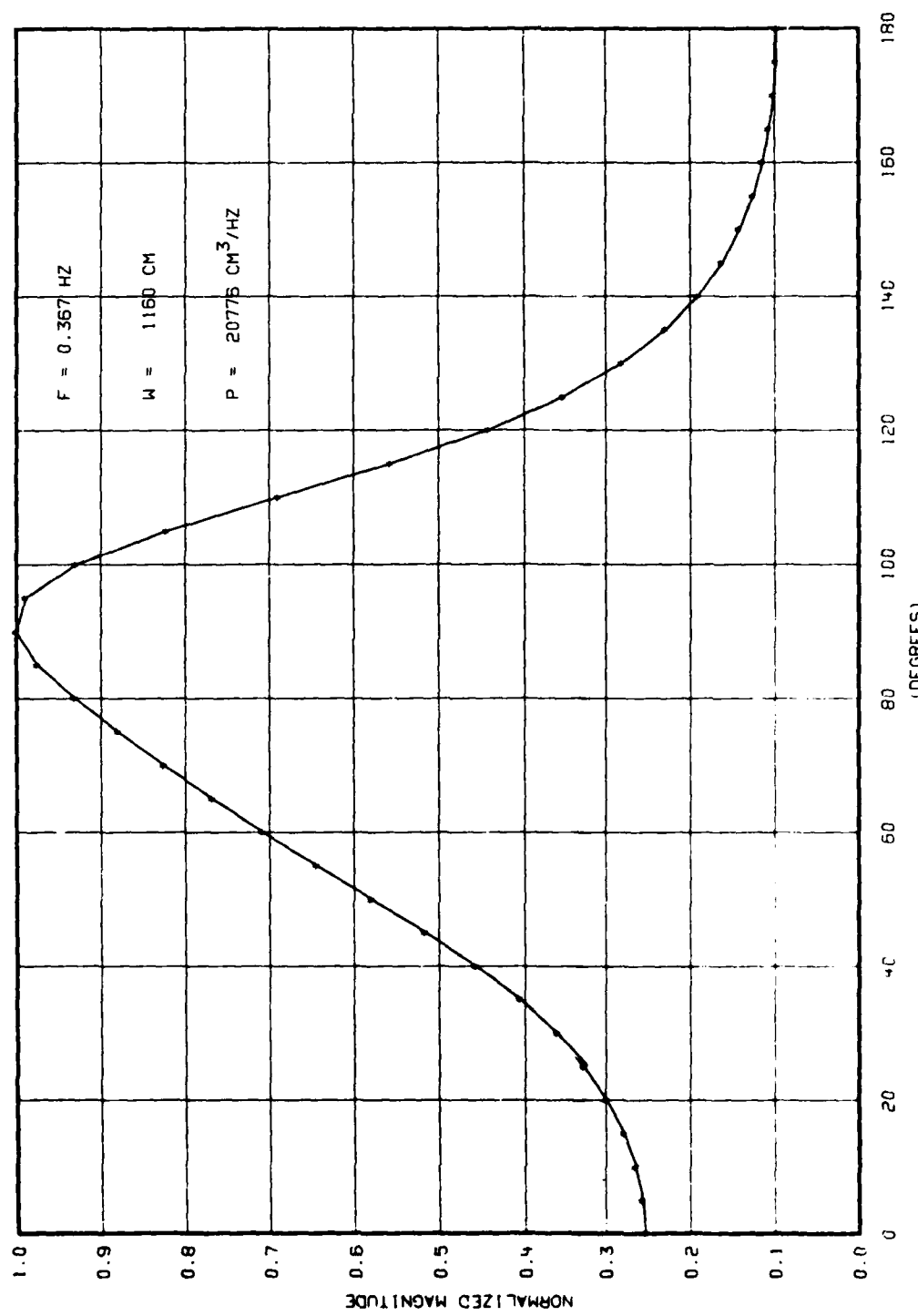


Figure F-9. Directional Spectrum for a Surface Wave Frequency of 0.367 Hz.

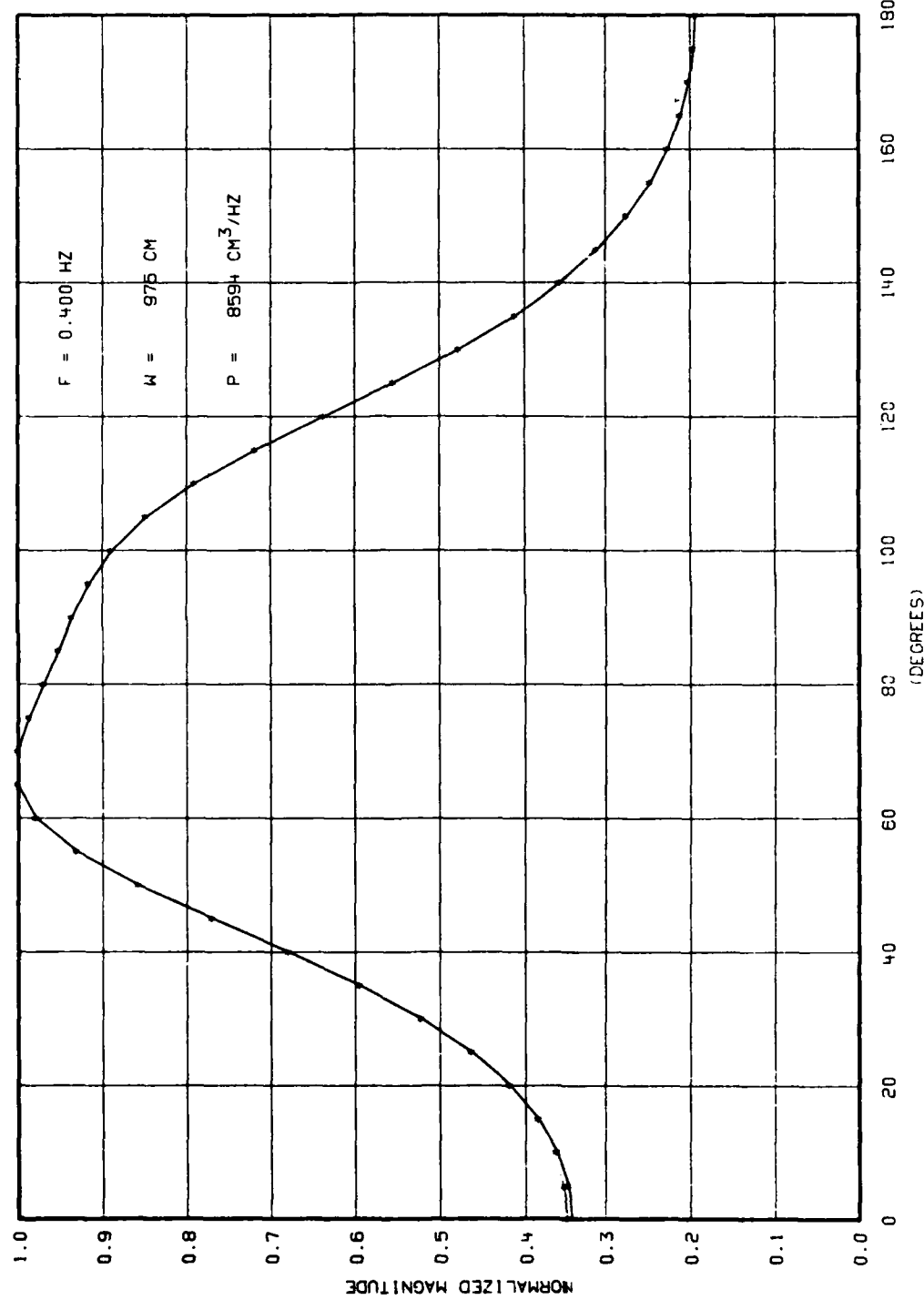


Figure F-10. Directional Spectrum for a Surface Wave Frequency of 0.400 Hz.

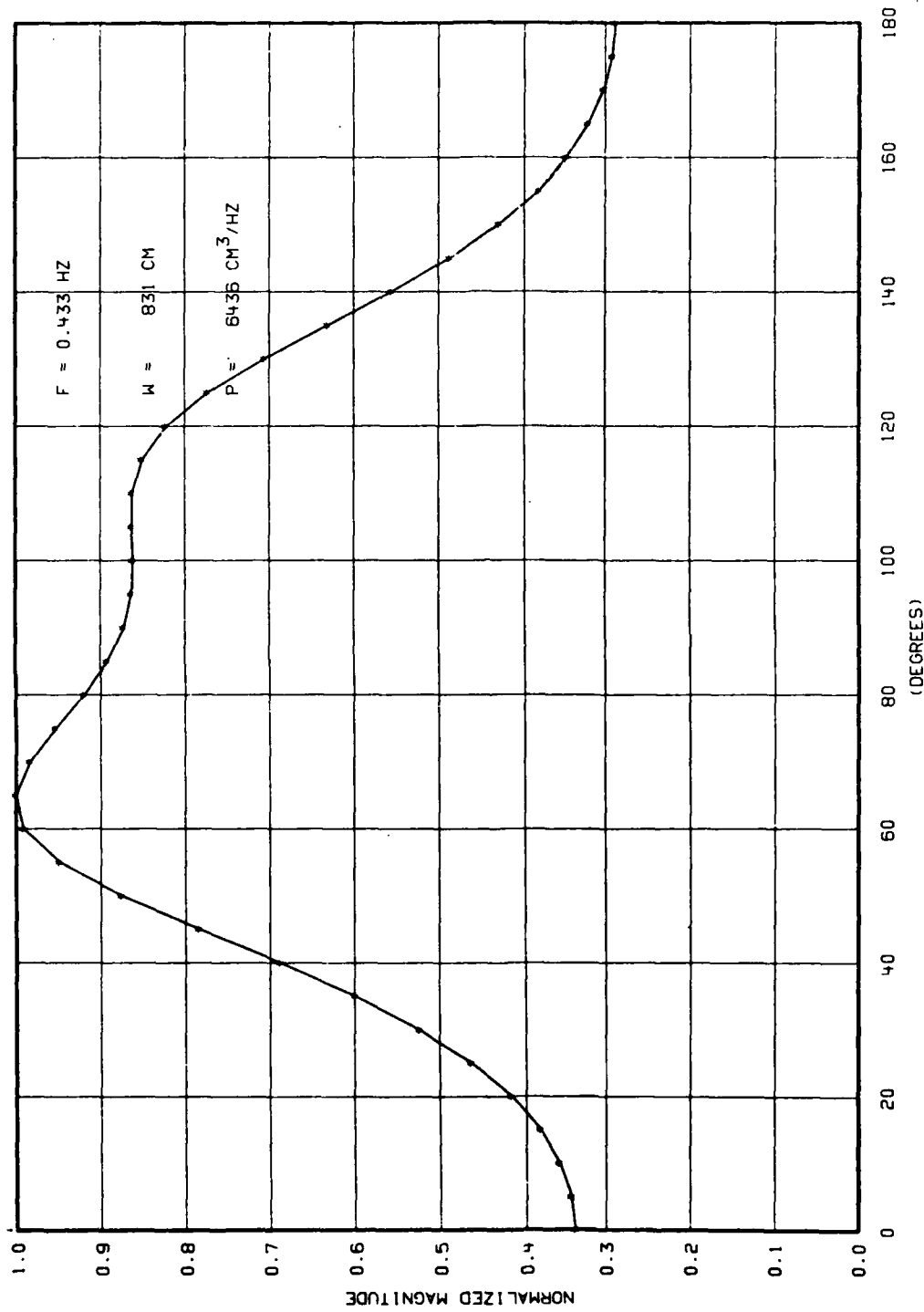


Figure F-11. Directional Spectrum for a Surface Wave Frequency of 0.433 Hz.

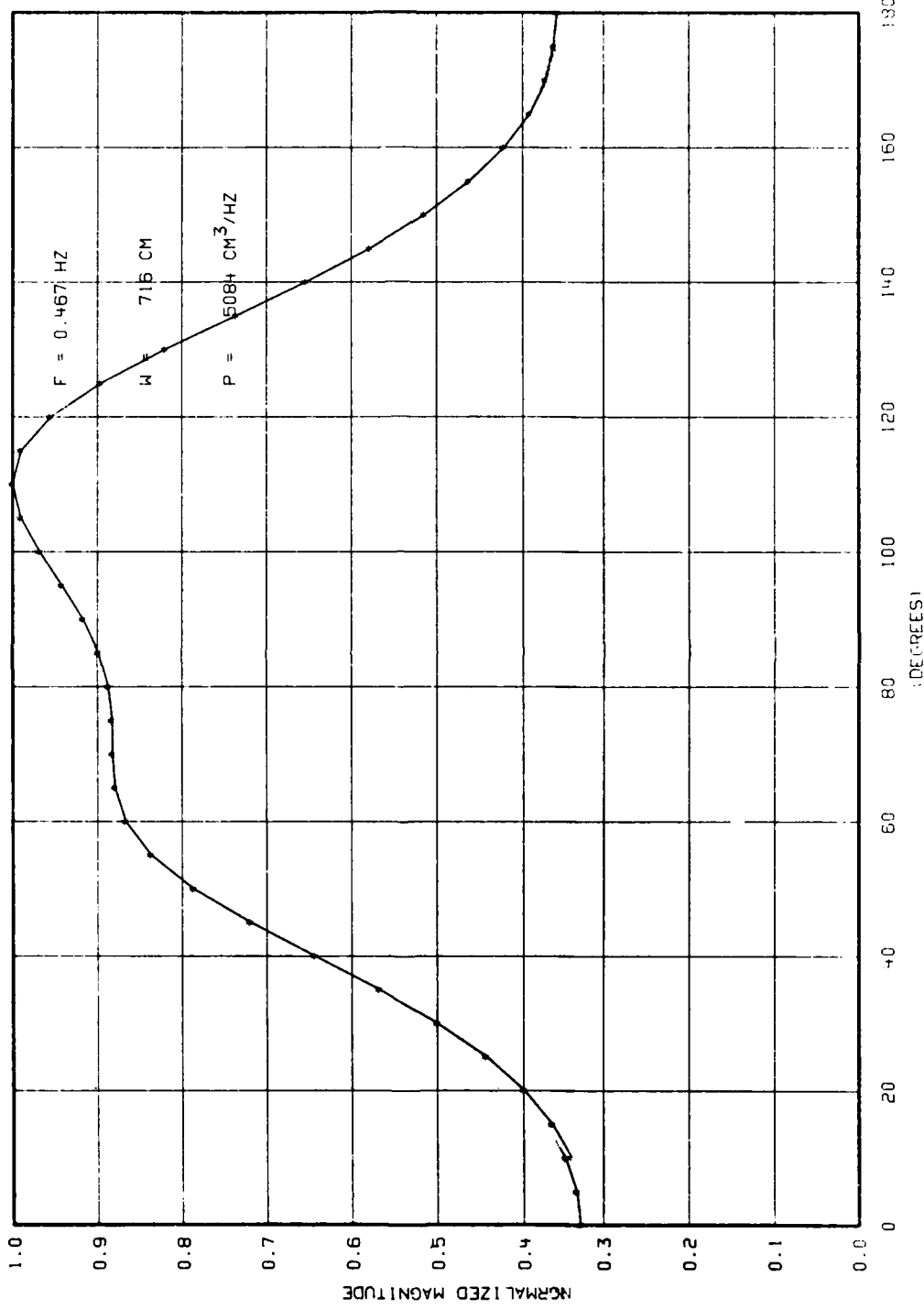


Figure F-12. Directional Spectrum for a Surface Wave Frequency of 0.467 Hz.

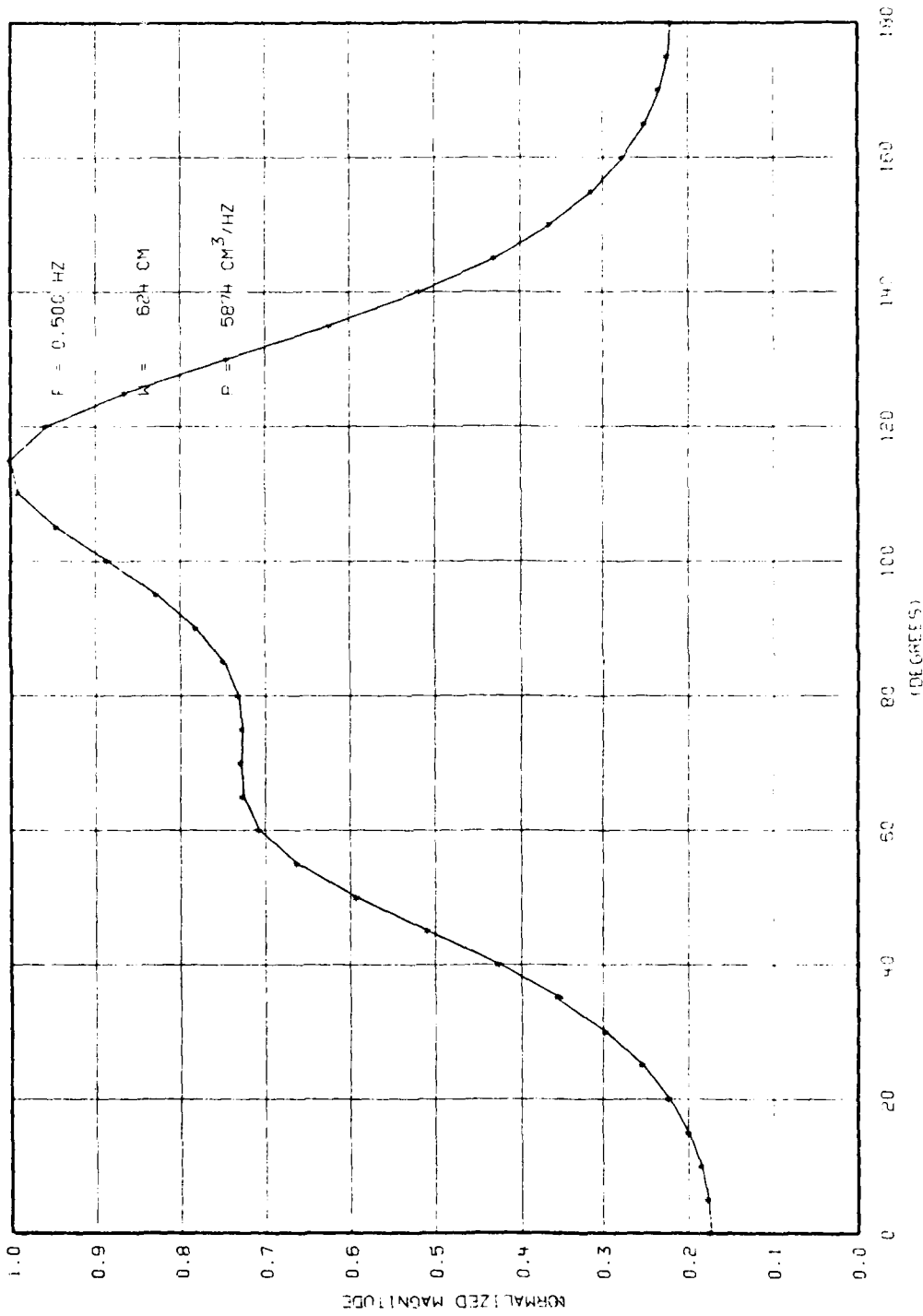


Figure F-13. Directional Spectrum for a Surface Wave Frequency of 0.500 Hz.

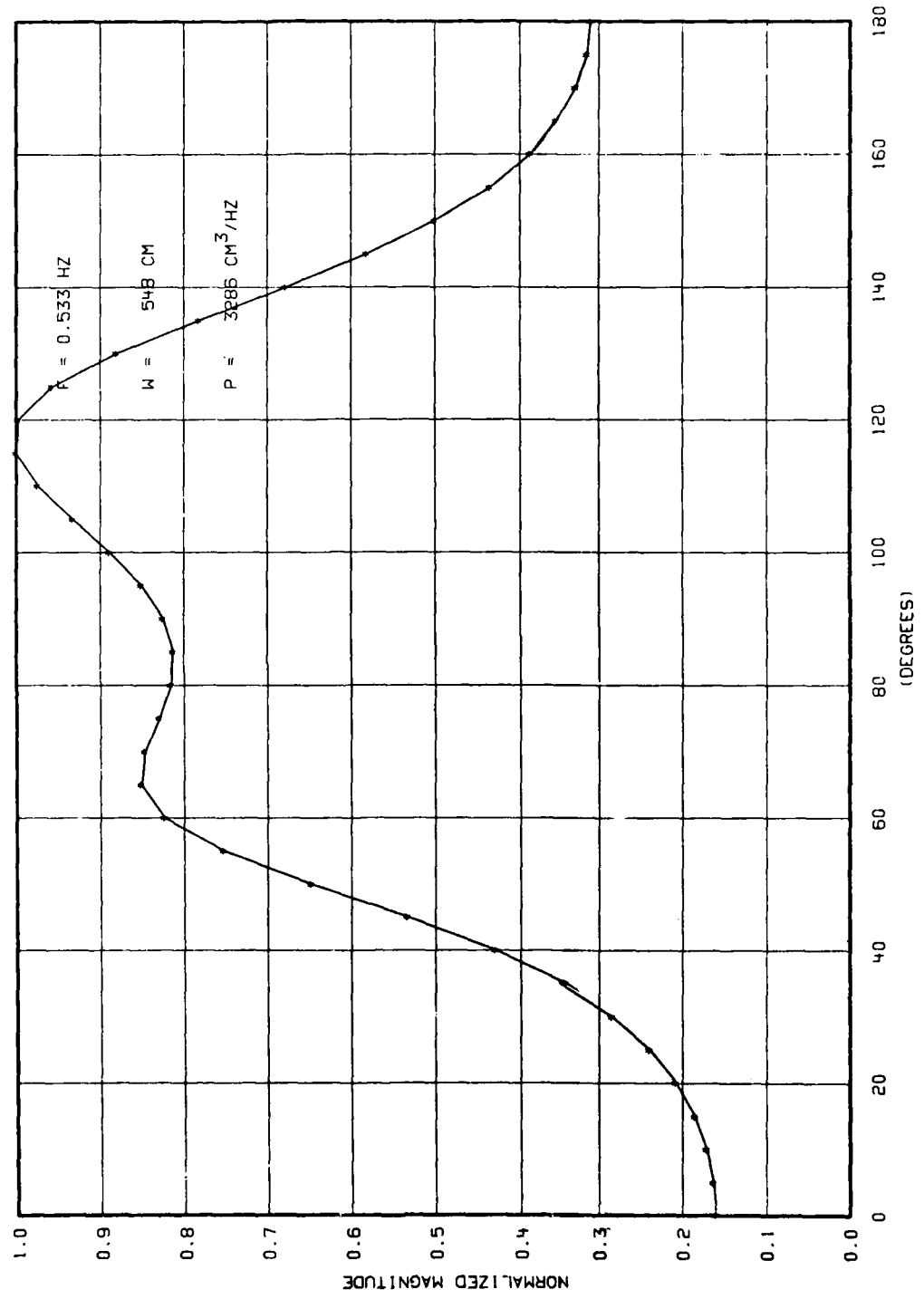


Figure F-14. Directional Spectrum for a Surface Wave Frequency of 0.533 Hz.

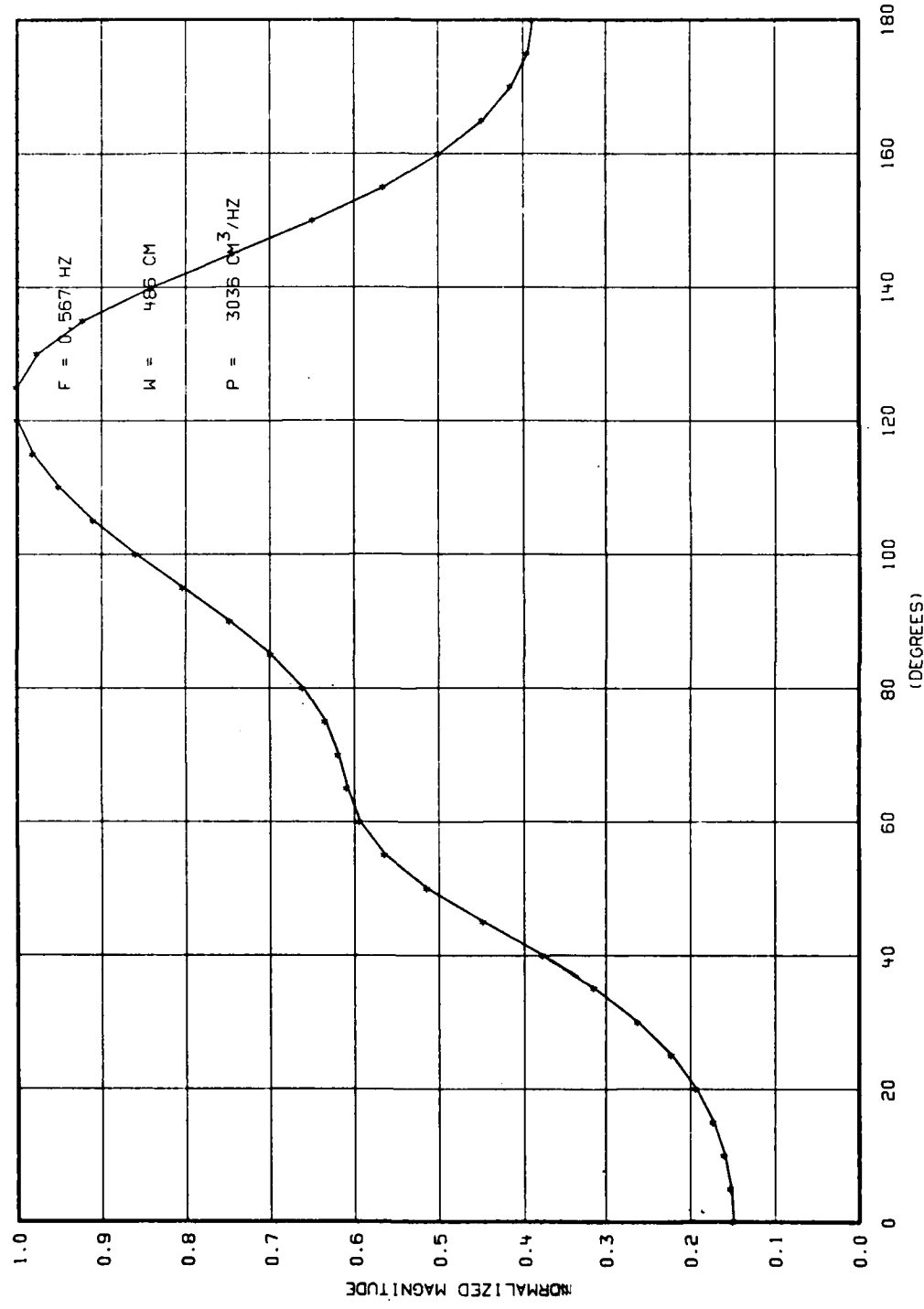
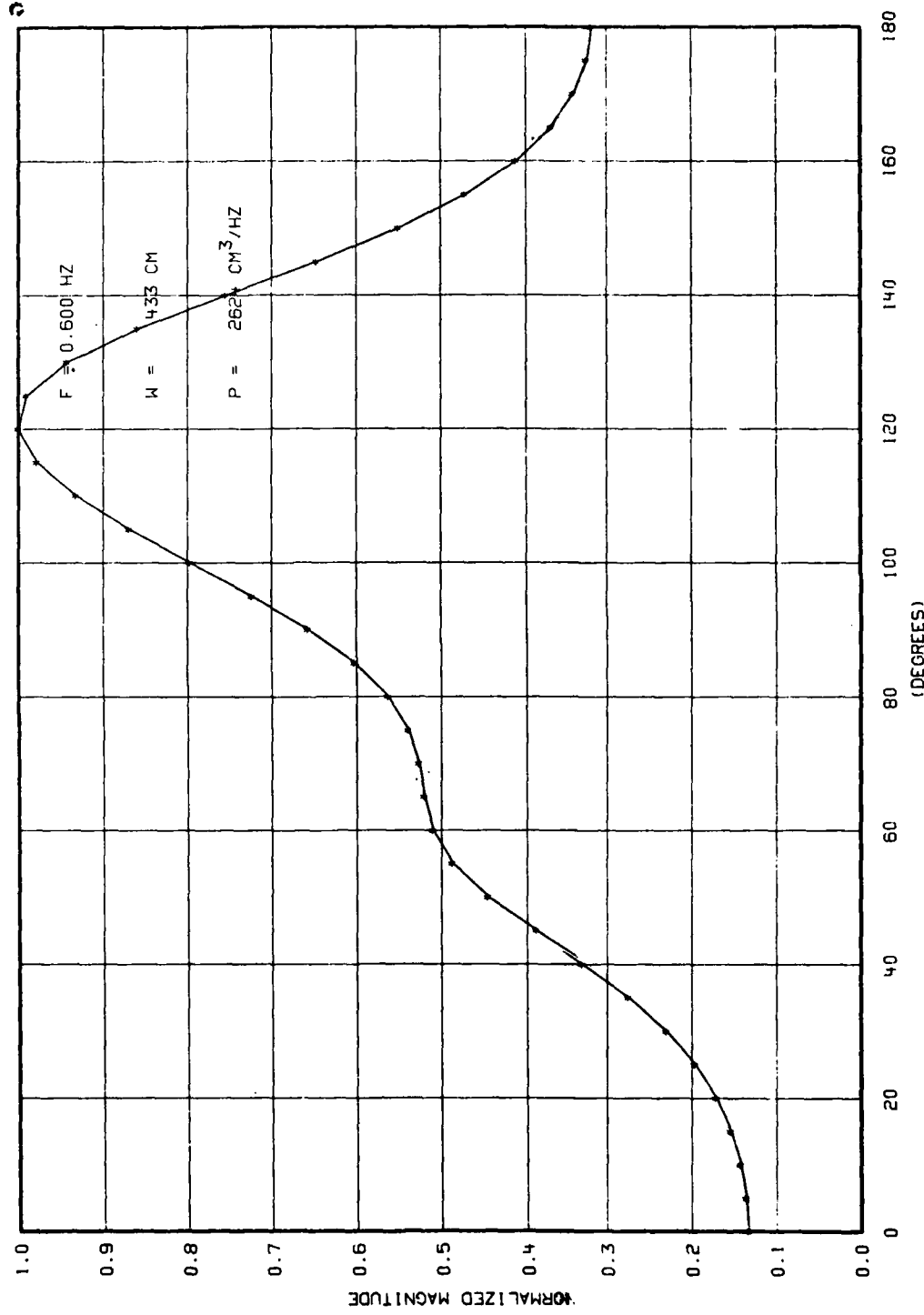


Figure F-15. Directional Spectrum for a Surface Wave Frequency of 0.567 Hz.

Figure F-16. Directional Spectrum for a Surface Wave Frequency of 0.600 Hz.



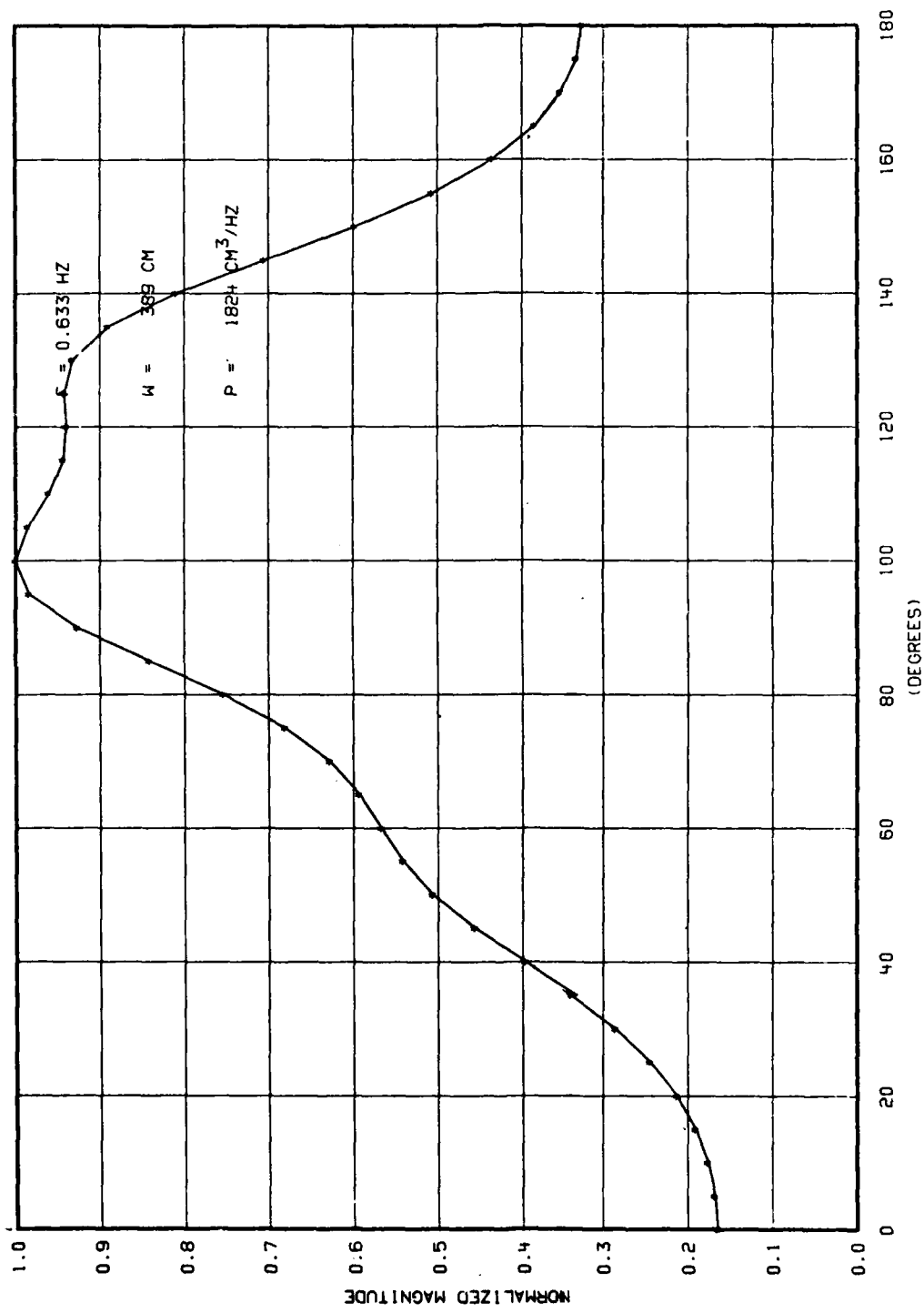


Figure F-17. Directional Spectrum for a Surface Wave Frequency of 0.633 Hz.

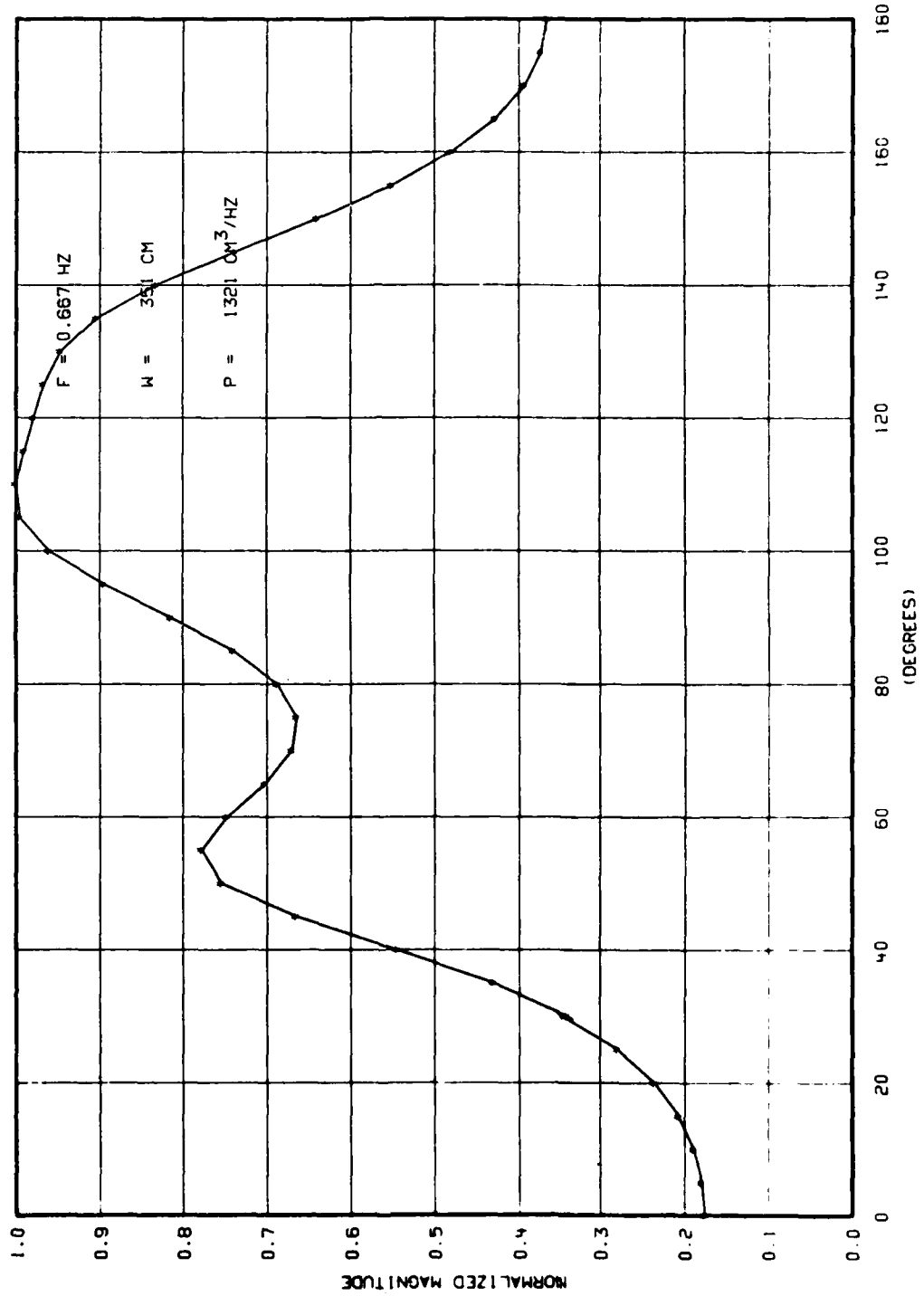


Figure F-18. Directional Spectrum for a Surface Wave Frequency of 0.667 Hz.

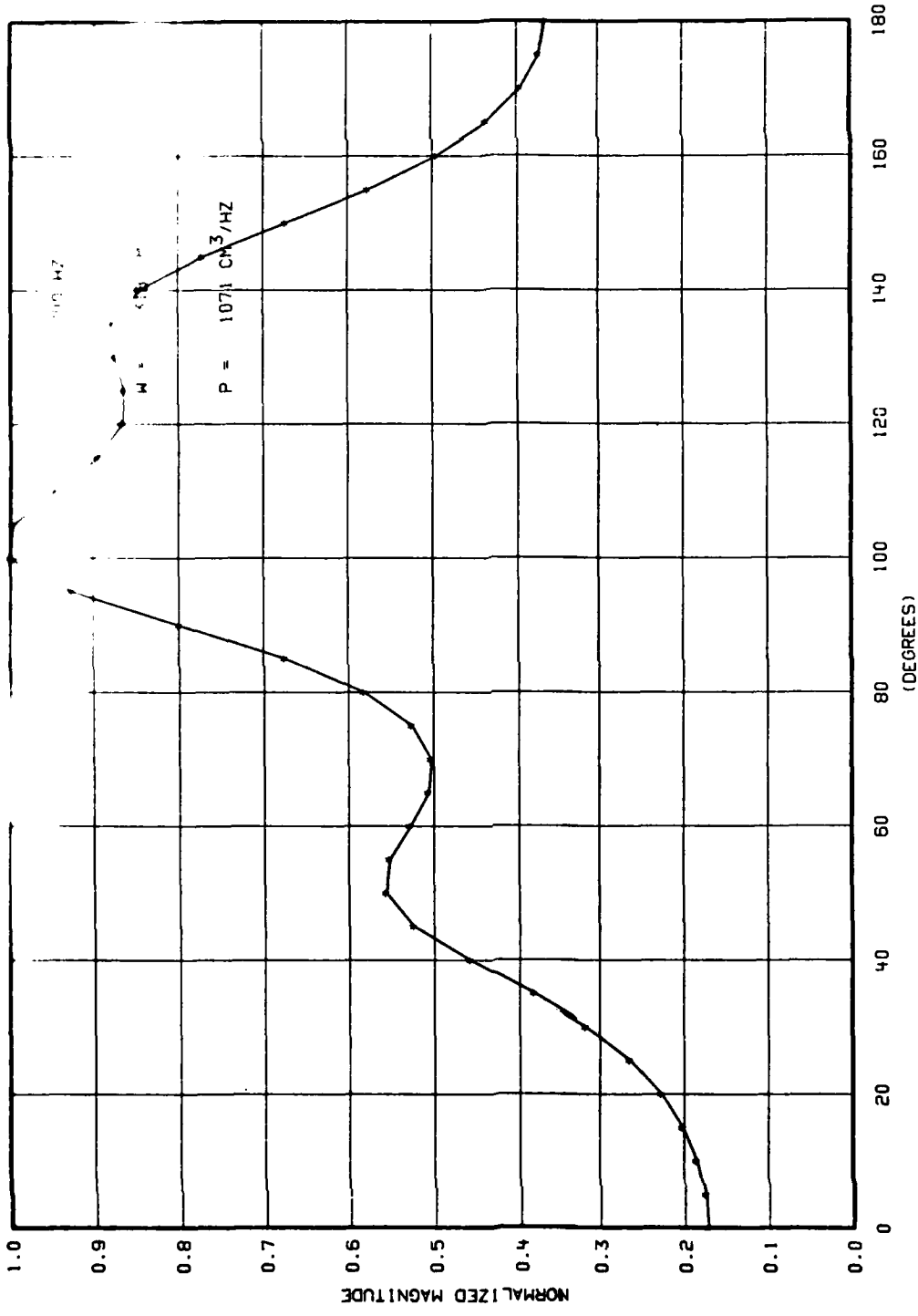


Figure F-19. Directional Spectrum for a Surface Wave Frequency of 0.700 Hz.

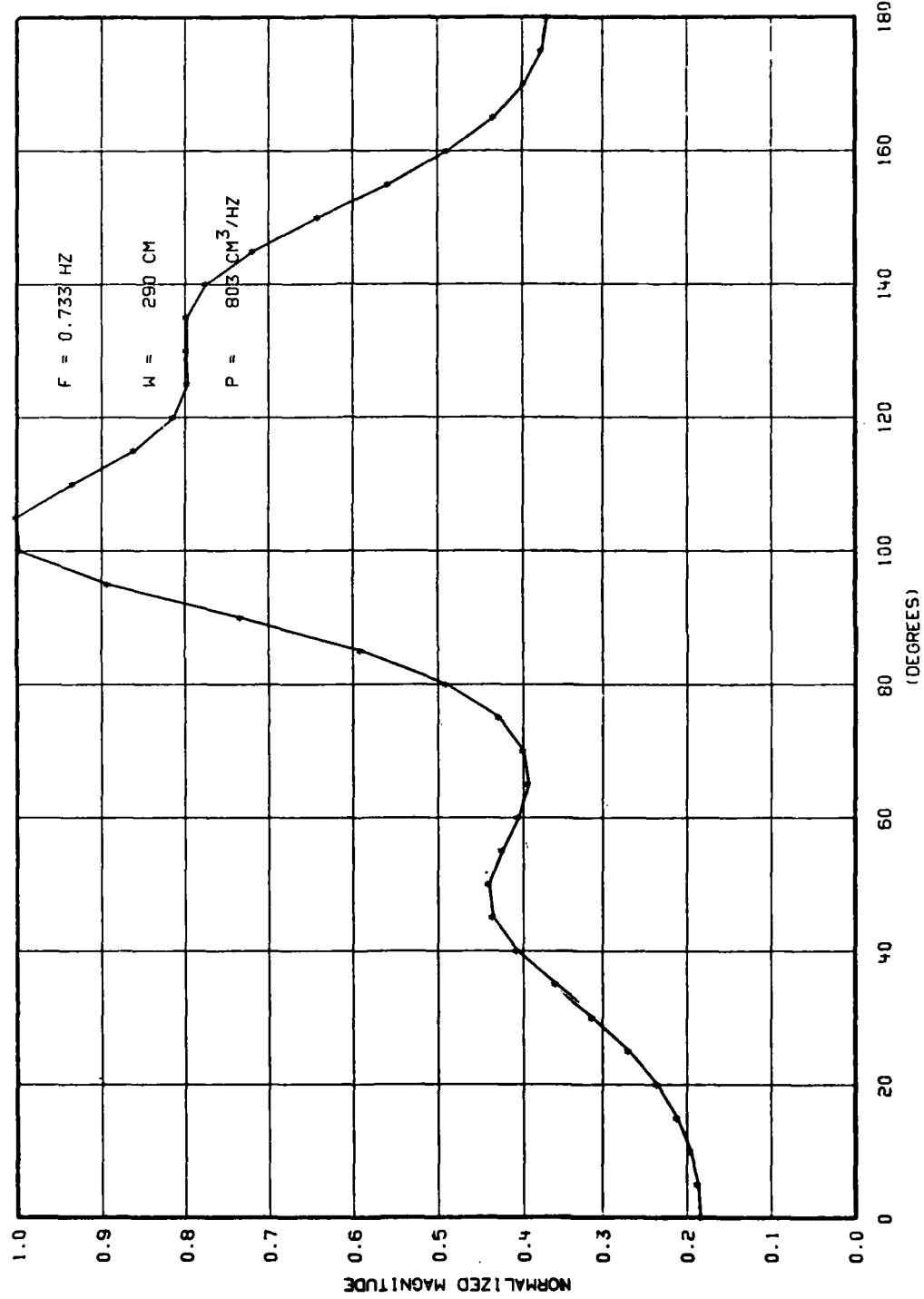


Figure F-20. Directional Spectrum for a Surface Wave Frequency of 0.733 Hz.

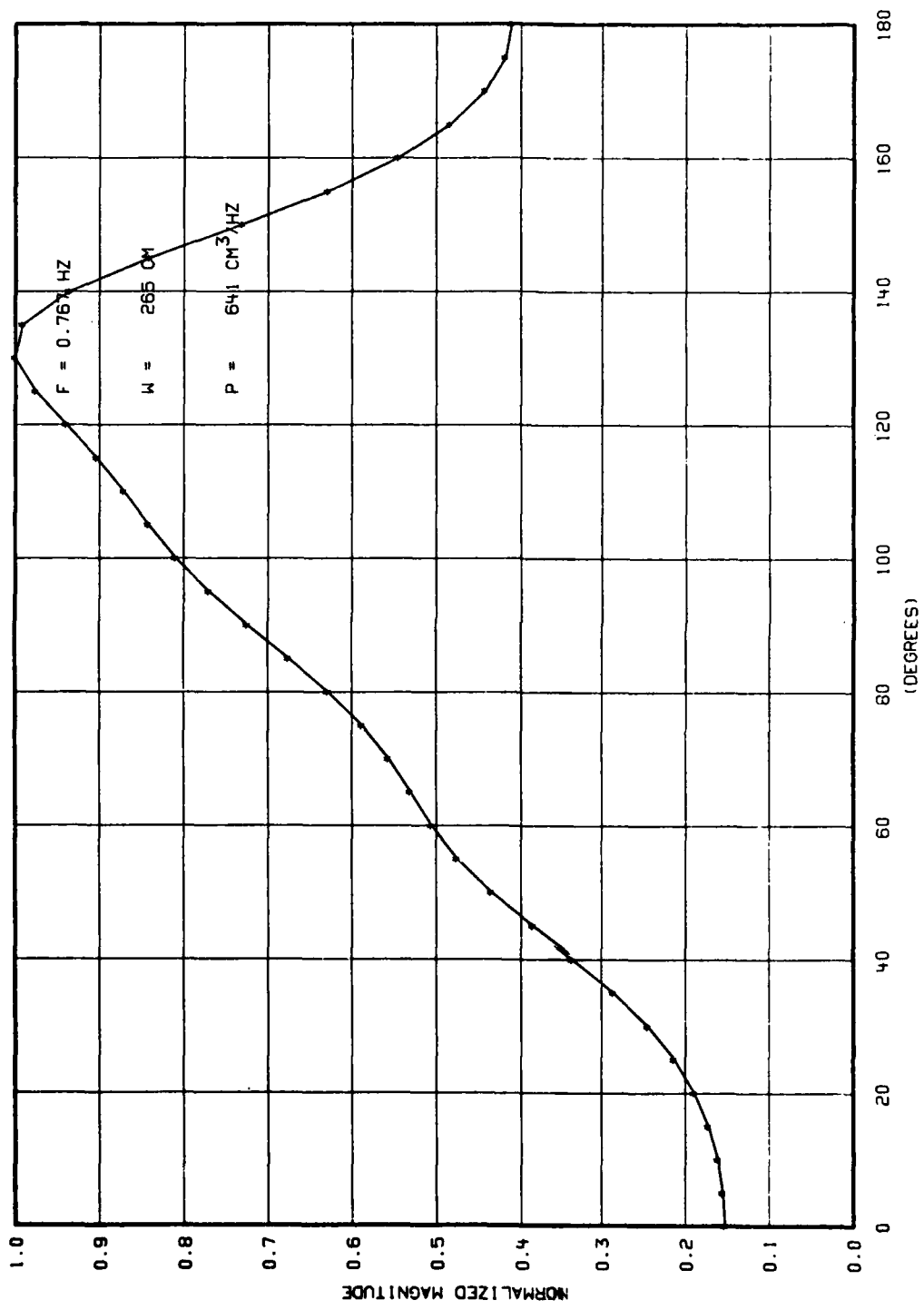


Figure F-21. Directional Spectrum for a Surface Wave Frequency of 0.767 Hz.

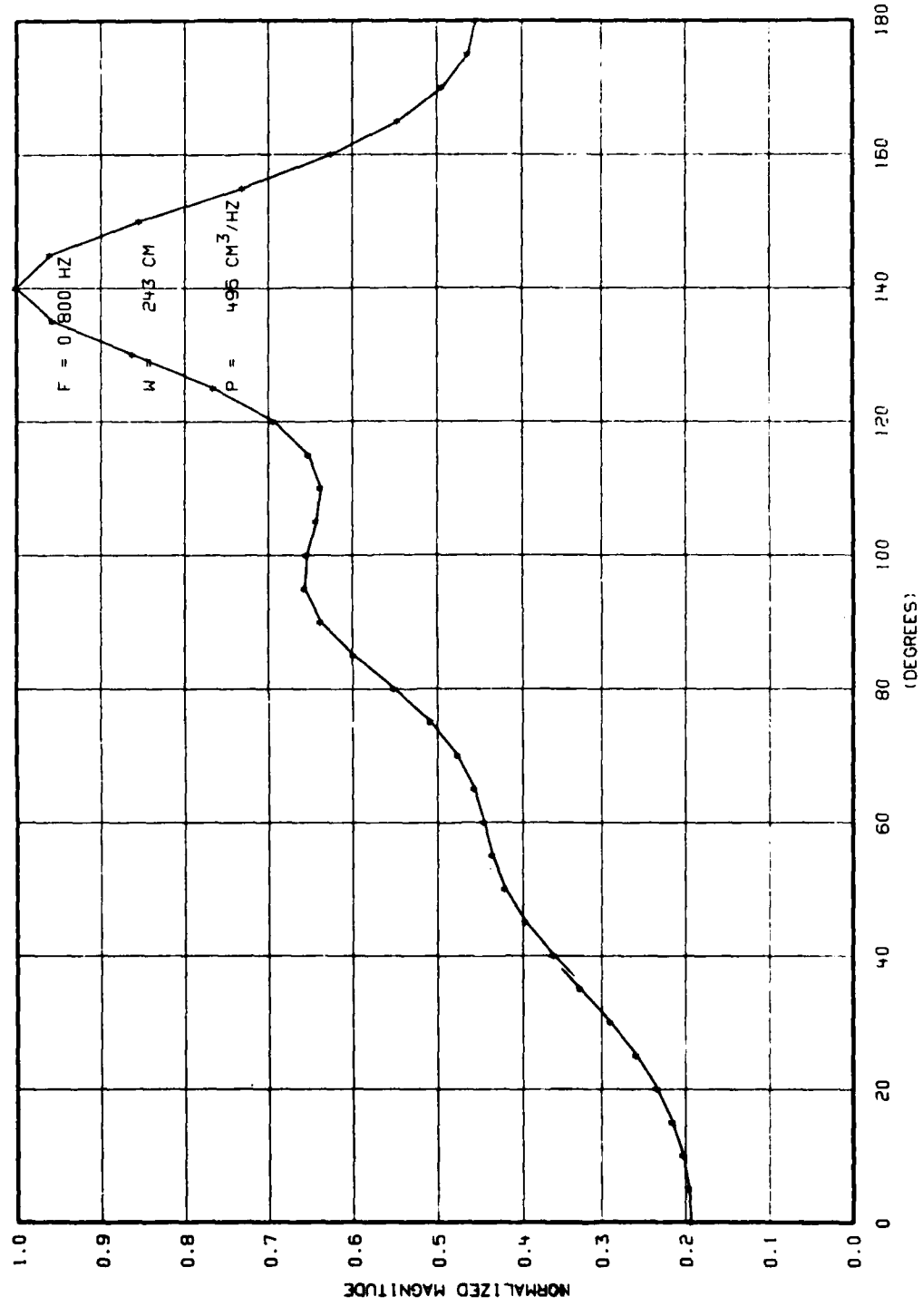


Figure F-22. Directional Spectrum for a Surface Wave Frequency of 0.800 Hz.

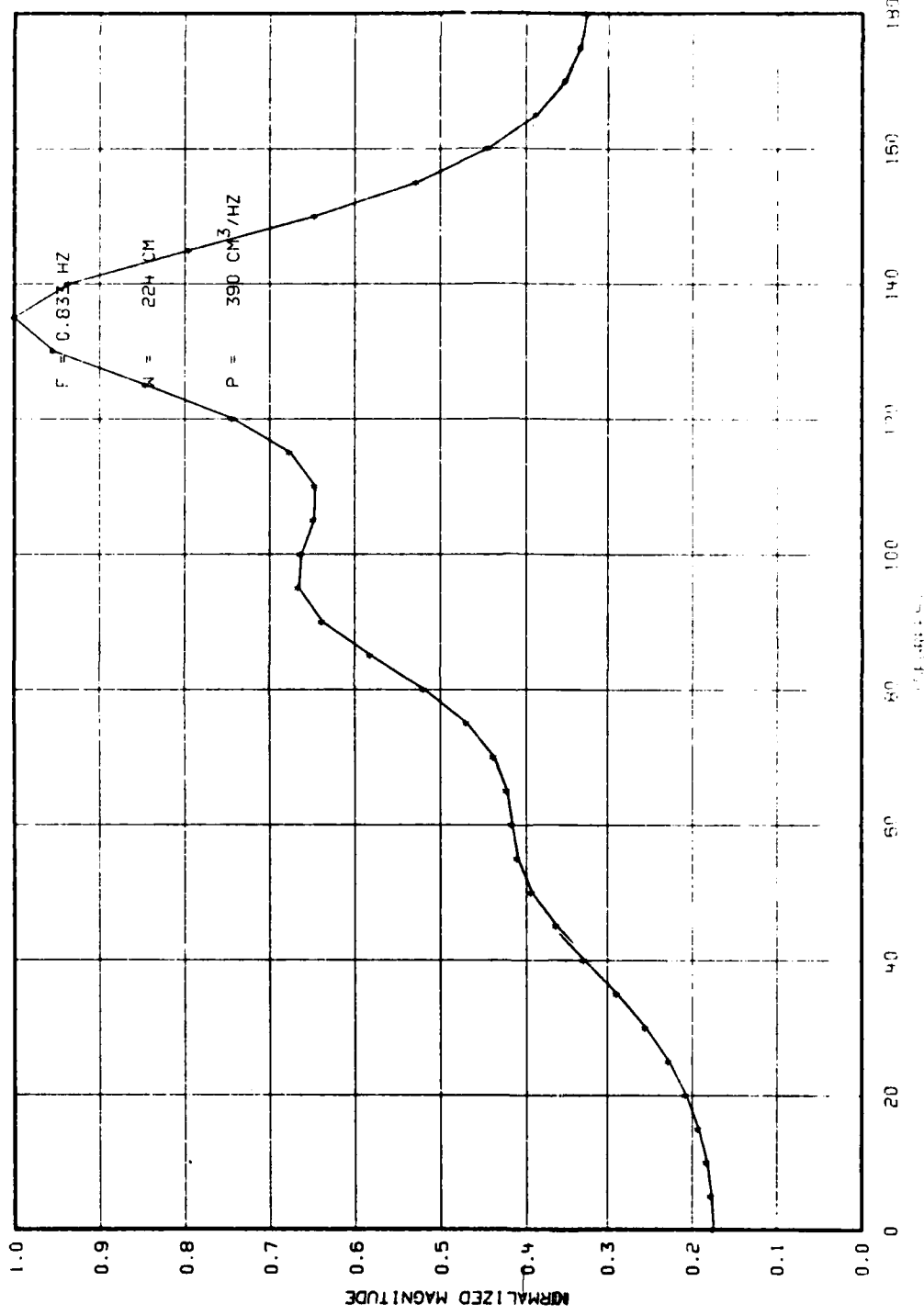


Figure F-23. Directional Spectrum for a Surface Wave Frequency of 0.833 Hz.

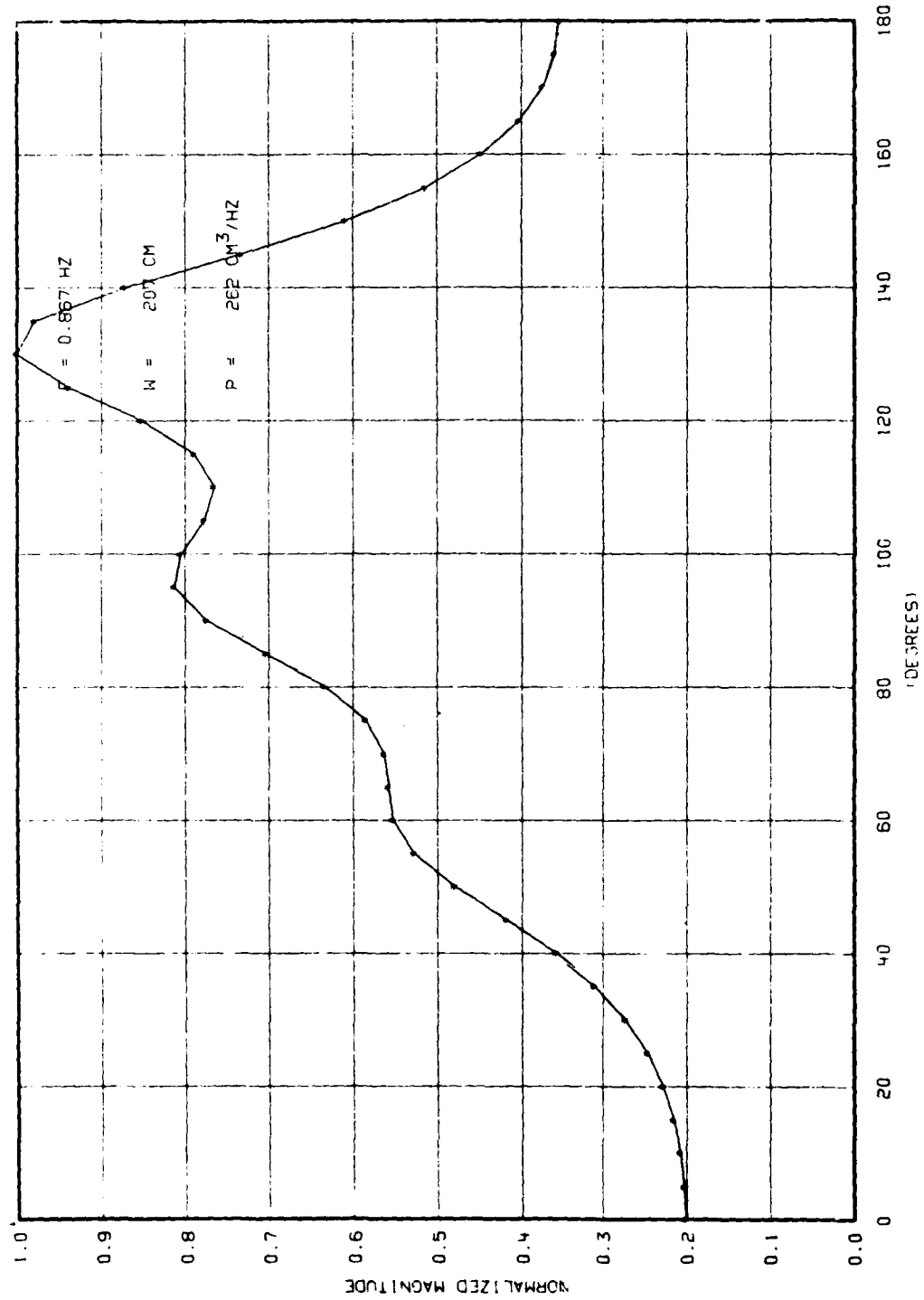


Figure F-24. Directional Spectrum for a Surface Wave Frequency of 0.867 Hz.

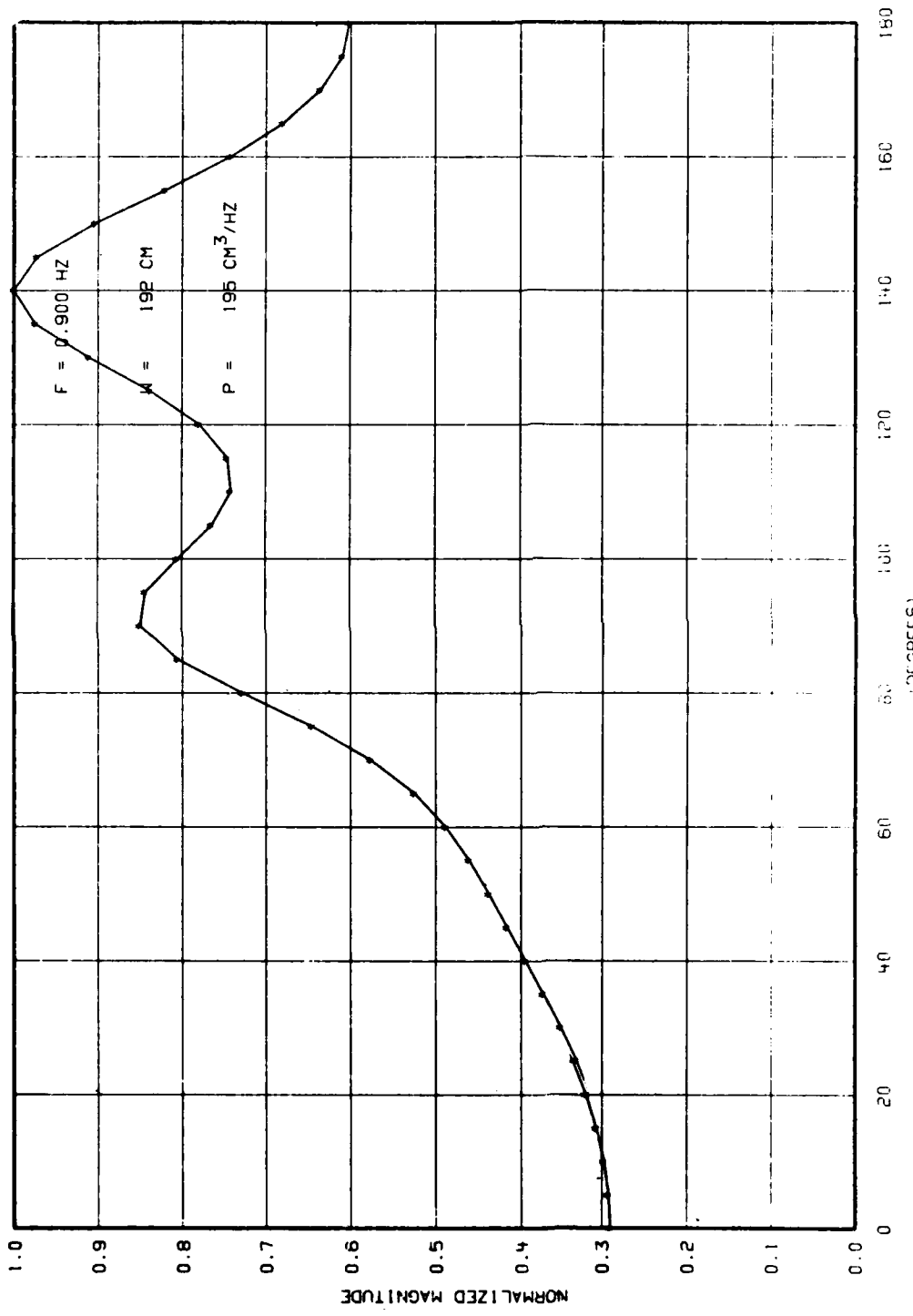


Figure F-25. Directional Spectrum for a Surface Wave Frequency of 0.900 Hz.

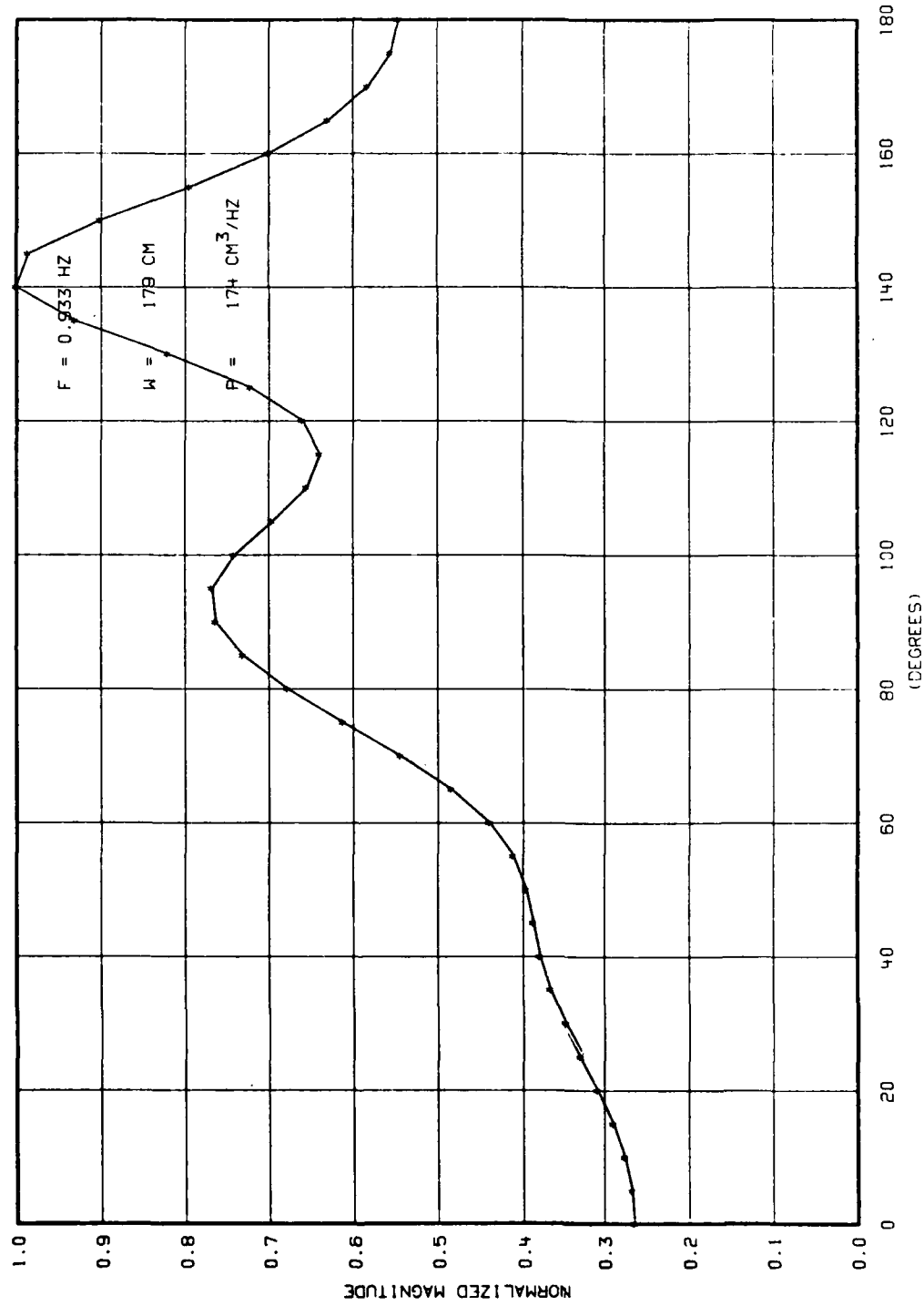


Figure F-26. Directional Spectrum for a Surface Wave Frequency of 0.933 Hz.

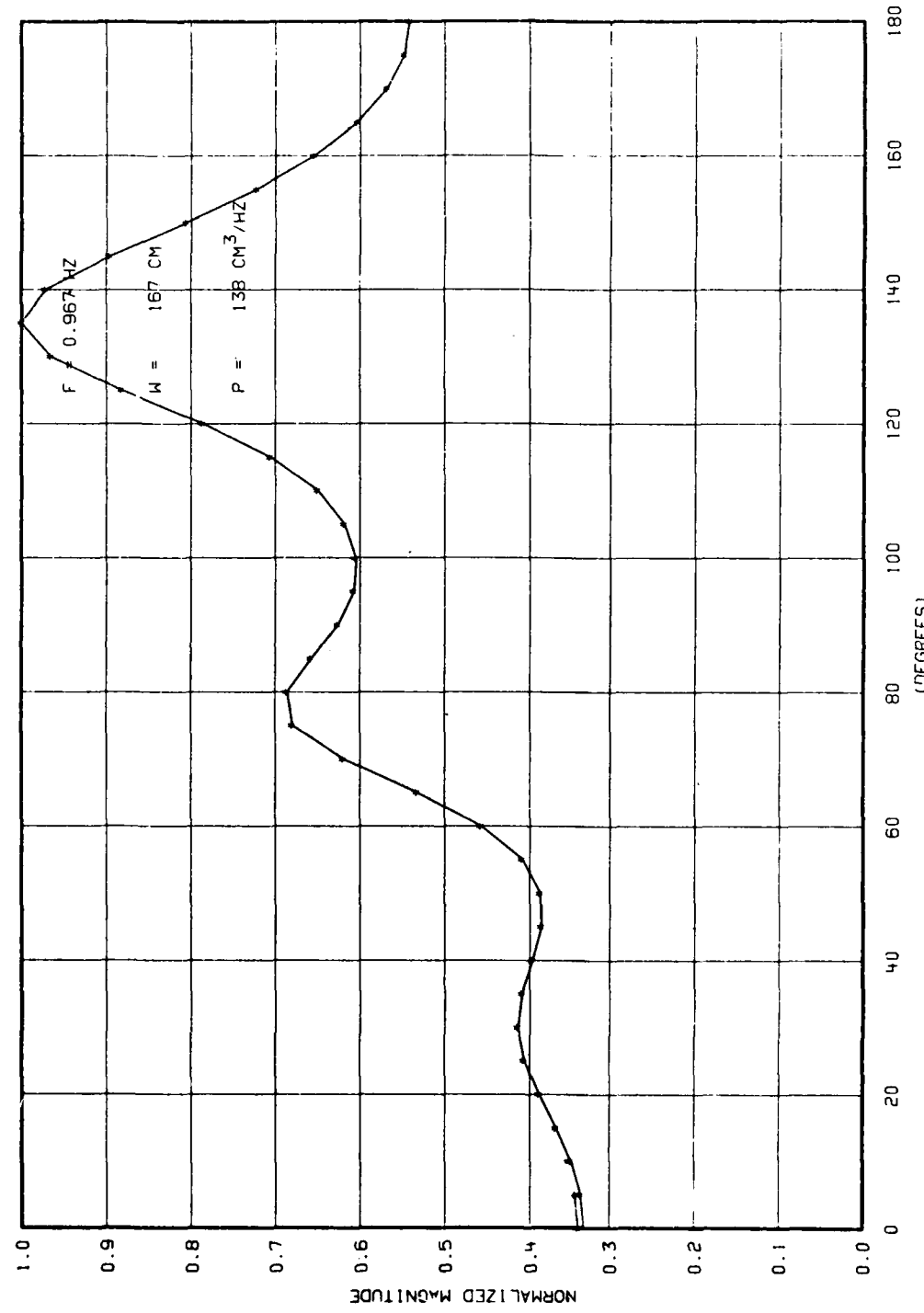


Figure F-27. Directional Spectrum for a Surface Wave Frequency of 0.967 Hz.

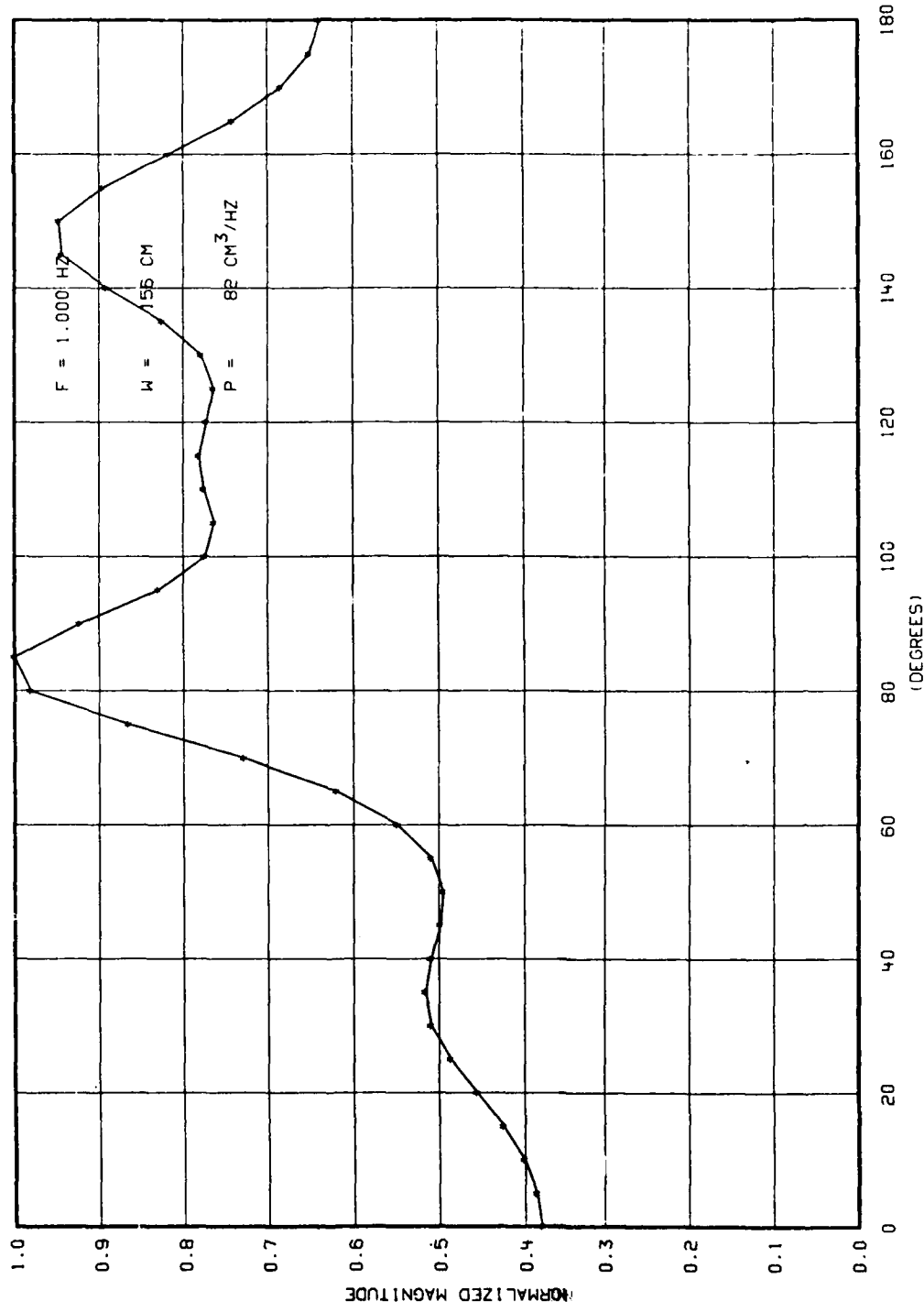


Figure F-28. Directional Spectrum for a Surface Wave Frequency of 1.000 Hz.

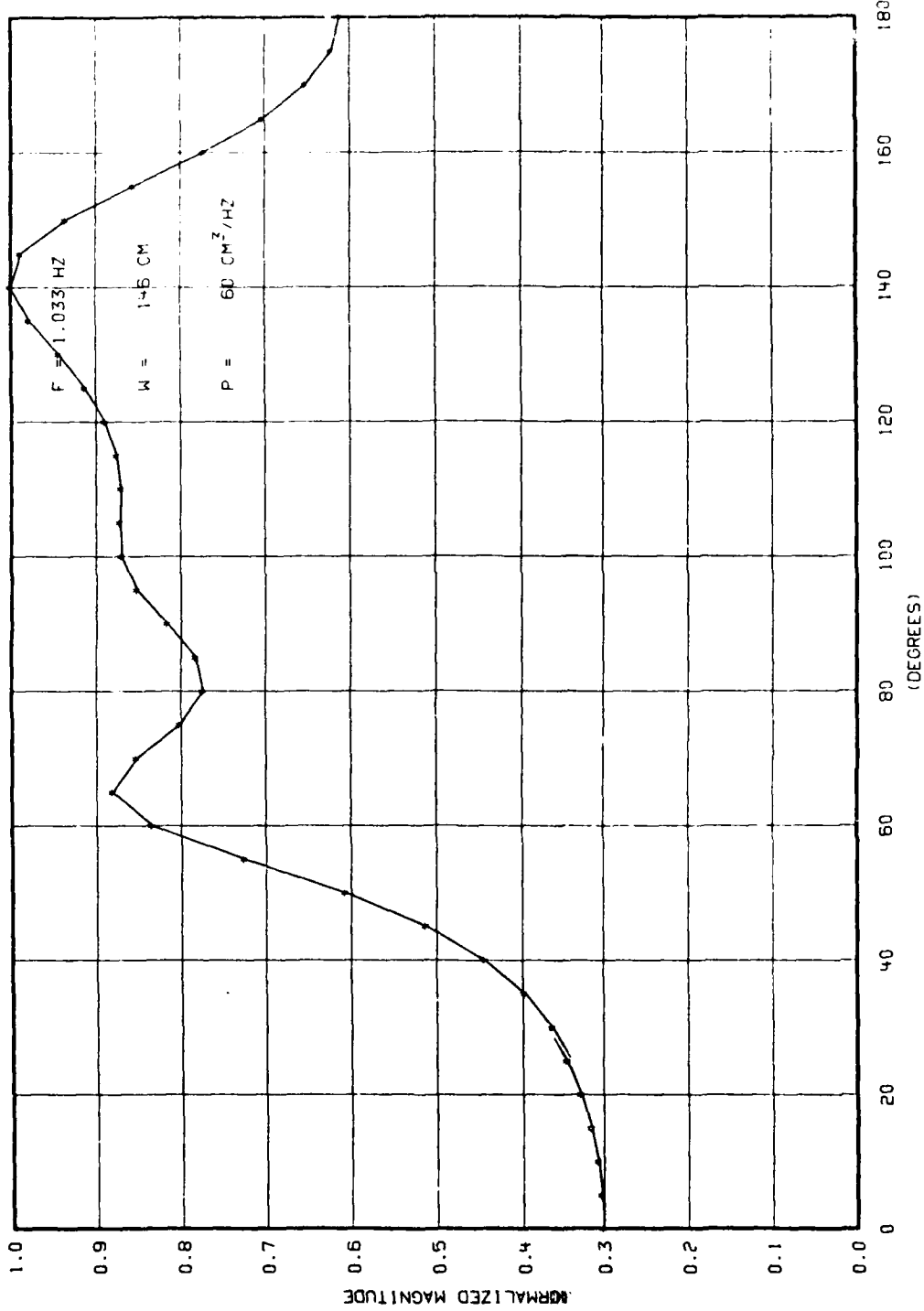


Figure F-29. Directional Spectrum for a Surface Wave Frequency of 1.033 Hz.

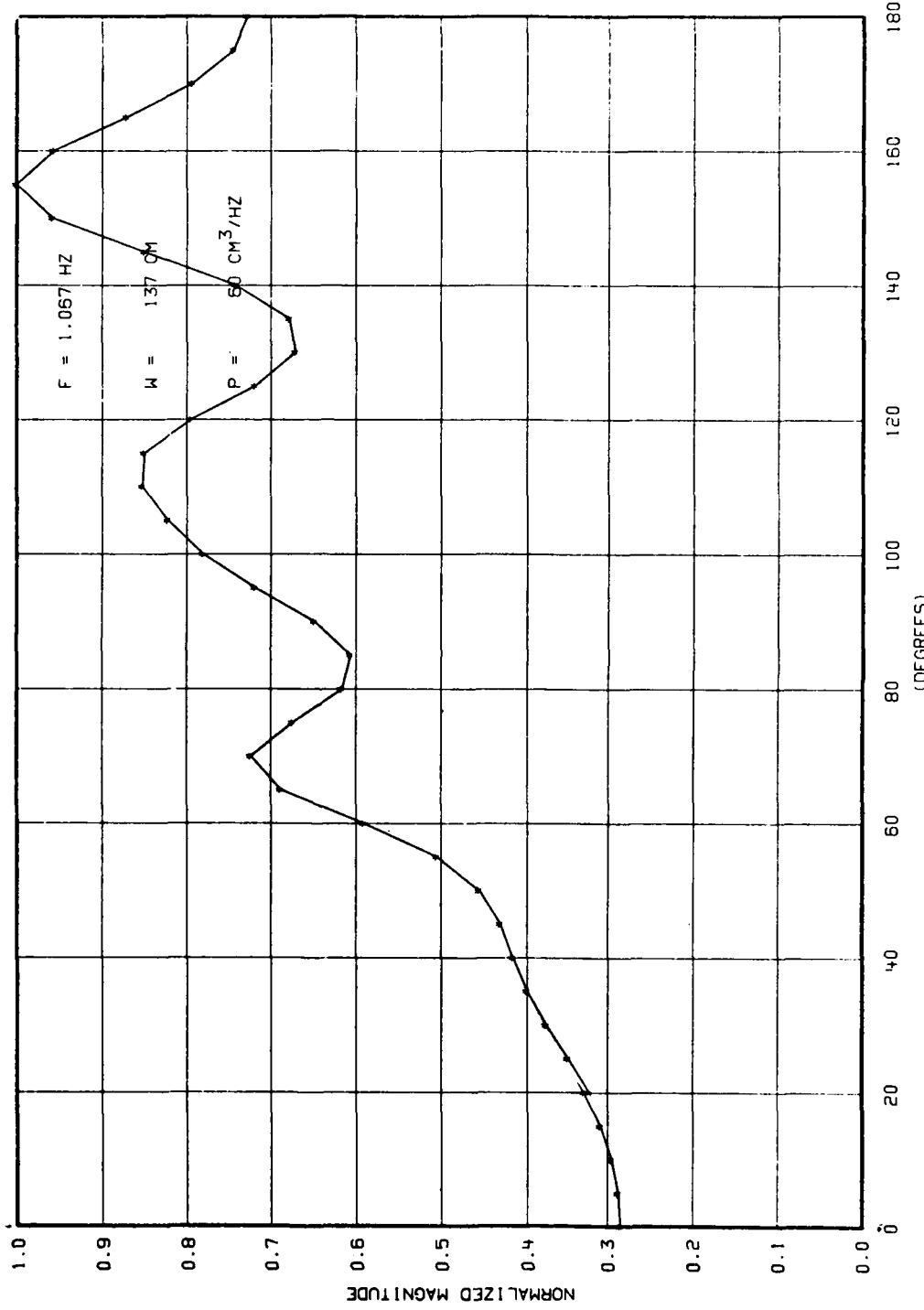


Figure F-30. Directional Spectrum for a Surface Wave Frequency of 1.067 Hz.

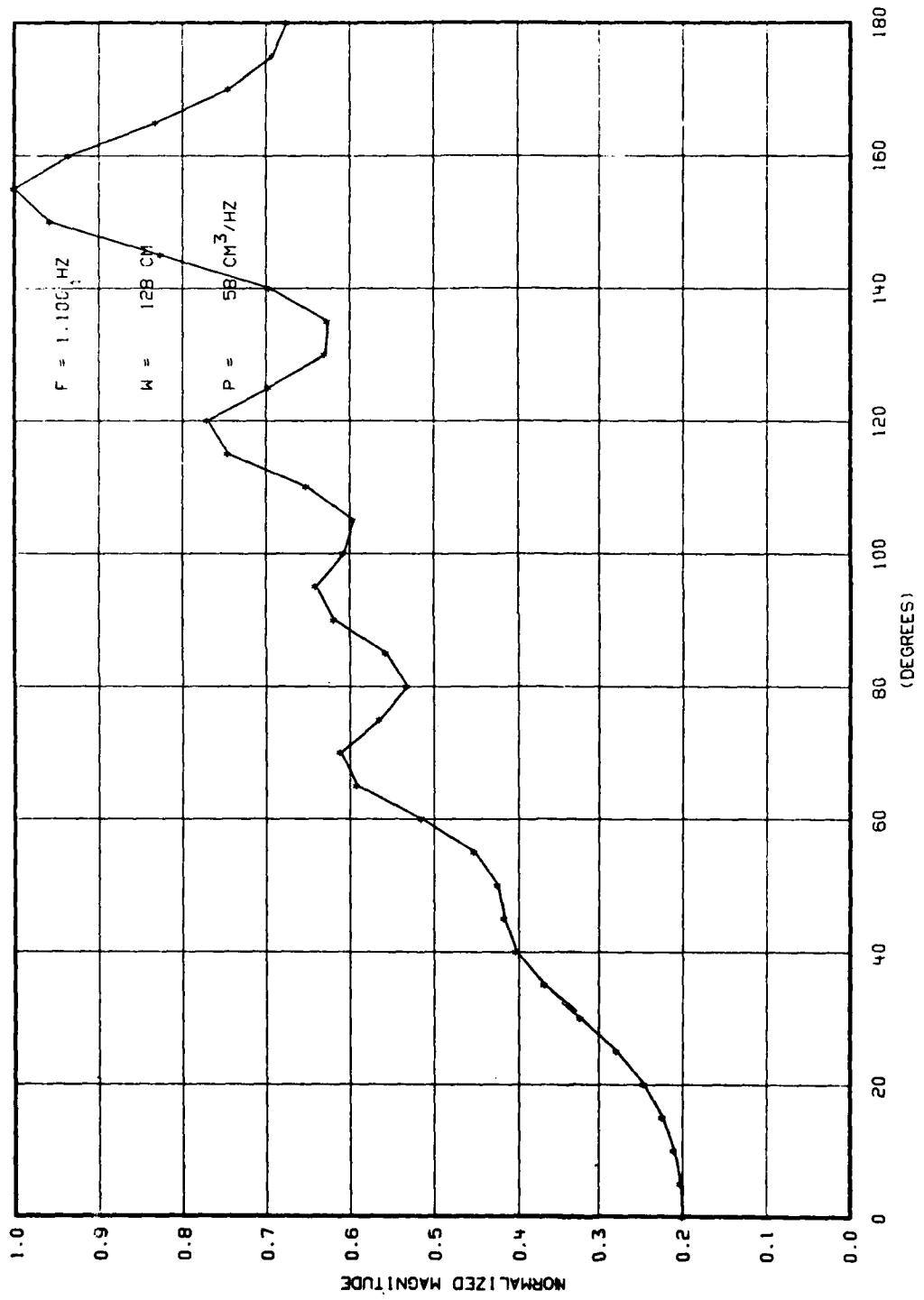


Figure F-31. Directional Spectrum for a Surface Wave Frequency of 1.100 Hz.

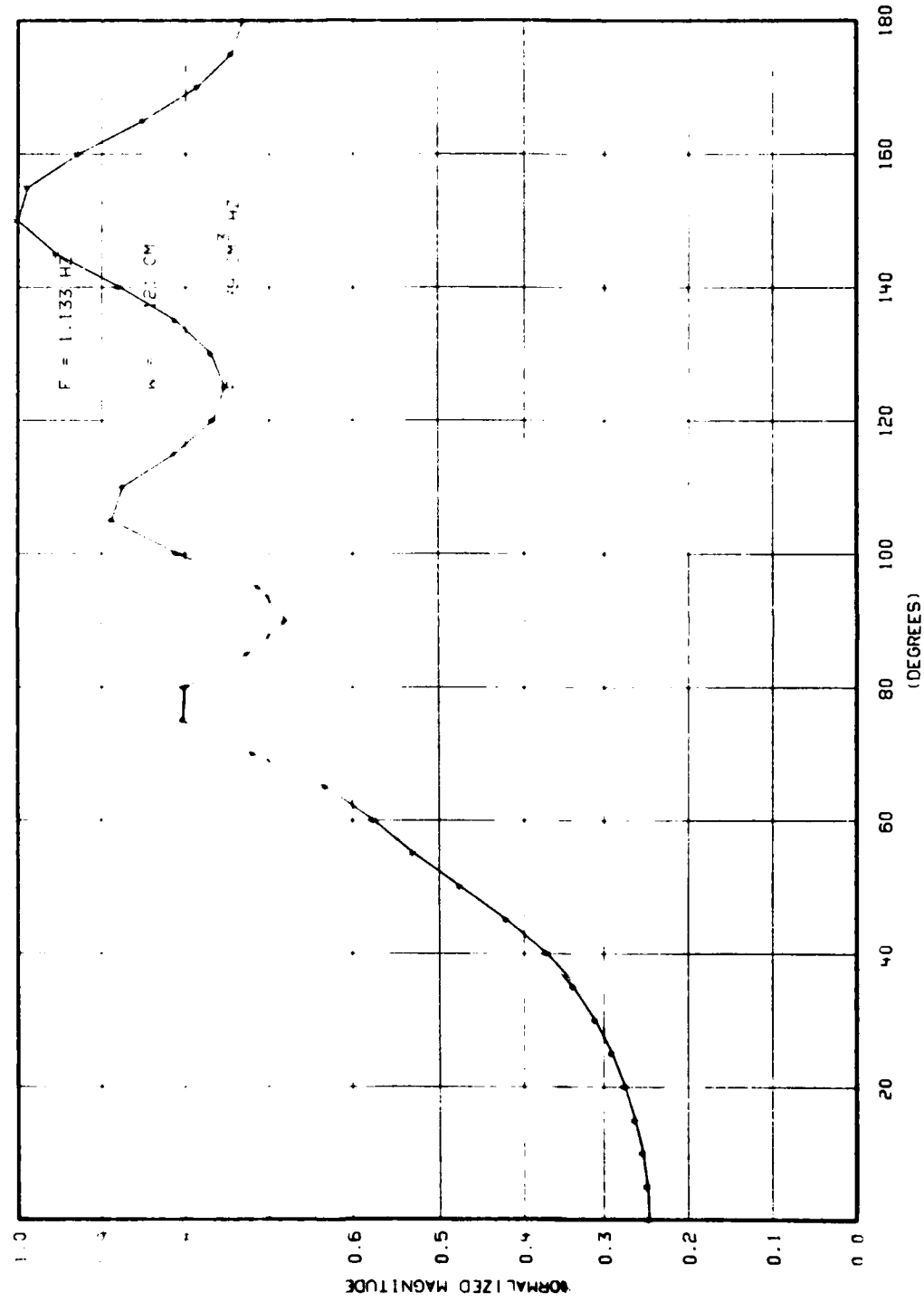


Figure F-32. Directional Spectrum for a Surface Wave Frequency of 1.133 Hz.

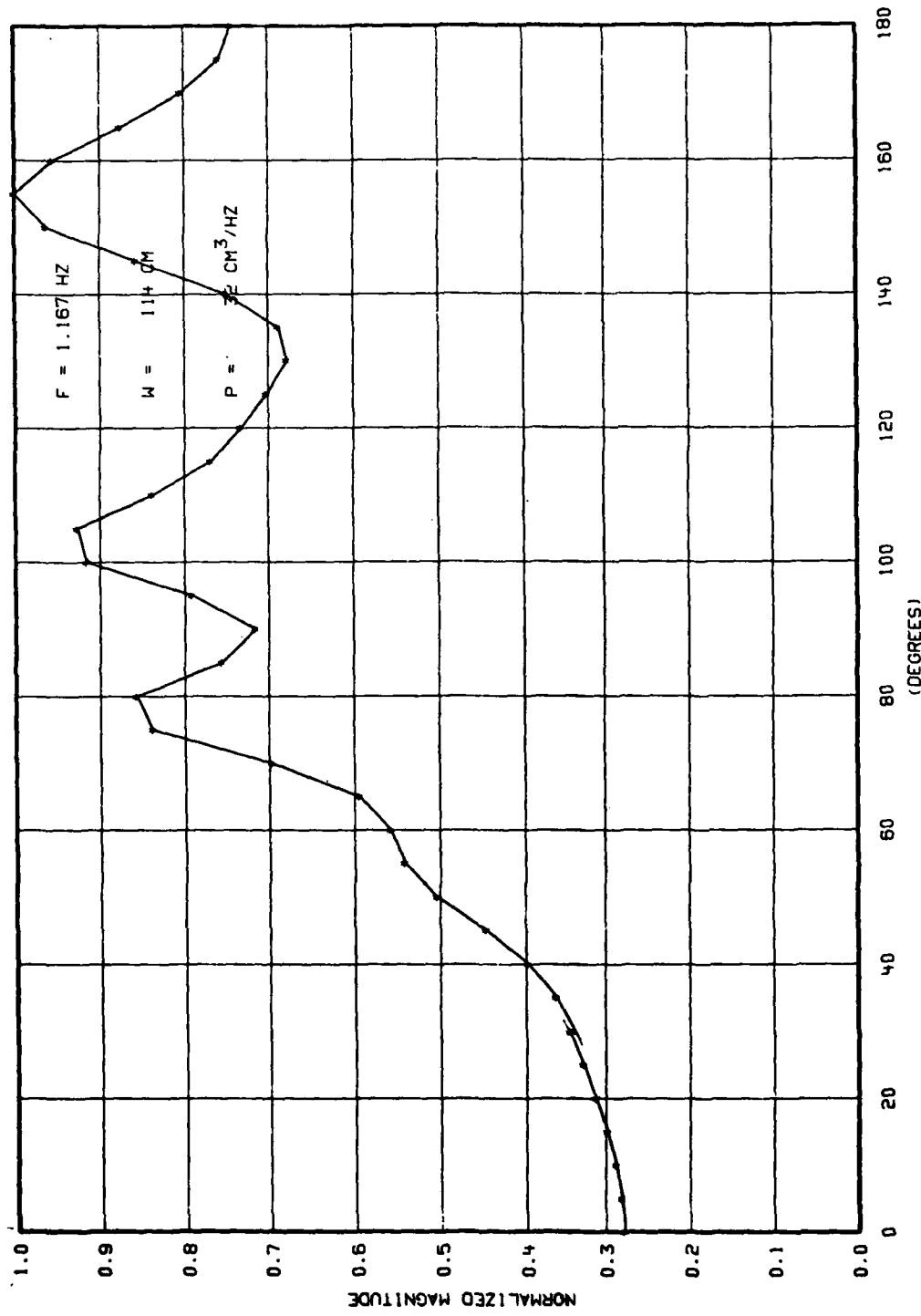


Figure F-33. Directional Spectrum for a Surface Wave Frequency of 1.167 Hz.

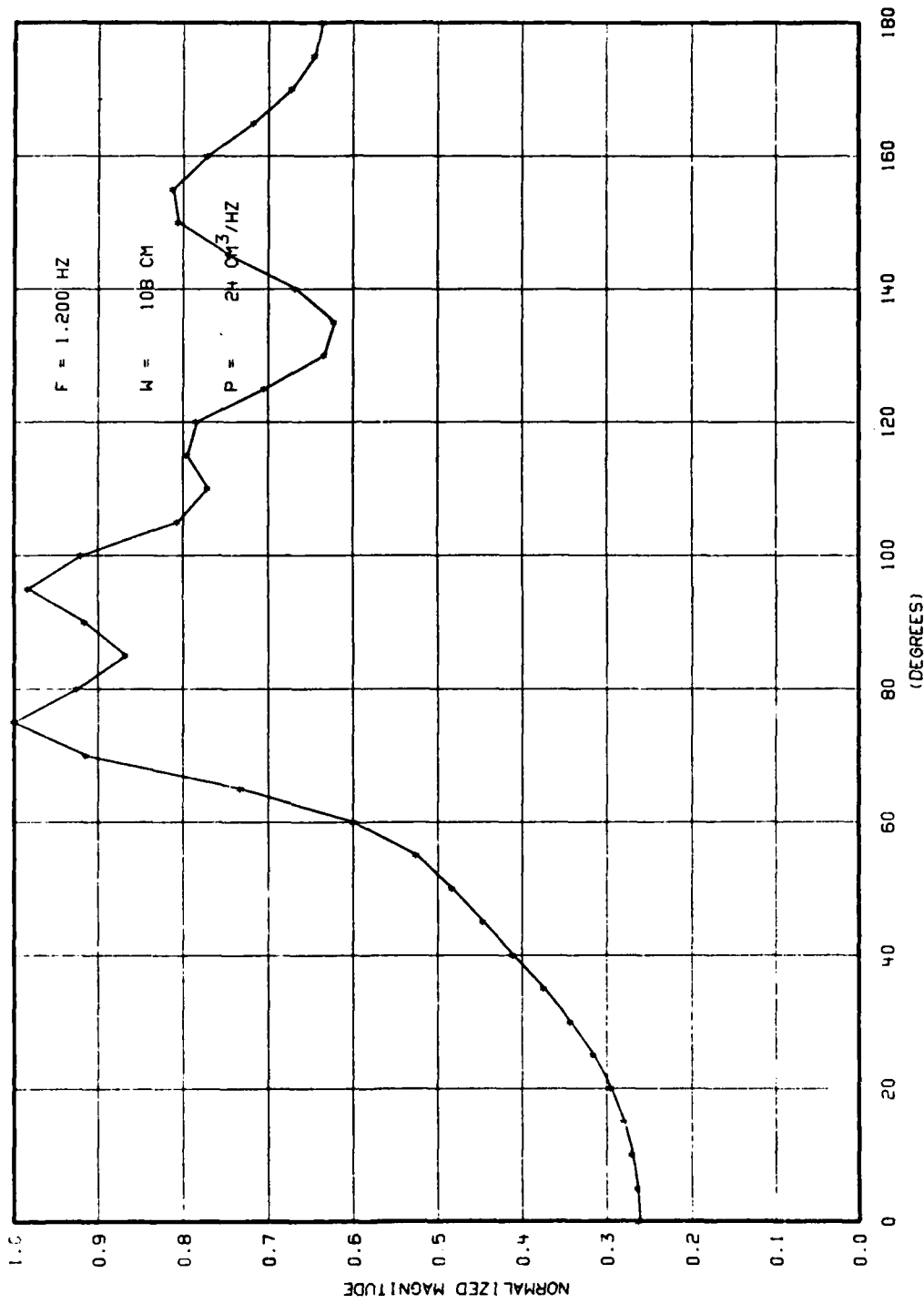


Figure F-34. Directional Spectrum for a Surface Wave Frequency of 1.200 Hz.

REFERENCES

- 1-1 Chapman, R. P. and Harris, J. H., "Surface Backscattering Strengths Measured with Explosive Sound Sources," J. Acoust. Soc. Am., 34, 1592-1597, 1962.
- 1-2 Liebermann, L. W., "Analysis of Rough Surfaces by Scattering," J. Acoust. Soc. Am., 35, 932, 1963.
- 1-3 Mellen, R. H., "Doppler Shift of Sonar Backscatter from the Surface," J. Acoustic. Soc. Am., 36, 1295-1396, 1964.
- 1-4 Roderick, W. I., "Acoustic Spectra of Specular and Near-Specular Scattering from a Three-Dimensional Traveling Sinusoidal Surface," J. Acoust. Soc. Am., 47, 112(A), 1970.
- 1-5 Igarashi, Y., and Stern, R., "Observation of Wind-Wave-Generated Doppler Shifts in Surface Reverberation," J. Acoust. Soc. Am., 49, 802-809, 1971.
- 1-6 Faure, P., "Theoretical Model of Reverberation Noise," J. Acoust. Soc. Am., 36, 259-269, 1964.
- 1-7 Swarts, R. L., "Doppler Shift of Surface Backscatter," J. Acoust. Soc. Am., 52, 457-461(L), 1972.
- 1-8 Crowther, P. A., "Measurements of the Spectrum of Sea Surface Reverberation at 10 kHz," Elliott Brothers (London) Ltd., Naval Div. Ref. No. ND(F)135.
- 2-1 Gallagher, J., "Mass Physical and Acoustic Properties of Surface Sediments in Block Island Sound," (unpublished Naval Underwater Systems Center Technical Memorandum), 1975.
- 2-2 Nalwalk, A. J., et al., "Final Report of Oceanographic Studies along the Block Island-Fisher Island (BIFI) Range in Block Island Sound from September 1972 to January, 1974," University of Connecticut, 1974.
- 2-3 Urick, R. J., Principles of Underwater Sound for Engineers, McGraw-Hill Book Company, Inc., New York, 1967.
- 2-4 Urick R. J., and Hoover, R. M., "Backscattering of Sound from the Sea Surface: Its Measurement, Causes, and Application to the Prediction of Reverberation Levels," J. Acoust. Soc. Am., 28, 1038-1042, 1956.
- 3-1 Beyer, R. T., Nonlinear Acoustics, written for the Naval Ship Systems Command, Department of the Navy, 1974.
- 3-2 Westervelt, P. J., "Parametric Acoustic Array," J. Acoust. Soc. Am., 35, 535-537, 1963.
- 3-3 Bellen, J. L. S., and Beyer, R. T., "Experimental Investigation of an End-Fire Array," J. Acoust. Soc. Am., 34, 1051-1054, 1962.

- 3-4 Berkay, H. O., "Possible Exploitation of Non-Linear Acoustics in Underwater Transmitting Applications," J. Sound Vib., 2, 435-461, 1965.
- 3-5 Mellen, R. H., Browning, D. G., and Konrad, W. L., "Parametric Sonar Transmitting Array Measurements," J. Acoust. Soc. Am., 49, 932-935, 1971.
- 3-6 Muir, T. G., and Willette, J. G., "Parametric Acoustic Transmitting Arrays," J. Acoust. Soc. Am., 52, 1481-1486, 1972.
- 3-7 Merklinger, H. M., "High Intensity Effects in the Non-Linear Acoustic Parametric End-Fire Array," Ph.D. Thesis (University of Birmingham, England, 1971).
- 3-8 Willette, J. G., "Difference Frequency Parametric Array Using an Exact Description of the Primary Sound Field," J. Acoust. Soc. Am., 52, 123(A), 1972.
- 3-9 Berkay, H. O., and Leahy, D. J., "Farfield Performance of Parametric Transmitters," J. Acoust. Soc. Am., 55, 539-546, 1974.
- 3-10 Bartram, J. F., "A Useful Analytical Model for the Parametric Acoustic Array," J. Acoust. Soc. Am., 52, 1042-1044, 1972.
- 3-11 Moffett, M. B., and Mellen, R. H., "Model for Parametric Acoustic Sources," J. Acoust. Soc. Am., 61, 325-337, 1977.
- 3-12 Konrad, W. L., (Personal Communication). Also, see "A Model for Parametric Sonar Radiator Design," NUSC Technical Memorandum PA4-229-71, 14 September 1971.
- 3-13 Kinsler, L. E., and Frey, A. E., Fundamentals of Acoustics, John Wiley and Sons, Inc., New York, 1962.
- 3-14 Lockwood, J. C., Muir, T. G., and Blackstock, D. T., "Directive Harmonic Generation in the Radiation Field of a Circular Piston," J. Acoust. Soc. Am., 53, 1148-1153, 1973.
- 4-1 Graeme, J. G., et al., Operational Amplifiers; Design and Applications, Burr-Brown Research Corporation, McGraw-Hill Book Company, Inc., 1971.
- 5-1 Middleton, D., An Introduction to Statistical Communication Theory, McGraw-Hill Book Company Inc., New York, New York, 1960.
- 5-2 Plemmons, T.D., "Spectra, Covariance Functions, and Associated Statistics of Underwater Acoustic Scattering From Lake Surfaces," Applied Research Laboratories, The University of Texas at Austin, ARL-TR-71-17, 1971.
- 5-3 Champeney, D. C., Fourier Transforms and Their Physical Applications, Academic Press Inc. London, LTD., 1973.
- 5-4 Bendat, J. S., and Piersol, A. G., Random Data: Analysis and Measurement Procedures, (Wiley-Interscience), John Wiley and Sons, Inc., New York, 1971.

- 5-5 Blackman, R. B., and Tukey, J. W., The Measurement of Power Spectra from the View of Communications Engineering, Dover Publications, Inc., New York, 1959.
- 5-6 Nuttall, A. H., "Spectral Estimation by Means of Overlapped Fast Fourier Transform Processing of Windowed Data," Naval Underwater Systems Center, NUSC Report No. 4169, 13 October 1971.
- 5-7 Roderick, W. I., and Cron, B. F., "Frequency Spectra of Forward-Scattered Sound from the Ocean Surface," J. Acoust. Soc. Amer., 48, 759-766, 1970.
- 5-8 Davenport, W. B., and Root, W. L., An Introduction to the Theory of Random Signals and Noise, McGraw-Hill Book Company, Inc., New York, 1958.
- 6-1 Beckmann, P., and Spizzichino, A., The Scattering of Electromagnetic Waves from Rough Surfaces, The Macmillan Company, New York, 1963.
- 6-2 Whalen, A. D., Detection of Signals In Noise, Academic Press, New York, 1971.
- 7-1 Marsh, H. W., "Doppler of Boundary Reverberation," J. Acoust. Soc. Am., 35, 1836(L), 1963.
- 7-2 Stevens, R. G., "On the Measurement of the Directional Spectra of Wind Generated Waves Using a Linear Array of Surface Elevation Detectors," Woods Hole Oceanographic Institution, Ref. No. 65-20 (Unpublished manuscript).
- 7-3 Bennett, C. M., "The Directional Analysis of Ocean Waves: An Introductory Discussion," Naval Coastal Systems Laboratory, Informal Report NCSL 144-72, December 1972.
- 7-4 Munk, W. H., Miller, G. R., Snodgrass, F. E., and Barber, N. F., "Directional Recording of Swell from Distant Storms," Philosophical Transactions of the Royal Society of London, Series A, Vol. 255, No. 1062, pp. 505-584, April 1963.
- 7-5 Longuet-Higgins, M. S., Cartwright, D. E., and Smith, N. D., "Observations of the Directional Spectrum of Sea Waves using the Motions of a Floating Buoy," Proc. Conf. on Ocean Wave Spectra, Easton, Md., Prentice-Hall, Englewood Cliffs, 1961.
- 7-6 Pierson, W. J., Jr. (Editor), "The Directional Spectrum of a Wind Generated Sea as Determined from Data Obtained by the Stereo Wave Observations Project," N. Y. University College of Engrg., Meteor. Pop. 2 (6), June 1960.
- 7-7 Barber, N. F., "The Directional Resolving Power of an Array of Wave Detectors," Proc. Conf. on Ocean Wave Spectra, Easton, Md., Prentice-Hall, Englewood Cliffs, New Jersey, 1961.

- 7-8 Nuttall, A. H., and Carter, G. C., "Estimation of the Two-Dimensional Spectrum of the Space-Time Noise Field for a Sparse Line Array," Naval Underwater Systems Center, NUSC Technical Report 4607, 22 August 1973.
- 7-9 Capon, J., "High-Resolution Frequency-Wavenumber Spectrum Analysis," Proc. IEEE, Vol. 57, 1408-1418, August 1969.
- 7-10 Capon, J., "Applications of Detection and Estimation Theory to Large Array Seismology," Proc. IEEE, Vol. 58, 760-770, May 1970.
- 7-11 MacKay, J. H., "On the Gaussian Nature of Ocean Waves," Engineering Experiment Station, Georgia Institute of Technology, Atlanta, Georgia, Project A-366, Internal Tech. Note 8 (see also, Kinsman, 1965).
- 7-12 Kinsman, B., Wind Waves, Prentice-Hall, Inc., Englewood Cliffs, New Jersey, 1965.
- 7-13 Phillips, O. M., The Dynamics of the Upper Ocean, University Press, Cambridge, 1966.
- 7-14 Carter, G. C., Knapp, C. H., and Nuttall, A. H., "Estimation of the Magnitude-Squared Coherence Function Via Overlapped Fast Fourier Transform Processing," IEEE Transactions on Audio and Electroacoustics, Vol. AU-21, 337-344, August 1973.
- 7-15 Capon, J., Greenfield, R. J., and Kolker, R. J., "Multidimensional Maximum-Likelihood Processing of a Large Aperture Seismic Array," Proc. IEEE, Vol. 55, 192-211, February 1967.
- 7-16 Lacoss, R. T., "Data Adaptive Spectral Analysis Methods," Geophysics 36, 661-675, 1971.
- 7-17 Nuttall, A. H., "Spectral Estimation by Means of Overlapped Fast Fourier Transform Processing of Windowed Data," Naval Underwater Systems Center, NUSC Report No. 4169, 13 October 1971.
- 7-18 Otnes, R. K., and Enochson, L., Digital Time Series Analysis, John Wiley and Sons, Inc., 1972.
- 8-1 Pierson, W. J. Jr., and Moskowitz L., "A Proposed Spectral Form for Fully Developed Wind Seas Based on the Similiarity Theory of S. A. Kitagorodskii," Geophysical Research Vol. 69, 5181-5190, 1964.
- 8-2 Carter, G. C., Knapp, C. H., and Nuttall, A. H., "Statistics of the Estimate of the Magnitude-Coherence Function," IEEE Transactions on Audio and Electroacoustic, Vol. AU-21, 388-389, August 1973.
- 9-1 Essen, H.-H., "Wave-Facet Interaction Model Applied to Acoustic Scattering from a Rough Sea Surface," Acustica, 31, 107-113, 1974.
- 9-2 Schwarze, H., "A Model for the Doppler Spread of Backscattered Sound from a Composite Roughness Sea Surface," SACLATCEN Memorandum SM-86, 1976.

- A-1 Nuttall, A. H., (Personal Communication)
- C-1 Zemanek, J., "Beam Behavior within the Nearfield of a Vibrating Piston," J. Acoust. Soc. Am., 49, 181-191, 1971.
- D-1 Roderick, W. I., "An Acoustic System for Measuring the Wave Height of Sea Surface Waves," J. Acoust. Soc. Am., 53, 352 (A). 1973.

INITIAL DISTRIBUTION LIST

Addressee	No. of Copies
COMOPTEVFOR	1
COMNLONTEVDET	1
COMSUBDEVGRUONE	1
COMSUBDEVGRUTWO	1
ASN(R&D) (D. E. Mann)	1
ONR Code 102-OS, 480, 486, 222	4
CNO Code OP-095, -0942U, -952, -95E, -951	5
NAVMAT Code MAT-08T, -08T2, -08T24	3
USDR&E (W. J. Perry)	1
NRL	1
NOO Code 02, 3400, 9320	3
NAVELECSYSCOMHQ Code 03, PME-124, ELEX 320	3
NAVSEASYS COM SEA-03C, -034, -06H, -06H1, -06H1-1, -06H1-4, -06H2, -09G3 (4)	11
NAVAIRDEV CEN	1
NAVWPNSCEN	1
DTNSRDC	1
NAVCOASTSYSLAB	1
NOSC	1
NISC	1
NAVPGSCOL	1
NAVWARCOL	1
APL/UW, Seattle	1
ARL/PENN STATE, State College	1
DIA DT-2C	1
Marine Physical Lab, Scripps	1
National Research Council, Committee Undersea Warfare	1
Woods Hole Oceanographic Institution	1
NORDA Code 110, 200, 300, 500, 600	5
DDC, Alexandria	12
Engineering Societies Library, United Engineering Center	1
Servicio De Hidrografia Naval (Dr. Jorge Novarini)	1
SACLANT	1
Instituto De Pesquisas Da Marinha (CDR Carlos E. Parente)	1